VOLUME EDITOR: J.B. GOODENOUGH

Localized to Itinerant Electronic Transition in Perovskite Oxides

Springer

98
Structure and Bonding

Localized to Itinerant Electronic Transition in Perovskite Oxides

Volume Editor: J.B. Goodenough

With contributions by
S.L. Cooper, T. Egami, J.B. Goodenough, J.-S. Zhou

Springer

The series *Structure and Bonding* publishes critical reviews on topics of research concerned with chemical structure and bonding. The scope of the series spans the entire Periodic Table. It focuses attention on new and developing areas of modern structural and theoretical chemistry such as nanostructures, molecular electronics, designed molecular solids, surfaces, metal clusters and supramolecular structures. Physical and spectroscopic techniques used to determine, examine and model structures fall within the purview of Structure and Bonding to the extent that the focus is on the scientific results obtained and not on specialist information concerning the techniques themselves. Issues associated with the development of bonding models and generalizations that illuminate the reactivity pathways and rates of chemical processes are also relevant.

As a rule, contributions are specially commissioned. The editors and publishers will, however, always be pleased to receive suggestions and supplementary information. Papers are accepted for *Structure and Bonding* in English.

In references *Structure and Bonding* is abbreviated *Struct. Bond.* and is cited as a journal.

Springer WWW home page: http://www.springer.de

Preface

Interest in the transition-metal oxides with perovskite-related structures goes back to the 1950s when the sodium tungsten bronzes Na_xWO_3 were shown to be metallic [1], the system $La_{1-x}Sr_xMnO_3$ was found to contain a ferromagnetic conductive phase [2], and $La_{0.5}Sr_{0.5}CoO_3$ was reported to be a ferromagnetic metal, but with a peculiar magnetization of 1.5 μ_B/Co atom [3].

Stoichiometric oxide perovskites have the generic formula AMO_3 in which the A site is at the center of a simple-cubic array of M sites; the oxide ions form $(180° - \phi)$ M—O—M bridges to give an MO_3 array of corner-shared $MO_{6/2}$ octahedra and the larger A cations have twelvefold oxygen coordination. Mismatch between the A—O and M—O equilibrium bond lengths introduces internal stresses. A compressive stress on the MO_3 array is accommodated by a lowering of the M—O—M bond angle from 180° to $(180° - \phi)$; a tensile stress on the M—O—M bonds is accommodated by the formation of hexagonal polytypes [4].

In the early 1950s, it was assumed that the transition-metal oxides would be sufficiently ionic that their d-state manifolds could be described by crystal-field theory and the interatomic spin-spin interactions by superexchange perturbation theory [5]. Early neutron-diffraction studies showed an antici-pated antiferromagnetic order of the MO_3 array in the insulators $LnCrO_3$ and $LnFeO_3$, where Ln is a lanthanide [6]. However, the anisotropic magnetic order in antiferromagnetic $LaMnO_3$ and the complex magnetic order found [7] in $La_{0.5}Ca_{0.5}MnO_3$ remained unreported until it was pointed out [8] that cooperative orbital ordering that removed the twofold σ-bonding e-orbital degeneracy at the high-spin Mn(III) ions could account for the magnetic order if the superexchange interactions were reexamined; this reexamination led to the first formulation of the rules for the sign of the superexchange interactions [8]. These predictions have since been fully corroborated [9–11].

The concept of a cooperative Jahn–Teller orbital ordering associated with localized e^1 and e^3 configurations, in which the orbital angular momentum L is quenched by the crystalline (ligand) fields, was rapidly extended to include the threefold-degenerate π-bonding manifolds where the cubic crystalline fields do not quench L completely [12]. In this case, two types of cooperative orbital ordering may occur: one quenches the residual L and the other maximizes L. Spin-orbit coupling prevents cooperativity in the paramagnetic state unless the cooperative distortions quench L; but where long-range collinear ordering of the spins occurs, spin-orbit coupling orders the orbital momenta even where

there is only a small concentration of Jahn–Teller ions [13]. The cooperativity in this case gives rise to a giant single-ion magnetocrystalline anisotropy and magnetostriction.

The ferromagnetic coupling in conductive $La_{1-x}Sr_xMnO_3$ led to the concept of double exchange, but the original formulation by Zener [14] was restricted to a two-manganese polaron that was assumed to move diffusively without an activation energy to give a global ferromagnetism. The latter assumption was not borne out experimentally and de Gennes [15], borrowing a spin-dependent transfer integral from Anderson and Hasegawa [16], made a more realistic double-exchange model for itinerant electrons in the presence of localized spins; but how itinerant electrons and localized spins from the same d manifold could coexist on an atom was not addressed until some years later [17] when it was also pointed out that the unusual magnetization of ferromagnetic, metallic $La_{0.5}Sr_{0.5}CoO_3$ could be understood as an intermediate spin state on the cobalt stabilized by itinerant σ^* electrons coexisting with a localized spin.

Meanwhile, the origin of the metallic conductivity of the Na_xWO_3 bronzes remained puzzling until it was pointed out [18] that strong W—O covalent bonding allowed the 180° W—O—W interactions across a bridging oxygen atom to be strong enough to transform the π-bonding d states from localized configurations into itinerant-electron states of a W—O antibonding π^* band. Recognition that the d electrons on the MO_3 array of an AMO_3 perovskite could be either localized or itinerant led to an early mapping of localized versus itinerant electronic behavior in the AMO_3 perovskites [19]. Moreover, it was found that narrow itinerant-electron σ^* bands containing a single e electron per atom did not undergo a cooperative Jahn–Teller ordering of localized orbitals; instead the cooperative oxygen displacements introduce a disproportionation reaction $2\sigma^{*1} = e^2 + e^0$ in which the e^2 configurations are localized and the e^0 configurations form molecular orbitals of an MO_6 complex [20]. This disproportionation reaction can be considered a segregation into an electron-rich, localized e^2 phase and an electron-poor, delocalized e^0 phase. This latter view of the disproportionation reaction makes it a special case of a more general phenomenon that is only now becoming recognized.

An extensive reexamination of the oxide perovskites was stimulated in 1986 by the discovery of high-temperature superconductivity in the perovskite-related system $La_{2-x}Sr_xCuO_4$ [21, 22] and the subsequent observation [23] of a colossal negative magnetoresistance (CMR) in the ferromagnetic system $(La_{1-y}Pr_y)_{0.7}Ca_{0.3}MnO_3$.

The ideal perovskite structure may be viewed as MO_2 planes alternating with AO rock-salt planes, which allows the formation of Ruddlesden–Popper [24] layered structures $AO \bullet (AMO_3)_n$; the original high-T_c, copper-oxide superconductors had the A_2MO_4 structure with M made a mixed-valent Cu(III)/Cu(II) ion by 10 to 22% substitution of Sr^{2+} or Ba^{2+} for La^{3+} on the A sites of the parent compound La_2CuO_4. The antibonding $x^2 - y^2$ orbitals of the Cu(III)/Cu(II) redox band are strongly hybridized with the $O:2p_x, 2p_y$ orbitals, so the Cu(III) ion is low-spin with fully occupied $3z^2 - r^2$ orbitals. Consequently, the Cu(III)/Cu(II) valence state is stable in square-coplanar oxygen

coordination, which allows the introduction of c-axis oxygen vacancies in the $CuO_{3-\delta}$ array to give eightfold oxygen coordination at smaller A cations. Moreover, AO-Φ-AO layers in which Φ is another oxide layer can be stabilized between the superconductive CuO_2 layers, all of which gives a rich chemistry to the superconductive copper oxides [25]. However, the essential features of the high-temperature-superconductor phenomenon are illustrated by the $La_{2-x}Sr_xCuO_4$ system.

High-T_c superconductivity in the layered copper oxides and the CMR phenomenon in the manganese oxide perovskites both occur at a transition from localized to itinerant electronic behavior, which has now focussed attention on the evolution of the electronic/structural properties at this cross-over in these mixed-valent oxide perovskites and at the Mott–Hubbard transition between strongly and weakly correlated electrons in the single-valent oxide perovskites. In perovskite-related structures, the study of the evolution of physical properties on crossing these transitions is made possible by a bandwidth that varies sensitively with the bending angle ϕ of the $(180° - \phi)$ M—O—M bond angle of the MO_3 array. This angle can be modulated by isovalent substitutions of smaller A-site cations without changing the valence state of the MO_3 array. The bandwidth is a measure of the strength of the M—O—M interactions, and this strength depends sensitively on the frequency $\omega_o(\phi)$ of the locally cooperative oxygen vibrations that couple strongly to the M-d electrons at cross-over.

The cross-over from localized to itinerant electronic behavior and the Mott-Hubbard transition cannot be described by the homogeneous theories of electronic states in solids that existed in 1986. Extensive experimental studies on these and related systems reveal the presence of dynamic phase segregations at lower temperatures that are associated with strong electron coupling to locally cooperative oxygen displacements. The phase segregations are driven by the appearance of a double-well potential at the equilibrium M—O bond length at cross-over. Locally cooperative, dynamic oxygen displacements are not revealed by conventional diffraction experiments; faster, local probes are required to observe them directly. These probes include the pair-density-function analysis of neutron-diffraction data from a synchrotron source as discussed in this volume by Egami as well as Mössbauer, NMR, NQR, and XAFS spectroscopies referred to in the other chapters. Indirect evidence for their existence is provided by transport and magnetic measurements, especially where these measurements can be correlated with observations of fast, local probes and with neutron-scattering data or the evidence from photoemission spectroscopy (PES) for spectral-weight transfer between itinerant and localized or vibronic electronic states. Evidence for strong electron coupling to cooperative, dynamic oxygen vibrations and its introduction of a variety of unconventional vibronic properties continues to accumulate rapidly as do the theoretical attempts to account for the data. This volume represents a progress report.

October 2000   John B. Goodenough

References

1. Brown BW, Banks E (1951) Phys Rev 84: 609
2. Jonker GH, Santen JH van (1950) Physica 16: 337
3. Jonker GH, Santen JH van (1953) Physica 19: 120
4. Goodenough JB, Kafalas JA, Longo JM (1972) In: Hagenmuller P (ed) Preparative methods in solid state chemistry. Academic Press, New York, chap 1
5. Anderson PW (1959) Phys Rev 115: 2
6. Koehler WC, Wollan EO (1957) J Phys Chem Solids 2: 100; Koehler WC, Wollan EO, Wilkinson MK (1960) Phys Rev 118: 58
7. Wollan EO, Koehler WC (1955) Phys Rev 100: 545
8. Goodenough JB (1955) Phys Rev 100: 564
9. Goodenough JB (1961) Magnetism and the chemical bond. Wiley Interscience, New York
10. Murakami Y, Hill JP, Gibbs D, Blume M, Koyama I, Tanaka M, Kawato H, Arima T, Hirota K, Endoh Y (1998) Phys Rev Lett 81: 582
11. Radaelli PG, Cox DE, Marezio M, Cheong S-W (1997) Phys Rev B55: 3015
12. Goodenough JB (1968) Phys Rev 171: 466
13. Wold A, Arnott RJ, Whipple E, Goodenough JB (1963) J Appl Phys 34: 1085
14. Zener C (1951) Phys Rev 82: 403
15. de Gennes P-G (1960) Phys Rev 118: 141
16. Anderson PW, Hasegawa H (1955) Phys Rev 100: 675
17. Goodenough JB (1971) Mat Res Bull 6: 967
18. Goodenough JB (1965) Bull Soc Chim France, No. 4: 1200
19. Goodenough JB (1972) Progress in Solid State Chemistry 5: 145
20. Goodenough JB (1975) J Solid State Chem 12: 148
21. Bednorz JE, Müller KA (1986) Z Physik B64: 189
22. Takagi H, Uchida S, Kitazawa K, Tanaka S (1987) J Appl Phys 26: L123
23. Hwang HY, Cheong S-W, Radaelli PG, Marezio M, Batlogg B (1995) Phys Rev Lett 75: 914
24. Ruddlesden SN, Popper P (1957) 10: 538; (1958) 11: 54
25. Goodenough JB, Manthiram A (1991) In: Rao CNR (ed) Chemistry of high temperature conductors. World Scientific, Singapore, Chap 1

Contents

Contents of Volume 97

Metal-Oxo and Metal-Peroxo Species in Catalytic Oxidations

Volume Editor: B. Meunier

General Considerations

John B. Goodenough

Texas Materials Institute, University of Texas at Austin, Austin, Texas 78712, USA
E-mail: jgoodenough@mail.utexas.edu

For reference, a few properties of AMO_3 perovskites are reviewed. Lattice distortions arising from the mismatch between equilibrium A—O and M—O bond lengths are discussed; a compressive stress on the MO_3 array gives cooperative rotations of the $MO_{6/2}$ octahedra that bend the $(180° - \phi)$ M—O—M bonds by an angle ϕ. Ligand-field wavefunctions for d electrons at transition-metal M atoms are used to distinguish, for single-valent MO_3 arrays, where the M—O—M interactions should be treated by superexchange perturbation theory from where they should be described by tight-binding band theory. Double-exchange and indirect-exchange interactions are also reviewed. The possible symmetries of the spin configurations of magnetic perovskites are specified. The virial theorem is employed to demonstrate the existence of lattice instabilities at a cross-over from localized to itinerant electronic behavior due to a double-well potential for the equilibrium M—O bond length with $(M—O)_{loc} > (M—O)_{itin}$. Long-range and short-range cooperative Jahn–Teller distortions are contrasted with charge-density-wave instabilities; polarons and correlation bags are contrasted with strong-correlation fluctuations.

Keywords: Perovskite distortions, Magnetic configurations, Fluctuation band narrowing, Interatomic exchange

1
Tolerance Factor

The cubic AMO_3 perovskite structure consists of an MO_3 array of corner-shared $MO_{6/2}$ octahedra with a larger A cation at the body-center position. As illustrated in Fig. 1, this structure allows formation of the Ruddlesden-Popper [1] rocksalt-perovskite intergrowth structures AO • $(AMO_3)_n$. In these phases, the mismatch of the equilibrium (M—O) and (A—O) bond lengths is given by the deviation from unity of the geometric tolerance factor

(a)

⬤(hatched)	◯	⬤
A	O	M

(b)

(c)

(d)

◯ X_{II}	⬤ X_I	⬤ A	● B

(e)
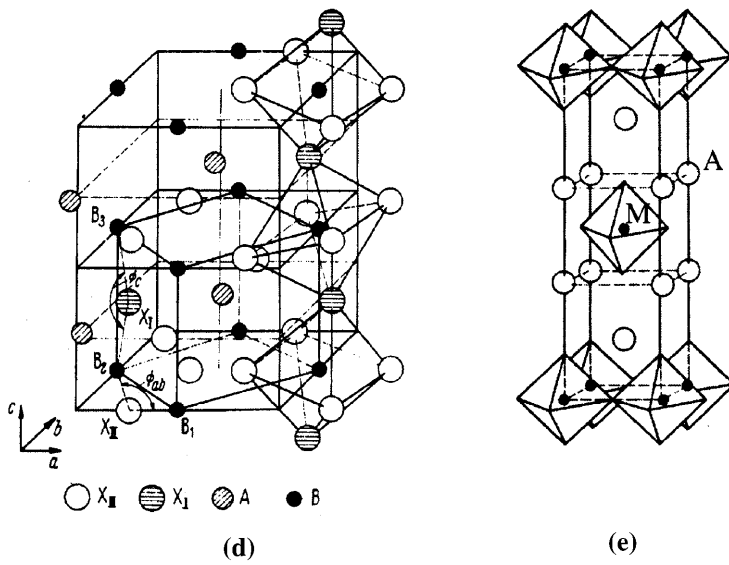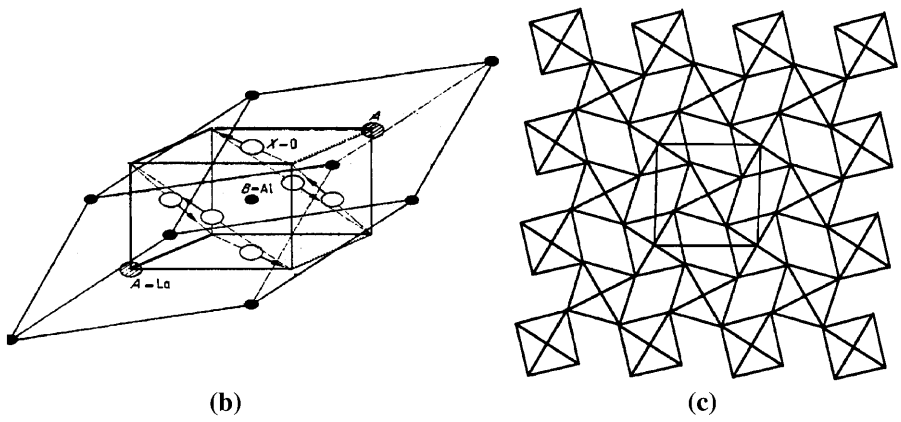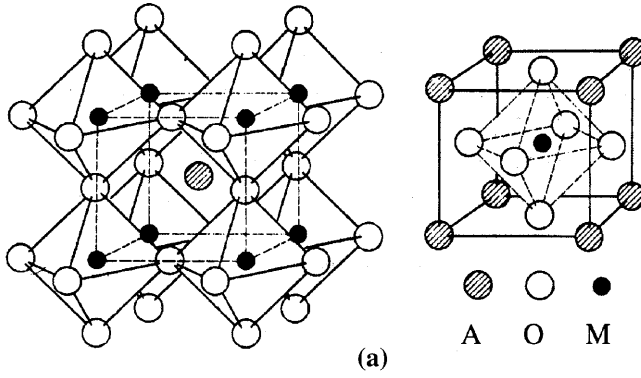
$$t \equiv (A\!-\!O)/\sqrt{2}(M\!-\!O) \tag{1}$$

where (A—O) and (M—O) are calculated for room temperature and atmospheric pressure from the tabulated sums of empirical ionic radii obtained from X-ray data [2, 3].

Of particular interest for the present volume are perovskite-related oxides in which M is a 3d-block transition-metal atom and the A sites are occupied by a lanthanide, yttrium, and/or an alkaline earth. Alkali ions can also be accommodated in the larger A sites, which are coordinated by twelve oxygen near neighbors. With a transition-metal atom M, the thermal expansion of the (A—O) bond is greater than that of the (M—O) bond, so t increases with temperature. Normally the (A—O) bond is also more compressible than the (M—O) bond, which makes t decrease with increasing pressure [4]. However, at a transition from localized to itinerant electronic behavior, an unusually high compressibility of the (M—O) bond results in a dt/dP > 0 (see Eq. (20) below) [5].

The AMO_3 structure accommodates a t > 1 by the formation of hexagonal polytypes [4]; the principal interest of these structures for the present discussion is the demonstration they provide for a dt/dP < 0 as the normal behavior.

The AMO_3 structure adjusts to a t < 1 by cooperative rotations of the $MO_{6/2}$ octahedra; these rotations create $(180° - \phi)$ M—O—M bond angles. For example, rotations about the [111] axis give rhombohedral $R\bar{3}c$ symmetry; rotations about a cubic [110] axis give orthorhombic Pbnm symmetry with $c/a > \sqrt{2}$ (in space group Pnma, $b/a > \sqrt{2}$). The bending angle ϕ increases with decreasing t, and ϕ increases discontinuously on passing from $R\bar{3}c$ to Pbnm symmetry. The Ruddlesden–Popper phases may also undergo cooperative rotations of the octahedra about a [110] axis to convert a high-temperature tetragonal (HTT) phase to orthorhombic symmetry; rotations about [010] and [100] axes in alternate basal planes give an enlarged tetragonal unit cell in a low-temperature tetragonal (LTT) phase.

The ability to adjust to a t < 1 allows for extensive cation substitutions on both the A and M sites; the structure is also tolerant of large concentrations of both oxygen and cation vacancies. The perovskites considered in this volume are stoichiometric with MO_3 arrays containing a single transition-metal atom M. Emphasis is given to the peculiar physical properties that occur at the transition from localized to itinerant electronic behavior and from Curie–Weiss to Pauli paramagnetism at a Mott–Hubbard transition on the MO_3 array. The transition from localized to itinerant electronic behavior can be approached from either the itinerant-electron side or the localized-electron side in single-valent MO_3 arrays by isovalent substitutions on the A sites that vary the tolerance factor t. It can also be crossed in mixed-valent

Fig. 1a–e. Some AMO_3 perovskite structures: **a** cubic (two views); **b** rhombohedral $R\bar{3}c$; **c** tetragonal (projection on (001) of MO_3 array); **d** orthorhombic (Pbnm); **e** tetragonal $La_2CuO_4{=}LaO \bullet LaCuO_3$

MO_3 arrays by aliovalent substitutions on the A sites. In all cases, the cross-over is marked by lattice instabilities. The Mott–Hubbard transition occurs on the itinerant-electron side, and this transition is also marked by lattice instabilities.

2
Electronic Considerations

The AMO_3 perovskites containing a 3d-block transition-metal atom M are sufficiently ionic that the Madelung energy stabilizes filled bonding bands that are primarily O-2p in character and separated from antibonding, primarily cation s and p bands by a large ($\sim$6 eV) energy gap. Lanthanide A-site cations introduce empty 5d states that overlap the antibonding s bands [6].

The $4f^n$ configurations at the Ln atoms are localized, and the intraatomic electron-electron coulomb energies are large, $U_{fn} > 5$ eV. Consequently the Ln atoms can have only a single valence state unless a $4f^n$ configuration happens to fall in the energy gap between the filled O-2p bands and the empty antibonding bands. The Ce^{4+} ion is too small to occupy the A site of a perovskite and the $Eu^{2+}:4f^7$ level, which is stable relative to the bottom of the 3d band in $EuTiO_3$, lies above the Fermi energy in the other $EuMO_3$ oxides containing a 3d-block transition-metal atom M. In the perovskite-related oxides to be discussed, only the $Pr:4f^2$ level lies close enough to the Fermi energy ε_F of a partially filled band to pose any ambiguity about the valence state of the Ln cation, and this ion only in the presence of the Cu(III)/Cu(II) redox couple. The examples discussed in this volume all contain Ln^{3+} ions with localized $4f^n$ and $4f^{n+1}$ configurations well-removed from the Fermi energy.

In the AMO_3 perovskites containing a 3d-block transition-metal atom M, the antibonding electrons of M-3d parentage may be either localized or itinerant [7]. In order to understand the transition from localized to itinerant electronic behavior, we begin with the construction of ligand-field 3d orbitals and then consider the nature of the interactions between localized ligand-field configurations on neighboring M cations and how the superexchange perturbation approximation breaks down.

2.1
Ligand-Field Considerations

The five 3d orbitals of a free atom are degenerate, but with more than one electron or hole in a 3d manifold, the spin degeneracy is removed by the ferromagnetic direct-exchange interactions between electron spins in orthogonal atomic orbitals. These exchange interactions produce the Hund intraatomic exchange field H_{ex}. The energy splitting between a high and lower localized spin state will be designated Δ_{ex}.

The atomic orbitals f_m with azimuthal orbital angular momentum operator L_z, where $L_z f_m = -i\hbar(\partial f_m/\partial \phi) = \pm m\hbar f_m$, have the angular dependencies

$$f_0 \sim (\cos^2 \theta - 1) \sim [(z^2 - x^2) + (z^2 - y^2)]/r^2$$
$$f_{\pm 1} \sim \sin 2\theta \exp(\pm i\phi) \sim [(yz \pm izx)]/r^2 \quad (2)$$
$$f_{\pm 2} \sim \sin^2 \theta \exp(\pm i2\phi) \sim [(x^2 - y^2) \pm ixy]/r^2$$

In an isolated octahedral site, the xy and (yz ± izx) orbitals only overlap the neighboring O-$2p_\pi$ orbitals while the $[(z^2 - x^2)+(z^2 - y^2)]$ and $(x^2 - y^2)$ orbitals only overlap the O-2s, $2p_\sigma$ orbitals. The resonance integrals $b^{ca} \equiv (f_m, H'\phi_o \approx \varepsilon_{mo}(f_m, \phi_o)$ describing the energy of a virtual charge transfer to the empty M-3d orbitals from the same-symmetry sum of near-neighbor oxygen orbitals ϕ_o contain both an overlap integral (f_m, ϕ_o) and a one-electron energy ε_{mo} that are larger for σ-bonding than for π-bonding. Therefore, the antibonding states of a σ-bond are raised higher in energy than those of a π-bond and, as a consequence, the cubic symmetry of the octahedral site raises the twofold-degenerate pair of σ-bonding e orbitals, the $[(z^2 - x^2) + (z^2 - y^2)]$ and $(x^2 - y^2)$ orbitals, above the threefold-degenerate set of π-bonding t orbitals xy, (yz ± izx) by an energy Δ_c and quenches the orbital angular momentum associated with m = ±2, see Fig. 2.

If the point-charge ionic model places the empty 3d orbitals of a degenerate manifold an energy ΔE_p above the O-2p orbitals and ΔE_s above the O-2s orbitals, the antibonding d-like states may be described in second-order perturbation theory to give the ligand-field wavefunctions

$$\psi_t = N_\pi(f_t - \lambda_\pi \phi_\pi)$$
$$\psi_e = N_\sigma(f_e - \lambda_\sigma \phi_\sigma - \lambda_s \phi_s) \quad (3)$$

provided the covalent-mixing parameters are $\lambda_\pi \equiv b_\pi^{ca}/\Delta E_p \ll 1$ and $\lambda_\sigma \equiv b_\sigma^{ca}/\Delta E_p \ll 1$. A larger ΔE_s keeps $\lambda_s \ll 1$ where Eq. (3) is applicable. If ΔE_p becomes too small or becomes negative, the perturbation expansion breaks down and an isolated MO_6 complex must be described by molecular-orbital (MO) theory. According to the second-order perturbation theory, the antibonding states are raised by the M—O interactions energy

$$\Delta \varepsilon = |b^{ca}|^2/\Delta E_i \quad (4)$$

and the cubic-field splitting is

$$\Delta_c = \Delta \varepsilon_\sigma - \Delta \varepsilon_\pi = \Delta_M + (\lambda_\sigma^2 - \lambda_\pi^2)\Delta E_p + \lambda_s^2 \Delta E_s \quad (5)$$

where Δ_M is a purely electrostatic energy that is small and of uncertain sign due to the penetration of the O^{2-}-ion electron cloud by the cation wavefunctions. Omitted from Eqs. (3) and (5) is the interaction of the ψ_t orbitals with the empty A-cation wavefunctions, which would lower the magnitude of an effective λ_π and increase Δ_c.

The cubic-field splitting Δ_c is the same order of magnitude as the intraatomic exchange energy Δ_{ex} and the d^4-d^7 configurations may be either high-spin t^3e^1, t^3e^2, t^4e^2, t^5e^2 where $\Delta_{ex} > \Delta_c$ or low-spin t^4e^0, t^5e^0, t^6e^0, t^6e^1
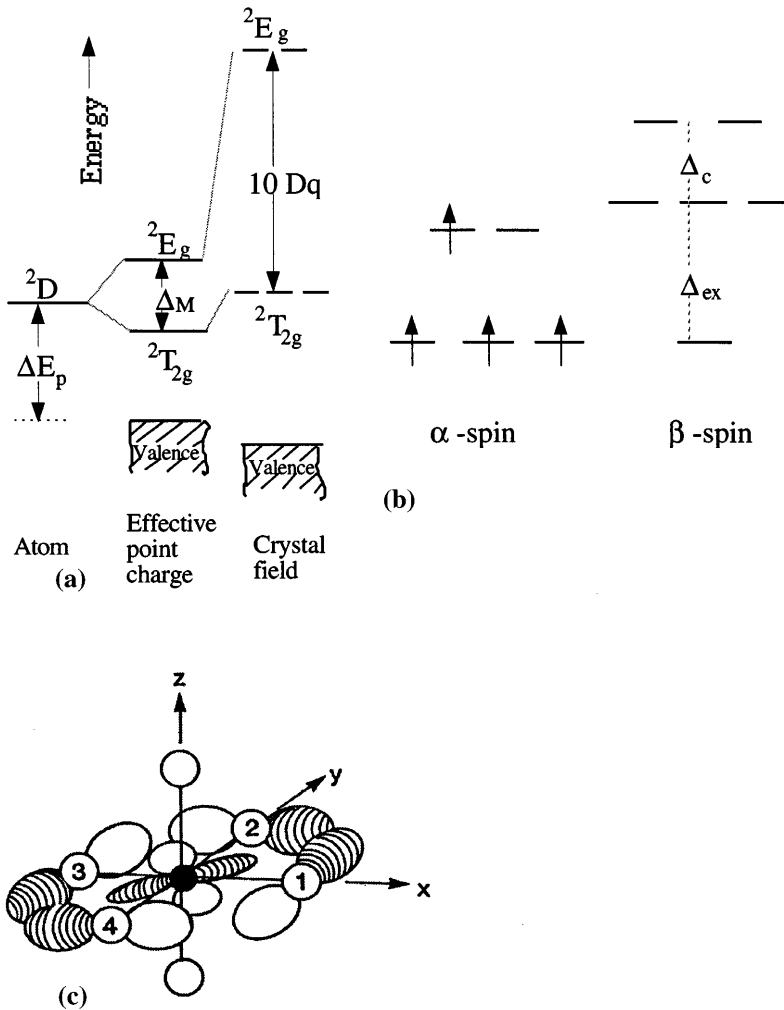
Fig. 2a–c. Schematic one-electron crystal-field splitting of the d-state manifold of a transition-metal atom M in a cubic AMO_3 perovskite: **a** $\Delta_{ex} = 0$; **b** $\Delta_{ex} > \Delta_c$ for high-spin Mn(III); **c** $\phi_\pi(xy) = p_y^{(1)} + p_x^{(2)} - p_y^{(3)} - p_x^{(4)}$ hybridizing with the Mn-xy orbitals

where $\Delta_c > \Delta_{ex}$. The covalent mixing of O-2p wavefunctions into ψ_t and ψ_e lowers the intraatomic exchange splitting Δ_{ex} and increases Δ_c.

Therefore, stronger covalent mixing stabilizes low-spin relative to high-spin configurations. Moreover, the effective energy U_{eff} required to add an electron to a d^n manifold to make it d^{n+1} must take into account Δ_c as well as Δ_{ex}. For an octahedral site, the $U_{\pi eff}$ for n = 3 and n = 8 is increased by Δ_c if $\Delta_c < \Delta_{ex}$, by Δ_{ex} if $\Delta_c > \Delta_{ex}$; for n = 5 it is increased by Δ_{ex} if $\Delta_c < \Delta_{ex}$ and for n = 6 by Δ_c if $\Delta_c > \Delta_{ex}$.

A comment on the celebrated Zaanen, Sawatzky, Allen [8] scheme is required. These authors begin with the free-ion energies of O^-/O^{2-} and the highest occupied $M^{(n+1)}/M^{n+}$ redox energies. They then calculate how the electrostatic crystalline fields of a point-charge model shift these energies relative to one another. If the Madelung energy does not shift the $M^{(n+1)}/M^{n+}$ level above the O^-/O^{2-} level, the energy gap between the lowest unoccupied $M^{n+}/M^{(n-1)+}$ redox energy and the highest occupied level is classified as a charge-transfer gap Δ; if the $M^{(n+1)+}/M^{n+}$ level lies above the O^-/O^{2-} level in the point-charge model, the energy gap is classified as a correlation gap U. Although these distinctions are useful for the interpretation of spectroscopic data and energy gaps, they have sometimes proven misleading when applied to the interpretation of transport data. In fact, as the $M^{(n+1)+}/M^{n+}$ level drops below the O^-/O^{2-} level, the antibonding states become pinned at the top of the bonding states as the ratio of O:2p to M:3d states in the strongly hybridized band changes from predominantly M:3d to predominantly O:2p. Hybridization gives the antibonding states the symmetry of the M:3d states, so we may still refer to σ^* and π^* bands. Pinning of the occupied antibonding band reduces U_{eff}, which in this case is referred to as Δ.

2.2
Interatomic Interactions

In the perovskite structure with 3d-block transition-metal atoms M, the dominant interactions between d-like orbitals centered at neighboring M atoms are the $(180° - \phi)$ M—O—M interactions. The spin-independent resonance integrals describing charge transfer between M atoms at R_i and R_j are

$$b_\pi^{cac} \equiv (\psi_{ti}, H'\psi_{tj}) \approx \varepsilon_\pi \lambda_\sigma^2$$
$$b_\sigma^{cac} \equiv (\psi_{ei}, H'\psi_{ej}) \approx \varepsilon_\sigma \lambda_\sigma^2 \cos\phi \tag{6}$$

where λ_π varies with the acidity of the A cations as well as with the bending angle ϕ and H' describes the perturbation of the potential at R_j caused by the presence of an M atom at R_i. The smaller term $\varepsilon_s \lambda_s^2$ is omitted from b_σ^{cac} for simplicity.

The interactions between localized spins on neighboring atoms are treated by a perturbation theory in which the spin-dependent resonance integrals for parallel and antiparallel coupling of spins are

$$t_{ij}^{\uparrow\uparrow} = b^{cac} \cos(\theta_{ij}/2) \quad \text{and} \quad t_{ij}^{\uparrow\downarrow} = b^{cac} \sin(\theta_{ij}/2) \tag{7}$$

for electron transfer between atoms whose spins are rotated by an angle θ_{ij} with respect to one another. The spin angular momentum is conserved in an electron transfer. Rules for the sign of the interatomic exchange interactions follow:

– *Direct exchange* between spins in orthogonal orbitals is a *potential exchange* as it does not involve electron transfer; like the intraatomic interactions, it is *ferromagnetic*.

– *Superexchange* interactions between spins **S** on like atoms is a *kinetic exchange* that involves virtual charge transfers between orbitals on neighboring atoms. These orbitals may be either

a) both *half-filled*, in which case spin transfers are constrained by the Pauli exclusion principle to be *antiferromagnetic*; in second-order perturbation theory,

$$\Delta\varepsilon_{ex}^{s} \sim -|t_{ij}^{\uparrow\downarrow}|^2/U_{eff} = Const + J_{ij}S_i \bullet S_j \tag{8}$$

where $J_{ij} \sim (2b_{ij}^2/4S^2 U_{eff})$, or

b) *half-filled and empty or half-filled and full*, in which case Δ_{ex} stabilizes a ferromagnetic charge transfer

$$\Delta_{ex}^{s} \approx Const - J_{ij}(S_i \bullet S_j) \tag{9}$$

where $J_{ij} \sim (2b_{ij}^2\Delta_{ex}/4S^2 U_{eff}^2)$ follows from third-order perturbation theory.

– *Double exchange* is also a *kinetic exchange*; this interaction involves a real charge transfer between two different valence states of the same M atom, each carrying a localized spin **S**, in a time τ_h that is short relative to the period ω_0^{-1} of the optical-mode lattice vibrations that would dress the charge carrier as a small polaron. Like molecular orbital or band theory, the real charge transfer is treated in first-order perturbation theory with Δ_{ex} stabilizing a *ferromagnetic* charge transfer:

$$\Delta\varepsilon_{ex}^{D} \sim czt_{ij}^{\uparrow\uparrow} = -czb_{ij}\cos(\theta_{ij}/2) \tag{10}$$

where c is the fractional occupancy of the M sites by a mobile charge carrier and z is the number of like nearest neighbors within a cluster or in a three-dimensional array.

– *Indirect exchange* is a coupling of localized spins at M atoms by a partially occupied broad band where Δ_{ex} is not large enough to remove totally the spin degeneracy of the broad band. The interaction is *ferromagnetic* at small separation, becomes *antiferromagnetic* at larger separation, and oscillates as the separation of the M atoms increases.

Bertaut [9] has adopted the notation of Koehler et al. [10] to describe the possible spin configurations compatible with the Pbnm crystallographic space group. Figure 3 represents the M atoms of an orthorhombic AMO_3 structure. Linear combinations of the spin components that transform into themselves are chosen as the base vectors of the irreducible representations:

$$F = S_1 + S_2 + S_3 + S_4$$
$$G = S_1 - S_2 + S_3 - S_4$$
$$C = S_1 + S_2 - S_3 - S_4$$
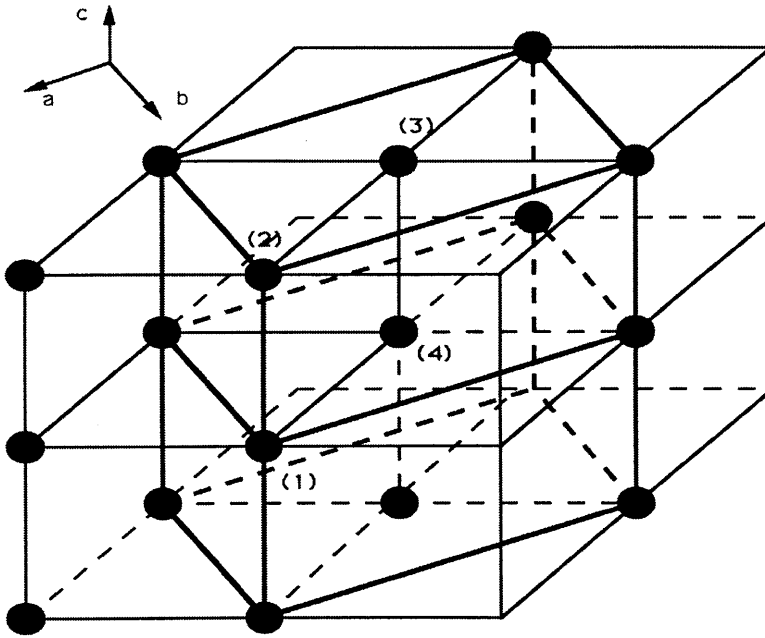$$A = S_1 - S_2 - S_3 + S_4$$

Fig. 3. Labeling of M-atom positions in the orthorhombic (Pbnm) structure of an AMO_3 perovskite

Subjecting these vectors to the crystallographic symmetry operations generates the four possible representations of the base vectors shown in Table 1. The x, y, z directions are taken parallel to the a, b, c axes of the orthorhombic unit cell. In orthorhombic perovskites, magnetocrystalline anisotropy of cooperatively tilted octahedra and/or Dzialoshinskii-Moriya *antisymmetric exchange* of the form $D_{ij} \bullet S_I \times S_j$ may be superimposed on the collinear-spin antiferromagnetic configuration stabilized by *symmetric exchange* of the form $J_{ij}S_i \bullet S_j$ to cant the spins, giving a weak ferromagnetic component. In this case, the spin configuration would be designated, for example, G_xF_z or C_yF_x as discussed in Goodenough and Zhou (this volume) for $LaVO_3$ and YVO_3. A large ferromagnetic component may be produced where an antiferromagnetic superexchange interaction varying as $\cos \theta$ competes with a double-exchange interaction varying as $\cos(\theta/2)$.

Table 1. Representations of base vectors of M-atom spins with space group Pbnm

Representations	Base	Vector for	M-atom spin
Γ_1	A_x	G_y	C_z
Γ_2	F_x	C_y	G_z
Γ_3	C_x	F_y	A_z
Γ_4	G_x	A_y	F_z

Where the MO_3 array is mixed-valent with both orbital and charge ordering, more complex spin configurations are found as discussed in Goodenough and Zhou (this volume) for $La_{0.5}Ca_{0.5}MnO_3$.

Spiral-spin configurations are found where the next-near-neighbor (nnn) interactions are competitive with the nearest-neighbor (nn) interactions. For example, where the nn spin-spin interactions are ferromagnetic and the nnn spin-spin interactions are antiferromagnetic, a ferromagnetic-spiral (helical) spin configuration propagating along a pseudocubic [111] axis would have the energy

$$W \sim -J_1 \cos\theta + J_2 \cos 2\theta \tag{11}$$

where J_1 and J_2 are, respectively, the magnitudes of the nn and nnn exchange parameters and θ is the angle of rotation of the spins between adjacent ferromagnetic (111) M-atom planes; there are 6 nn and 6 nnn M atoms, respectively, in nn and nnn (111) planes. Minimization of W with respect to θ gives

$$\cos\theta_o = J_1/4 J_2 \tag{12}$$

and a helical spin configuration is more stable than ferromagnetic order provided

$$4 J_2 > J_1 \tag{13}$$

Finally, extrapolation of the rules for the sign of the superexchange interaction, Eqs. (8) and (9), to itinerant-electron magnetism leads to the following rules for bands containing n electrons per band orbital ($0 \leq n \leq 2$ because of spin degeneracy):

1. Half-filled bands (n = 1) are antiferromagnetic.
2. Bands with $0 < n \leq 1/2$ or $3/2 \leq n < 2$ would be half-metallic ferromagnets with full magnetization $M = N \mu_B$ or $(2 - n)N \mu_B$ per band orbital, where N is the number of transition-metal atoms per unit volume, if narrow enough for total removal of the spin degeneracy; if the intraatomic electron-electron interactions are not strong enough to remove completely the spin degeneracy of the band, a spin-density wave (SDW) may be stabilized.
3. Bands with $1/2 < n < n_c$ or $n_c < n < 3/2$ would be ferromagnetic with a reduced magnetization $M = (1 - n)N \mu_B$ or $(n - 1)N \mu_B$ (only the antibonding orbitals of the band are magnetized). At $n_c \approx 2/3$ or $4/3$, there is a transition to antiferromagnetic order as the filling approaches n = 1.

The transition from localized to itinerant electronic behavior occurs where the interatomic interactions become greater than the intraatomic interactions. A measure of the strength of the interatomic interactions is the bandwidth W and of the strength of the intraatomic interactions is the energy U_{eff}; the transition from localized to itinerant electronic behavior occurs where

$$W \approx U_{eff} \tag{14}$$

In the absence of a localized spin on the M atoms, the tight-binding bandwidths are

$$W_\pi \approx 2\,zb_\pi^{cac} \quad \text{and} \quad W_\sigma \approx 2\,zb_\sigma^{cac} \tag{15}$$

where the number of like nearest neighbors is $z = 6$ for an MO_3 array. A $\lambda_\sigma > \lambda_\pi$ and a small ϕ makes

$$W_\sigma > W_\pi \tag{16}$$

The intraatomic interactions, on the other hand, are stronger the weaker the covalent mixing, which makes the on-site coulomb energies

$$U_\pi > U_\sigma \tag{17}$$

A $W_\pi < U_{\pi eff}$ can leave a t^3 manifold localized in the presence of a $W_\sigma > U_\sigma$ that transforms a single e electron per M atom into an itinerant electron occupying an antibonding σ^* band.

In $SrFeO_3$ and $CaFeO_3$, for example, a high-spin Fe(IV):$3d^4$ configuration has a $U_{\pi eff} = U_\pi + \Delta_c > U_\sigma$ and a $W_\pi < U_{\pi eff}$ with $W_\sigma > U_\sigma$. Consequently both a localized t^3 configuration and itinerant electrons in a narrow σ^* band coexist on the same atoms in the $(FeO_3)^{2-}$ array. Since the σ^* band has e-orbital parentage, it is orbitally twofold-degenerate and lifting of the spin degeneracy by Δ_{ex} leaves the majority-spin band half-filled. Therefore, $SrFeO_3$ is metallic, and the nearest-neighbor interactions are ferromagnetic as would be expected for a double-exchange interaction with a bandwidth

$$W_\sigma \approx 2\,zt_{ij}^{\uparrow\uparrow} \sim \varepsilon_\sigma \lambda_\sigma^2 \cos\phi \langle \cos(\theta_{ij}/2) \rangle \tag{18}$$

However, the long-range magnetic order is not ferromagnetic; a ferromagnetic spiral-spin configuration propagates along the cubic [111] direction below an antiferromagnetic Néel temperature $T_N = 130$ K, which indicates the presence of competing next-near-neighbor antiferromagnetic interactions. This magnetic order shows that the localized spins with $S = 3/2$ of the t^3 configurations may be coupled by the itinerant σ^*-band electrons via an indirect exchange, which occurs where the σ^* band is too broad for complete removal of the spin degeneracy of the σ^* electrons by the intraatomic exchange field H_{ex}.

Substitution of Ca for Sr increases ϕ and narrows the σ^* band, which could result in a change from a spiral-spin to ferromagnetic order. Instead, $CaFeO_3$ undergoes a charge-transfer reaction below 290 K between neighboring Fe(IV) atoms:

$$2\,Fe(IV) = Fe(IV + \delta) + Fe(IV - \delta) \tag{19}$$

where $\delta \to 1$ as the temperature is lowered [11]. This "negative-U" charge-density wave (CDW) may be described in the limit $\delta = 1$ as a phase

segregation into molecular-orbital (MO) states within a low-spin, diamagnetic $(FeO_6)^{7-}$ cluster and localized $Fe(III):t^3e^2$ configurations on alternate iron atoms of the FeO_3 array. The localized-spin $S = 5/2$ configurations couple antiferromagnetically via superexchange across the clusters; the next nearest-neighbor t^3-$O:2p_\pi$-t^3 antiferromagnetic and e^2-$O:2p_\sigma$-e^0 ferromagnetic interactions are not strong enough to stabilize a collinear-spin state. Such a segregation of the σ^*-band electrons into occupied localized states and empty MO states occurs as W_σ is narrowed toward the transition from itinerant to localized electronic behavior; it can be brought about in the perovskite structure by long-range cooperative oxygen displacements. We turn, therefore, to the role of oxygen displacements in the perovskite structure in response to lattice instabilities.

3
Oxygen Displacements

Cooperative displacements of the oxygen atoms from the middle of a $(180° - \phi)$ M—O—M bond may be superimposed on the structural modifications introduced by the mismatch of the mean equilibrium (A—O) and (M—O) bond lengths. This situation was first proposed [12] for $Mn(III):t^3e^1$ ions in $LaMnO_3$ and is now well-established where cooperative oxygen displacements remove a ground-state orbital degeneracy at a localized-electron configuration. This situation represents a cooperative Jahn–Teller orbital-ordering distortion.

As discussed in connection with Eq. (2), the cubic-field splitting quenches the orbital angular momentum of the twofold-degenerate e^1 configuration. Therefore, removal of the orbital degeneracy of the $Mn(III):t^3e^1$ configuration by a local Jahn–Teller (J-T) deformation of the octahedral site to tetragonal or orthorhombic symmetry is not constrained by spin-orbit coupling, and a cooperative J-T distortion of the lattice may occur in the paramagnetic state. On the other hand, the cubic-field splitting leaves $m = 0, \pm 1$ for the azimuthal orbital angular momentum quantum number of orbitally threefold degenerate t^n (n = 1, 2, 4, or 5) configurations. For a t^2 configuration at a V^{3+} ion, for example, a cooperative distortion of the octahedral sites may either quench or maximize the orbital angular momentum L. If the distortion quenches L, it may occur at any temperature; but if it maximizes L, it is constrained by spin-orbit coupling to occur where the spins are ordered nearly collinearly below a magnetic-ordering temperature [13]. This latter situation is well-illustrated by $LaVO_3$ and YVO_3 [14, 15].

In $LaMnO_3$, a first-order cooperative J-T distortion of the octahedral sites occurs at a $T_t \approx 875$ K; oxygen-atom displacements within the *a-b* plane of the orthorhombic Pbnm structure create long O···Mn···O bonds alternating with short O—Mn—O bonds such that each Mn atom has two short and two long bonds within an *a-b* plane. The O—Mn—O bonds along the *c*-axis are of intermediate length. The e-orbital degeneracy is removed by a site distortion to either tetragonal or orthorhombic symmetry or, as in $LaMnO_3$, to an intermediate distortion corresponding to a linear combination of the two. This

cooperative distortion changes the axial symmetry from $c/a > \sqrt{2}$ to $c/a < \sqrt{2}$ without changing the Pbnm space group. In order to distinguish the orbitally ordered phase with $c/a < \sqrt{2}$, the orbitally ordered phase has been designated O′ as distinct from O-orthorhombic [16]. Dynamic J-T deformations can give an O*-orthorhombic phase with $c/a \approx \sqrt{2}$.

The contrast between the oxygen displacements associated with this J-T orbital ordering, Fig. 4c, and the oxygen displacements found in low-temperature $CaFeO_3$, Fig. 4a, is significant; the former removes a localized-electron orbital degeneracy whereas the latter reflects the instability of a narrow σ^* band associated with what is formally an isoelectronic configuration: $Mn(III):t^3e^1$ and $Fe(IV):t^3\sigma^{*1}$.

Where the cooperative oxygen displacements are static and long-range-ordered, they can be established by a diffraction experiment. However, above the long-range ordering temperature, we can expect dynamic local cooperative
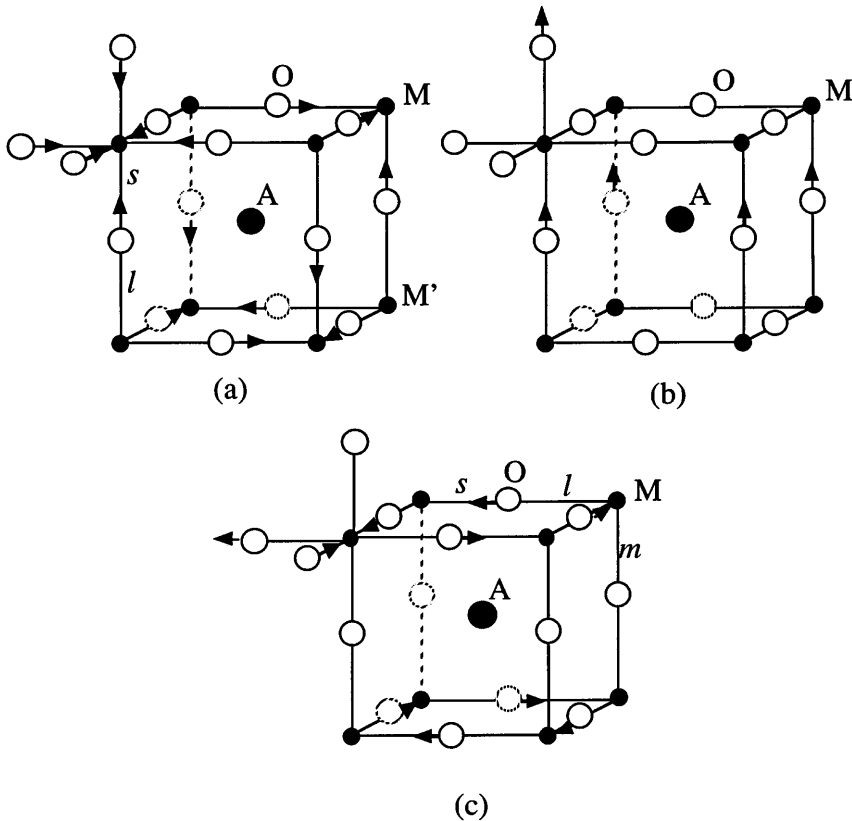

Fig. 4a–c. Cooperative oxygen displacements of oxygen towards one neighboring atom and away from the other found in low-temperature: **a** $CaFeO_3$ (disproportionation); **b** $PbTiO_3$ (ferroelectric); **c** $LaMnO_3$ (Jahn–Teller orbital order). Cooperative rotations of the $MO_{6/2}$ octahedra may coexist with these displacements

displacements to introduce strong electron-lattice interactions. Strong electron coupling to dynamic oxygen displacements are more difficult to establish. In a mixed-valent polaronic conductor, cooperative short-range oxygen displacements define the volume of the dielectric polaron; these displacements normally confine a mobile charge carrier to a single-site, thus defining a small polaron. However, at the cross-over from localized to itinerant electronic behavior, a dynamic Jahn–Teller deformation may increase the size of the polaron, as is discussed in Goodenough and Zhou (this volume) for the system $(La_{1-y}Nd_y)_{0.7}Ca_{0.3}MnO_3$.

If the volume of the electrons increases discontinuously on passing from localized to itinerant behavior, then the mean kinetic energy $\langle T \rangle$ of the electrons decreases discontinuously. According to the virial theorem for central-force fields, which states

$$2\langle T \rangle + \langle V \rangle = 0 \tag{20}$$

the magnitude of the mean potential energy $|\langle V \rangle|$ must then also decrease discontinuously. For antibonding electrons, a decrease in $|\langle V \rangle|$ is achieved by a decrease in the mean equilibrium $\langle M{-}O \rangle$ bond length; and if the change in $\langle T \rangle$ and $\langle Mn{-}O \rangle$ is discontinuous, the transition is first-order. At such a first-order phase change, the equilibrium $(M{-}O)$ bond length is described by a double-well potential and the localized-electron equilibrium bond length is larger than that for the itinerant electrons:

$$(M{-}O)_{loc} > (M{-}O)_{itin} \tag{21}$$

If the first-order transition were global, the system could undergo a simple dilatation of the lattice without any change in symmetry. Such a transition appears to occur in the metastable $B8_1$ phase of NiS quenched from high temperature [17] although the transition is accompanied by a small distortion [18]. In a mixed-valent perovskite, the structure allows for a phase segregation by short-range cooperative oxygen displacements at temperatures that are too low for atomic diffusion. Consider, for example, the system $PbTi_{1-x}Zr_xO_3$, which has a unit-cell volume that increases linearly with x in accordance with Végard's law. Pair-distribution analysis of pulsed-neutron data for this system has revealed a shift of the oxygen atoms from Zr toward Ti in a Ti${-}$O${-}$Zr bond and a larger bending of a Zr${-}$O${-}$Zr bond so as to allow the (Ti${-}$O) and (Zr${-}$O) bond lengths to retain their equilibrium values [19]. It follows from this observation that a segregation into localized and itinerant electronic phases within an MO_3 array can be accommodated by short-range cooperative oxygen displacements that define regions of shorter and longer mean $(M{-}O)$ bond lengths. In such a case, the cooperative oxygen displacements need not be static, but rather may be present as short-range fluctuations. Such a situation would introduce an important electron-lattice interaction even in a single-valent system. The formation of polarons in a mixed-valent system represents a strong electron-

lattice coupling, and Holstein [20] has shown that a polaron bandwidth may be described as

$$W = W_b \exp(-\lambda \varepsilon_p / \hbar \omega_O) \tag{22}$$

where W_b is the tight-binding bandwidth without electron-lattice interactions, ε_p is the stabilization energy of a polaron defined by cooperative atomic displacements of period ω_O^{-1}, and $\lambda \sim \varepsilon_p / W_b$ is a measure of the strength of the electron-lattice coupling. A similar expression

$$W = W_b \exp(-\lambda \varepsilon_{sc} / \hbar \omega_O) \tag{23}$$

can be expected for a single-valent system in which strong-correlation fluctuations are stabilized by an ε_{sc} in regions with $(M\text{—}O)_{loc}$ bond lengths defined by cooperative oxygen displacements of period ω_O^{-1} within a sea of Fermi-liquid electrons in a matrix with bond lengths $(M\text{—}O)_{itin} < (M\text{—}O)_{loc}$. This situation may be found on the approach to localized-electron behavior from the itinerant-electron side. On the approach to itinerant-electron behavior from the localized-electron side, small polarons (single M site) or correlation bags (cluster of M sites) may be described by molecular orbitals with $(M\text{—}O)_{itin}$ in a localized-electron matrix with $(M\text{—}O)_{loc}$. At cross-over, hybridization of electronic states and lattice vibrational modes of the same symmetry may produce heavy vibronic fermions.

Goodenough and Zhou (this volume) review the temperature dependences of the resistivity $\rho(T)$ and the thermoelectric power $\alpha(T)$ under different hydrostatic pressures P. These dependences, if used in conjunction with magnetic, structural, $^{18}O/^{16}O$ isotope-exchange, and photoemission data, provide critical information about the different types of electron-lattice interactions that occur in any given system.

4
References

1. Ruddlesden SN, Popper P (1957) Acta Cryst 10: 538; (1958) Acta Cryst 11: 54
2. Shannon RD, Prewitt CT (1969) Acta Cryst B25: 725
3. Shannon RD, Prewitt CT (1970) Acta Cryst B26: 1046
4. Goodenough JB, Kafalas JA, Longo JM (1972) In: Hagenmuller P (ed) Preparative methods in solid state chemistry. Academic Press, New York, Chap 1
5. Goodenough JB (1992) Ferroelectrics 130: 77
6. Oliver MR, Dimmock JO, McWhorter AL, Reed TB (1972) Phys Rev B5: 1078
7. Goodenough JB (1971) Prog Solid State Chem 5: 145
8. Zaanen J, Sawatzky GA, Allen JW (1985) Phys Rev Lett 55: 418
9. Bertaut EF (1963) In: Rado GT, Suhl H (eds) Magnetism: a treatise on modern theory and materials. Academic Press, New York, Chap 4

10. Koehler WC, Wollan EO, Wilkinson MK (1960) Phys Rev 118: 58
11. Takano M, Nakanishi N, Takeda Y, Naka S, Takada T (1977) Mat Res Bull 12: 923
11. a. Woodward PM, Cox DE, Moshopoulu E, Sleight AW, Morimoto S (2000) Phys Rev B 62: 844
12. Goodenough JB (1955) Phys Rev 100: 564
13. Goodenough JB (1968) Phys Rev 171: 466
14. Nguyen HC, Goodenough JB (1995) Phys Rev B52: 324
15. Ren Y, Palstra TTM, Khomskii DI, Pellegrin E, Nugroho AA, Menovsky AA, Sawatzky GA (1998) Nature 396: 441
16. Goodenough JB, Longo JM (1970) In: Hellwege KH (ed) Landolt-Börnstein Tabellen. New Series III/4a. Springer, Berlin Heidelberg New York, p 126
17. Sparks JT, Komoto T (1967) Phys Lett 25: 398; (1968) Revs Mod Phys 40: 752
18. Trahan J, Goodrich RG, Watkins SF (1970) Phys Rev 82: 2859
19. Teslic S, Egami T, Vieland D (1997) Ferroelectrics 194: 271
20. Holstein T (1959) Ann Phys (Paris) 8: 325

Transport Properties

John B. Goodenough and J.-S. Zhou

Texas Materials Institute, University of Texas at Austin, Austin, Texas 78712, USA
E-mail: jgoodenough@mail.utexas.edu

The resistivity $\rho(T)$ and thermoelectric power $\alpha(T)$ under different hydrostatic pressures are correlated with structure and other physical properties of single-valent and mixed-valent AMO_3 perovskites in which M is a first-row transition element. Special attention is given to transitions from localized to itinerant electronic behavior in the MO_3 array that are induced by pressure or by substitution on the A sites of isovalent or aliovalent cations. The lattice instabilities at this cross-over are shown to give rise to multicenter polarons on one side, strong-correlation fluctuations on the other, and to the formation of vibronic states at cross-over. Dynamic phase segregation gives rise to a colossal magnetoresistance (CMR) in mixed-valent manganese oxides; in the copper-oxide superconductors with perovskite-related structure, lattice instabilities are manifest in a spinodal segregation below room temperature between an antiferromagnetic parent phase and the superconductive phase on one side, to the superconductive phase and an itinerant-electron phase containing strong-correlation fluctuations on the other. The normal state of the superconductive phase is a complex polaron and vibronic liquid covering the compositional range $0.1 < p < 0.25$ holes/Cu atom just below 300 K. On cooling, ordering of the holes narrows the compositional range of the superconductive phase to a quantum critical point at $p_c \approx 1/6$. Where ordering of the holes leads to itinerant electrons in the CuO_2 sheets, itinerant-electron states hybridize with optical phonons propagating along Cu—O—Cu chains; the heavy fermions produce a superconductive gap with symmetry $(x^2 - y^2) + ixy$.

Keywords: Transition-metal perovskites, Metal-insulator transitions, Colossal magnetoresistance, High-temperature superconductivity, Multicenter polarons, Strong-correlation fluctuations, Heavy-fermion vibrons, Spinodal phase segregation, Cooperative orbital ordering

1
Single-Valent 3d-Block Perovskites

Table 1 summarizes the localized vs itinerant character of the $3d^n$ configurations of single-valent AMO_3 perovskites with 3d-block transition-metal atoms M. Configurations t^n and e^m refer to localized electrons, π^{*n} and σ^{*m} to itinerant electrons in narrow antibonding bands of t-orbital or e-orbital parentage. In the perovskite structure, deviation from unity of the tolerance factor

$$t \equiv (A{-}O)/\sqrt{2}(M{-}O) \tag{1}$$

is a measure of the mismatch of the equilibrium (A—O) and (M—O) bond lengths. In all families with t < 1, isovalent substitution of a smaller A cation reduces the strengths of both the π and σ M—O—M interactions. For background, refer to Goodenough, the first paper of this volume.

Table 1. Electronic configurations at first-row transition-metal ions M in AMO_3 perovskites

M	Perovskite	Configuration	Remarks[a]
Ti(IV)	$(Ca,Sr)TiO_3$	$\pi^{*0}\sigma^{*0}$	I
	$(Ba,Pb)TiO_3$	$\pi^{*0}\sigma^{*0}$	I, Ferroelectric
Ti(III)	$LaTiO_3$	$\pi^{*1}\sigma^{*0}$	s.c., Type-G AF ($T_N = 149$ K)
	$YTiO_3$	$\pi^{*1}\sigma^{*0}$	s.c., F ($T_C = 30$ K)
V(IV)	$(Ca,Sr)VO_3$	$\pi^{*1}\sigma^{*0}$	"metal", scf
V(III)	$(La,Y)VO_3$	$t^2\sigma^{*0}$	s.c. Type-C AF, J-T $T_{LS} < T < T_t$, LS $T < T_{LS} < T_N < T_t$
Cr(IV)	$SrCrO_3$	$\pi^{*2}\sigma^{*0}$	metal
	$CaCrO_3$	$\pi^{*2}\sigma^{*0}$	s.c., Type-G AF ($T_N = 90$ K)
Cr(III)	$LnCrO_3$	$t^3\sigma^{*0}$	I, Type-G AF
Mn(IV)	$(Ca,Sr)MnO_3$	$t^3\sigma^{*0}$	I, Type-G AF
Mn(III)	$LaMnO_3$	t^3e^1	I $\rightarrow$ cond @ T_t, J-T $T < T_t$, disp. fluctuations $T > T_t$, Type-A AF
Fe(IV)	$SrFeO_3$	$t^3\sigma^{*1}$	metal, AF(helix q$\|\langle 111\rangle$)
	$CaFeO_3$	$t^3\sigma^{*1}$	"metal", disp. $T < T_t$, AF(helix q$\|\langle 111\rangle$)
		$t^4\sigma^{*0}$	high-pressure phase
Fe(III)	$LnFeO_3$	t^3e^2	I, Type-G AF
Co(IV)	$SrCoO_3$	$\pi^{*5}\sigma^{*0}$	metal, F ($T_c = 212$ K)
Co(III)	$LaCoO_3$	$t^6\sigma^{*0} \rightarrow t^5\sigma^{*1}$	I $\rightarrow$ cond.
Ni(III)	$LaNiO_3$	$t^6\sigma^{*1}$	"metal", scf.
	$PrNiO_3$	$t^6\sigma^{*1}$	s.c.- metal @ $T_t = T_N$, SDW/CDW
	$SmNiO_3$	$t^6\sigma^{*1}$	s.c.- metal @ $T_t > T_N$, SDW/CDW
	$YNiO_3$	$t^6\sigma^{*1}$	s.c., disp. $T < T_t$, AF $T_N < T_t$
Cu(III)	$La_{1-x}Nd_xCuO_3$	$t^6\sigma^{*2}$	"metal", scf.

[a] I = insulator, s.c. = semiconductor, cond. = conductor, AF = antiferromagnetic, F = ferromagnet, scf = strong-correlation fluctuations, J-T = cooperative Jahn-Teller orbital ordering, LS = J-T that maximizes orbital angular momentum, dis. = disproportionation $2\sigma^{*1} = e^0 + e^2$, SDW/CDW = spin/charge-density wave.

1.1
The Titanates

1.1.1
Ti(IV)

$CaTiO_3$ and $SrTiO_3$ have empty π^* and σ^* bands; the bottom of the π^* band is located about 3.1 eV above the $O:2p^6$ valence band [1]. They are dielectric insulators. A tolerance factor $t < 1$ in $CaTiO_3$ is accommodated by a cooperative rotation of the $TiO_{6/2}$ octahedra about the cubic [110] axis to give an O-orthorhombic ($c/a > \sqrt{2}$) distortion. At room temperature, $SrTiO_3$ is cubic with a $t \approx 1.0$. On lowering the temperature, the larger thermal expansion of the Sr—O bond relative to the Ti—O bond reduces t; and below 110 K, the structure accommodates a $t < 1$ by a cooperative rotation of the $TiO_{6/2}$ octahedra about the cubic [001] axis to give tetragonal symmetry. In $BaTiO_3$, the structure accommodates to a $t > 1$, which would stretch the Ti—O bond from its equilibrium value, either by the formation of a 6H polytype or

by a series of long-range-cooperative ferroelectric oxygen displacements. A 6H perovskite polytype retains close-packed AO_3 planes, but these planes have hexagonal stacking alternating with two cubic stackings. The ferroelectric distortions create short and long Ti—O···Ti bonds; on lowering the temperature, static cooperative oxygen-atom displacements occur first along one, then along two, and finally along all three cubic axes [2]. Itoh et al. [2a] have induced a ferroelectric transition below a $T_c = 23$ K in $SrTiO_3$ by the substitution of ^{18}O for ^{16}O; the heavier ^{18}O softens the frequency of the optical-mode vibration that becomes static in the ferroelectric phase.

Accommodation of a lattice instability by long-range-cooperative oxygen displacements is a characteristic feature of the perovskite structure; the long-range order minimizes the elastic energy associated with local deformations. In the case of ferroelectric $BaTiO_3$, the oxygen displacements stabilize the electrons of the narrow TiO_3 π bands by localizing the electrons in Ti—O molecular π orbitals in which the oxygen atoms form stronger covalent bonding with one Ti(IV) near neighbor than they can achieve by sharing their covalent bond strength with two Ti(IV) near neighbors. In this respect, the ferroelectric Ti—O···Ti π bond is analogous to the asymmetric hydrogen bond O—H···O. Where long-range-cooperative oxygen displacements are static, as in ferroelectric $BaTiO_3$, they can be detected directly by X-ray and neutron diffraction. Where the oxygen displacements are dynamic, they give rise to a large dielectric susceptibility. However, where the perovskites are electronic conductors, oxygen displacements that are short-range cooperative and/or dynamic are more difficult to detect and characterize. This latter problem is a principal theme of this review.

1.1.2
Ti(III)

$LaTiO_3$ and $YTiO_3$ have a single electron per titanium atom in a narrow π^* band of the TiO_3 array; both compounds are O-orthorhombic with $c/a > \sqrt{2}$ as a result of a $t < 1$. Although they are isostructural (except for a larger distortion in $YTiO_3$) and isoelectronic, $LaTiO_3$ is a Type-G (See Table 1 of Goodenough, this volume) antiferromagnet and $YTiO_3$ is ferromagnetic [3, 4]. Figure 1 shows the $La_{1-x}Y_xTiO_3$ phase diagram; narrowing the π^* band by substitution of Y(III) for La(III) reduces the antiferromagnetic Néel temperature from $T_N \approx 140$ K for $LaTiO_3$ in the range $0 = x < 0.8$ and increases the ferromagnetic Curie temperature to $T_C \approx 30$ K for $YTiO_3$ in the range $0.8 < x = 1.0$; long-range magnetic order appears to be suppressed at the cross-over from antiferromagnetic to ferromagnetic order [4]. With increasing atomic number of the lanthanide ion Ln in $LnTiO_3$, T_N of the TiO_3 decreases from La to Sm whereas a ferromagnetic T_C of the TiO_3 array increases from Gd to Dy [5]. The long-range magnetic order and semiconductive character of the system $La_{1-x}Y_xTiO_3$ shows that the system is on the strong-correlation side of the Mott–Hubbard transition with an on-site electrostatic energy $U_\pi > W_\pi$. However, the lack of a cooperative Jahn–Teller deformation below T_N signals
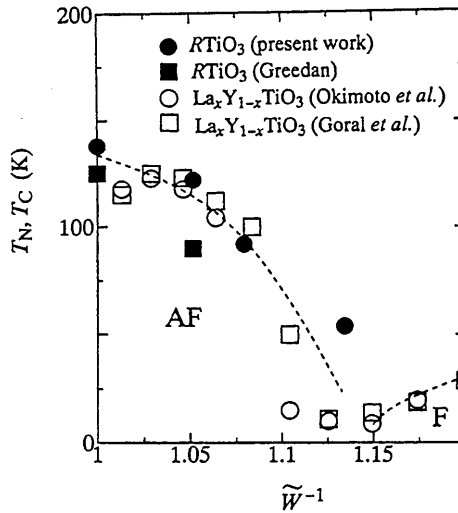
Fig. 1. Magnetic transition temperatures for the system $La_{1-x}Y_xTiO_3$. The antiferromagnetic (AF) phase is weakly ferromagnetic with spin canting; after [4]

that $LaTiO_3$ is an itinerant-electron antiferromagnet in which the interatomic interactions remain competitive with the intraatomic interactions. Substitution of Y for La weakens the interatomic interactions, and the energy gap $E_g = (U_\pi - W_\pi)$ increases from about 0.2 eV in $LaTiO_3$ to 1.2 eV on approaching $YTiO_3$ [4]. Ferromagnetic order is to be expected for a narrow band that is less than one-quarter filled, which is what is found in $YTiO_3$ with a larger ratio U_π/W_π. Antiferromagnetism shows that, with the smaller U_π/W_π ratio of $LaTiO_3$, U_π is not large enough to remove totally the spin degeneracy of a lower Hubbard band even though it is large enough to create an energy gap $E_g = (U_\pi - W_\pi)$ and Curie-Weiss paramagnetism [5]. Photoemission spectra (PES) have shown [6] the coexistence of electrons in Fermi-liquid states and in a lower Hubbard band in $LaTiO_{3+\delta}$, $\delta = 0.03 \pm 0.01$. Analysis of $^{47,49}Ti$ frequency-swept NMR spectra [6a] indicates that the NMR spectrum of $YTiO_3$ is consistent with a model of orbital ordering of itinerant electrons to account for the ferromagnetic order whereas that of $LaTiO_3$ can be explained without orbital ordering. These results indicate that the system $La_{1-x}Y_xTiO_3$ is on the strong-correlation side of the Mott–Hubbard metal-insulator transition, but only approaches from the itinerant-electron side the transition from itinerant to localized electronic behavior. The pressure dependence $dT_N/dP > 0$ in $LaTiO_3$ [7] reflects the increase in T_N with bandwidth found in the $La_{1-x}Y_xTiO_3$ system and $LnTiO_3$ family rather than an increase in the super-exchange coupling between localized spin configurations. Apparently a distinction needs to be made between the Mott–Hubbard and itinerant-localized electronic transitions.

1.2
The Vanadates

1.2.1
V(IV)

Like the system $La_{1-x}Y_xTiO_3$, the system $Sr_{1-x}Ca_xVO_3$ contains one electron per formula unit in a narrow π^* band. However, the O-orthorhombic distortion is smaller and decreases with decreasing x until $SrVO_3$, which appears to be cubic at room temperature. The V^{4+}/V^{3+} redox couple is more stable than the Ti^{4+}/Ti^{3+} couple, which increases the covalent mixing parameter λ_π and hence the bandwidth $W_\pi \approx \varepsilon_\pi\lambda_\pi^2$ (See Eqs. (6) and (15) of Goodenough, this volume). Unlike $La_{1-x}Y_xTiO_3$, the system $Sr_{1-x}Ca_xVO_3$ remains metallic to lowest temperatures for all x [8]. Dougier et al. [9] reported that stoichiometric $SrVO_3$ exhibits a ferromagnetic spin-density wave below 85 K; but it undergoes a first-order loss of oxygen to $SrVO_{2.9}$ in which case it remains Pauli paramagnetic to lowest temperatures. A small deviation from oxygen stoichiometry renders $CaVO_3$ antiferromagnetic like $LaTiO_3$ [10]. It is clear that the stoichiometric system $Sr_{1-x}Ca_xVO_3$ approaches the Mott–Hubbard electronic transition from the itinerant-electron side whereas the system $La_{1-x}Y_xTiO_3$ lies between the Mott–Hubbard and itinerant-localized electronic transitions.

In the absence of long-range magnetic order, the approach to a first-order Mott–Hubbard transition could manifest itself in lattice instabilities that stabilize strong-correlation fluctuations in a Fermi-liquid background (see Eq. (20) of Goodenough, this volume and following text). The volume of such a fluctuation would be defined by cooperative oxygen displacements of period $\omega_O^{-1} \approx 10^{-12}$ s; ω_O is the frequency of the cooperative oxygen displacements that define the volume of a second-phase fluctuation. Evidence that this is the case comes from photoemission spectroscopy (PES), which is a fast enough experimental probe to see fluctuations on time scales shorter than ω_O^{-1}.

Morikawa et al. [11] have performed an elegant study of $SrVO_3$ and $CaVO_3$ with inverse, high-resolution PES (Fig. 2). The data show the coexistence of two d-electron spectra: one is located well below the Fermi energy and corresponds to strongly correlated states in a lower Hubbard band (split by U_π from an empty upper Hubbard band); the other corresponds to itinerant-electron (Fermi-liquid) states having a sharply defined Fermi surface. Moreover, Fig. 2 also shows a significant transfer of states from the Fermi-liquid to the strongly correlated spectrum in $CaVO_3$ compared to $SrVO_3$ as should be expected for a narrower π^* band in $CaVO_3$. Although the density of states in the lower Hubbard band is amplified by greater electron localization at the surface, transfer of spectral weight to the strongly correlated states also occurs in the bulk. Inoue et al. [12] performed similar measurements on the $Sr_{1-x}Ca_xVO_3$ system; they showed a continuous transfer of states with increasing x from the Fermi-liquid to the strongly correlated spectrum and an effective mass m^* for the Fermi-liquid states that passed through a maximum with increasing x. This behavior is quite different from the conventional Mott–
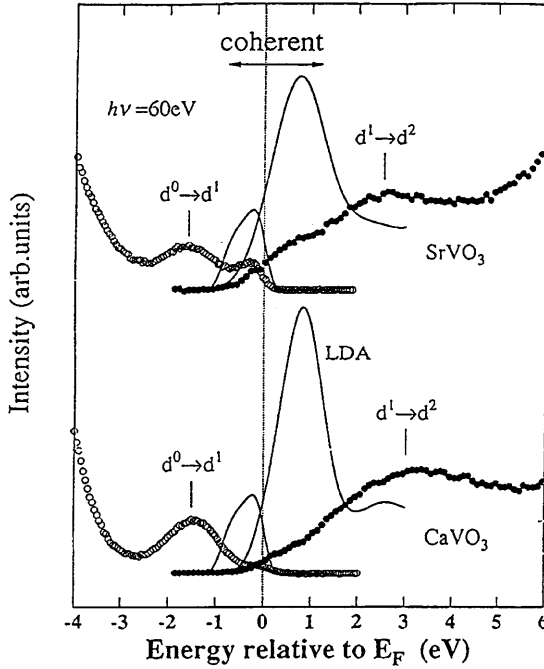
Fig. 2. Photoemission and inverse-photoemission spectra of $SrVO_3$ and $CaVO_3$ in the V-3d band region compared with an LDA band-structure calculation by Takegahara K (1994) J Electron Spectrosc Relat Phenon 66: 303; after [11]

Hubbard picture of a smooth, global opening of an energy gap as the bandwidth of a single-valent system narrows from that of a Pauli-paramagnetic metal to that of a Curie–Weiss magnetic insulator. The PES data clearly show that, in the absence of an itinerant-electron antiferromagnetic SDW and the opening of an energy gap $E_g = (U_\pi - W_\pi)$ as found in $LaTiO_3$, there can be a dynamic segregation into localized-electron configurations within a matrix containing itinerant electrons as a result of short-range-cooperative oxygen displacements. Since the π^* states are antibonding, the equilibrium $(V—O)_{loc}$ bond length for the strong-correlation fluctuations would be greater than the $(V—O)_{itin}$ equilibrium bond length for the Fermi-liquid matrix, as was predicted in Eq. (21) of Goodenough, this volume, from the virial theorem. These PES data have led us to suggest [13] that the phase diagram of Fig. 3 should, at least in this case, replace the conventional Mott–Hubbard model; U/U_c is the critical condition for the opening of an energy gap $E_g = (U - W)$, and the Mott–Hubbard model is modified by the introduction of a two-phase region at the approach to $U = U_c$. Brinkman and Rice [14] have predicted a ratio of the effective electron mass to the bare electron mass

$$m^*_{e-e}/m_b = [1 - (U/U_c)^2]^{-1} \qquad (2)$$
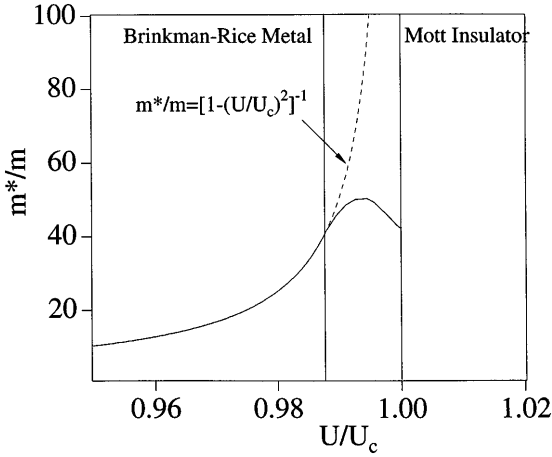
Fig. 3. Schematic variation of a normalized effective mass vs normalized Hubbard energy U for a mass-enhanced metal; after [13]

for a strongly correlated, globally homogenous system of electronic quasi-particles. This ratio is plotted in Fig. 3; a departure from the predicted ratio would occur where the homogeneous system breaks down into a heterogeneous electronic system. In accordance with the PES data, m^*_{e-e}/m_b for the Fermi-liquid states is shown reaching a maximum within the range where strong-correlation fluctuations coexist with Fermi-liquid electrons. Depression of the m^*_{e-e}/m_b curve of the Fermi-liquid phase from the Brinkman–Rice curve in the two-phase region increases with the transfer of spectral weight from the Fermi surface to the lower Hubbard band associated with strong-correlation fluctuations. This behavior would suggest that a phase segregation of strong-correlation volumes of longer (V—O) bond length reduces the mean (V—O) bond length of the background, thereby increasing the tight-binding bandwidth W_b even though strong electron coupling to the fluctuations lowers the overall bandwidth (Eq. (23) of Goodenough, this volume)

$$W = W_b \exp(-\lambda \varepsilon_{sc}/\hbar \omega_O) \tag{3}$$

where ε_{sc} is the stabilization energy of the strong-correlation fluctuations and $\lambda \sim \varepsilon_{sc}/W_b$ is an electron-lattice coupling parameter.

In order to test whether the maximum in m^*/m_b observed by PES is a true reflection of the approach of U_π to U_c as indicated in Fig. 3 or is a consequence of the presence of two different isovalent A-site cations, we [13] studied the temperature dependence of the resistivity $\rho(T)$ and the thermoelectric power $\alpha(T)$ of $CaVO_3$ under different hydrostatic pressures P. Pressure would, according to a two-phase model, transfer spectral weight from the strong-correlation spectrum to the Fermi-liquid spectrum so as to give an unusually high compressibility of the average (V—O) bond length and, according to the

analysis of the PES data, should increase rather than decrease m^*/m_b as occurs on substitution of Sr(II) for Ca(II). We were not in a position to measure the compressibility, but we could observe the increase in m^*/m_b.

The resistivity of a polycrystalline sample of $CaVO_3$ showed a typical metallic temperature dependence, $\rho(T) \sim T^2$, but it became higher above room temperature than is calculated on the basis of itinerant-electron scattering with a mean-free-path as short as one V—O—V distance, which makes $CaVO_3$ a "bad" metal. The resistivity also showed an unusually strong decrease with pressure as might be expected if pressure transfers charge carriers from a lower Hubbard band to the Fermi surface of a Fermi liquid. Pressure would increase not only W_b, but also ω_O, of Eq. (3), thereby broadening W. However, resistivity data on a polycrystalline sample may not be considered definitive, and they do not provide a measure of m^*.

The thermoelectric power $\alpha(T)$ is a transport property that is not affected by the grain boundaries of a polycrystalline sample, and the pressure variation of its magnitude at room temperature, $d|\alpha(300 \text{ K})|/dP$, shows the sign of the variation of m^* with pressure for a Fermi liquid. Figure 4 compares the $\alpha(T)$ data under hydrostatic pressure P for $CaVO_3$ and Pt.

Interpretation of Fig. 4 begins with a general expression for the thermo-electric power:

$$\alpha = \alpha_O + \delta\alpha \tag{4}$$

where $\delta\alpha$ is a low-temperature enhancement normally associated in a metal with a phonon drag having a maximum contribution at a temperature $T_{max} \approx 0.2\theta_D$; θ_D is the Debye temperature [15]. Above room temperature in the oxide perovskites, $\alpha \approx \alpha_O$ where

$$\alpha_O(T) = -\frac{k}{e} \int \frac{(\varepsilon - \varepsilon_F)}{kT} \frac{\sigma(\varepsilon)}{\sigma} \, d\varepsilon \tag{5}$$

in which $\sigma(\varepsilon) = f(\varepsilon)[1 - f(\varepsilon)]N(\varepsilon)\mu(\varepsilon)$ is the product of the Fermi distribution function $f(\varepsilon)$, the energy density of one-particle states $N(\varepsilon)$, and the particle mobility $\mu(\varepsilon)$ at an energy ε relative to the band edge. In a metallic conductor, α_O becomes Mott's expression:

$$\alpha_O \approx -\frac{\pi^2 k^2 T}{3e\varepsilon_F} \left\{ \frac{\partial \ln \sigma(\varepsilon)}{\partial \ln \varepsilon} \right\}_{\varepsilon=\varepsilon_F} \tag{6}$$

A band-structure calculation [16] indicates that the Fermi surface is not perturbed strongly enough by its interaction with the Brillouin-zone boundary to make $\{\partial \ln \sigma(\varepsilon)/\partial \ln \varepsilon\}_{\varepsilon=\varepsilon_F}$ sensitive to volume changes. Consequently the pressure sensitivity of α_O for an electron gas varies as $1/\varepsilon_F \sim V^{2/3}$. Electron-phonon interactions of coupling strength λ introduce into α a factor $(1 + \lambda)$ that is also pressure-dependent [17]. In a homogeneous electronic system, this factor gives rise to an effective mass m^*_{e-ph} that is calculated by a renor-malization procedure similar to that used by Brinkman and Rice [14] to obtain m^*_{e-e}/m_b due to electron-electron interactions. Therefore, we assume that
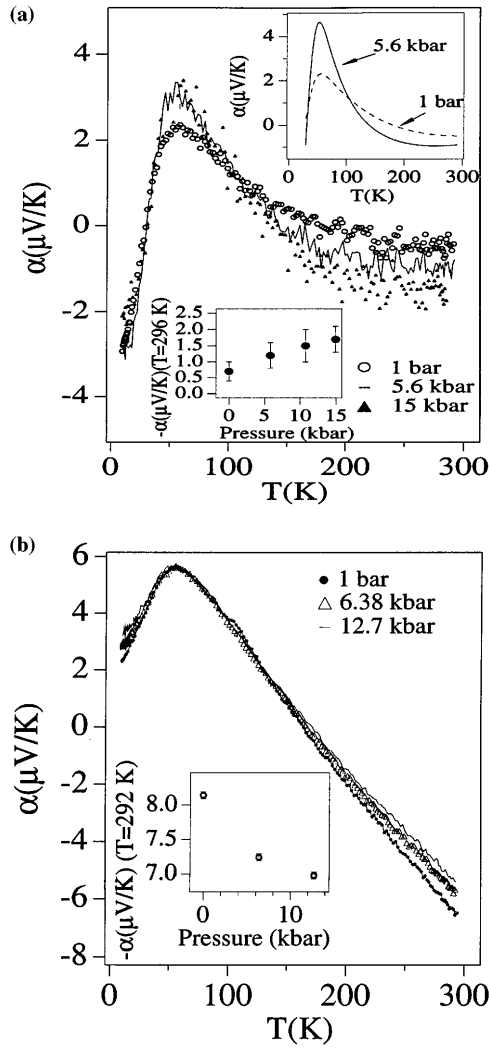
(a)

(b)

Fig. 4a,b. Temperature dependence of the Seebeck coefficient $\alpha(T)$ of: **a** $CaVO_3$; **b** Pt under three different hydrostatic pressures in a self-clamped device. *Lower insets*: room-temperature variation of $|\alpha|$ with pressure. *Upper inset* in (a): fitted curves for a uniform pressures vs T; after [13]

m^*_{e-e}/m_b adds another pressure-dependent factor to α and consider the pressure dependence of

$$\alpha \approx \left(m^*_{e-e}/m_b\right)(1 + \lambda)\alpha_O \tag{7}$$

Broadening of the bandwidth W by the application of hydrostatic pressure reduces the curvature of $\varepsilon(k)$ so as to reduce $(1 + \lambda)$ as well as the volume V.

Moreover, placement of U_π/U_c to the left of the maximum in m^*_{e-e}/m_b in Fig. 3 would also give rise to an m^*_{e-e}/m_b that decreases with pressure. Therefore, we can predict unambiguously a $\partial|\alpha(300\ K)|/\partial P < 0$ for a metal with a homogeneous electronic system, which is what is observed in Fig. 4 for $\alpha(300\ K)$ of Pt. On the other hand, Fig. 4 shows a $\partial|\alpha(300\ K)|/\partial P > 0$ for CaVO$_3$, which can only be explained within the framework of an m^*_{e-e}/m_b that increases with the bandwidth, a deduction that is consistent with the analysis of the PES data that found a maximum in m^*_{e-e}/m_b with increasing x in the system Sr$_{1-x}$Ca$_x$VO$_3$. We therefore conclude that the maximum in m^*_{e-e}/m_b is an intrinsic property of a heterogeneous electronic system and is not an artifact of two A cations of different size.

The other significant feature of Fig. 4 is the difference in the effect of hydrostatic pressure on the phonon-drag term $\delta\alpha$ for Pt and CaVO$_3$. At ambient pressure, both Pt and CaVO$_3$ show a phonon-drag enhancement with a T$_{max} \approx 60$ K that is characteristic of a metal with a T$_{max} \approx 0.2\theta_D$. This enhancement becomes negligible at room temperature [15]. A modest electron-phonon coupling parameter λ and long-range acoustic phonons are pre-requisites for the phonon-drag enhancement. In the pressure range of the experiments of Fig. 4, pressure would produce a negligible change in λ and θ_D for a homogeneous electronic system, so no appreciable change in either T$_{max}$ or the magnitude of $\delta\alpha$ can be anticipated, as is demonstrated for Pt. On the other hand, the magnitude of $\delta\alpha$ in CaVO$_3$ is seen to increase dramatically with pressure, a response that we interpret to signal an increase in the correlation length of the phonons. This deduction is also consistent with the PES evidence for a heterogeneous electronic system in which the concentration of localized-electron fluctuations decreases with increasing bandwidth. We therefore conclude that a $\partial|\alpha(300\ K)|/\partial P > 0$ and a suppression of $\delta\alpha$ that may be partially restored by pressure are signatures for the presence of strong-correlation fluctuations in a Fermi-liquid matrix in a compound that, to a diffraction experiment, appears to be single-phase and electronically homogeneous. Thus the pressure dependences of $\alpha(T)$ and $\rho(T)$ become a useful indirect measure of the presence of lattice instabilities as a single-valent system approaches the Mott–Hubbard transition from the itinerant-electron side.

1.2.2
V(III)

A reduced covalent mixing at V(III) relative to V(IV) makes $W_\pi < U_\pi$ in the LnVO$_3$ perovskites. However, the t^2 configuration at the V(III) ions of LaVO$_3$ appears to be near the transition from localized to itinerant electronic behavior:

1. A small increase in the V—O bond length despite a larger compressive stress on going to smaller Ln^{3+} ions [18] indicates, according to the virial theorem of Eq. (2) of Goodenough, this volume, that the V(III):t^2 configurations became more localized as the bending angle ϕ of the V—O—V bonds increases.

2. The Curie–Weiss paramagnetic susceptibility [19] has a $\mu_{eff} = 3.84\ \mu_B$ compared to a spin-only $2.83\ \mu_B$ and a Weiss constant $\theta = -665$ K.
3. The system $La_{1-x}Y_xVO_3$ exhibits a broad $(0.08 < x < 0.92)$ two-phase region.
4. Preparation under 15 kbar pressure transforms the structure of $LaVO_3$ from pseudocubic to O-orthorhombic and suppresses the orbital ordering associated with localized t^2 configurations in ambient-pressure $LaVO_3$ [20].

Nevertheless, $LaVO_3$ and YVO_3 undergo, on cooling, cooperative orbital orderings characteristic of localized t^2 configurations, and a first-order transformation from one type of orbital ordering to another on cooling below a $T_t < T_N$ gives rise to a remarkable reorientation of a weak ferromagnetic moment in opposition to the magnetizing field [20a].

In an undistorted octahedral site, removal of the spin degeneracy by intraatomic exchange still leaves a threefold orbital degeneracy for a localized t^2 configuration; this degeneracy may be removed by a cooperative local distortion of the V(III) octahedral sites. Two types of distortions may occur: one quenches the orbital angular momentum **L** at each site; the other maximizes **L**. In the paramagnetic phase, spin-orbit coupling suppresses a cooperative, static deformation that would maximize **L**; but a distortion that quenches **L**, and hence the spin-orbit coupling, is allowed. On the other hand, long-range magnetic ordering of the spins into a collinear configuration can stabilize, through the spin-orbit coupling, a long-range ordering of the individual **L**s and a cooperative distortion that maximizes the **L**s, thereby introducing a giant magnetostriction and magnetocrystalline anisotropy [21]. In $LaVO_3$, a first-order orbital-ordering transition occurs below a $T_t = 137$ K $< T_N = 142$ K [22] and in YVO_3 below a $T_t = 77$ K $< T_N = 116$ K [23]. Magnetometer studies [20, 24, 25] have demonstrated a giant magnetocrystalline anisotropy below T_t, which shows that the cooperative orbital ordering appearing below T_t maximizes the individual **L**s.

$LaVO_3$ undergoes a transition from pseudocubic (tetragonal $c/\sqrt{2}a \approx 0.99$) to rhombohedral symmetry above 850 °C [26, 27]. If prepared under a pressure of 15 kbar, $LaVO_3$ has the usual O-orthorhombic $(c/a < \sqrt{2})$ structure, and it behaves as a conventional antiferromagnet with no evidence of a cooperative orbital ordering [20]. On heating in H_2 atmosphere, an irreversible first-order phase change from the O-orthorhombic to the pseudocubic phase occurs below 350 °C with a small volume change $\Delta V \approx 5\ \text{Å}^3$. These data suggest that, in stable $LaVO_3$, a cooperative orbital ordering that quenches the individual **L**s is responsible for the pseudocubic structure; in the high-pressure phase, the orbital ordering is suppressed as a result of a transition from localized to itinerant antiferromagnetism. In that case, a tetragonal $c/\sqrt{2}a < 1$ distortion in the localized-electron phase signals stabilization of one electron in the M—O orbital xy, which can only be compatible with a quenched **L** if each octahedron is locally distorted to orthorhombic symmetry so as to remove the (yz ± izx) degeneracy giving m = ±1. A global tetragonal $(c/a\sqrt{2} < 1)$ symmetry is compatible with a local orthorhombic distortion of the $VO_{6/2}$ octahedra that alternates long and short O—V—O bonds in the basal planes so as to

stabilize the second d electron per V(III) ion alternately in yz and zx orbitals with a G-type (Table 1 of Goodenough, this volume) orbital ordering. As pointed out by Ren et al. [28], this orbital ordering introduces antiferromagnetic V—O—V superexchange interactions in the basal planes by Eq. (8) of Goodenough, this volume, and ferromagnetic superexchange interactions along the c-axis by Eq. (9) of Goodenough, this volume, to give C-type magnetic ordering (Table 1 of Goodenough, this volume). Alternatively, the yz orbitals and zx orbitals could be stabilized in alternate c-axis chains with a C-type orbital ordering, which would give a G-type antiferromagnetic order. A small energy difference between these two alternatives may account for the two different magnetic orderings reported by neutron-diffraction experiments for YVO_3 [29, 30]. Superimposed on the orbital ordering would be a cooperative rotation of the c-axis chains as in low-temperature $SrTiO_3$; the rotations would shorten the a axis, but not the c-axis, to render the structure pseudocubic. Finally, if the spins of the antiferromagnetic component lie in the a-b plane, then the first type of orbital ordering would give a spin configuration C_yF_x, the ferromagnetic component arising from a local magnetocrystalline anisotropy and the cooperative rotation of the c-axis chains. The second type of orbital ordering would not yield a net ferromagnetic component as a result of the cooperative rotations of the c-axis chains. Since $LaVO_3$ exhibits a weak ferromagnetism in the short interval $T_t < T < T_N$, a spin configuration C_yF_x is predicted for this interval.

The magnetic order of $LaVO_3$ in the 5 K interval $T_t < T < T_N$ has not been probed by neutron diffraction. However, Bordet et al. [31] have reported a C_yF_x canted-spin configuration at $100 K < T_t$ where the cooperative distortion maximizes the individual $\mathbf{L}$s. Orientation of $\mathbf{L}$ and $\mathbf{S}$ along the b-axis can only occur with a rhombohedral ($\alpha > 60°$) distortion of the individual octahedra in which the a_1 orbital ($m = 0$) of t-orbital parentage is oriented through an octahedral-site face that has been rotated about the a-axis so as to place its center on the b-axis. Retention of a half-filled orbital in the a-b plane keeps antiferromagnetic V—O—V superexchange interactions in that plane, and the c-axis superexchange via twofold-degenerate $e_\pm$ orbitals remains ferromagnetic (Eq. 9 of Goodenough, this volume) since the intraatomic exchange Δ_{ex} favors electron transfer to an empty orbital. A cooperative rotation of the c-axis chains of corner-shred octahedra about the c-axis would cant the spins to give a weak ferromagnetic component along the a-axis, i.e., the observed configuration C_yF_x.

Not addressed in this analysis is the remarkable finding that, on traversing T_t, the ferromagnetic component reverses its orientation; on cooling, it is in opposition to the magnetizing field $\mathbf{H}_a$ [20, 20a], which gave rise to the initial report of an anomalous diamagnetism in $LaVO_3$ [24, 25]; see Fig. 5. This phenomenon is even more spectacular in YVO_3 where single-crystal measurements have shown that the ferromagnetic component remains along the a-axis, but it reverses sign on traversing T_t whether the ferromagnetic component just above T_t is aligned or misaligned with $\mathbf{H}_a$, see Fig. 6 [28]. Misalignment just above T_t occurs in a small $\mathbf{H}_a$ because of a smooth reversal of the ferromagnetic component with decreasing temperature in the interval
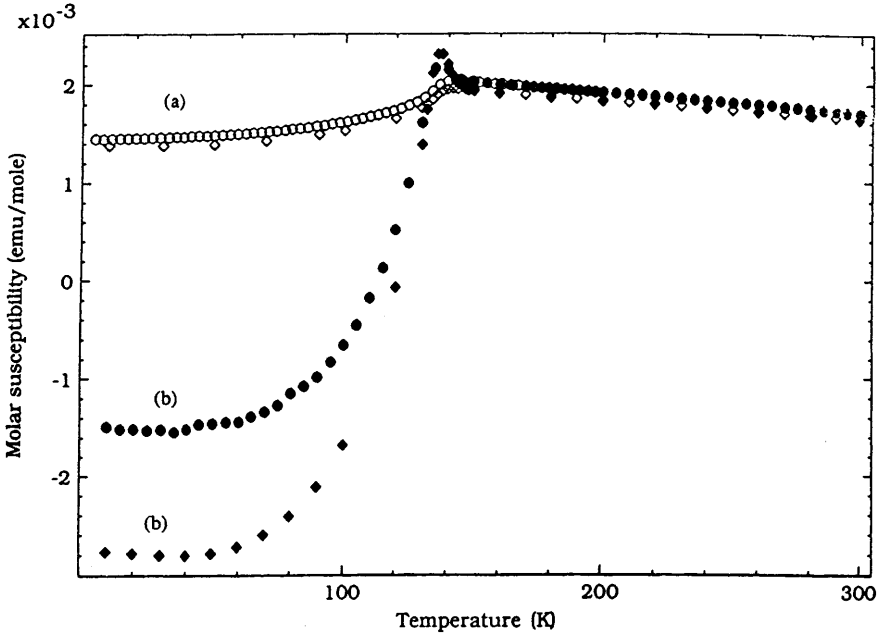
Fig. 5. Molar susceptibility vs temperature for LaVO$_3$ measured in 1 kOe after (a) zero-field cooled and (b) cooled in a field of 1 kOe from room temperature to 5 K for a sample sintered at 1100 °C (*circles*) and 1400 °C (*diamonds*); after [20]

$T_t < T < T_N$. Based on the assumption that the spin canting is due to antisymmetric exchange, one of us proposed that the phenomenon in LaVO$_3$ reflects a reversal of the Dzialoshinskii vector $\mathbf{D}_{ij}$ as a result of persistent atomic currents giving an orbital moment that opposes the discontinuous flux change at the first-order transition. Alternatively, the reversal of the ferromagnetic component may be due to a local crystalline anisotropy field and a reversal of the sign of the cooperative c-axis rotations on traversing the transformation from an orbital ordering that quenches the **L**s to one that maximizes the **L**s. The giant magnetocrystalline anisotropy prevents the magnetic fields $\mathbf{H}_a$ that have been applied from reorienting the ferromagnetic component in the direction of $\mathbf{H}_a$. In the interval $T_t < T < T_N$ of YVO$_3$, applied fields were able to suppress the smooth reversal of the ferromagnetic component with decreasing temperature, but below T_t the local magnetocrystalline anisotropy is too large.

Interpretation of this phenomenon has been hampered by conflicting neutron-diffraction data for YVO$_3$. Kawano et al. [29] have reported a C_yF_x magnetic order above T_t and a G-type arrangement below T_t whereas Zubkov et al. [30] reported a C_yF_x magnetic order below T_t and a G_xF_z arrangement above T_t. An orbital ordering that quenches the **L**s would be G-type to give a C_yF_x magnetic order in the range $T_1 < T < T_N$. Below T_t, an orbital ordering that maximizes the **L**s would correspond to $d_{xy}^1(d_{yz} \pm id_{zx})^1$ and give G-type
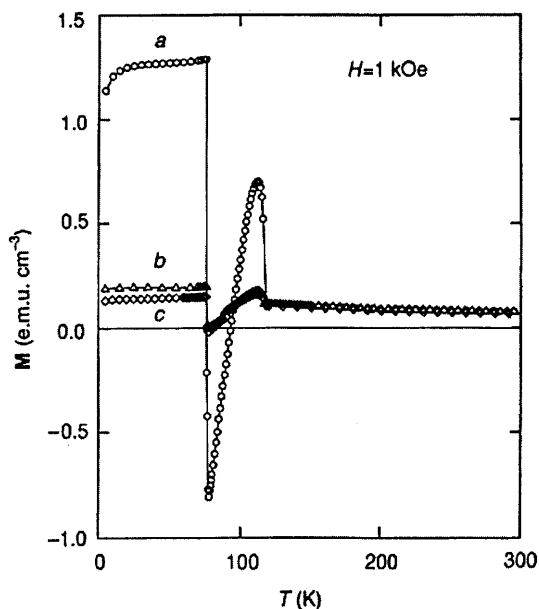
Fig. 6. Temperature dependence of the magnetization of single-crystal YVO$_3$ in a magnetic field of 1 kOe applied along the a-, b-, and c-axes, respectively. Transition at T$_N$ = 116 K is second-order, at T$_t$ ≈ 77 K is first-order; after [28]

magnetic order. A study [30a] with resonant x-ray scattering confirms the G-type orbital order and C$_y$F$_x$ magnetic order in the range T$_t$ < T < T$_N$, but leaves ambiguous whether the orbital ordering is C-type or corresponds to d$_{xy}^1$(d$_{yz}$ ± id$_{zx}$)^1.

1.3
The Chromates

1.3.1
Cr(III)

The orbital angular momentum is completely quenched to first-order in the Cr(III):t^3 configuration; each t orbital is half-filled, and the intraatomic exchange field H$_{ex}$ couples the spins ferromagnetically to give a net Cr(III)-ion spin S = 3/2. The t^3-O:2p$_\pi$-t^3 superexchange interactions between nearest neighbor Cr(III) ions are therefore antiferromagnetic (See Eq. 8 of Goodenough, this volume); LaCrO$_3$ and YCrO$_3$ order antiferromagnetically (Type G) below a T$_N$ = 290 K and 141 K, respectively. As in the V(III) vanadates, a more acidic A-site cation and a larger orthorhombic distortion in YCrO$_3$ due to a smaller tolerance factor t < 1 weakens the (180° − ϕ) Cr—O—Cr superexchange interactions, which lowers T$_N$ as shown in Fig. 7 [32].
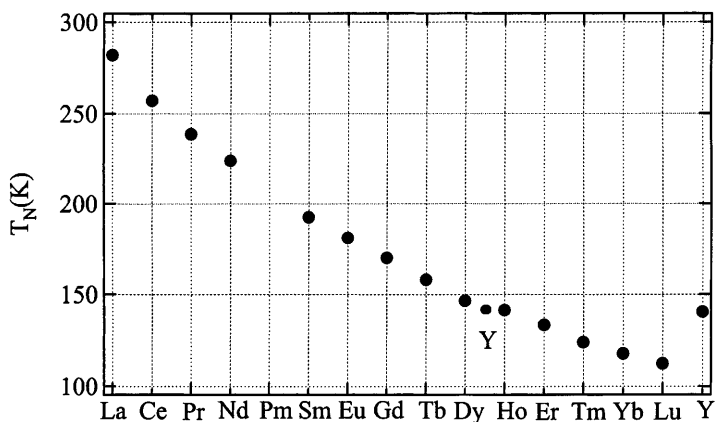
Fig. 7. Variation of the Néel temperature with lanthanide ion for $LnCrO_3$; after [32]

1.3.2
Cr(IV)

Decreasing the valence state of the CrO_3 array from 3− to 2− by oxidizing the Cr(III) to Cr(IV) lowers the redox energy for the empty t^3 manifold at Cr(IV) relative to the energy of the empty low-spin t^4 manifold at a Cr(III) ion by $U_{eff} = U_\pi + \Delta_{ex}$. A corresponding decrease of ΔE_p increases significantly the Cr:t-O:2p_π covalent-mixing parameter $\lambda_\pi = b_\pi^{ca}/\Delta E_p$ of Eq. (3) of Goodenough, this volume, thereby increasing $W_\pi \approx \varepsilon_\pi \lambda_\pi^2$. Moreover, U_{eff} is reduced from $U_\pi + \Delta_c$ to U_π, and a $W_\pi \geq U_\pi$ is found in the Pauli paramagnetic metal $SrCrO_3$; however, a $W_\pi < U_\pi$ is found in $CaCrO_3$, which is an itinerant-electron antiferromagnetic insulator with $T_N = 90$ K and an energy gap $E_g = (U_\pi - W_\pi)$ as in $LaTiO_3$ [33]. It follows that with increasing x, the $Sr_{1-x}Ca_xCrO_3$ system crosses the Mott–Hubbard transitions from the itinerant-electron side at some $x = x_c$. However, this system is synthesized under high pressure, so it still awaits systematic study.

1.4
The Manganates

The t^3 configurations at both Mn(III) and Mn(IV) ions are localized; they impart a net spin S = 3/2 and antiferromagnetic t^3-O:2p_π-t^3 superexchange interactions as they do with Cr(III) ions. However, oxidation of Cr(III) to Cr(IV) has been achieved under high oxygen pressure whereas oxidation of Mn(IV) to Mn(V) in an MnO_3 array has not been reported. Of particular interest is the localized e^1 electron at a high-spin Mn(III):t^3e^1 ion since it occupies twofold-degenerate σ-bonding orbitals, which makes Mn(III) a strong Jahn–Teller (J-T) ion. As discussed in connection with Eqs. (2) and (3) of Goodenough, this volume, the cubic-field splitting quenches the orbital angular momentum of the e^1 configuration, so removal of the orbital degeneracy is not

constrained by spin-orbit coupling; a cooperative J-T distortion of the LaMnO$_3$ lattice may occur in the paramagnetic state, and it is found below a T$_{JT}$ ≈ 750 K [34]. It was known that the orbital degeneracy of a localized e^1 configuration may be removed by a local deformation of the octahedral Mn(III)-ion site to tetragonal or orthorhombic symmetry or a linear combination of the two [35]. In 1955, on the basis of neutron data by Wollan and Koehler [36] showing ferromagnetic a-b planes coupled antiparallel to one another along the c-axis (Type A antiferromagnetic order, see Goodenough, this volume) and an orthorhombic axial ratio c/a < √2, Goodenough [37] predicted an orbital ordering by cooperative oxygen-atom displacements within the a-b planes that create long O···Mn···O bonds alternating with short O—Mn—O bonds, Fig. 4c of Goodenough, this volume. Such a distortion would create e^1···O:2p$_\sigma$-e^0 superexchange interactions that, according to Eq. (9) of Goodenough, this volume, are ferromagnetic. Since the σ-bond interactions are stronger than the π-bond interactions, the ferromagnetic coupling dominates the antiferromagnetic t^3-O:2p$_\pi$-t^3 interactions in the a-b planes; but there is no ferromagnetic interaction along the c-axis. This observation resulted in the first formulation of the Goodenough-Kanamori rules for the sign of the superexchange interactions. It was also pointed out that an axial ratio c/a < √2 was a signature of the presence of static J-T orbital ordering; the O′-orthorhombic c/a < √2 distortion was therefore distinguished from the O-orthorhombic (c/a > √2) distortion. Since the c-axis oxygen atoms share covalent bonding equally on opposite sides whereas the basal-plane oxygens do not, the c-axis Mn—O bond length is intermediate between the short and long bond lengths in the a-b planes; however, it remains closer in length to the short bond to give the O′ axial ratio c/a < √2. Recent neutron [38] and X-ray [39] diffraction experiments on LaMnO$_3$ have fully corroborated these predictions. The atomic moments are oriented along the b-axis and an antisymmetric spin-spin interaction with a Dzialoshinskii [40] vector $\mathbf{D}_{ij}$ parallel to the a-axis cants the spin to give a weak ferromagnetic component along the c-axis (configuration A$_y$F$_x$ of Table 1 of Goodenough, this volume).

   Kanamori [41] provided a mathematical description of the orbital ordering, but his analysis does not distinguish between the two possible arrangements of the oxygen displacements in the basal planes: in-phase and out-of-phase stacking along the c-axis. Mizokawa et al. [42] have recently argued that this degeneracy is lifted by the A-O interactions, a larger tilting of the MO$_{6/2}$ octahedra (i.e., a smaller t < 0) favoring the in-phase stacking.

   The observation [34, 43] that the Curie–Weiss paramagnetic susceptibility has a larger Weiss constant in the temperature interval T > T$_{JT}$ compared with that for T$_N$ < T < T$_{JT}$ indicates that the magnetic interactions become isotropically ferromagnetic above T$_{JT}$. On the assumption that stoichiometric LaMnO$_3$ remains an insulator above T$_{JT}$, Goodenough et al. [44] postulated a strong electron coupling to dynamic local J-T deformations, which would favor isotropic ferromagnetic superexchange interactions, and the appearance of ferromagnetism in the system LaMn$_{1-x}$Ga$_x$O$_3$ appeared to confirm that postulate [44, 45]. Moreover, temperature-dependent neutron-diffraction studies through T$_{JT}$ = 750 K, Fig. 8, have identified a pseudo-cubic O* phase
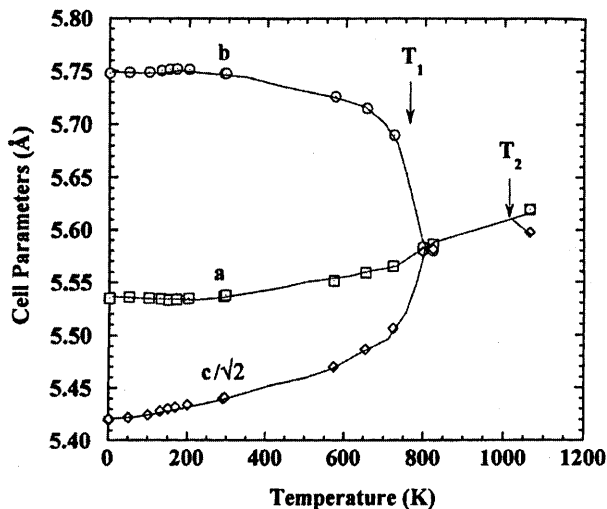
Fig. 8. Cell parameters of LaMnO₃ as a function of temperature. The $MnO_{6/2}$ octahedra became nearly regular in O* phase, but thermal parameter of the oxygen atoms increases significantly; after [38]

with $c/a \leq \sqrt{2}$ where short-range orbitally ordered fluctuations persist above T_{JT}. However, measurements of the temperature dependence of the transport properties of single-crystal LaMnO₃ through $T_{JT} = 750$ K have shown that stoichiometric LaMnO₃ becomes conductive above T_{JT} [34].

Figure 9 shows the resistivity $\rho(T)$ and the thermoelectric power $\alpha(T)$ of a single crystal of LaMnO₃ as measured in a vacuum of 10^{-3} torr. An irreversible change of the room-temperature $\alpha(300$ K) from −600 μV/K to about +550 μV/K on thermal cycling to 1100 K reflects a small-polaron conduction without spin degeneracy – see Eq. (11). Initially the crystal contains a small fraction c = 0.0009 of Mn(II) ions; but on heating above 500 K, it becomes oxidized to a similarly small fraction of Mn(IV) ions. The $\rho(T)$ and $\alpha(T)$ curves were reversible after the first cycle. The second significant feature of Fig. 9 is a drop on heating in both $\alpha(T)$ and $\rho(T)$ to a nearly temperature-independent value for T > T_t. The drops in $\alpha(T)$ and $\rho(T)$ represent a change from a small to a large fraction of mobile e electrons even though the crystal remains nominally single-valent Mn(III) and the e electrons remain strongly coupled to locally cooperative, dynamic oxygen displacements. Van Roosmalen and Cordfunke [46] have analyzed the relation between the partial pressure of oxygen and the value of δ in LaMnO₃₊δ to conclude that a partial disproportionation reaction 2Mn(III) = Mn(IV) + Mn(II) occurs and is responsible for a surprisingly large oxidation of LaMnO₃ in air. (The oxidized formula is better written as $La_{1-\varepsilon}Mn_{1-\varepsilon}O_3$ since the perovskite structure does not accept interstitial oxygen.) In air, the Mn(II) are oxidized to Mn(III), but little oxidation occurs in 10^{-3} torr. Nevertheless, the small oxidation that occurs makes the ratio Mn(II)/Mn(IV) < 1, so an $\alpha > 0$ is found at T > T_t in Fig. 9. The nearly temperature-independent α and ρ above T_t as well as a $\rho \approx 10^{-1}$ Ωcm cannot
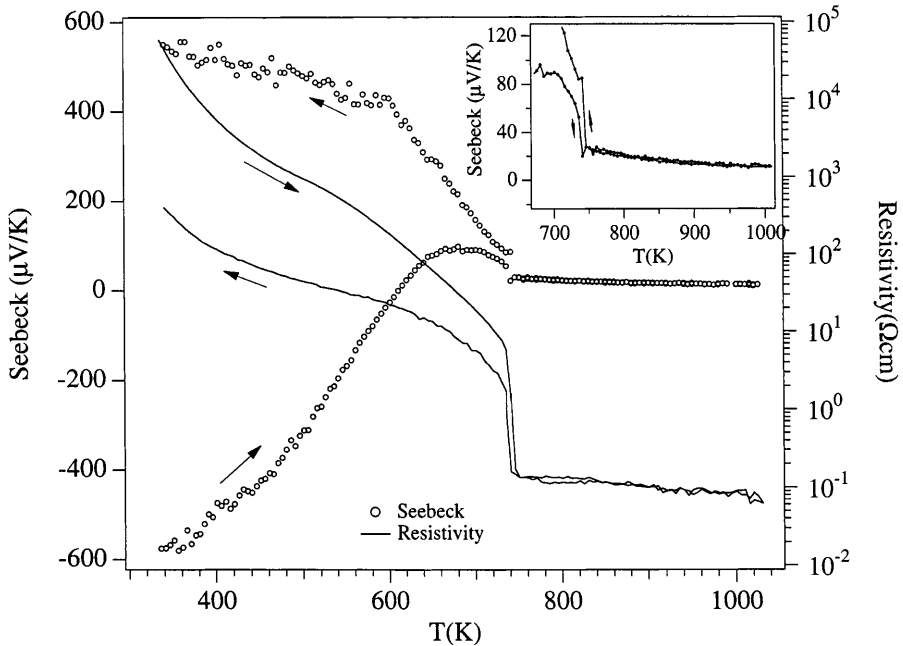
Fig. 9. Resistivity $\rho(T)$ and thermoelectric power $\alpha(T)$ taken on cycling a virgin single crystal of $LaMnO_3$ from room temperature to 110 K measured in a vacuum of 10^{-3} torr; after [34]

be described by a conventional band model; it would appear that the Mn(IV) holes and Mn(II) electrons both move diffusively, but with a motional enthalpy $\Delta H_m < kT$. A real charge transfer of both e electrons from Mn(II) to Mn(III) and e holes from Mn(IV) to Mn(III) give first-order ferromagnetic spin-spin interactions (double exchange) that are stronger than the higher-order superexchange interactions; see Goodenough, this volume.

Figure 10 shows the Curie-Weiss paramagnetic susceptibility $\chi(T)$ and its inverse $\chi^{-1}(T)$ for the same single crystal of $LaMnO_3$ as measured under 10^{-3} torr [34]. No significant anisotropy was observed, but the Weiss constant is seen to increase abruptly from $\theta = 52$ K for $300 < T < 650$ K to $\theta = 177$ K for $T > 750$ K without any observable change in the Curie constant $C = 3.41$. This value of C corresponds to a $\mu_{eff} = 5.2\ \mu_B$, which is to be compared to a spin-only $\mu_{eff} = 4.9\ \mu_B$ for $S = 2$ and a $\mu_{eff} = 5.0\ \mu_B$ for a full disproportionation into Mn(II) with $S = 5/2$ and Mn(IV) with $S = 3/2$. The data are compatible with a partial disproportionation with retention of high-spin states at all the cations and with an isotropic ferromagnetic interaction setting in abruptly above T_t. We are thus led to the conclusion that a cooperative orbital ordering in the O'-orthorhombic phase suppresses the disproportionation reaction by localizing the e electrons in the long Mn—O bonds, which prevents breathing-mode displacements of the oxygen atoms at the cations. On raising the temperature through T_t, the locally cooperative oxygen displacements become short-range fluctuations that permit the formation of breathing-mode
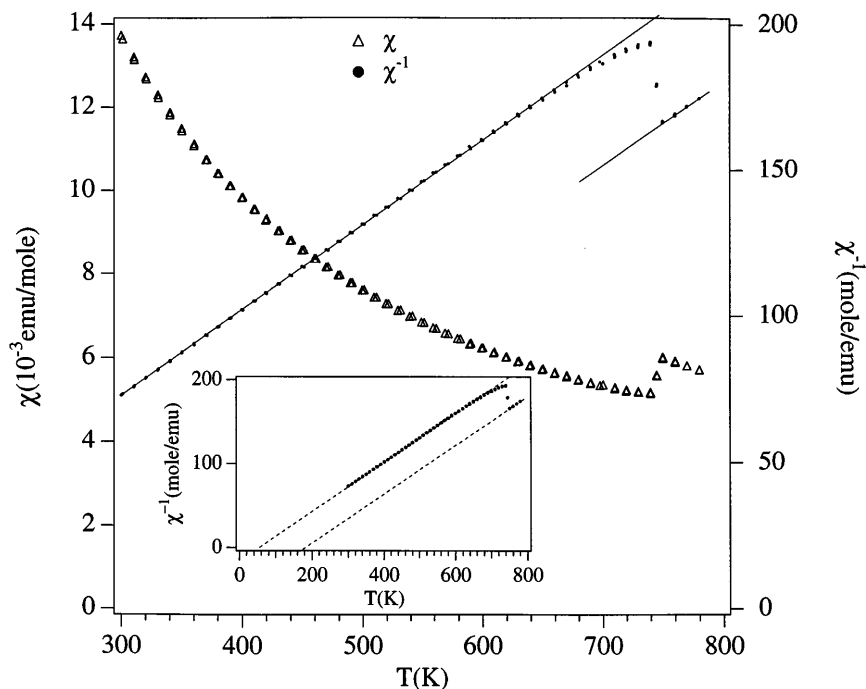
Fig. 10. Magnetic susceptibility $\chi(T)$ and its inverse $\chi^{-1}(T)$ for single-crystal LaMnO$_3$ measured in a vacuum of 10^{-3} torr; $\chi_{\parallel}$ and $\chi_{\perp}$ could not be resolved in the paramagnetic O′ phase, but they were resolved below T$_N$; after [34]

displacements. The formation of six short Mn—O bonds creates empty molecular e orbitals at Mn(IV) ions; six long Mn—O bonds stabilize localized Mn(II) configurations. The disproportionation reaction may thus be considered a segregation into localized electrons and delocalized holes. This unusual situation occurs because U$_\sigma$ for the majority-spin e band places the e electrons at the cross-over from localized to itinerant behavior. At cross-over, the e electrons are strongly coupled to locally cooperative oxygen displacements that include breathing as well as J-T vibrational modes.

1.5
The Ferrates

1.5.1
Fe(III)

The high-spin Fe(III):t^{3}e^2 configuration is localized with all the d-like orbitals half-filled and spin-aligned by intraatomic direct exchange to give a net spin S = 5/2 as well as antiferromagnetic t^3-O:2p$_\pi$-t^3 and e^2-O:2p$_\sigma$-e^2 superexchange interactions. The LnFeO$_3$ perovskites are all Type G antiferromagnets. Addition of a sixth d-like electron costs an energy U$_{eff}$ = U + Δ_{ex}, which is

large, but ΔE_p is small enough for a relatively large λ_σ and λ_π to give a large T_N. Substitution of smaller Ln(III) ions for La(III) increases the bending of the Fe—O—Fe bond angle, which reduces the superexchange interaction and systematically lowers T_N; see Fig. 11.

1.5.2
Fe(IV)

Like Mn(III), the Fe(IV) ion of the $AFeO_3$ (A = Ca, Sr, Ba) perovskites is in a high-spin state. Unlike $LaMnO_3$, the system $Sr_{1-x}Ca_xFeO_3$ is metallic at room temperature. Since the empty t^3e^2 configuration at an Fe(IV) ion is at a smaller energy ΔE_p from the $O:2p^6$ band than the empty t^3e^2 configuration at an Mn(III) ion, the Fe(IV)-O covalent mixing is larger, which makes W_σ larger and $U_{eff} = U_\sigma$ smaller in $Sr_{1-x}Ca_xFeO_3$ than in $LaMnO_3$, see Eq. (3) of Goodenough, this volume. Since $LaMnO_3$ was found to approach the cross-over from localized to itinerant e-electron behavior, it follows that we can expect $W_\sigma \geq U_\sigma$ in the Fe(IV) perovskites, which would place each single e electron per Fe(IV) ion in an itinerant-electron state of a σ^* band. On the other hand, a $W_\pi < W_\sigma$ and a $U_{\pi eff} = U_\pi + \Delta_{ex}$ keeps the t^3 configuration localized; itinerant σ^* electrons coexist with localized t^3 configurations in the $(FeO_3)^{2-}$ array [47]. The localized spins S = 3/2 of the t^3 configurations introduce a strong intraatomic exchange that tends to remove the spin degeneracy of the σ^* band, which would stabilize a high-spin $t^3\sigma^{*1}$ state. However, complete removal of the spin degeneracy of the σ^* band would yield a half-metallic ferromagnet at low temperatures whereas $SrFeO_3$ forms a ferromagnetic-spiral spin configuration propagating along the pseudocubic [111] direction with a wave vector $|q| = 0.112(2\pi/a_O)$ and $\mu_{Fe} < 4$ μ_B [48, 49]. As discussed following Eq. (11) in Goodenough, this volume, such a spiral-spin configuration signals, in addition to ferromagnetic nearest-neighbor interactions, the presence of antiferromagnetic next-near-neighbor interactions. An oscillation from ferromagnetic to antiferromagnetic interactions on increasing separation of the Fe atoms implies a σ^* bandwidth W_σ that is too broad for complete removal of
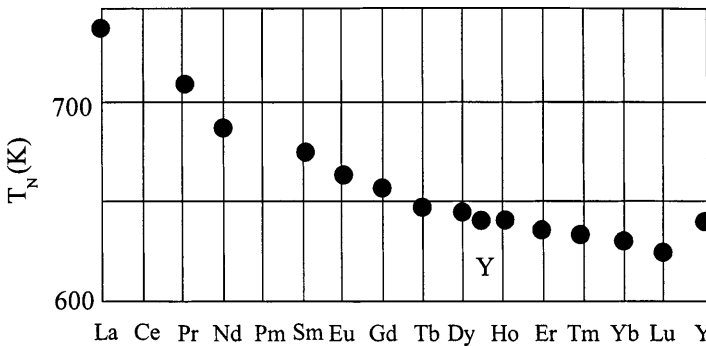
Fig. 11. Variation of the Néel temperature with lanthanide ion for $LnFeO_3$; after [32]

the spin degeneracy; the localized spins S = 3/2 would then be coupled by an indirect exchange via σ^*-band electrons on the itinerant-electron side of the Mott–Hubbard transition.

Finally, a σ^* band on the itinerant-electron side of the Mott–Hubbard transition in the presence of localized t^3 spins S = 3/2 signals covalent-mixing parameters $\lambda_\sigma \gg \lambda_\pi$ and therefore a cubic-field splitting Δ_c (Eq. 5 of Goodenough, this volume) that approaches Δ_{ex}. To test this deduction, hydrostatic pressure was used to induce a transition from the high-spin to the low-spin states in $CaFeO_3$; the transition was observed to occur at a pressure $P_c \approx 30$ GPa [50].

$CaFeO_3$ has a smaller t < 1 than $SrFeO_3$, and the σ^* band of its high-spin $t^3\sigma^{*1}$ configuration is close enough to the Mott–Hubbard transition for lattice instabilities due to strong-correlation fluctuations. Whereas a cooperative J-T orbital ordering stabilizes localized t^3e^1 configurations relative to a dispro-portionation reaction in $LaMnO_3$, a cooperative disproportionation reaction is stabilized to lowest temperatures in $CaFeO_3$. Mössbauer data [51] first indicated the onset of cooperative oxygen displacements below $T_t = 290$ K; the breathing-mode displacements create $Fe(IV + \delta)O_6$ molecular-orbital clusters alternating with strong electron correlations at $Fe(IV - \delta)$ ions, the magnitude of the displacements and of the transferred charge δ increasing smoothly with decreasing temperature. Figure 12 shows how the hyperfine fields H_i and isomer shifts at 4 K decrease with increasing x in the system $Ca_{1-x}Sr_xFeO_3$ [51a]. The translational symmetry of the oxygen displacements creates distinguishable Fe atoms on alternating {111}Fe-atom planes, which opens an energy gap at the Fermi energy. Direct observation of the cooperative oxygen displacements towards alternate Fe atoms has confirmed the deduction from the Mössbauer data [52, 52a]. With two distinguishable Fe-atom spins, antiferromagnetic order below a $T_N = 115$ K suggests antiferromagnetic next-nearest-neighbor interactions stabilize a helical-spin configuration propaga-ting along a [111] axis of the pseudocubic structure, and this deduction has now also been confirmed [52b].

1.6
The Cobaltates

$LaCoO_3$ exhibits yet another example of strong coupling of the e electrons to variations in the ⟨M—O⟩ bond length. Interpretation of the electronic properties is subtle because three spin states are possible at the Co(III) ions: a low-spin (LS) state $t^6\sigma^{*0}(^1A_1)$, a high-spin (HS) state $t^4e^2(^5T_2)$, and an intermediate-spin (IS) state t^5e^1. Initially, only the HS and LS states were considered at lower temperatures whereas it turns out that the IS state is more stable than the HS state [53].

In the interval 0 < T < 35 K, essentially all the Co(III) atoms of $LaCoO_3$ are LS. However, localized spins associated with surface cobalt [54, 55] give a weak ferromagnetism at 5 K; see Fig. 13a. Strong Co:e − O:2p_σ covalent mixing transforms the empty e orbitals of the bulk CoO_3 array into a narrow σ^* band of itinerant-electron states separated from a filled π^* band by an energy gap
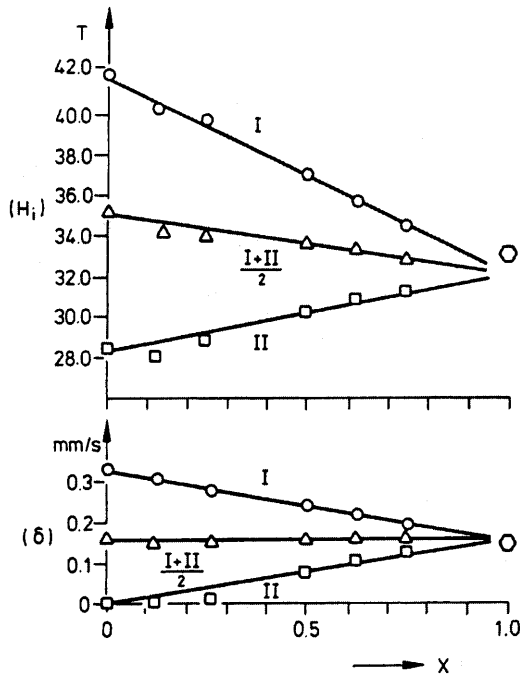
Fig. 12. Variation with composition x of the two (I and II) hyperfine fields H_i and isomer shifts (δ) at 4 K in the system $Ca_{1-x}Sr_xFeO_3$; after [51a]
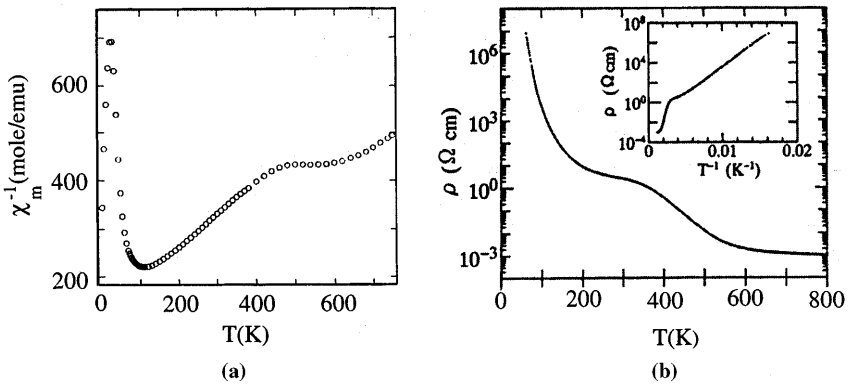
Fig. 13. a Inverse molar magnetic susceptibility $\chi^{-1}(T)$ for polycrystalline $LaCoO_3$. **b** $\rho(T)$ for single-crystal $LaCoO_3$; after [55, 56]

$E_g = 0.1$ eV [56]. However excitation to a localized IS state stabilized by a local J-T distortion requires only ca. 0.03 eV. As a result, the excitations of interest are changes in the spin state of the Co(III) and not the creation of Co(IV) + Co(II) species. The temperature dependence of the higher-spin

excitations appearing above 35 K and their character have been studied extensively.

In the interval 35 < T < 110 K, the concentration of thermally excited IS states increases exponentially with temperature. It was initially assumed that an HS state was being excited. However, the IS state is stabilized by a local dynamic J-T deformation that has been observed by infrared spectroscopy [57]. The thermally excited IS states are localized where present in low concentration; they may be considered strong-correlation fluctuations within the empty σ^* band of the LS matrix. Expansion of the mean Co—O bond length associated with localized e electrons at the IS cobalt applies a pressure on the Co—O bond length on the opposite side of the oxygen atom. Hydrostatic pressure has been shown [58] to stabilize the LS state as does reduction of the lattice parameter in $YCoO_3$ [59]. Therefore, the population of IS/HS ions appears to stabilize near 50% in the range 110 < T < 350 K as a result of short-range ordering of LS and IS/HS cobalt [60]. Conversely, a doped hole exists as a polaronic LS Co(IV) species with short Co—O bond lengths, which stabilizes IS or HS configurations on the neighboring Co atoms that couple ferromagnetically to it to create a superparamagnetic polaron with a spin S = 10 − 16 [56].

Bhide et al. [61] used Mössbauer data to investigate the evolution with temperature of two distinguishable Co(III); they found two states of cobalt with the population of a higher-spin Co(III) reaching a sharp maximum at 200 K. The relatively abrupt cut-off of two distinguishable cobalt has been interpreted by Raccah and Goodenough [60] to be due to a decrease in the configuration fluctuation time of a dynamic short-range ordering of the LS and IS states from $\tau > 10^{-8}$ s below 200 K to $\tau < 10^{-8}$ s above.

Examination of the volume thermal expansion obtained from neutron-diffraction data [62] shows a remarkable leveling off above 110 K, particularly in the range 250 < T < 400 K, that is followed by a sharp increase in the range 400 ≤ T ≤ 600 K. These data are consistent with a stabilization of the concentration of IS states, which we take to be ca. 50% rather than 100%, over the temperature interval 110 < T < 350 K followed by a sharp increase with temperature of the IS population in the range 350 < T < 550 K where the resistivity drops by over two orders of magnitude, Fig. 13b; above 650 K, $LaCoO_3$ is a good conductor with $\rho \sim 10^{-3}$ Ωcm obtained with a single-crystal measurement [62], but $\rho(T)$ does not have a metallic temperature dependence. Soft X-ray absorption from 80 K to 630 K confirmed the existence of strong covalent bonding at LS Co(III) at low temperatures and mixed LS and higher-spin states above 420 K; it gave no evidence of charge disproportionation [62a]. A Co-K-EXAFS measurement from 300 K to 750 K showed a cobalt coordination of 6 oxygen at 1.92 Å in the range 300 < T < 400 K that splits in two to 50–50 Co—O distances at 1.66 Å and 2.2 Å in the range 523 K ≤ T ≤ 750 K [63]. These EXAFS data would imply the following evolution: a fast configuration transfer ($\tau_h < \omega_O^{-1}$) between IS and LS cobalt in the range 300 < T < 400 K; at higher temperatures, the CoO_3 array adjusts to a higher e-electron population by a dynamic ordering into HS and LS states before transforming to a majority phase containing all IS cobalt with vibronic

e electrons in an itinerant σ^* band. The drop in resistivity above 400 K indicates that there is little charge transfer associated with the configuration fluctuations below 400 K, but that in the range $523 \leq T \leq 750$ K where dynamic ordering of HS and LS Co(III) occurs, there is also a transfer of spectral weight to itinerant vibronic states at ε_F that increases smoothly with temperature. Photoemission data were found to be more consistent with IS Co(III) at high temperatures [64].

1.7
The Nickelates

Early neutron-diffraction studies of the $LaMO_3$ perovskites failed to find any magnetic order in $LaNiO_3$. This observation was clarified in 1965 [65] when it was demonstrated that $LaNiO_3$ is metallic with Ni(III) in the LS state $t^6\sigma^{*1}$ as a result of strong Ni:e-O:$2p_\sigma$ covalent bonding. In the Zaanen, Sawatzky, Allen Model (see discussion and Sect. 2.1 of Goodenough, this volume), the Ni(IV)/Ni(III) redox energy is pinned at the top of the O-2p bands to make $LaNiO_3$ a charge-transfer-gap oxide with a $W_\sigma > U_{eff} = \Delta \approx 1$ eV. However, a systematic investigation of other members of the $LnNiO_3$ family was prevented by an inability at that time to prepare suitable samples at atmospheric pressure. The difficulty of preparing samples increases severely as the radius of the rare-earth ion decreases. In 1971, Demazeau et al. [66] prepared the $LnNiO_3$ family under 60 kbar oxygen pressure, but the samples were too small for a systematic study of their oxygen stoichiometry and physical properties. In 1991, Vassiliou et al. [67] succeeded in preparing $NdNiO_3$ in 1 bar oxygen, and Lacorre et al. [68] obtained under modest oxygen pressures (150–200 bar) sintered pellets of the $LnNiO_3$ family from $LaNiO_3$ to $EuNiO_3$ that were convenient for transport measurements. The availability of samples suitable for measurement was rapidly exploited, and Fig. 14 shows a preliminary phase diagram [69]. The temperature T_t marks an insulator-metal transition; a peculiar antiferromagnetic order sets in below $T_N \leq T_t$. It is apparent from Fig. 14 that variation of the radius of the Ln^{3+} ion in $LnNiO_3$ allows exploration of the change in electronic properties of a quarter-filled band on passing through the Mott–Hubbard transition from the itinerant-electron side.

$LaNiO_3$ is rhombohedral $R\bar{3}c$, but all the other members are orthorhombic Pbnm [70]. With decreasing ionic radius of the lanthanide ion (i.e., with decreasing tolerance factor $t < 1$ defined by Eq. (1) of Goodenough, this volume), the equilibrium Ni—O bond lengths remain constant, but the bending angle ϕ of the $(180° - \phi)$ Ni—O—Ni bonds increases with decreasing t. Figure 14 shows that T_t and T_N change systematically with the value of t calculated from the sums of tabulated ionic radii, which indicates that T_t and T_N are both strongly dependent on ϕ. The Ni—O bond lengths increase discontinuously by about 0.2% on cooling through T_t, which is consistent with more localized, i.e., more strongly correlated, electrons in the antiferromagnetic phase below T_t (see discussion of Eq. (20) of Goodenough, this volume).

The magnetic order below T_N is unusual [71, 72]; ferromagnetic Ni(III) layers are alternately coupled ferromagnetically and antiferromagnetically on
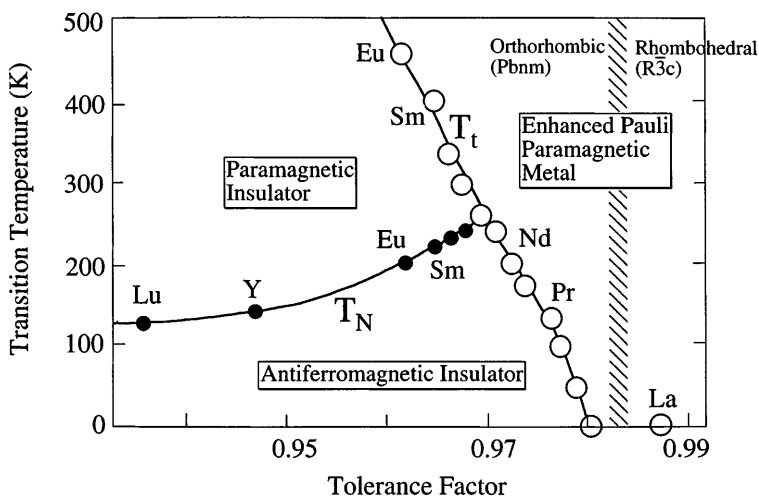
Fig. 14. The insulator-metal transition T_t and the Néel temperature T_N for the $LnNiO_3$ family; adapted from [69]

traversing a pseudocubic [111] axis. The magnetic moment on the Ni atoms is 0.93 μ_B. Given the itinerant character of the conduction electrons, the orbital ordering proposed in [72] is unrealistic; the magnetic order can be better understood as a charge-density/spin-density wave (CDW/SDW) propagating along the pseudo cubic [111] axis with a **q** vector for the SDW twice that for the CDW [73]. A segregation of holes to the ferromagnetic bilayers would give rise to two-dimensional narrow bands more than three-quarters filled (hence ferromagnetic with an atomic moment close to the ionic value) coupled by antiferromagnetic superexchange across ionic O^{2-} (111) planes. However, the neutron data showed little difference in the Ni—O bond lengths across the ferromagnetically and antiferromagnetically coupled layers, which is unexpected. Whereas the $LnNiO_3$ perovskites with Ln = Sm or Eu showed little structural change at $T_N < T_t$ and only an increase in all the Ni—O bond lengths on cooling through T_t [72], room-temperature $YNiO_3$ exhibits a disproportionation into two types of Ni sites: the average Ni—O bond lengths at neighboring sites are 1.923 Å and 1.994 Å [74]. The CDW would appear to reflect a transfer of electronic charge from molecular orbitals at the sites with short Ni—O bonds to localized orbitals at the sites with long Ni—O bonds, thus representing another form of segregation of differently hybridized d-like antibonding orbitals. Where there is a phase segregation into extended and localized electronic states in a single-valent system, ordering into a CDW commonly takes the form of a disproportionation reaction; ordering into itinerant-electron slabs alternating with slabs of strongly correlated electrons (slabs become stripes in a two-dimensional array) is more common in mixed-valent systems. Therefore a rearrangement into a disproportionation CDW from the CDW/SDW found below T_N in the $LnNiO_3$ family may not require a large energy.

Our interpretation of the CDW/SDW configuration below T_N in the $LnNiO_3$ perovskites as an ordering of two phases with, respectively, strongly and weakly correlated electrons implies the existence of the following other physical properties: (i) an unusually large compressibility of the Ni—O bonds, (ii) a sensitive stabilization with hydrostatic pressure of the Fermi-liquid phase relative to the strongly correlated electronic phase, (iii) strong electron interactions with oxygen vibrational modes and, therefore, (iv) a stabilization of the ordered phase by the exchange of ^{18}O for ^{16}O, and (v) a disordered-phase bandwidth W described by Eq. (3) that varies sensitively with the bending angle ϕ through the dependence of ω_O on ϕ rather than through $W_b \sim \cos \phi$. Measurement of the compressibility is not available, but evidence that all the other predictions are fulfilled is at hand.

Obradors et al. [75] found a $dT_t/dP = -4.2$ K/kbar in $NdNiO_3$ with a similar dramatic stabilization of the metallic phase of $PrNiO_3$ with pressure.

Massa et al. [76] and Mroginski et al. [77] have reported evidence from reflectivity, transmission, and photo-induced infrared spectra of strong electron coupling to Ni—O vibrational modes. However, a more direct indication that T_t depends sensitively on the oxygen vibrational modes comes from the observation by Medarde et al. [78] of a 10 °C increase in T_t on substitution of ^{18}O for ^{16}O.

We [79] measured the resistivity $\rho(T)$ and thermoelectric power $\alpha(T)$ under different hydrostatic pressures P for four oxygen-stoichiometric (3.00 ± 0.01) samples prepared under 600 bar oxygen pressure: $LaNiO_3$, $PrNiO_3$, $NdNiO_3$, and $Sm_{0.5}Nd_{0.5}NiO_3$, Fig. 15. Our purposes were (a) to obtain a measure of the variation with P of T_N as well as T_t, (b) to look for evidence of strong-correlation fluctuations in the metallic phase of rhombohedral $LaNiO_3$ and of the orthorhombic samples at temperatures $T > T_t$, and (c) to determine whether the dramatic effect of pressure on T_t is primarily due to a stiffening of ω_O in Eq. (3) rather than an increase in W_b. We call attention to four aspects of the data of Fig. 15.

1.7.1
LaNiO₃

Three features of Fig. 15a are noteworthy: (i) the $\rho(T)$ curves, which are similar at ambient pressure to those reported by others [80, 81], have a temperature dependence typical for a Fermi liquid; however, they are too high and pressure-sensitive for a conventional metal with a mean-free path of more than one lattice parameter; (ii) the low-temperature phonon-drag enhancement, which has a maximum at $T_{max} \approx 70$ K in the oxide perovskites, is largely suppressed; but it is partially restored by pressure; (iii) a $d|\alpha(300 \text{ K})|/dP > 0$ (α is enhanced by 15% in 14 kbar pressure) indicates an anomalous increase in m^* with pressure. Features (ii) and (iii) were also found in $CaVO_3$ where they were shown (see Sect. 1.2.1) to be a signature for the existence of strong-correlation fluctuations in a Fermi liquid. The features (i) and (iii) are also present in the metallic phase of the orthorhombic samples, see Fig. 15b, c;
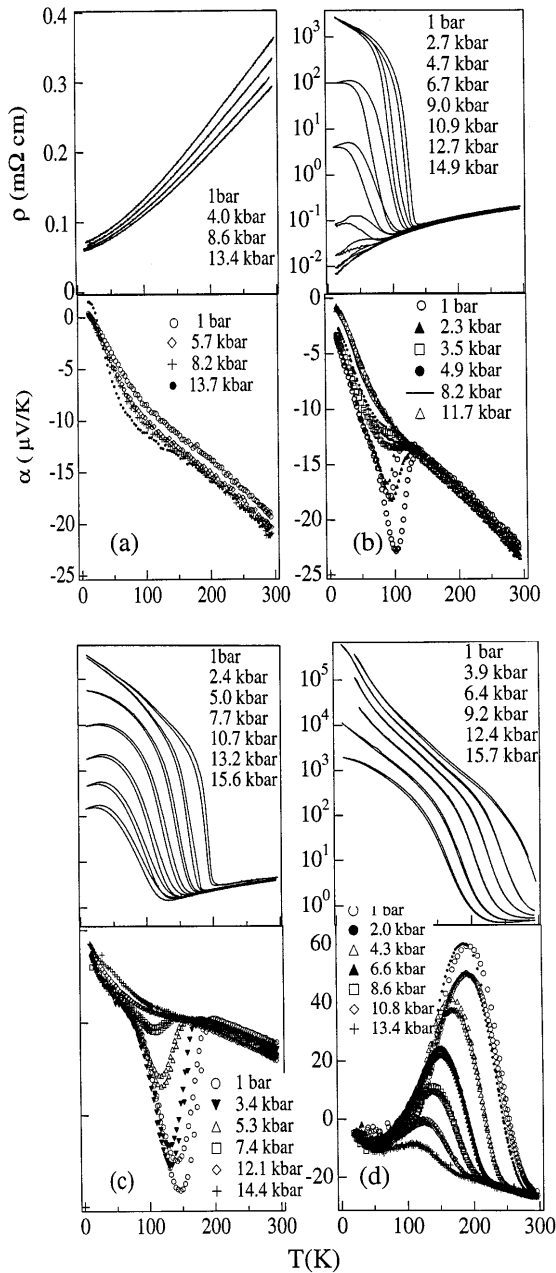
Fig. 15a–d. The resistivity $\rho(T)$ and thermoelectric power $\alpha(T)$ under different hydrostatic pressures for: **a** LaNiO$_3$; **b** PrNiO$_3$; **c** NdNiO$_3$; **d** Sm$_{0.5}$Nd$_{0.5}$NiO$_3$; after [79]

feature (ii) could not be observed in the orthorhombic samples where T_t remained too high.

1.7.2
Pressure Dependence of $\rho(T)$

The $\rho(T)$ and $\alpha(T)$ data for $PrNiO_3$, Fig. 15b, show in $\rho(T)$ a first-order insulator-metal transition at $T_N = T_t \approx 130$ K that is matched by a sharp increase in $|\alpha(T)|$ on cooling through T_t. Pressure has a remarkable influence. Between 2.7 kbar and 4.7 kbar, the low-temperature ($T \leq 50$ K) $\rho(T)$ curve changes from a semiconductive to a metallic temperature dependence; and with increasing pressure $P \geq 4.7$ kbar, the jump in $\rho(T)$ and $|\alpha(T)|$ on cooling through T_t decreases with T_t, disappearing above 13 kbar even though a weakly first-order transition is retained at $T_t \approx 80$ K, Fig. 16. The remarkable change in $\rho(15$ K$)$ by six orders of magnitude is an intrinsic phenomenon indicating a dramatic increase in the number and/or mobility of the charge carriers in the CDW/SDW phase over a limited pressure range $\Delta P \approx 10$ kbar. This unusual behavior suggests that the low-temperature phase changes from a static to a mobile CDW/SDW under pressure. Depinning of the CDW/SDW implies a stiffening of the cooperative oxygen vibrations that become soft to pin it; a simple broadening of W_b under pressure might lower T_t, but it would not depin the CDW/SDW. According to this model, the increased pressure required to depin the CDW/SDW for smaller Ln^{3+} ions implies ω_O decreases as the bending angle increases. A $W = W_b \cos \phi$ would not have a strong
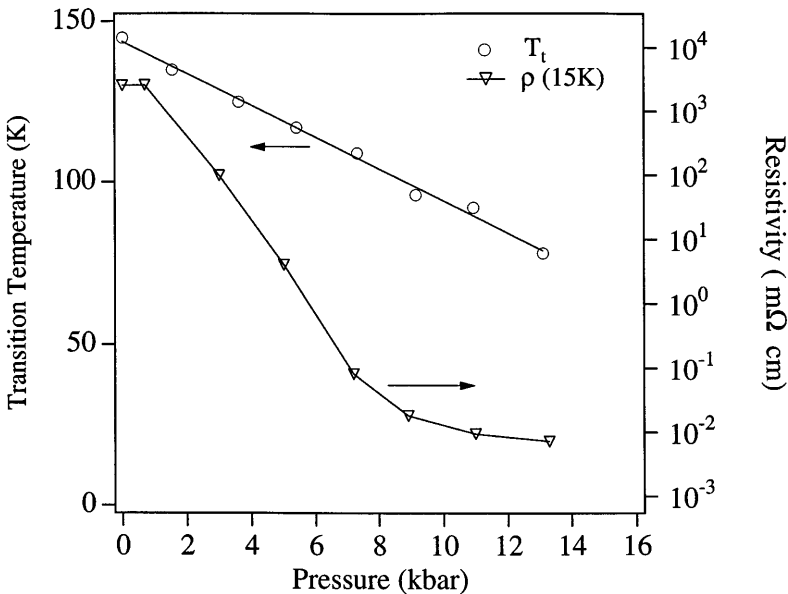
Fig. 16. Variations with pressure of T_t and $\rho(15$ K$)$ for $PrNiO_3$; after [79]

dependence on the tolerance factor t for small ϕ, but an $\omega_O = \omega_O(\phi)$ in $W = W_b \exp(-\lambda\varepsilon_{sc}/\hbar\omega_O)$ would make W vary sensitively with t and therefore T_t vary sensitively with t if T_t occurs at a critical $W = W_c$.

1.7.3
Evolution of Thermal Hysteresis with T_t

Although the neutron-diffraction data show an increase in the mean Ni—O bond length on cooling through T_t for all samples and no discernable change at $T_N < T_t$ [70], our transport data show a systematic decrease in the thermal hysteresis at T_t as $T_t = T_N$ increases; for the sample with $T_t < T_N$, we found a small thermal hysteresis in $\rho(T)$ only at temperatures below T_t. Alonso et al. [82] found, by differential scanning calorimetry, that the heat flow at $T_t > T_N$ in EuNiO$_3$ is only about half the value observed for NdNiO$_3$ where $T_t = T_N$. Vobornik et al. [83] found a sharp change in the photoemission spectra near the Fermi energy ε_F on passing from PrNiO$_3$ and NdNiO$_3$ with $T_t = T_N$ to SmNiO$_3$ and EuNiO$_3$ with $T_t > T_N$. PrNiO$_3$ and NdNiO$_3$ showed an abrupt change in the density of occupied Fermi-liquid states at ε_F and a transfer of spectral weight from ε_F on cooling through $T_t = T_N$ that continued over an extended temperature range below T_t. In contrast, the density of Fermi-liquid states at ε_F in SmNiO$_3$ and EuNiO$_3$ was small; there was no sharp cut-off at ε_F and there was no observable transfer of spectral weight from Fermi-liquid to strongly correlated states on cooling through $T_t > T_N$. They concluded that there is a qualitative difference between systems with $T_t = T_N$ and those with $T_t > T_N$. It appears that the density of strong correlation fluctuations is significantly higher in the metallic phases with a high $T_t > T_N$, which reduces the first-order volume expansion on cooling through T_t. Granados et al. [84] also concluded from their transport measurements on PrNiO$_3$ that the CDW/ SDW phase coexists with the metallic phase below $T_t = 130$ K over the range 70 K $\leq T \leq T_t$. All these data are compatible with an order-disorder transition at T_t in which the order parameter, defined as the volume of strongly correlated electrons at temperature T divided by that at $T = 0$ K, decreases with a Brillouin temperature dependence to zero at a temperature $T_t^* = T_N$, but with $T_t^* \approx T_t > T_N$. The order-disorder transition is first-order so long as a $T_t^* > T_t$ gives a discontinuous change in the volume of strongly correlated electrons on ordering into a CDW, but the volume change induced by an expansion of the Ni—O bond length is reduced by a compensating change in the bending angle ϕ.

1.7.4
Comparisons for Same T_t with/without Pressure

In order to distinguish further between a $W = W_b$ and a $W = W_b \exp (-\lambda\varepsilon_{sc}/\hbar\omega_O)$, we compared (Fig. 17) two samples of different composition having the same T_t, one under pressure and the other at ambient. Under pressure, the locally cooperative oxygen-vibration frequency ω_O would increase with a reduction of the Ni—O bond length and of the bending angle
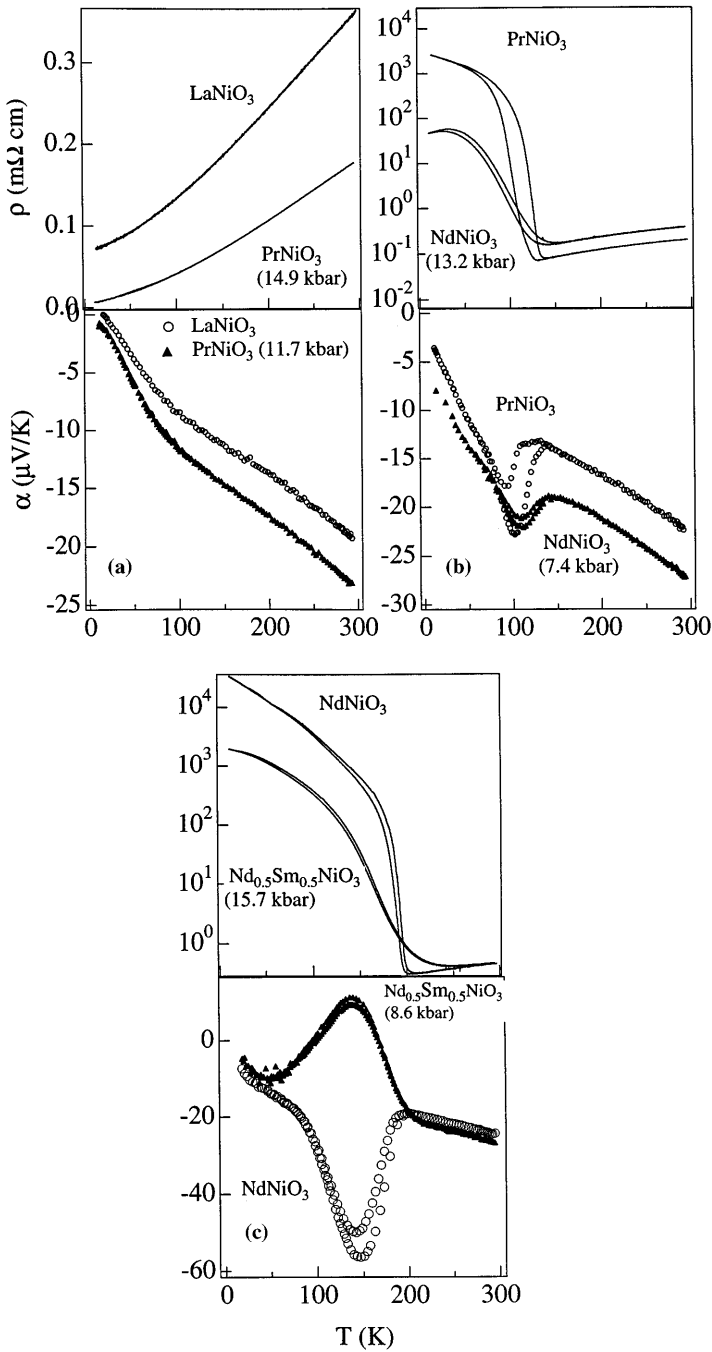
Fig. 17a–c. Comparisons of $\rho(T)$ and $\alpha(T)$ for two compounds with the same T_t, one at atmospheric pressure and the other under hydrostatic pressure; after [79]

ϕ; W_b would also increase with an increase in λ_σ as the NiO bond length and ϕ decrease. If $W = W_b$, pressure would be equivalent to increasing t and we should expect samples with the same T_t to have similar properties. However, if $W = W_b \exp(-\lambda\varepsilon_{sc}/\hbar\omega_O)$, then stiffening of ω_O in the exponential would not only have a stronger influence on W than the broadening of W_b, it would also influence other properties to make different compounds with the same T_t have quite different properties even though T_t occurs at a critical bandwidth W_c.

Comparison of $PrNiO_3$ at 14.9 kbar with $LaNiO_3$ at ambient shows metallic $PrNiO_3$ has a lower $\rho(T)$ that extrapolates to a much lower residual value at T = 0 K; there is no indication of an orthorhombic-rhombohedral transition below 15 kbar in $PrNiO_3$. Similarly, the transport properties of $PrNiO_3$ at ambient are quite different from those for $NdNiO_3$ at 13.2 kbar having the same T_t. More striking is the difference between $NdNiO_3$ at ambient and $(Nd_{0.5} Sm_{0.5}) NiO_3$ under 15.7 kbar with the same T_t, Fig. 17c. Figure 15d shows that, on cooling through the interval from T_t to T_N in $(Nd_{0.5} Sm_{0.5})NiO_3$, $\alpha(T)$ increases to a maximum at T_N; the magnitude of the interval $T_N < T < T_t$ changes little with pressure contrary to what would be expected from Fig. 14 if hydrostatic pressure simply increased W_b.

The increase in $T_N < T_t$ with decreasing bending angle ϕ is not, as has been suggested, an indication that the low-temperature phase contains localized e electrons that interact via superexchange interactions. A narrow, quarter-filled σ^* band should be ferromagnetic if the correlations are strong enough to remove completely the spin degeneracy (see Goodenough, this volume). We have seen, in the case of $La_{1-x}Y_xTiO_3$, that a larger bandwidth increases T_N for an itinerant-electron SDW in a band that would become ferromagnetic were it narrowed. However, the fact that pressure lowers T_N whereas increasing t raises it indicates that changing ω_O by decreasing the Ni—O bond length is more important than changes induced by increasing ϕ and that stabilization of long-range order below T_N for $W < W_c$ depends not only on W_b, but also on ω_O.

We [85] also investigated the evolution at ambient pressure of the magnetic susceptibility of the NiO_3 array in these samples; the data are shown in Fig. 18 together with $\rho(T)$ to locate T_t. The Ln^{3+}-ion contribution was obtained from $LnAlO_3$ perovskites and subtracted out. Both Landau diamagnetism and Van Vleck paramagnetism are small in magnitude compared with the measured $\chi(T)$, so no correction was made for these contributions.

Interpretation of the $\chi(T)$ data begins with a distinction between Stoner and mass enhancements. The electronic specific-heat parameter γ increases with the mass enhancement [14]. By measuring both $\chi(T)$ and γ at low temperatures, Sreedhar et al. [80] determined a Stoner factor S = 0.58, well below the S = 1 for a ferromagnetic instability. These nickel oxides are clearly on the itinerant-electron side of the transition from localized to itinerant

Fig. 18a–d. Temperature dependence of resistivity $\rho(T)$, magnetic susceptibility $\chi(T)$, and inverse susceptibility $\chi^{-1}(T)$ for the NiO_3 array of **a** $LaNiO_3$; **b** $PrNiO_3$; **c** $NdNiO_3$; **d** $Sm_{0.5}Nd_{0.5}NiO_3$. *Straight line* in (d) is a linear fit to $\chi^{-1}(T)$ above T_N; after [85]
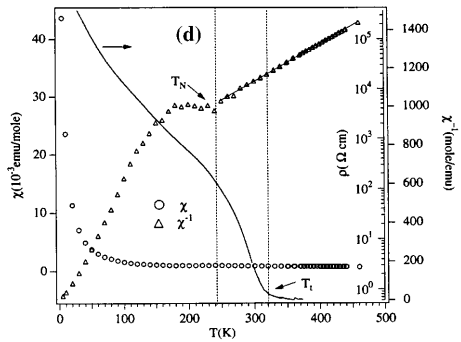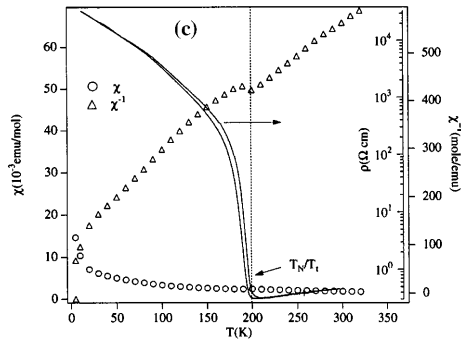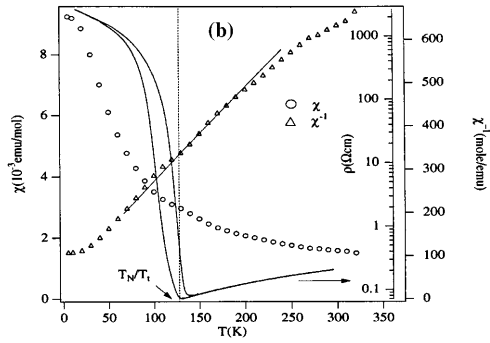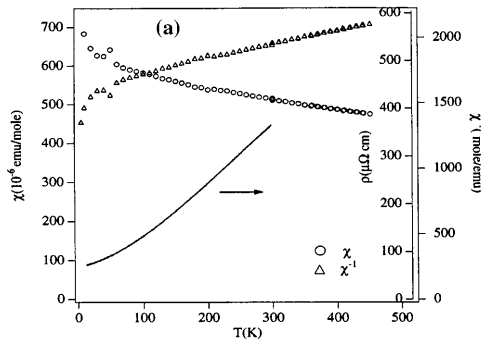
electronic behavior. Moreover, the curvature of the temperature dependence of $\chi(T)$ for mass enhancement is opposite to that for Stoner enhancement. Mott [86] was the first to point out this distinction, but he was unable to find a suitable experimental example to test his prediction that a flattening of the $\varepsilon_{\mathbf{k}}$ vs $\mathbf{k}$ dispersion at the Fermi energy of a mass-enhanced metallic system would give a temperature dependence below a temperature T_d.

Qualitatively, the $\chi(T)$ data for LaNiO$_3$ in Fig. 18a appears to fit the Mott prediction for a homogeneous electronic system. However, a weak temperature dependence persisting above the apparent $T_d \approx 200$ K does not conform to the Mott picture. Alternatively, this $\chi(T)$ curve may be described by a model containing two electronic phases in which

$$\chi = a\chi_O + b\chi_{cw} \tag{8}$$

where χ_O is the susceptibility of a mass-enhanced, conductive Fermi-liquid phase with a $T_d \approx 200$ K and χ_{cw} is a Curie–Weiss component from strong-correlation fluctuations.

Significantly, the $\chi^{-1}(T)$ curve for Nd$_{0.5}$Sm$_{0.5}$NiO$_3$, Fig. 18d, shows no anomaly at T_t as defined by $\rho(T)$. This observation demonstrates that the CDW below a $T_t > T_N$ is not stabilized by either Fermi-surface nesting or the onset of a homogeneous Mott–Hubbard transition. However, it is compatible with an order-disorder transition for strong-correlation fluctuations.

The $\chi^{-1}(T)$ curves of Fig. 18b, c for PrNiO$_3$ and NdNiO$_3$ show only a small anomaly at $T_N = T_t$ in a field of 10 kOe; the Curie–Weiss component χ_{cw} above T_N clearly increases with decreasing A-cation size and therefore bandwidth W. The behavior below T_N is uncharacteristic of a localized-electron antiferromagnet. Although the anomaly in $\chi^{-1}(T)$ at T_N increases as the band narrows, $\chi(T)$ continues to increase with decreasing T below T_N in all samples. This anomalous situation is not due to spin canting since there is no difference between the $\chi(T)$ for field-cooled and zero-field-cooled samples. Moreover, it does not fit the Moriya [87] description of the evolution from Pauli to Curie–Weiss paramagnetism, a description that is based on an extension of paramagnon theory rather than on the Brinkman–Rice mass enhancement used by Mott. A paramagnetic-type susceptibility below T_N would appear to imply retention of paramagnetic strong-correlation fluctuations below a T_N for the matrix.

We draw the following conclusions from the magnetic data:

1. The enhancement of $\chi(T)$ in the metallic phase exhibits temperature and bandwidth dependencies that are not described by existing models of homogeneous electronic systems, but they are consistent with a heterogeneous model of strong-correlation fluctuations in a mass-enhanced matrix as deduced from our transport measurements.
2. The lack of any change in $\chi(T)$ on traversing the insulator-metal transition at $T_t > T_N$ is incompatible with a homogeneous model of Fermi-surface nesting or a Mott–Hubbard transition, but it can be understood as an order-disorder transition of preexisting strong-correlation fluctuations.

3. The behavior of $\chi(T)$ below T_N is not characteristic of localized-spin antiferromagnetism, including canted-spin antiferromagnetism. In a magnetic field of 1 T, it exhibits a behavior like that of a paramagnet. It is as though the NiO_3 array disproportionates in a high magnetic field into alternating diamagnetic and paramagnetic nickel sites as is implied by the observation of Alonso et al. [74] for $YNiO_3$, the disproportionation suppressing long-range magnetic order.

Finally, Ghosh et al. [88] have reported low-energy excitations in $LaNiO_3$ that require the existence of two conditions: (i) a collection of two-level systems with a broad distribution and (ii) a flat density of states at low energy. Both of these conditions are fulfilled by the model of strong-correlation fluctuations in a Fermi-liquid matrix.

1.8
The Cuprates

Rhombohedral $LaCuO_3$ was first prepared by Demazeau et al. [89] under an oxygen pressure of 65 kbar. At lower oxygen pressures, tetragonal and orthorhombic $LaCuO_{3-\delta}$ phases have been obtained [90, 91]. Rhombohedral $LaCuO_3$ contains nominal $Cu(III):t^6\sigma^{*2}$; it is metallic [90] with a strongly hybridized σ^* band that is half-filled. A half-filled band has antiferromagnetic correlations whereas the quarter-filled band of $LaNiO_3$ has ferromagnetic correlations. Early magnetic-susceptibility data indicate the presence of a strong enhancement of the Pauli paramagnetism and therefore an approach to the Mott–Hubbard transition from the itinerant-electron side [92]. This observation suggested substitution of Nd for La to reduce the tolerance factor t and therefore narrow further the σ^* band. We were able to prepare single-phase, rhombohedral $La_{1-x}Nd_xCuO_3$ over the range $0 \leq x \leq 0.6$, and we have studied the evolution with x of the paramagnetic susceptibility as well as the pressure dependence of the transport properties.

Figure 19 shows $\alpha(T)$ under different pressures for x = 0, 0.25, and 0.5 [93]. We call attention to three features:

1. The value of $\alpha(300\ K)$ is small for all x, which indicates either little curvature of the $\varepsilon(\mathbf{k})$ vs $\mathbf{k}$ dispersion curve at the Fermi energy ε_F or a fortuitous cancellation of positive and negative contributions from different parts of the Fermi surface; this observation is inconsistent with the curvature of $\varepsilon(\mathbf{k})$ at ε_F of the band-structure calculations based on a homogeneous quasiparticle model.
2. The phonon-drag component is increasingly suppressed as x increases, but it is enhanced by the application of pressure.
3. The pressure dependence of $\alpha(300\ K)$ is small for x = 0, but becomes positive for x > 0.

According to the discussion of Fig. 3, these last features are the signature for strong-correlation fluctuations in a Fermi liquid that approaches the Mott–Hubbard transition from the itinerant-electron side. We should, therefore,
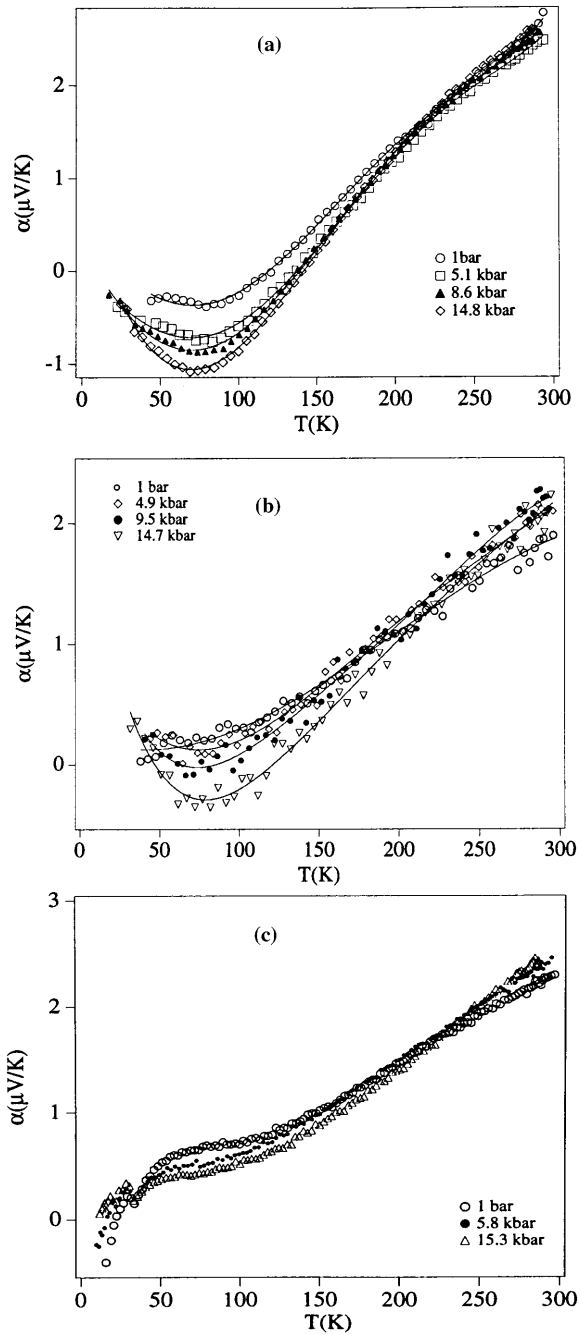
Fig. 19a–c. Temperature dependence of the thermoelectric power $\alpha(T)$ of $La_{1-x}Nd_xCuO_3$ under different pressures: **a** $x = 0$; **b** $x = 0.25$; **c** $x = 0.30$; after [94]

expect to find a systematic enhancement of the paramagnetic susceptibility of the CuO_3 array as x increases. Figure 20 shows the susceptibility data after subtraction of the Nd contribution as obtained from $NdAlO_3$ [94]. Four features are noteworthy:

1. The $\chi(T)$ curve for x = 0 is temperature-independent above 200 K, but it is enhanced relative to a conventional Pauli paramagnetism by at least two orders of magnitude.
2. The temperature dependence of $\chi(T)$ below 200 K cannot be attributed to a Curie–Weiss paramagnetism from magnetic impurities.
3. As x increases, $\chi(T)$ for the CuO_3 array becomes temperature-dependent above 200 K, but the $\chi^{-1}(T)$ curve gives a negative Weiss constant that has too large a magnitude and a Curie constant that is too large to represent a homogeneous array of localized spins.
4. The susceptibility of the CuO_3 array at 300 K increases linearly with x more than tenfold on going from x = 0 to x = 0.6.

These features indicate Eq. (8) is applicable and support the evidence from transport data for a heterogeneous electronic model as the Mott–Hubbard transition is approached from the itinerant-electron side. The mass-enhanced contribution χ_O would have a $T_d \approx 200$ K like that for the $LnNiO_3$ family,
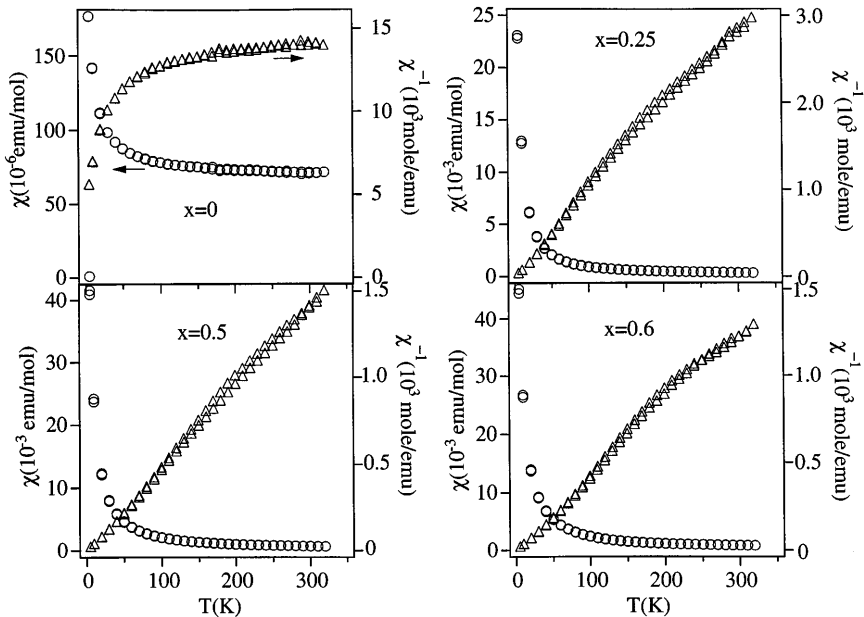
Fig. 20. Temperature dependence of molar magnetic susceptibility $\chi(T)$ and its inverse $\chi^{-1}(T)$ for the CuO_3 array of $La_{1-x}Nd_xCuO_3$. The small difference between field-cooled and zero-field-cooled data below room temperature appears to be due to a lateral displacement of the sample in the bore of the SQUID on thermal cycling; after [94]

which may indicate it is characteristic of χ_O at the phase limit for the homogeneous mass-enhanced electronic system.

2
Mixed-Valent 3d-Block Perovskites $Ln_{1-x}A_xMO_3$

Oxygen-stoichiometric perovskites may become mixed-valent if a disproportionation occurs in the MO_3 array as was discussed for high-temperature $LaMnO_3$ and low-temperature $CaFeO_3$. The MO_3 array may also become mixed-valent with the introduction of cation or oxygen vacancies. However, atomic vacancies and M-atom substitutions strongly perturb the periodic potential of the MO_3 array. Therefore, this review considers only oxygen-stoichiometric systems $Ln_{1-x}A_xMO_3$ in which Ln is a lanthanide and A = Ca or Sr; in these systems, only the charge of the MO_3 array varies with x with minimal perturbation of its periodic potential by the aliovalent cation substitutions. However, for a fixed value of x, isovalent substitutions for the Ln^{3+} or A^{2+} ions prove useful where these substitutions induce on the MO_3 array strong-correlation magnetism, charge/orbital ordering, or changes between itinerant-electron behavior and polaronic conduction.

2.1
The Titanates

2.1.1
$La_{1-x}Sr_xTiO_3$

$SrTiO_3$ has an empty π^* band; substitution of La for Sr introduces one electron per La^{3+} ion into the π^* band. $LaTiO_3$ (see Sect. 1.1.2) is a single-phase itinerant-electron antiferromagnet containing strongly correlated π^* electrons on the TiO_3 array. At a given site, we assume the electrons of the Hubbard band carry electrons of both majority and minority spin. This situation differs from that in the $Sr_{1-x}Ca_xVO_3$ system where the electrons in the lower Hubbard band coexist with Fermi-liquid electrons and appear to represent strong-correlation fluctuations without long-range ordering into either a CDW or a SDW. For small band filling, namely $0.5 < x < 1.0$, the electron-electron interactions are weak and the electrons are described by conventional band theory. Clearly, the electron-electron interactions must increase with the band filling until they reach U_π in $LaTiO_3$. This situation has attracted groups in Japan to investigate the evolution of the electron correlations with band filling and ourselves to examine the character of the transition from antiferromagnetic insulator to Pauli paramagnetic metal.

Fujishima et al. [95] used optical-conductivity spectra to monitor the increase in effective mass of the electrons with La concentration. Kumagai et al. [96] measured the electronic specific heat γ at low temperatures and compared it to the magnetic susceptibility χ obtained by Tokura et al. [97] on the same samples; see Fig. 21. The Wilson ratio χ/γ remained nearly constant over the entire range of x, which indicates that the divergence of γ and χ on
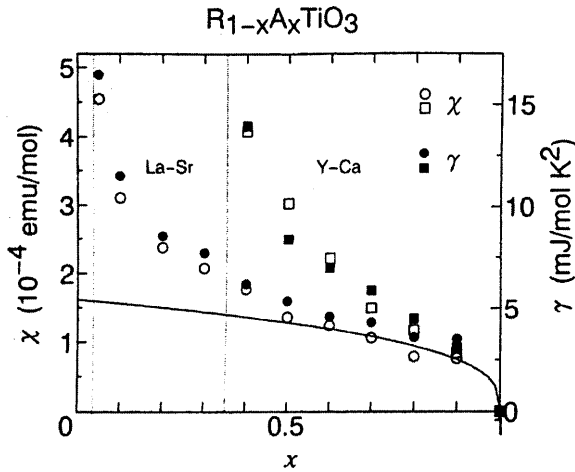
Fig. 21. Compositional dependence x of the electronic heat capacity parameter γ and Pauli paramagnetic susceptibility $\chi(T)$ in the metallic region of the systems $La_{1-x}Sr_xTiO_3$ (*circles*) and $Y_{1-x}Ca_xTiO_3$ (*squares*); after [96]

approaching the critical on-site electrostatic energy U_c is entirely due to a Brinkman–Rice mass enhancement, see Eq. (2); there is little Stoner enhancement. Moreover, there is no evidence that m^* goes through a maximum on the approach to the Mott–Hubbard transition in this mixed-valent system. Furukawa et al. [98] have used $^{47/49}$Ti and ^{139}La nuclear magnetic resonance (NMR) to investigate whether antiferromagnetic (AF) fluctuations of Ti(III) spins exist in the metallic state near the Mott–Hubbard transition. They found no evidence for the growth of AF spin correlations on approaching the Mott–Hubbard transition from the metallic side and concluded that the on-site electron-electron interactions drive the insulator-metal transition in this system.

We [99] have studied the evolution of structural, magnetic, and transport properties across the insulator-metal transition. Figure 22 shows the variation of the cell volume with x for $La_{1-x}Sr_xTiO_3$. The strong deviation from Vegard's law for decreasing x < 0.5 reflects the larger volume occupied by strongly correlated electrons. According to the virial theorem (Eq. 21 of Goodenough, this volume) more localized antibonding electrons result in a larger equilibrium Ti—O bond length. A first-order expansion of the volume with decreasing x occurs in a narrow two-phase region 0.04 < x < 0.08. The antiferromagnetic phase has a large canted-spin ferromagnetic component, but there is no cooperative J-T orbital ordering below T_N that optimizes the orbital magnetic moment as occurs where there are localized-electron spins in $LaVO_3$ and YVO_3. Figure 23 shows the variation of the Néel temperature T_N with x; it drops precipitously from 145 K to 100 K in the range $0 \leq x < 0.05$ and remains constant across a narrow two-phase domain $0.05 \leq x \leq 0.08$ where the net canted-spin moment at 10 K, M(10 K), decreases continuously to zero with increasing x. There is no anomaly in either $\alpha(T)$ or $\rho(T)$ at T_N in
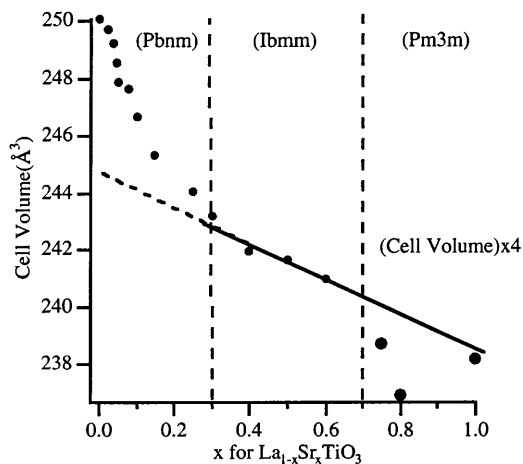
Fig. 22. Unit-cell volume vs x for $La_{1-x}Sr_xTiO_3$; after [99]
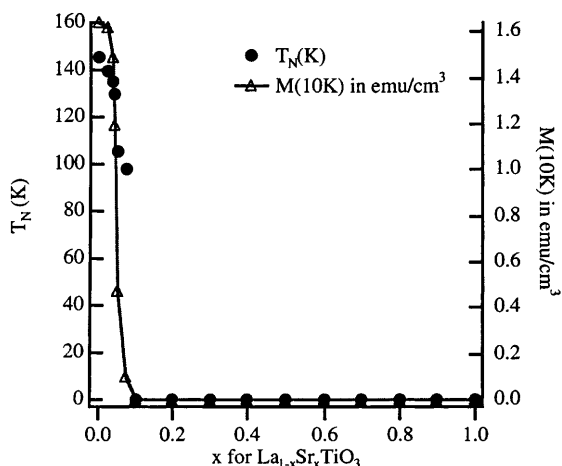
Fig. 23. Néel temperature T_N and magnetization at 10 K, M(10 K), vs x for $La_{1-x}Sr_xTiO_3$; after [99]

the single-phase antiferromagnetic composition. The antiferromagnetic phase changes from a p-type small-polaron conductor to a p-type metal at $x \geq 0.044$ before becoming an n-type metal for $x = 0.05$ where the metallic phase dominates the conduction. Under hydrostatic pressure, the $x = 0.044$ sample changes from a p-type to an n-type conductor; pressure stabilizes the metallic phase relative to the antiferromagnetic phase as it has the smaller volume.

We conclude that the $La_{1-x}Sr_xTiO_3$ system exhibits a nearly classic Mott–Hubbard transition as the π^* band is filled toward an integral number of electrons per Ti atom. The transition is first-order and exhibits a volume

expansion with increasing electron localization in accordance with the virial theorem. Segregation into two electronic phases is confined to a narrow compositional range.

2.1.2
$Y_{1-x}Ca_xTiO_3$

Since $YTiO_3$ has stronger electron correlations than $LaTiO_3$ and is ferromagnetic rather than antiferromagnetic, it is of interest to compare the evolution with x of the physical properties of $Y_{1-x}Ca_xTiO_3$ with those of $La_{1-x}Sr_xTiO_3$. At large x, both systems change from n-type dopant of the π^* band to n-type metallic behavior as the concentration of trivalent ions increases from x = 1.0 to x = 0.9. However, the narrower π^* bands associated with the smaller and more acidic Y and Ca cations give rise to a more abrupt onset of an enhanced m* and an insulator-metal transition at a larger value of x [100]. As in the $La_{1-x}Sr_xTiO_3$ system, the Wilson ratio χ/γ remains nearly constant, indicating a Brinkman–Rice mass enhancement with little Stoner enhancement [96]. The insulator-metal transition occurs in the interval $0.3 < x < 0.4$ where there appears to be a two-phase region. The Curie-Weiss paramagnetism changes from a positive to a negative Weiss constant in the interval $0 < x < 0.1$; for $0.1 \leq x \leq 0.35$, the susceptibility $\chi(T)$ exhibits a behavior typical of a canted-spin antiferromagnet as in $LaTiO_3$ as might be expected for weaker correlations. Thus the system acts as would be anticipated from an extrapolation of the $La_{1-x}Sr_xTiO_3$ system.

2.2
The Vanadates

The three systems $La_{1-x}Sr_xVO_3$, $La_{1-x}Ca_xVO_3$, and $Y_{1-x}Ca_xVO_3$ have been studied. Each system illustrates a transition from localized $V^{3+}:^3T_{1g}$ configurations in antiferromagnetic $LaVO_3$ and YVO_3 to itinerant π^* electrons in metallic $SrVO_3$ and $CaVO_3$. The π^* band is narrowest in the $Y_{1-x}Ca_xVO_3$ system and broadest in the $La_{1-x}Sr_xVO_3$ system. Three points of comparison with the $La_{1-x}Sr_xTiO_3$ and $Y_{1-x}Ca_xTiO_3$ systems are to be noted:

1. The π^* band of a VO_3 array contains an additional electron; it is therefore narrower than that of a corresponding TiO_3 array, which means that perturbation of the periodic electron potential on the MO_3 array by aliovalent A-site cations is a larger fraction of the bandwidth W_π in the VO_3 array.
2. A transition from localized to itinerant electronic behavior occurs with increasing x in the VO_3 array whereas in the TiO_3 array there is only a crossing of the Mott–Hubbard transition from strongly to weakly correlated electrons.
3. Although the π^* band of a VO_3 array is narrower than that of a TiO_3 array, the energy ΔE_p is smaller, which means that a stronger transfer with increasing x of O-2p character into the π^* band can be expected for the VO_3

array. Pen et al. [101] have confirmed, with X-ray-absorption and resonant-photoemission spectroscopy, a strong transfer of O-2p spectral weight into the π^* band of $Y_{1-x}Ca_xVO_3$ with increasing x.

In an early study, Reuter and Wollnik [102] reported that the system $La_{1-x}Ca_xVO_3$ forms a solid solution over the entire compositional range. Dougier et al. [103] reported an insulator-metal (I-M) transition occurs at $x_c \approx 0.26$ within a single-phase domain $0 \leq x \leq 0.5$ and interpreted it within a homogeneous model as an Anderson transition, the Fermi energy ε_F dropping across a mobility edge in the lower π^* band corresponding to the V^{4+}/V^{3+} redox couple. Nguyen and Goodenough [104] confirmed a metal-insulator transition at $x_c \approx 0.26$ and interpreted it within a heterogeneous electronic model to represent a percolation threshold for the formation of a narrow π^* band associated with V atoms nearest-neighbor to Ca atoms. In the sister system $La_{1-x}Sr_xVO_3$, which has a broader π^* band, Dougier and Hagenmuller [105] reported a smooth I-M transition at $x_c = 0.225$. In this system, the antiferromagnetic Néel temperature T_N falls monotonically from 142 K at x = 0 to 100 K near x = 0.2, dropping abruptly to 0 K at x_c. Mahajan et al. [106] reported a lattice parameter varying linearly with x according to Végard's law and a room-temperature paramagnetic susceptibility that varies smoothly with x through x_c, becoming temperature-independent, but strongly enhanced, below 400 K for all x > x_c. On the other hand, in the $Y_{1-x}Ca_xVO_3$ system, which has the narrowest π^* band, Kasuya et al. [107] found an I-M transition at x ≈ 0.5. Analysis of their X-ray data indicates a linear variation of the atomic volume over the range $0 \leq x \leq 0.7$ with an abrupt drop in the range 0.7 < x < 0.8 [104].

We draw the following conclusions from these data:

1. Doping $LaVO_3$ with Sr initially creates molecular-orbital clusters at the 8 vanadium atoms nearest-neighbor to a Sr^{2+} ion and the I-M transition occurs at the percolation threshold for the Sr^{2+} ions. However, the abrupt drop in T_N at x_c signals an associated broadening of the π^* band that drops the Fermi energy ε_F below a mobility edge in the hole-rich percolating phase and induces an emptying below 400 K of the localized $^3T_{1g}$ states, which become Anderson-localized states lying above ε_F.

2. On the other hand, doping YVO_3 with Ca appears to create, initially, small-polaron V(IV) centers at one of the vanadium atoms nearest-neighbor to a Ca^{2+} ion; at the percolation threshold for the Ca^{2+} ions, the π^* band remains too narrow to drop ε_F below a mobility edge, so the electron transport is either polaronic or by variable-range hopping of holes. For x > 0.5 there is a shift from hole to electron transport, and the variable-range hopping of electrons occurs via tunneling without an activation energy. Delocalization of the electrons into itinerant-electron states appears to occur, according to the virial theorem, only in the range 0.7 < x < 0.8 where there is an abrupt decrease in the unit-cell volume.

3. The system $La_{1-x}Ca_xVO_3$ behaves in an intermediate manner [104]. The I-M transition occurs at a higher $x_c = 0.26$ compared with $x_c = 0.225$ in the

$La_{1-x}Sr_xVO_3$ system, but below $x_c \approx 0.5$ found for $Y_{1-x}Ca_xVO_3$. Moreover, there was evidence of spin-glass behavior with a spin-blocking temperature T_{sg} that increased from 140 K for x = 0.3 to a maximum of 280 K at x = 0.6, decreasing to 265 K at x = 0.8. A Curie–Weiss paramagnetism was found above a structural phase transition at $T_t \approx 640$ K over the entire range $0 \leq x \leq 1$. In this case, the hole-poor volume clearly retains localized $^3T_{1g}$ configurations beyond the I-M transition at $x_c = 0.26$.

2.3
The Chromates

The metallic end member $SrCrO_3$ is a high-pressure phase. At ambient pressure, the system $La_{1-x}Sr_xCrO_3$ is a small-polaron conductor in the range $0 < x < 0.5$ with a motional enthalpy $\Delta H_m \approx 0.1$ eV for the Cr(IV) holes in the Cr(IV)/Cr(III) redox couple with a shallow trapping of the holes at the Sr^{2+} ions [108–112].

2.4
The Manganates

The manganese-oxide perovskites $Ln_{1-x}A_xMnO_3$ (Ln = lanthanide, A = alkaline-earth) have been studied extensively and intensively because they exhibit an intrinsic colossal magnetoresistance (CMR) at and above a ferromagnetic Curie temperature T_C as well as an extrinsic giant magnetoresistance associated with tunneling of electron spins across grain boundaries below T_C. Here we consider only the intrinsic phenomenon.

As discussed in Sect. 1.4, all the manganese atoms contain localized t^3 configurations with a spin S = 3/2; these localized spins introduce a strong intraatomic exchange energy Δ_{ex} that removes the spin degeneracy of the e electrons. In the end member $LaMnO_3$, the e electrons approach the transition from localized to itinerant electronic behavior from the localized-electron side; a cooperative J-T orbital ordering stabilizes electron localization at lower temperatures. In the solid solutions $Ln_{1-x}A_xMnO_3$, each alkaline-earth cation A^{2+} removes an e electron from the Mn(IV)/Mn(III) redox couple, which introduces the possibility of fast e-electron transfer from Mn(III) to Mn(IV) atoms and stabilizes electron delocalization relative to ordering of the electrons into localized orbitals.

For small x, the O′—O* transition temperature T_{JT} associated with a cooperative J-T orbital ordering drops steeply with increasing x. On the other hand, long-range coulomb interactions between charge carriers may collaborate with orbital ordering to localize the electrons at lower temperatures, especially at critical Mn(IV)/Mn ratios such as 1/2. Therefore, the $Ln_{1-x}A_xMnO_3$ phase diagrams exhibit a competition between delocalization of the e electrons into itinerant σ^* bands or molecular orbitals and their localization at Mn(III) ions.

The holes may be localized either as small-polaron $Mn(IV)O_{6/2}$ complexes or in a molecular orbital of a two-manganese Mn(III)—O—Mn(IV) polaron.

At higher temperatures, thermal expansion favors localization of the charge carriers as mobile dielectric polarons in a pseudocubic O* phase having dynamic, locally cooperative J-T deformations; at lower temperatures, long-range orbital ordering may localize the e electrons into (001) planes of an O′ structure while mobile small-polaron holes prevent the static ordering within the (001) planes found in $LaMnO_3$. In this case, the magnetic superexchange coupling would remain ferromagnetic within the (001) planes and antiferromagnetic between $LaMnO_3$. On the other hand, fast electron transfer within a two-manganese polaron introduces a ferromagnetic double-exchange interaction within the polaron. Where two-manganese polarons are formed, orientation of their axes along the c-axis would introduce a ferromagnetic double-exchange component varying as $\cos(\theta/2)$ that competes with the antiferromagnetic c-axis superexchange interaction that varies as $\cos\theta$; see Eqs. (8) and (10) of Goodenough, this volume; optimization of the total c-axis exchange energy with respect to the angle θ between spins in neighboring (001) planes may produce a canted-spin configuration in which the ferromagnetic component increases with the concentration of two-manganese polarons that have their axes oriented along the c-axis. In this case, a large ferromagnetic component below a Curie temperature T_c may occur even where the two-manganese polarons become stationary in a ferromagnetic insulating state.

The formation of two-manganese polarons is an intermediate step between small-polaron and itinerant electronic behavior. Itinerant e electrons within an O* or R phase introduce metallic conductivity as well as ferromagnetic double-exchange interactions. We refer to this ferromagnetic coupling as de Gennes double exchange to distinguish it from the Zener double exchange within a two-manganese cluster. The de Gennes double exchange is strong enough to give a full ferromagnetic moment at lowest temperatures.

Where there is a segregation into a more conductive ferromagnetic phase and a paramagnetic phase near the O′—O* phase boundary, an applied magnetic field stabilizes the ferromagnetic phase relative to the paramagnetic phase; growth of the more conductive phase to the percolation threshold is the origin of the colossal magnetoresistance (CMR) found where the two phases coexist. In addition, changes in the tolerance factor alter the bandwidth W, particularly where the coexistence of two phases makes $W = W_\sigma \exp(-\lambda\varepsilon_a/\hbar\omega_O)$, where W_σ is the tight-binding bandwidth; see Eq. (23) of Goodenough, this volume. Therefore, the CMR phenomenon can be manipulated sensitively for a given Mn(IV)/Mn ratio by changes in the mean ionic radius of the larger cations on A sites of the AMO_3 perovskites. We illustrate the competition between localized and itinerant e-electron behavior in three systems: $(La_{1-y}Ln_y)_{0.7}Ca_{0.3}MnO_3$, $La_{1-x}Ca_xMnO_3$, and $La_{1-x}Sr_xMnO_3$.

2.4.1
$(La_{1-y}Ln_y)_{0.7}Ca_{0.3}MnO_3$

In the systems $(La_{1-y}Ln_y)_{0.7}Ca_{0.3}MnO_3$, the ratio Mn(IV)/Mn = 0.3 is held constant and the bandwidth is decreased by substituting smaller Ln^{3+} ions for

La^{3+}. In these systems, the competition of interest is between a more conductive ferromagnetic phase and a polaronic paramagnetic/antiferromagnetic phase. At this Mn(IV)/Mn ratio, the ferromagnetic phase appears to be hole-rich with a tendency to be stabilized as a charge-density wave (CDW) to lower the coulomb repulsion between charge carriers. A first-order transition between phases allows segregation into two phases. Segregation at lower temperatures is possible as it is accomplished by cooperative oxygen displacements, and this type of diffusionless phase segregation may be dynamic. A dynamic phase segregation is not detected by a conventional diffraction experiment, which is why this phenomenon has remained unnoticed until recently.

The CMR phenomenon found for Mn(IV)/Mn = 0.3 is illustrated by the system $La_{0.7-y}Pr_yCa_{0.3}MnO_3$; Fig. 24 from Hwang et al. [113] shows, on a logarithmic scale, the change in resistivity $(\rho_{0T}-\rho_{5T})$ on applying a magnetic field of 5T, normalized to ρ_{5T}, as a function of temperature. The system becomes ferromagnetic below a first-order transition at the Curie temperature T_C, which is marked by an arrow for the different values of y in the compositional range $0 \leq y \leq 0.7$. This CMR phenomenon is representative of that found in the range $0.1 \leq x \leq 0.375$ of the system $La_{1-x}Ca_xMnO_3$ and $La_{1-x}Sr_xMnO_x$; it is to be distinguished from the CMR phenomenon found near x = 0.5 where an itinerant-electron ferromagnetic phase competes with a charge-ordered/orbitally-ordered antiferromagnetic phase, see phase diagrams of Figs. 35 and 38.

Two features of Fig. 24 are to be noted: first, the extraordinary decrease in T_C with the isovalent substitution of Pr^{3+} for La^{3+}, from 250 K at y = 0 to about 80 K at y = 0.6, and second, the dramatic increase in the negative magnetoresistance just above T_C as T_C decreases. The resistivity ρ_{0T} shows a
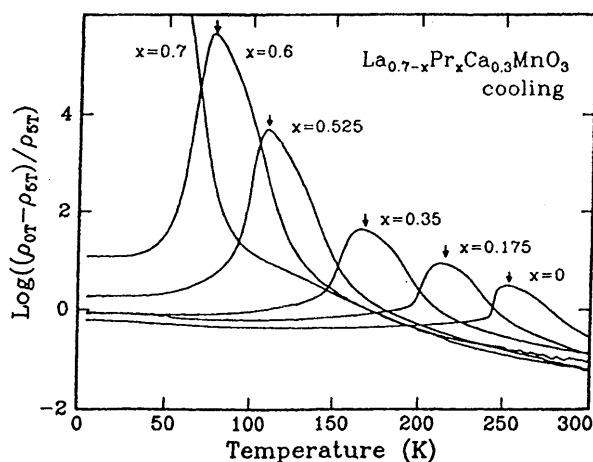
Fig. 24. CMR at 5 T on cooling for different compositions 0 = x = 0.6 in the system $La_{0.7-x}Pr_xCa_{0.3}MnO_3$. The *arrows* indicate the Curie temperature T_C; after [113]

first-order transition at T_C from polaronic behavior above T_C to a more conductive behavior below T_C and T_C increases with an applied magnetic field in the range $0 \leq y \leq 0.6$. For $y = 0.7$, the conductivity remains polaronic on cooling through a second-order transition at an antiferromagnetic Néel temperature T_N. A change from the O^* to the O' orthorhombic structure also occurs on increasing y beyond $y = 0.6$.

These dramatic changes are caused by a decrease in the $(180° - \phi)$ Mn—O—Mn bond angle on substitution of the smaller Pr^{3+} ion. According to Eq. (18) of Goodenough, this volume, the width of a narrow σ^* band below T_C would be given by

$$W_\sigma \sim \varepsilon_\sigma \lambda_\sigma^2 \cos \phi \langle \cos(\theta_{ij}/2) \rangle \tag{9}$$

where θ_{ij} is the angle between spins on neighboring Mn atoms. Alignment of the spins below T_C favors stabilization of itinerant-electron states ($\tau_h < \omega_O^{-1}$) relative to localization of the charge carriers in polaronic states ($\tau_h > \omega_O^{-1}$), where $\tau_h \sim \hbar/W$ is the time for an electron to tunnel from an Mn(III) to an Mn(IV) near neighbor and ω_O^{-1} is the period of the locally cooperative oxygen displacements that would localize the mobile holes as either a small polaron, i.e., an Mn(IV) ion, or as a two-Mn polaron, i.e., an Mn(III)—O—Mn(IV) pair in which the hole is confined to a molecular orbital. However, the remarkable changes with Pr^{3+}-ion substitution cannot be accounted for by the relatively small change in $\cos \phi$. On the other hand, a transition from polaronic to itinerant electronic behavior may be first order according to the virial theorem, Eq. (20) of Goodenough, this volume. Therefore, it would appear that the bandwidth should not be $W = W_\sigma$, but have the form of Eq. (23) of Goodenough, this volume

$$W = W_\sigma \exp(-\lambda \varepsilon_a / \hbar \omega_O) \tag{10}$$

that is applicable where there is a coexistence of two phases; ε_a is an activation energy to convert from one phase to the other and $\omega_O = \omega_O(\phi)$ decreases with increasing bending angle ϕ of the $(180° - \phi)$ Mn—O—Mn bonds. The experimental data on the manganese-oxide perovskites supports such a model.

To investigate this model, we [114, 114a] undertook a study of the transport and magnetic properties of the system $(180° - \phi)$ $(La_{1-y}Ln_y)_{0.7}Ca_{0.3}MnO_3$ over the compositional range $0.2 \leq y \leq 1.0$, corresponding to ambient tolerance factors $0.964 \geq t \geq 0.946$ that span the transition from ferromagnetic order below a T_C with a CMR at and above T_C to antiferromagnetic order below a T_N. We chose Nd over Pr for Ln to minimize any interference in the measured properties of the MnO_3 array from interactions with $4f^n$ configurations on the rare-earth atom.

Figure 25 shows the temperature dependence of the thermoelectric power $\alpha(T)$ for several compositions in the range $0.2 \leq y \leq 0.75$. At atmospheric pressure, the $0.55 \leq y \leq 1$ samples with $0.946 \leq t \leq 0.952$ are in the O'-orthorhombic phase and undergo a second-order polaronic-polaronic transition at a Néel temperature T_N to a weakly canted antiferromagnetic-spin
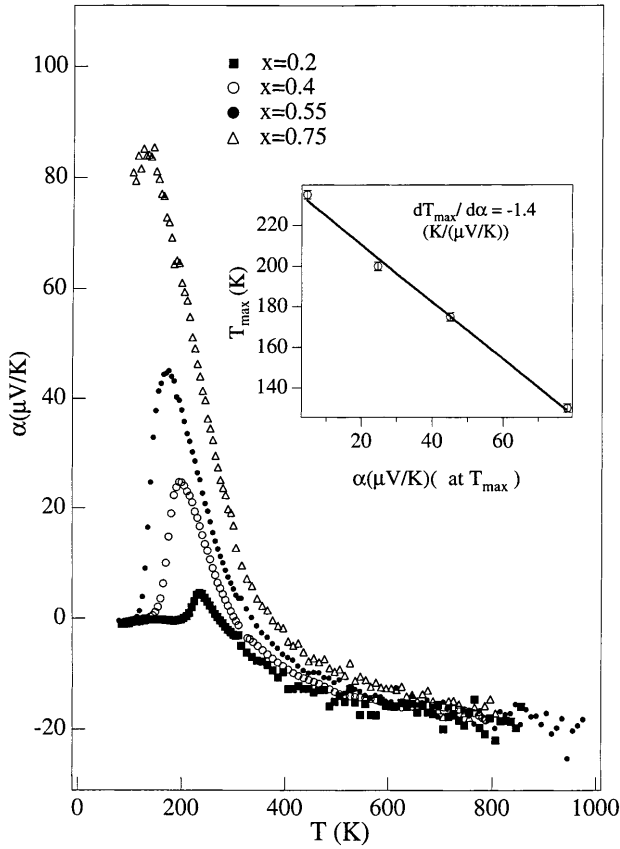
Fig. 25. Thermoelectric power $\alpha(T)$ for several compositions $0.20 \leq x \leq 0.75$ of the system $(La_{1-x}Nd_x)_{0.7}Ca_{0.3}MnO_3$; after [114]

configuration. The $0 \leq y \leq 0.55$ samples are in the pseudocubic O*-ortho-rhombic phase $(c/a \approx \sqrt{2})$ and undergo a first-order phase change at a ferromagnetic Curie temperature T_C. The temperature dependence of the resistivity $\rho(T)$ exhibits a strong maximum at T_C in the O* phase; $\rho(T)$ continues to increase with decreasing temperature below T_N in the O' phase, and we could not obtain a stable measure of $\alpha(T)$ below T_N in this phase. The maximum in $\alpha(T)$ occurs at a $T_{max} > T_C$ in the O* phase. Five other features of Fig. 25 are to be noted.

First, at high temperature, $\alpha(T)$ approaches a temperature-independent value of -20 μV/K in the O* samples, a somewhat larger value in the O' sample of Fig. 26. A temperature-independent α is indicative of polaronic conduction in which the statistical term

$$\alpha = (k/e)\ln[\beta(1-c)/c] \tag{11}$$
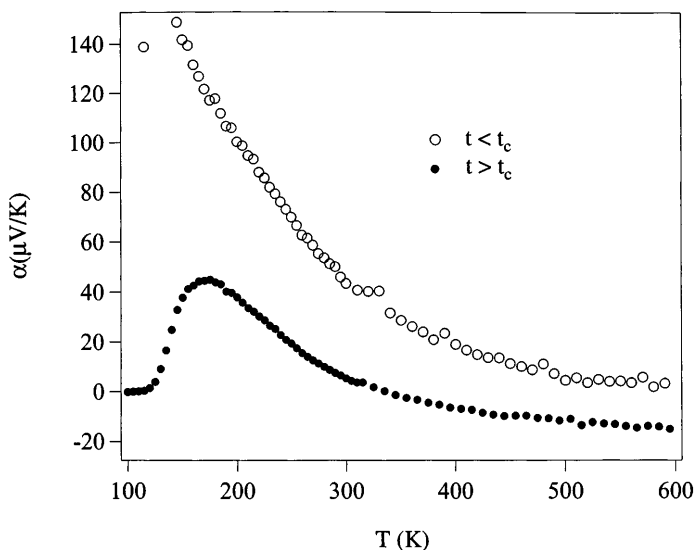
Fig. 26. High-temperature thermoelectric power $\alpha(T)$ for $x = 1.0$ ($t = 0.946 < t_c$) and $x = 0.55$ ($t = 0.957 > t_c$) of the system $(La_{1-x}Nd_x)_{0.7}Ca_{0.3}MnO_3$; after [114a]

dominates any transport contribution. In Eq. (11) the spin-degeneracy factor is $\beta = 1$ because of the strong intraatomic exchange at the Mn atoms; c is the fraction of available sites that are occupied by charge carriers. For small polarons, $c = xN/N = x$ would give a value $\alpha = +38$ μV/K whereas a two-Mn polaron would correspond to $c = xN/(N/2) = 2x$ to give the observed $\alpha = -20$ μV/K. Therefore, we conclude that at high temperatures there is a progressive transition with increasing tolerance factor from small polarons to two-Mn polarons as t increases, complete conversion occurring for $t > 0.955$. At still higher values of t, a transition from two-Mn polarons to itinerant-electron behavior can be anticipated. Indeed, in $La_{2/3}(Ca_{1-x}Sr_x)_{1/3}MnO_3$ the transition at T_C changes from first-order to second-order with increasing x [115] and the electrons become itinerant in the paramagnetic phase of $La_{0.65}Ba_{0.35}MnO_3$, which has the highest value of the tolerance factor t [116]. Confirmation of two-Mn polarons was found in the $La_{1-x}Ca_xMO_3$ system by Mössbauer spectroscopy for $x = 0.20$ [117, 118] and by Mn K-edge X-ray extended fine structure (EXAFS) for $x = 0.25$ [119].

The existence of two-Mn polarons was postulated by Zener [120] in his initial formulation of the ferromagnetic double-exchange interaction, see Eq. (10) of Goodenough, this volume. He envisaged the e electron of an Mn(III)—O—Mn(IV) pair would occupy a molecular orbital (MO) in which fast electron transfer ($\tau_h < \omega_O^{-1}$) occurred to couple parallel the localized spins $S = 3/2$ from the t^3 configurations. To account for the observed global ferromagnetic coupling and metallic temperature dependence of the resistivity found below T_C in $La_{0.7}Ca_{0.3}MnO_3$, Zener further postulated that these polaronic pairs move diffusively, but without an activation energy. Implicit in

the Zener model is a polaron mobility $\mu_P = eD_O/kT$ in which the temperature-independent diffusion coefficient $D_O \sim \tau_O^{-1}$ contains a transfer time $\tau_O < \tau_s$ for diffusion of the MO, where τ_s is the spin-relaxation time. Although the global ferromagnetic coupling of this model is not correct, nevertheless we have chosen [114] to refer to the two-Mn polarons as *Zener polarons* to distinguish them from the conventional one-site small polaron.

Second, the sharp increase in $\alpha(T)$ as T decreases to T_{max} indicates a trapping out of the mobile Zener polarons. Coexisting with the polaronic phase are hole-rich clusters; shortening of the $\langle$Mn—O$\rangle$ bonds within a cluster would create a transition from $\tau_h > \omega_O^{-1}$ to $\tau_h = \omega_O^{-1}$ for all nearest neighbors within a cluster. The volume of the hole-rich phase increases with the number of holes that are trapped in it and, as does that of a conventional magnetic polaron, with their mobility. As ω_O hardens with increasing tolerance factor t, the holes of the minority phase become more mobile, which enlarges the volume of this phase at a given temperature $T = T_C$. The mobility of the matrix polarons also increases with t and with the alignment of the spins on the application of an external magnetic field H_a. Moreover, a greater hole mobility increases the double-exchange component of the ferromagnetic interactions. Therefore, the Curie temperature T_C increases with t and H_a; at T_C the minority phase crosses the percolation threshold to become the majority phase. The sharp growth of the minority phase as T decreases through T_C reflects spin alignment of the matrix. The first-order character of the transition at T_C indicates a discontinuous increase in the volume fraction of the more conductive phase on crossing T_C.

Independent evidence for superparamagnetic clusters above T_C is apparent in the inverse paramagnetic susceptibility vs temperature shown in Fig. 27; the huge difference $\theta - T_C$, where θ is the high-temperature Weiss constant, indicates an anomalously extensive range of short-range ferromagnetic order above T_C. A dynamic phase segregation by cooperative atomic displacements would create mobile phase boundaries, and the application of a magnetic field would stabilize the ferromagnetic, conductive clusters relative to the polaronic, paramagnetic matrix, thereby increasing the trapping of mobile Zener polarons by the ferromagnetic clusters and increasing the size of the clusters. The CMR phenomenon follows immediately from a two-phase model in which a conductive, superparamagnetic minority phase present above the long-range ferromagnetic-ordering temperature T_C of the matrix grows in a magnetic field to beyond its percolation threshold [121].

Further evidence for phase segregation above and below T_C has been obtained with a variety of other techniques in addition to Mössbauer [117, 118] and EXAFS [119]. In $La_{0.7}Ca_{0.3}MnO_3$, Quijada et al. [122] have been able to describe the structure of the low-energy optical conductivity with a two-phase model. Kim et al. [123] came to a similar conclusion from their optical-conductivity data, and Zhao et al. [124] used pulsed laser excitation to reveal a fast transient associated with photoionization of the polaronic phase and a slow transient associated with the ferromagnetic phase in $La_{0.7}Ca_{0.3}MnO_3$. Sakaie et al. [125] have confirmed with ^{139}La NMR a slow correlation time for the spin-spin fluctuations of the ferromagnetic clusters and reported an
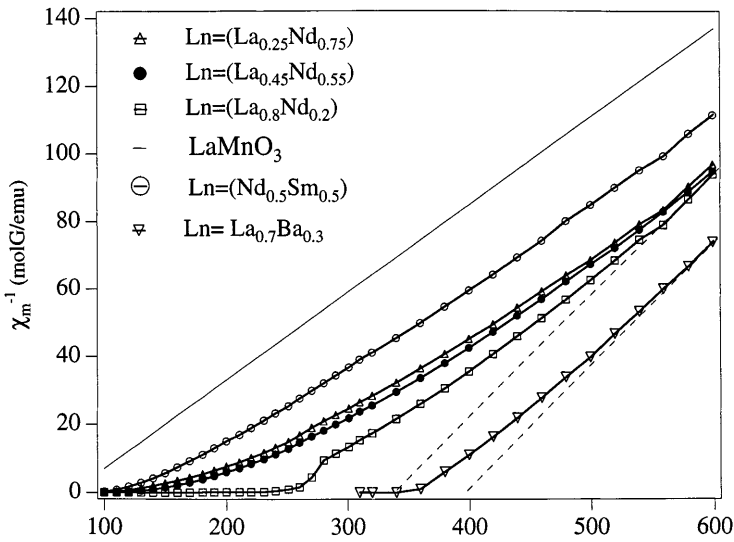
Fig. 27. Inverse paramagnetic susceptibility vs temperature for several samples $Ln_{0.7}Ca_{0.3}MnO_3$ compared with $LaMnO_3$ and $La_{0.7}Ba_{0.3}MnO_3$; after [114a]

anomalous temperature and field dependence of the spin-lattice relaxation. Lu et al. [126] and Fäth et al. [127] have used tunneling scanning spectroscopy on, respectively, x = 0.35 and x = 0.30 of $La_{1-x}Ca_xMnO_3$ films deposited epitaxially on a single-crystal $SrTiO_3$ substrate to observe directly the coexistence of the FM phase and a polaronic phase both above and below T_C and how the spatial extent of the FM phase increases to beyond a percolation threshold on decreasing the temperature through T_C or on applying a magnetic field above T_C. The CMR phenomenon occurs where the conductive FM phase reaches a percolation threshold in the paramagnetic phase. De Teresa et al. [128] demonstrated this phenomenon with neutron scattering.

Whereas we have proposed a phase segregation associated with a cross-over from the $\tau_h > \omega_O^{-1}$ in a polaronic phase to a $\tau_h < \omega_O^{-1}$ in a ferromagnetic phase [114, 129], Nagaev [130] and Emin [131] have argued that the CMR phenomenon reflects growth in a magnetic field of the volume of a conventional magnetic polaron. Dagotto et al. [132, 133], on the other hand, have provided a more detailed theory than our virial-theorem argument for a two-phase model resulting from the cross-over from localized to itinerant electronic behavior. In the same spirit, Alexandrov and Bratovsky [134, 135] rebutted the Nagaev model and emphasized the role of electron-lattice interactions in the collapse of the itinerant carriers to bound pairs (Zener polarons) in the paramagnetic phase to account for the transition from a ferromagnetic metal to a paramagnetic insulator. What is apparent is the critical role played by the locally cooperative oxygen-vibration period ω_O^{-1} relative to the tunneling time $\tau_h \sim \hbar/W$ and of two distinguishable phases coexisting over an extended temperature range on either side of T_C.

Third, the maximum in $\alpha(T)$ at a T_{max} a little above T_C increases dramatically as the tolerance factor t is lowered to the O'—O^* phase boundary appearing in the interval $0.952 < t < 0.957$. Comparison of Fig. 25 and Fig. 28 shows a pressure dependence $dt/dP > 0$, which is anomalous according to Eq. (1) of Goodenough, this volume, and indicates an unusually large compressibility of the $\langle Mn$—$O \rangle$ bond. From the virial theorem, we can understand such a large compressibility as an indication of a double-well $\langle Mn$—$O \rangle$ potential at a cross-over from localized to itinerant electronic behavior. The large compressibility of the $\langle Mn$—$O \rangle$ bond length in the two-phase domain has been corroborated by several experiments.

Radaelli et al. [136] have used high-resolution neutron diffraction to show for $La_{0.75}Ca_{0.25}MnO_3$ an anomalous decrease in the volume on cooling through T_C as the fraction of the ferromagnetic volume increased. The decrease in mean cell volume occurred despite an increase in the $(180° - \phi)$ Mn—O—Mn bond angle because a significant decrease in the $\langle Mn$—$O \rangle$ bond length overcompensated the increase in bond angle. De Teresa et al. [137] measured the magnetoresistance (MR) and the magnetothermal expansion (MS) for $La_{2/3}Ca_{1/3}MnO_3$ and found a strong correlation between the two in the paramagnetic phase just above T_C. They concluded that the localized charges
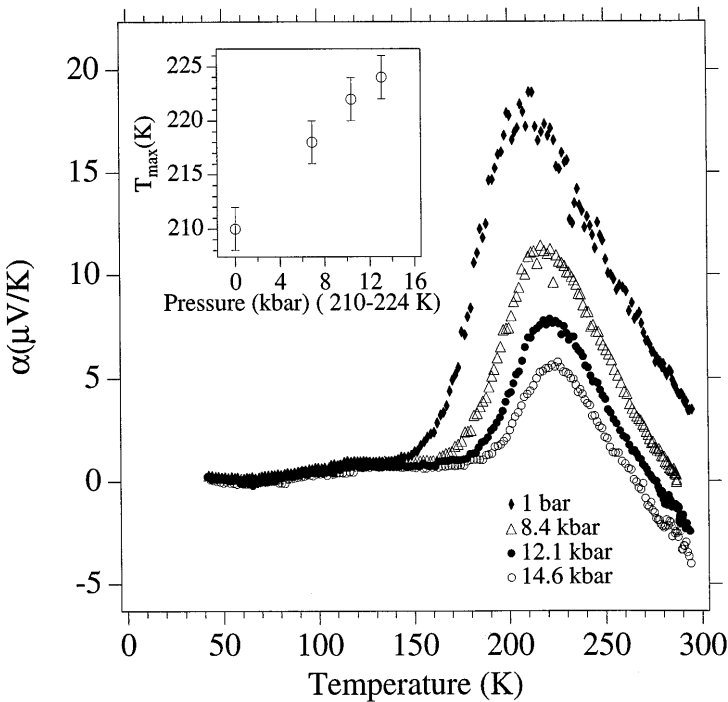
Fig. 28. Pressure dependence of $\alpha(T)$ for $(La_{0.6}Nd_{0.4})_{0.7}Ca_{0.3}MnO_3$ with $t = 0.960 > t_c$; after [114]

in a polaronic phase above T_C are released from the polaronic self-trapping by applying a magnetic field, resulting not only in a large MR, but also in a large volume contraction.

Neumeier et al. [138] and Laukhin et al. [139] have reported an anomalously large increase in T_C with pressure that increases as T_C decreases; the effect disappears in the O′ phase at T_N. Fontcuberta et al. [140] have also shown that isovalent substitutions in $(La_{1-x}Ln_x)_{2/3}(Ca_{1-y}Sr_y)_{1/3}MnO_3$ yield a pressure dependence that increases with the extent of local disorder at the A-site cations, but that the variations with the ionic radii of the A-site cations are not enough to account for the large dT_C/dP observed. De Teresa et al. [141] have provided a comprehensive investigation of $La_{2/3}Ca_{1/3}MnO_3$ that links the large pressure dependence of T_C directly to the coexistence of two distinguishable phases, a ferromagnetic phase of smaller volume and a polaronic phase of larger volume.

Fourth, Jaime and Salamon [142] have pointed out that $\alpha(T)$ increases more sharply than exponentially on cooling to T_{max} and that the additional entropy transported increases on crossing the O′—O* phase boundary. Trapping of the Zener polarons appears to transform the mobile polarons remaining in the Mn(IV)-poor matrix into small polarons as the concentration of mobile holes in this phase decreases. Such a transformation would double the number of sites available to a polaron and would therefore increase the α of Eq. (11) by reducing $c = (1 − r)2x$ toward $c = (1 − r)x$, where r is the ratio of trapped to free polarons. In the O′ phase, most of the polarons appear to be small polarons at T_N.

Fifth, Fig. 29 shows the temperature dependence of the resistivity $\rho(T)$ as a function of pressure for the x = 0.75 sample, which is just on the O′ side of the O′—O* phase boundary at atmospheric pressure, and Fig. 30 shows a change in $\alpha(T)$ with pressure for the same sample [143]. A resistivity maximum occurs at T_C where a long-range Weiss molecular field increases the volume of the ferromagnetic phase to beyond percolation. The drop in $\rho(T)$ on cooling through T_C is continuous even though the thermal hysteresis in $\rho(T)$ shows that the magnetic transition is first-order.

It has been commonly assumed that the metallic temperature dependence below T_C signals itinerant-electron behavior However, Fig. 29 shows that $\rho(T)$ remains above the itinerant-electron limit near the O′—O* phase boundary, and the drop in $\alpha(T)$ to a small temperature-independent value, as shown in Fig. 30, is not characteristic of a conventional metal. Since Eq. (11) is not applicable at low temperatures, we turn to Eq. (5), the fundamental expression for the electronic contribution to the thermoelectric power. It follows from Eq. (5) that a temperature-independent $\alpha \approx 0$ µV/K below T_C implies $\sigma(\varepsilon − \varepsilon_F) \approx \sigma(\varepsilon_F − \varepsilon)$, which means that there is little dispersion in the e-electron energies $\varepsilon(\mathbf{k})$. Figure 31 reveals retention in low applied magnetic field of a magnetic heterogeneity below T_C. Moreover, the specific-heat data of Fig. 32 [144] show that the Λ-point anomaly at T_C vanishes on the approach to the O′—O* phase boundary (x = 0.55 sample), which we interpret to indicate an exchange of spin entropy for configurational or lattice-vibration entropy. Moreover, a $dT_C/dP > 0$ and a first-order phase change at T_C indicate,
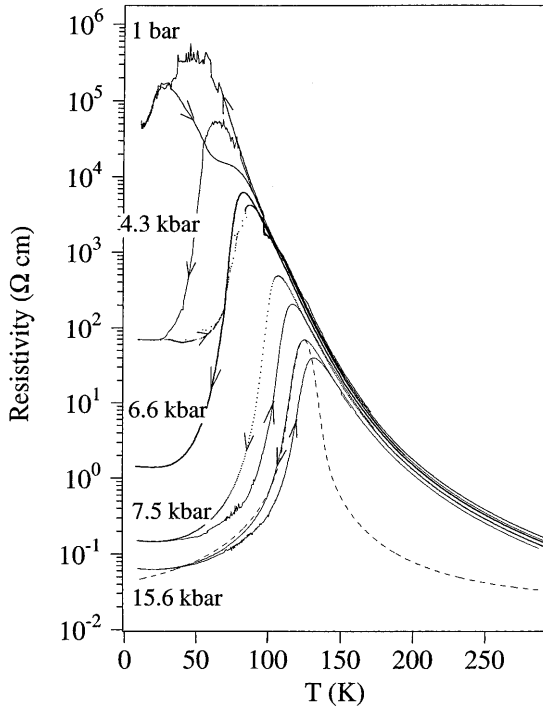
Fig. 29. Pressure dependence of $\rho(T)$ for $(La_{0.25}Nd_{0.75})_{0.7}Ca_{0.3}MnO_3$ with t = 0.952 < t_c; after [143]

according to the virial theorem of Goodenough, this volume, a discontinuous decrease in the mean electronic kinetic energy on cooling through T where a large volume of the majority-phase polaronic matrix changes to a conductive ferromagnetic phase. It would seem to follow that in the ferromagnetic phase, where $\tau_h \approx \omega_O^{-1}$, conductive electrons are strongly coupled to phonon modes as might occur with a travelling charge-density wave. Clarification of the character of the charge carriers in the ferromagnetic phase remains a challenge.

For further evidence of strong electron coupling to oxygen vibrations in a system that has two electronic phases, we turn to studies of $^{18}O/^{16}O$ isotope exchange. Isotope exchange does not change the Mn—O—Mn bond angle ($180° - \phi$), which should leave W_σ unchanged, but it does change $\omega_O \sim M_O^{-1/2}$, where M_O is the oxygen mass, and therefore W of Eq. (10) and $\tau_h \sim \hbar/W$.

Zhao et al. [145–147] were the first to show a dramatic decrease of T_C on the exchange of ^{18}O for ^{16}O. If on cooling through T_C the transition was from a global polaronic phase with $\tau_h > \omega_O^{-1}$ to a global itinerant-electron phase with $\tau_h \sim \hbar/W < \omega_O^{-1}$, then the exchange of ^{18}O for ^{16}O, which decreases $\omega_O \sim M_O^{-1/2}$, should favor the itinerant-electron phase with $\tau_h < \omega_O^{-1}$ and therefore raise T_C. The fact that $^{18}O/^{16}O$ exchange decreases T_C is, therefore, evidence that T_C depends on a bandwidth W described by Eq. (10) resulting
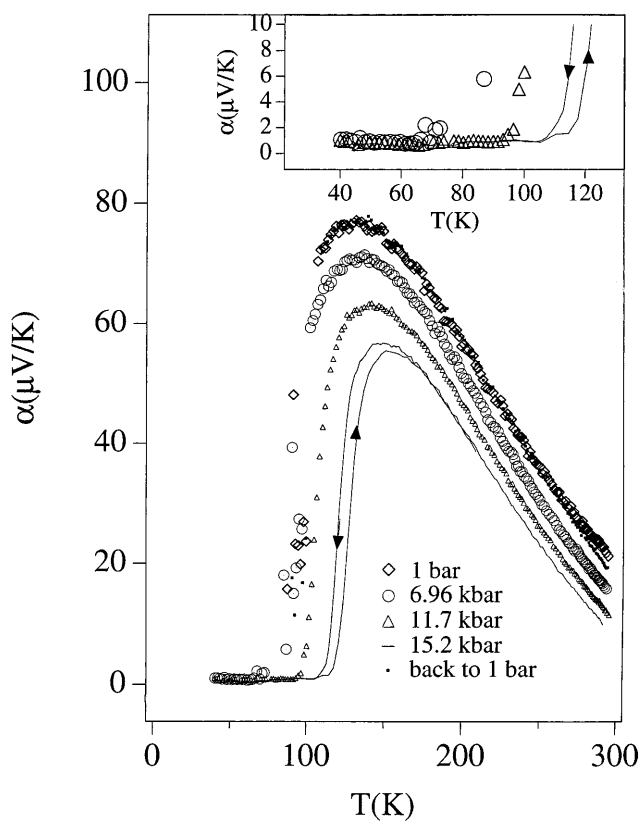
Fig. 30. Pressure dependence of $\alpha(T)$ for $(La_{0.25}Nd_{0.75})_{0.7}Ca_{0.3}MnO_3$ with t = 0.952 < t_c; after [148]
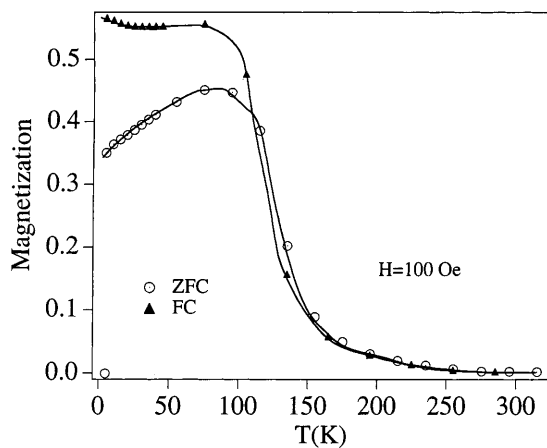
Fig. 31. Low-field magnetization vs temperature for $(La_{0.45}Nd_{0.55})_{0.7}Ca_{0.3}MnO_3$ with t > t_c; after [114a]
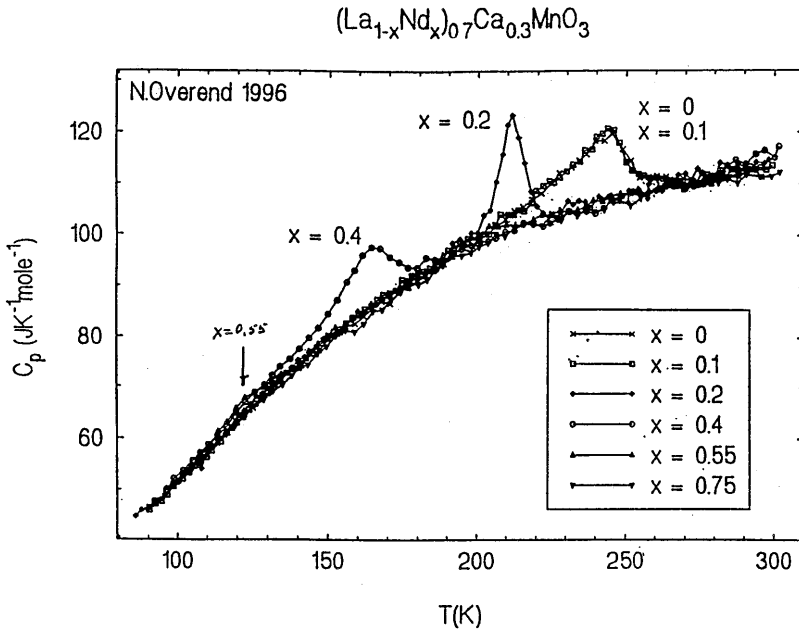
Fig. 32. Specific heat vs temperature for several samples with t > t_c for $(La_{1-x}Nd_x)_{0.7}Ca_{0.3}$ MnO_3; after [144]

from the two-phase character of the electronic system; a decrease in W with increasing M_O favors the polaronic phase and lowers T_C if the transition is governed by the bandwidth W rather than by W_σ.

If the dramatic change in T_C with tolerance factor t in Fig. 24 is due to a change in $\omega_O(\phi)$, as is suggested by a T_C determined by a critical value of the bandwidth W described by Eq. (10), then the critical ambient tolerance factor t_c for the $O'—O^*$ transition should increase and T_C decrease accordingly on the exchange of ^{18}O for ^{16}O. In order to probe this deduction, we [148] undertook additional isotope-exchange experiments.

Figure 33 compares the $\alpha(T)$ curves at atmospheric pressure for the ^{18}O and ^{16}O $(La_{0.25}Nd_{0.75})_{0.7}Ca_{0.3}MnO_3$ sample of Figs. 29 and 30. Comparison of these two curves with Fig. 26 shows that the change in $\alpha(T)$ on exchanging ^{18}O for ^{16}O is equivalent to reducing t. This experiment provides direct evidence that the sensitivity with respect to t of the magnetic and transport properties exhibited in Fig. 24 may depend more on the sensitivity to t of $\omega_O(\phi)$ than of W_σ. Chechersky et al. [149] have provided further confirmation of this conclusion. They followed with Mössbauer spectroscopy the temperature dependence through T_C of the two-phase character of an $La_{0.8}Ca_{0.2}MnO_3$ sample and found the strength of the exchange interactions at 78 K were not changed by $^{18}O/^{16}O$ exchange whereas a considerable softening of the anharmonic $Mn—^{18}O—Mn$ vibrations reduced the volume fraction of the ferromagnetic phase at a given temperature.
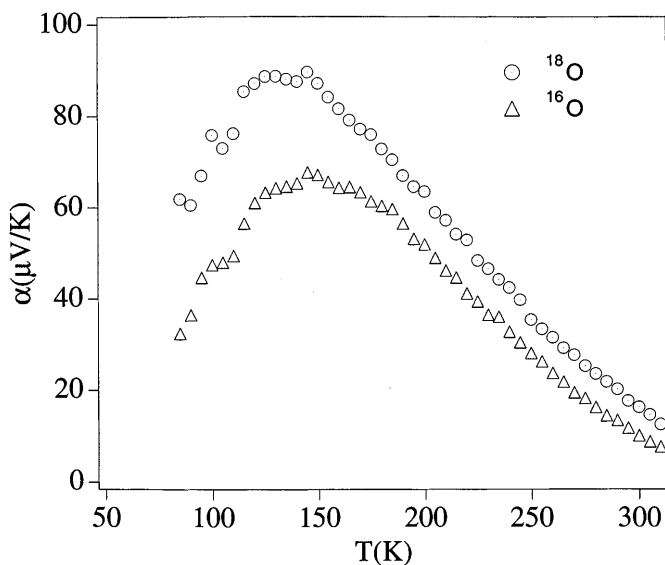
Fig. 33. Comparison of $\alpha(T)$ for ^{16}O vs ^{18}O at atmospheric pressure for $(La_{0.25}Nd_{0.75})_{0.7}Ca_{0.3}MnO_3$ of Figs. 29 and 30; after [148]

To obtain information on the variation of T_C with pressure for ^{18}O vs ^{16}O, we [148] used the fact that $\rho(T)$ for $(La_{0.25}Nd_{0.75})_{0.7}Ca_{0.3}MnO_3$ in Fig. 29 has its maximum value at T_C. Three additional features of Fig. 29 are noteworthy:

1. The $\rho(T)$ curves are relatively insensitive to pressure for $T > T_C$, but they change dramatically for $T < T_C$ on crossing the transition at P_c. The critical pressure P_c, which may represent the O'—O^* transition, is sharply defined.
2. There is no thermal hysteresis in the $\rho(T)$ curve at atmospheric pressure where $(La_{0.25}Nd_{0.75})_{0.7}Ca_{0.3}MnO_3$ is in the O' phase at T_C, but a pronounced thermal hysteresis appears at pressures $P > P_c$.
3. The thermal hysteresis, which marks a change from a second-order to a first-order transition at T_C on crossing the O'—O^* phase boundary, decreases as T_C increases with pressure $P > P_c$.

Figure 34a compares the evolution with pressure of T_C and the thermal hysteresis at T_C of the $(La_{0.25}Nd_{0.75})_{0.7}Ca_{0.3}MnO_3$ sample with ^{16}O and ^{18}O. A shift of $\Delta P_c \approx 9$ kbar on isotope exchange reflects the increase in effective t_c on the $^{18}O/^{16}O$ exchange, and a giant isotope coefficient $dlnT_C/dlnM_O \approx 4.9$ appears abruptly on conversion from the O' to the O^* phase; no measurable isotope shift was found in the antiferromagnetic O' phase containing small-polaron holes. Ordering of the occupied e-electron orbitals into the (001) planes in the O' phase is stabilized by a softer $\omega_O \sim M_O^{-1/2}$. The large isotope shift of T_C is thus seen to be associated with an instability of the static J-T orbital ordering on the approach to a transition from localized to itinerant electronic behavior where the $\langle Mn$—$O \rangle$ bond length has a double-well
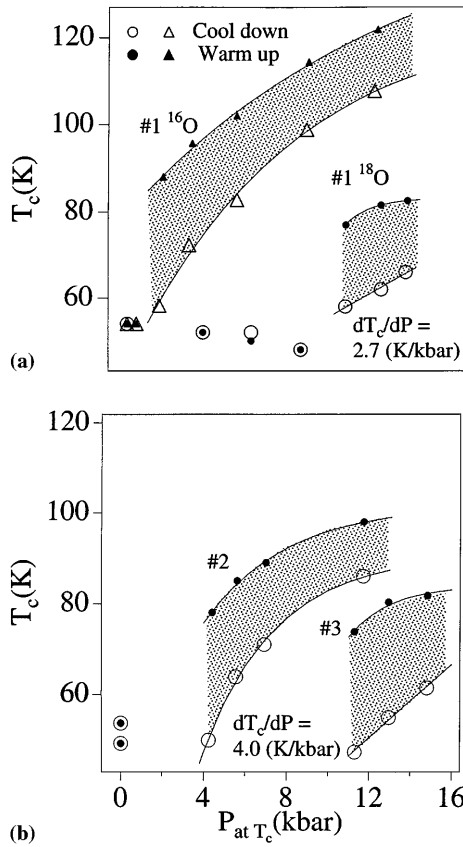
Fig. 34a,b. Variation of T_c with increasing and decreasing pressure for ^{16}O vs ^{18}O for: **a** $(La_{0.25}Nd_{0.75})_{0.7}Ca_{0.3}MnO_3$ (#1) of Figs. 29 and 30; **b** $(La_{0.2}Nd_{0.8})_{0.7}Ca_{0.3}MnO_3$ (#2) and $(La_{0.15}Nd_{0.85})_{0.7}Ca_{0.3}MnO_3$ (#3); after [148]a and b need to be inserted onto the actual figure, a for the top part and b for the bottom part

potential. It is at such a transition that we find the coexistence of two phases, one with shorter and the other with longer $\langle Mn$—$O \rangle$ bonds.

The magnitude of ΔT_C in the O^* phase on $^{18}O/^{16}O$ exchange increases with the magnitude of $dT_C/dt > 0$, which is a maximum just above t_c. Our isotope shifts of T_C in samples $t > t_c$ at ambient pressure were similar to those reported by Zhao et al. [145–147]. Franck et al. [150] have reported an analogous finding in $La_{1-x}Ca_xMnO_3$ for $0.2 < x < 4.3$. In the O' phase, T_N is determined only by superexchange interatomic interactions; the small-polaron hopping rate is too slow relative to a spin-relaxation time for a double-exchange coupling to be operative. However, the charge carriers are more mobile in the O^* phase and they contribute a double-exchange component to the ferromagnetic interactions that is larger the more mobile the holes. The $dT_C/dt > 0$ reflects an increase with tolerance factor t in the double-exchange contribution to the magnetic interactions in the less

conductive matrix and therefore in the number and/or range of fast hole transfers in this phase as the $(180° − \phi)$ Mn—O—Mn bond angle increases. The larger mass M_O of an ^{18}O softens $\omega_O \sim M_O^{-1/2}$, which lowers ω_O (ϕ) for a given value of ϕ. The large dT_C/dt thus reflects a critical dependence on ω_O (ϕ) of the number and range of the holes undergoing fast electron transfer in the matrix phase in the compositional range where a polaronic matrix contains a second, ferromagnetic phase with more delocalized holes. In addition, the activation energy of the matrix polarons above T_C is increased by a softer ω_O, so the matrix Zener polarons are more easily converted to small polarons. An increased polaron conversion on the exchange of ^{18}O for ^{16}O is made evident by the increase in $\alpha(T)$ above T_C in Fig. 33. Therefore, the number and range of holes undergoing fast transfer in the matrix phase appears to increase sensitively with a hardening of $\omega_O(\phi)$ at the cross-over from localized to itinerant electronic behavior.

In order to identify any dependence of M_O on the character of the charge carriers in the majority itinerant-electron phase below T_C, we minimized any pressure dependence by examining a ^{16}O sample of lower t having a P_c close to that of the ^{18}O $(La_{0.25}Nd_{0.75})_{0.7}Ca_{0.3}MnO_3$ sample. For this purpose, we measured the pressure dependence of $\rho(T)$ for two additional ^{16}O samples, #2 and #3 with $(La_{0.2}Nd_{0.8})$ and $(La_{0.15}Nd_{0.85})$ corresponding, respectively, to t = 0.951 and 0.949. Figure 34b shows that the ^{16}O sample #3 has nearly the same $P_c \approx 11$ kbar as the ^{18}O sample having a t = 0.952. It follows that the exchange of ^{18}O for ^{16}O is equivalent to a shift of tolerance factor $\Delta t \approx − 0.03$; hydrostatic pressure is equivalent to an increase of t by $dt/dP \approx + 2.7 \times 10^{-3}$ per kbar. From Fig. 34, we also observe at 11 kbar for ^{16}O $(La_{0.15}Nd_{0.85})_{0.7}Ca_{0.7}MnO_3$ and ^{18}O $(La_{0.25}Nd_{0.75})_{0.7}Ca_{0.3}MnO_3$, respectively, a thermal hysteresis $\Delta T_C = 27$ K and 19 K; on cooling, a $dT_C/dP \approx 4.0$ K/kbar and 2.7 K/kbar. For a first-order phase change, the thermal hysteresis ΔT_C should be proportional to the volume change ΔV at the transition, which in turn would be proportional to the change in the mean electronic potential $\Delta \langle V \rangle$. From the virial theorem, Eq. (20) of Goodenough, this volume, it follows that

$$\Delta T_C \sim \Delta \langle T \rangle |_{T_C} \tag{12}$$

is a measure of the change $\Delta \langle T \rangle$ of the mean kinetic energy of the charge carriers. At temperatures $T > T_C$, the charge carriers are polaronic and the ratio of small to Zener polarons at t_c can be expected to be equal or larger for the ^{18}O sample at P_c. Itinerant electrons below T_C would have a mean kinetic energy essentially independent of M_O, so a $\Delta T_C(^{18}O) \geq \Delta T_C(^{16}O)$ would follow from Eq. (12), which is just the opposite to what is observed. Therefore, we again conclude that in the O^* phase near the $O'—O^*$ phase boundary, the charge carriers below T_C are not conventional itinerant electrons, but are strongly coupled to the phonons in a "vibronic" state with a mean kinetic energy that is more sensitive to M_O than that of the free polarons at temperature $T > T_C$. This conclusion is compatible with the observation, Figs. 29 and 30, that the transport properties below T_C are not those of a conventional metal. We also note that a larger dT_C/dP of the ^{16}O vs ^{18}O sample

is consistent with the smaller trapping energy of the polarons in the paramagnetic phase of the ^{16}O sample evident in Fig. 33.

In summary, the extraordinary sensitivity to t, temperature, pressure, and magnetic field of the magnetic and transport properties of the O^* phase of the $(La_{1-x}Ln_x)_{0.7}Ca_{0.3}MnO_3$ perovskites can be attributed to strong electron-lattice coupling in a ferromagnetic polaronic phase exhibiting dynamic J-T distortions coexisting with a ferromagnetic more conductive phase with a higher T_C. The more conductive phase has a smaller $\langle Mn-O \rangle$ bond length and a $\tau_h < \omega_O^{-1}$ whereas the polaronic phase has a $\tau_h > \omega_O^{-1}$, where $\omega_O = \omega_O(\phi)$ softens with increasing bending angle ϕ. Application of an external magnetic field above T_C or an increase in the Weiss molecular field with decreasing temperature through T_C stabilizes the more conductive phase relative to the polaronic phase, and the CMR phenomenon reflects growth of the minority conductive phase to beyond its percolation threshold. Long-range ferromagnetic order on cooling across T_C stabilizes a discontinuous growth of the more conductive phase having a smaller volume, so the magnetic transition is first-order. The magnitude of T_C reflects the relative contributions of a stronger double-exchange and a weaker superexchange component of the ferromagnetic interatomic exchange interactions in the less conductive matrix; the double-exchange component increases with the bandwidth $W = W_\sigma \exp(-\lambda\varepsilon_a/\hbar\omega_O)$, where $W_\sigma \sim W_o \cos(\phi)$ is the tight-binding bandwidth, and therefore T_C increases sensitively with the hardening of $\omega_O(\phi)$ as ϕ decreases. The O' to O^* transition reflects a change from static to dynamic J-T distortions at a critical bandwidth $W = W_c$, and below T_N in the O' phase, any ferromagnetic phase remains below the percolation threshold.

2.4.2
$La_{1-x}Ca_xMnO_3$

A tentative phase diagram for the oxygen-stoichiometric system $La_{1-x}Ca_xMnO_3$ is shown in Fig. 35; the diagram is a refinement of one developed by Uehara et al. [151]. Studies of the properties of the system have been plagued by a lack of oxygen stoichiometry, particularly for compositions with smaller x where a disproportionation reaction $2Mn(III) = Mn(II) + Mn(IV)$ at temperatures $T > T_{JT}$ results in an oxidation of the Mn(II) with the appearance of cation vacancies. Dabrowski et al. [152, 153] have made a careful study of the conditions under which cation vacancies are formed and their influence on the physical properties of the $La_{1-x}Ca_xMnO_3$ system. This problem may account for the failure to observe any change with x in the Mn(IV)/Mn ratio in the range $0 < x < 0.3$ with either Mn K-edge X-ray absorption spectroscopy [154] or by high-resolution Mn K_β emission spectroscopy made on the same samples [155], which were reported to be R-rhombohedral for x < 0.2. Wold and Arnott [156] reported a transition in $LaMnO_3$ from the O'-orthorhombic to R-rhombohedral on oxidation of $LaMnO_3$.

The $O'-O^*$ transition at T_{JT} is first-order and, as shown in Fig. 35, decreases sharply from 750 K with increasing x in the range $0 \le x \le 0.21$. The O' phase $(c/a < \sqrt{2})$ has cooperative orbital ordering of the occupied e
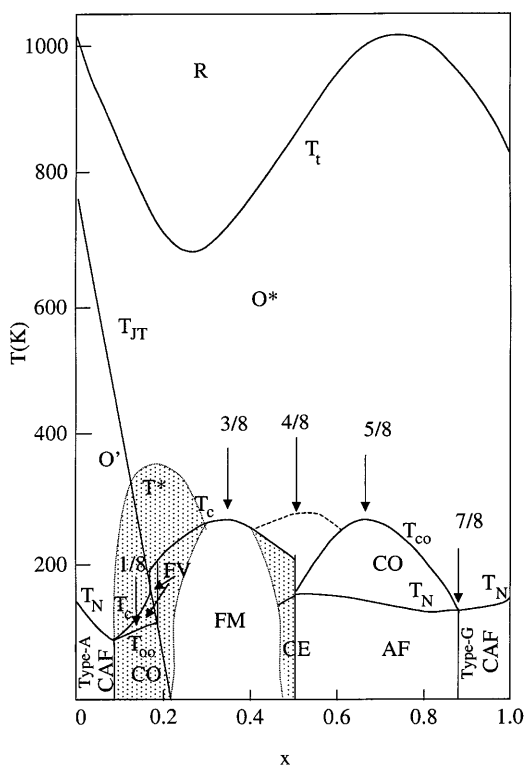
Fig. 35. Tentative phase diagram for the system $La_{1-x}Ca_xMnO_3$; adapted from [151]

orbitals at the Mn(III) into the (001) planes, but not necessarily the ordering within the (001) planes found in $LaMnO_3$; the O* phase $c/a \leq \sqrt{2}$ is pseudocubic, but the MnO_6 octahedra are rotated ca. 20° about the *b*-axis (space group Pbnm) relative to the ideal cubic-perovskite structure [157], and locally cooperative, dynamic J-T deformations sustain a $(c/a \leq \sqrt{2})$. High-resolution neutron powder diffraction [136, 158, 159], extended X-ray absorption fine structure (EXAFS) [160], and optical-conductivity spectra [161] have established the presence of dynamic distortions of the $MnO_{6/2}$ octahedra in the O* phase above T_C and a dramatic suppression of these distortions in the ferromagnetic, metallic (FM) phase below T_C.

Above T_C, the conductivity of the O* phase fits the adiabatic small-polaron model $\sigma = (A/T) \exp(-E_a/kT)$ over the entire doping range [162]. As already discussed, an electron tunnels from an Mn(III) to either an Mn(IV) ion or a Zener Mn(III)—O—Mn(IV) pair in a time $\tau_h > \omega_O^{-1}$, where ω_O^{-1} is the period of the locally cooperative oxygen displacements that, for x < 0.5, dress the mobile holes as Mn(IV) ions or as Mn(III)—O—Mn(IV) pairs. Fast electron transfer $(\tau_h < \omega_O^{-1})$ occurs within a Zener polaron.

On cooling through T_C in the range 0.10 < x < 0.30, there is a first-order volume contraction associated with a discontinuous increase in the volume

fraction of a more conductive ferromagnetic phase [136] where electrons tunnel between all nearest neighbors in a time $\tau_h \lesssim \omega_O^{-1}$. In contrast, the transition from the paramagnetic to the canted-spin Type-A antiferromagnetic order (CAF phase) in the range $0 \leq x \leq 0.08$ is second-order; the charge carriers of the CAF matrix remain small polarons, and there is no increase in the volume of more conductive, ferromagnetic clusters on cooling through T_N.

The initial substitution of Ca for La is charge-compensated by the introduction of Mn(IV) ions that, at lower temperatures, become trapped at one of the 8 nearest neighbors to a Ca^{2+} ion [162a]. Elastic and inelastic neutron scattering has indicated that, by $x = 0.05$, hole-rich ferromagnetic droplets form within the CAF matrix with a correlation length $\xi:\approx 8-10$ Å [163]. These droplets probably represent capture of two Mn(IV) at a Ca^{2+} ion. The Néel temperature T_N decreases with increasing x as the $LaMnO_3$ matrix is diluted with ferromagnetic clusters within which there is fast Mn(III)—O—Mn(IV) electron transfer, which gives a ferromagnetic double-exchange coupling according to Eq. (10) of Goodenough, this volume. The existence of ferromagnetic clusters within an antiferromagnetic matrix was found below T_N over the range $0.05 \leq x \leq 0.10$ with evidence that the phase segregation extends into the paramagnetic phase [164].

A segregation into two phases, one with a $\tau_h > \omega_O^{-1}$ and the other with a $\tau_h < \omega_O^{-1}$ is consistent with the virial theorem of Goodenough, this volume, which calls for a longer $\langle Mn—O \rangle$ bond length in the polaronic phase with $\tau_h > \omega_O^{-1}$ than in the hole-rich phase with $\tau_h < \omega_O^{-1}$. However, condensation of the holes into a hole-rich phase associated with Ca^{2+} ions must compete with coulomb repulsions that would order the Mn(IV) ions as far apart as possible. In the range $0.50 \leq x \leq 0.75$, orbital and charge ordering are found below a T_{co}. However, in the intermediate range $0.10 \leq x \leq 0.20$, the influence of the coulomb repulsions is more subtle.

In both the $La_{1-x}Ca_xMnO_3$ and $La_{1-x}Sr_xMnO_3$ systems, a CAF-FV transition from Type-A antiferromagnetic order with weak spin canting below a T_N to a strong spin canting below a T_C occurs within the O′ phase field. Moreover, a conductive to insulating transition occurs below a $T_{oo} < T_C$ in the O′ phase. A sound-velocity anomaly at T_{oo} and at T_C allows tracking of these temperatures vs x [165]. A neutron-diffraction study [166] for an $x = 1/8$ sample observed a c-axis modulation below T_{oo} that was interpreted to signal an ordering of the holes into alternate (001) planes and an ordering within these planes giving a maximum T_{oo} at $x = 1/8$. However, this interpretation fails to account for retention of a large ferromagnetic component of the magnetic order below T_{oo}. Within the O′ phase, the occupied e orbitals at Mn(III) ions are ordered into the (001) planes, but not necessarily long-range-ordered within the (001) planes. In the absence of a double-exchange interaction, this orbital ordering gives ferromagnetic e^1-O-e^0 superexchange interactions dominant within the (001) planes and antiferromagnetic t^3-O-t^3 superexchange interactions between planes to give Type-A antiferromagnetic order as in $LaMnO_3$. In order to get a large spin canting or ferromagnetism, it is necessary to introduce a c-axis ferromagnetic double-exchange interaction.

As the tolerance factor t increases with x, we have seen that the transition from small-polaron to itinerant-electron behavior in the manganese-oxide perovskites occurs via an intermediate step in which two-manganese Zener polarons are formed; ferromagnetic Zener double exchange occurs between the two Mn atoms of a Zener polaron. If the axes of the Zener polarons lie within the (001) planes, they will not change the Type-A antiferromagnetic order. However, if the axes are oriented along the c-axis, they introduces a ferromagnetic double-exchange component that increases with the concentration of Zener polarons having their axes parallel to the c-axis. Moreover, if the holes order into alternate (001) planes below T_{co}, but randomly and/or dynamically form Zener polarons with Mn(III) above and below the plane, the canted charge ordering would give a c-axis modulation and insulating behavior while introducing a necessary c-axis double exchange for strong spin canting. We therefore conclude that the FV phase contains Zener polarons with a c-axis Zener double exchange to give a large canted-spin ferromagnetism below T_{oo}. The local deformations fluctuate in the FV phase.

In the range $0.08 < x \leq 0.16$, a first-order contraction of the volume on cooling through T_C to the FV phase indicates a discontinuous increase in the number of Zener polarons and in the volume fraction of the more conductive ferromagnetic phase. A polaronic antiferromagnetic minority phase retained below T_C has a volume fraction that decreases with $T < T_C$. The order-disorder transition at T_{oo} is second-order. The charge-ordered (CO) phase is restricted to the O′ phase field since orbital ordering is critical for stabilization of this phase. A discontinuous increase in T_C occurs on crossing from the O′ to the O* phase; the change from the FV to the FM phase near $x = 0.16$ is well-defined, but it is smooth [167].

Another anomaly in the sound velocity was found [165] at a T^* a little below room temperature at $x = 0.10$; we suggest that this anomaly occurs where the ferromagnetic hole clusters condense into an FV phase of larger volume. Direct evidence for phase segregation above as well as below T_C has been observed by several techniques in addition to the Mössbauer spectroscopy [117, 118] and Mn K-edge EXAFS [119] already cited in connection with the $(La_{1-x}Ln_x)_{0.7}Ca_{0.3}MnO_3$ systems. Allodi et al. [168, 169], Papavassiliou et al. [170], and Dho et al. [171] have used ^{139}La and ^{55}Mn NMR to show the growth of the volume fraction of a ferromagnetic phase with increasing x.

A colossal magnetoresistance like that found in the $(La_{1-x}Ln_x)_{0.7}Ca_{0.3}MnO_3$ system is found in the speckled region $T_C < T < T^*$ where a ferromagnetic minority phase is present in the polaronic matrix of lower T_C. The compositional range of the CMR phenomenon and the sharp rise in T_C vs x are characteristic of the coexistence of a more conductive ferromagnetic phase and a polaronic phase. Where the volume fraction of the ferromagnetic phase increases significantly on cooling through T_C, the transition is first-order with a smaller polaronic volume below T_C. Comparison with the $(La_{1-x}Pr_x)_{0.7}Ca_{0.3}MnO_3$ system shows the two-phase region reflects changes in the tolerance factor more than the change in Mn(IV)/Mn ratio.

Another type of CMR phenomenon occurs where an antiferromagnetic-insulator CO phase competes with the conductive FM phase in the compo-

sitional range $0.4 < x \leq 0.5$. The Type-C antiferromagnetic CO phase was initially found [36] in $La_{0.5}Ca_{0.5}MnO_3$ and its complex magnetic order interpreted [37] in terms of the charge and orbital ordering illustrated in Fig. 36. The predicted charge and orbital ordering has since been fully corroborated [172]. Ahn and Millis [173] and Kuwahara et al. [174] have explored the interplay of charge and orbital ordering responsible for the CE phase. Subsequent studies have shown that the FM and CE phases form a two-phase mixture in the range $0.4 < x \leq 0.5$ [175]. The phase diagram shows a $T_{co} < T_C$ where the CE phase percolates through the sample below T_{co}; the FM phase is stable in the temperature range $T_{co} < T < T_C$. In $Nd_{0.5}Sr_{0.5}MnO_3$ also, the CE phase appears below a $T_{co} < T_C$ at the Mn(IV)/Mn = 0.5 composition [176]; application of a magnetic field stabilizes the conductive FM phase, suppressing the CE insulator phase, Fig. 37. A similar stabilization of the FM relative to the CE phase is found in $La_{0.5 + \delta}Ca_{0.5 - \delta}MnO_3$, $0 \leq \delta < 0.1$; the result is a CMR phenomenon again associated with the coexistence of an antiferromagnetic-insulator phase and the FM phase with a first-order transition on going from one phase to the other. A small increase in tolerance factor in $Pr_{0.5}Sr_{0.5}MnO_3$ leads to a Type-A antiferromagnetic order below a $T_N < T_C$ accompanied by a distortion to monoclinic ($P2_1/n$) symmetry with no evidence of charge ordering [177]. However, there is an ordering of the occupied e orbitals into the (001) planes. In monoclinic $Pr_{0.5}Sr_{0.5}MnO_3$ the orbital ordering stabilizes an $(x^2 - y^2)$ σ^* band, which results in a significant increase in the $(180° - \phi)$ Mn—O—Mn bond angles in the ferromagnetic planes relative to that between these planes. These structural distortions are quite different from those found for the Type-A antiferromagnetic phase in $LaMnO_3$ [178]. Here also, competition between the conductive FM phase and the AF phase leads to a CMR phenomenon with a phase diagram that varies with applied magnetic field [179]. Wang et al. [179a] have shown that, in addition to pressure and an applied magnetic field, even slight oxygen non-stoichiometry can dramatically change the low-temperature properties due to changes in the volume fraction of the FM phase coexisting with Type-A and/or
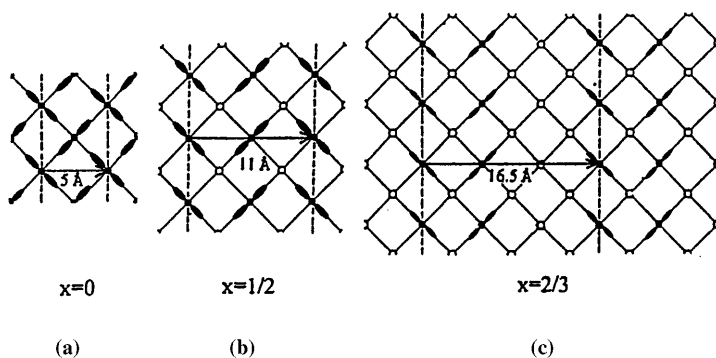
Fig. 36a–c. Charge and orbital ordering in the orthorhombic basal plane for; **a** $x = 0$; **b** $x = 1/2$; **c** as proposed by Mori et al. for $x = 2/3$ [194, 195]
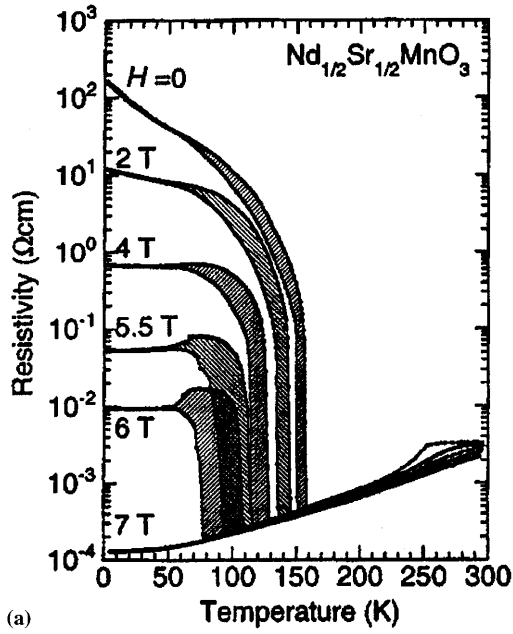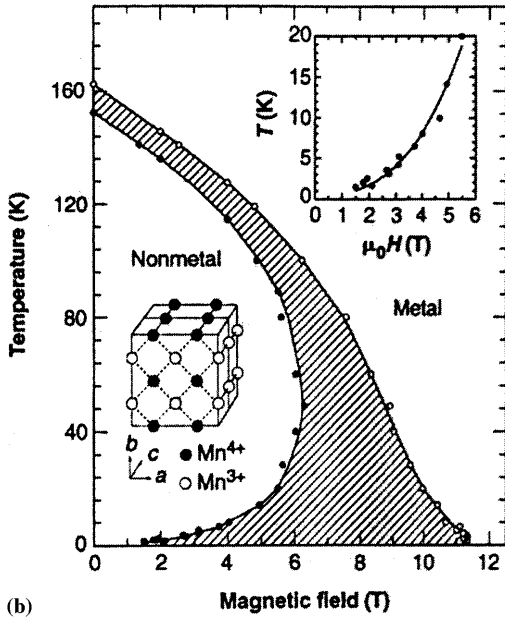
Fig. 37. **a** Temperature dependence of the resistivity $\rho(T)$ of $Nd_{0.5}Sr_{0.5}MnO_3$ under various magnetic fields. **b** Temperature-field phase diagram; after [176]

Type-CE antiferromagnetic phases. Yunoki et al. [180] have explored a half-doped two-orbital model with both cooperative and non-cooperative J-T coupling in the large electron-lattice-coupling ($\lambda \geq 1$) regime to show that the CE phase is stabilized for an intermediate-strength antiferromagnetic interaction J_{AF} and is further stabilized for larger λ whereas for smaller J_{AF}, a larger λ is required to stabilize the CE relative to the FM phase. The transition between the two phases was shown to be first-order, so the two phases may coexist. Moreover, for large λ and smaller J_{AF}, the Type-A antiferromagnetic phase becomes a third competitor in their analysis. Increasing the tolerance factor favors the FM phase relative to the antiferromagnetic phases [181]; the Type-A antiferromagnetic order with itinerant $(x^2 - y^2)$ σ^* electrons represents an intermediate phase between the FM and CE phases. The antiferromagnetic phase also occurs at a $T_{co} < T_C$ in $La_{0.52}Sr_{0.48}MnO_3$ [182].

Local probes of the evolution of the magnetic order with temperature in the neighborhood of x = 0.5 have revealed that the long-range-ordering transitions at T_C and T_N are not global. Papavassiliou et al. [183] investigated the spin ordering with [139]La NMR and found a paramagnetic-insulator (PI) phase coexisting with the FM phase well below T_C and the FM phase coexisting with the AFI phase well below T_N. A similar finding was obtained with [139]La and [55]Mn NMR by Allodi et al. [184]. Yoshimori et al. [185] used [139]La NMR to probe the FM microdomains and their stabilization relative to the CO phase by the application of a magnetic field. Roy et al. [186] had also shown that the relative volume fraction of the more conductive FM phase could be enlarged by either an external magnetic field or a reduction in the Mn(IV)/Mn ratio. An electron diffraction study by Chen and Cheong [187] had initially discovered domains of incommensurate charge ordering in the FM matrix in the range $T_{co} < T < T_C$ with a first-order change at T_{co} to long-range ordering of the commensurate CE phase below T_{co}. The existence of two phases was not due to any inhomogeneity in the Ca-ion distribution and did not appear to be due to a segregation into hole-rich and hole-poor domains. Dark-field images at 95 K showed CE domains a few thousand angstroms in diameter separated by twin boundaries parallel to an Mn—O—Mn bond axis. The charge-ordered phase was found [188] to have a large excess specific heat compared to the FM phase; this excess entropy can only originate from excitations of non-magnetic origin. Application of a magnetic field of 8.5 T, which transformed the resistivity to a metallic temperature dependence, left the specific heat unchanged with no evidence of a kT term from mobile charge carriers. We believe these data indicate that the charge carriers remain strongly coupled to the oxygen vibrations and therefore behave as vibrons. Further evidence of the strong electron coupling to the period ω_O^{-1} of the oxygen vibrational modes comes from ^{18}O/^{16}O isotope exchange, which increases T_{co} of $La_{0.5}Ca_{0.5}MnO_3$ by 9 K in zero magnetic field [189] and of $Nd_{0.5}Sr_{0.5}MnO_3$ by 21 K [190]. Raman spectra show an anomalous softening of the 494 cm^{-1} and 604 cm^{-1} modes below T_{co} [191].

In these segregations between the FM and antiferromagnetic CE or Type-A phases, the competitive phases appear to have similar Mn(IV)/Mn ratios; the phase segregations do not require a separation into hole-rich and hole-poor

domains. Therefore, although the CMR phenomenon is associated with the growth of a more conductive FM phase of smaller volume in a magnetic field, the conductive phase is not hole-rich in the neighborhood of x = 0.5. Uehara et al. [192] have recently emphasized this point in a study of the CMR phenomenon in $La_{5/8-y}Pr_yCa_{3/8}MnO_3$. Although T_C reaches its maximum value at x = 3/8 in $La_{1-x}Ca_xMnO_3$ and $La_{1-x}Sr_xMnO_3$, lowering the tolerance factor in $Pr_{1-x}Ca_xMnO_3$ completely suppresses the conductive FM phase even at x = 3/8; charge ordering at a $T_{co} \approx 230$ K is followed, on cooling, by anti-ferromagnetic order below a $T_N = 160$ K [193]. The relative stability of the FM phase clearly depends on a time for the Mn(III) to Mn(IV) electron transfer that is $\tau_h < \omega_O^{-1}$, where ω_O varies sensitively with ϕ. Uehara et al. [192] found that in the system $La_{5/8-y}Pr_yCa_{3/8}MnO_3$, T_C decreases smoothly with increasing y from 275 K at y = 0 to ca. 210 K at y = 0.25 where the mean A-cation radius reached a critical value $\langle R_A \rangle = 1.34$ Å below which charge-ordering sets in at a $T_{co} \approx 210$ K; at the transition, T_C dropped abruptly to 80 K, decreasing smoothly with a further increase in y to below 50 K where the volume fraction of the percolating FM phase vanished for y > 0.4. Moreover, the resistance of the FM phase increased by seven orders of magnitude in the range $0.25 \leq y \leq 0.4$, which is much greater than predicted if due only to changes in the percolation pathways, and the transition at T_C developed a large thermal hysteresis; in the range $0 \leq y < 0.2$, the magnetic-ordering transition at T_C was second-order. The magnetoresistance indicated the existence, in zero magnetic field, of a non-percolating FM phase coexisting with the CO matrix in the interval $T_C < T < T_{co}$. An electron-microscopy study provided direct evidence of the two phases with a typical size of the CO and FM regions on the order of several thousand angstroms, which was argued to be too large for a separation into hole-rich and hole-poor phases. Where segregation into hole-rich and hole-poor regions occurs, the two phases have been found to order into planes of small width to form a CDW. Where there is a competition between a CO and the FM phase, ordering into a CDW is not found. At the $O'—O^*$ boundary, there is a competition between the FV phase and a CO phase; stabilization of the FV phase in a magnetic field traps holes from the polaronic matrix, but growth of the FV phase may not require the acquisition of additional holes.

Finally, in the range 7/8 < x < 1.0 of the $La_{1-x}Ca_xMnO_3$ phase diagram of Fig. 35, the charge carriers are small-polaron Mn(III) ions above and below the second-order magnetic transition temperature T_N to a Type-G antiferromagnetic order. However, in the range 0.5 < x < 7/8, the nature of the charge ordering below T_{co} is not established. Mori et al. [194, 195] have observed in thin films planes of a $La_{0.5}Ca_{0.5}MnO_3$-type phase alternating with planes of the $CaMnO_3$-type phase, see Fig. 36c, in a series of x = n/(n+2) phases, where n is the number of Mn(IV) planes in the $CaMnO_3$-type slabs. However, Radaelli et al. [196] have found, with high-resolution synchrotron X-ray and neutron powder diffraction, no evidence for these stripes in a bulk $La_{1/3}Ca_{2/3}MnO_3$ sample; the Mn(III) ions appear to be separated as far apart as possible rather than ordered into $La_{0.5}Ca_{0.5}MnO_3$-type slabs.

2.4.3
$La_{1-x}Sr_xMnO_3$

Substitution of Pr for La in $(La_{1-y}Pr_y)_{1-x}Ca_xMnO_3$ reduces the tolerance factor t and suppresses the FM phase; substitution of Sr for Ca in $La_{1-x}(Ca_{1-y}Sr_y)_xMnO_3$ increases t and enlarges the stability range of the FM phase. Figure 38 is a tentative phase diagram for the system $La_{1-x}Sr_xMnO_3$. Construction of the phase diagram from data taken from several different sources [197–202] is complicated by two factors, sensitivity of the competing phases to the oxygen stoichiometry and the coexistence of two phases extending either side of the depicted first-order phase boundaries.

In the range $0 < x < 0.1$, the canted-spin Type-A antiferromagnetic component is oriented along the *b*-axis and the weak ferromagnetic component is along the *c*-axis; the Dzialoshinskii vector $\mathbf{D}_{ij}$ is along the *a*-axis in space group Pbnm. A ^{139}La study [203] has revealed the presence below T_N of a second phase in the x = 0.05 sample similar to what is found in the system $La_{1-x}Ca_xMnO_3$.
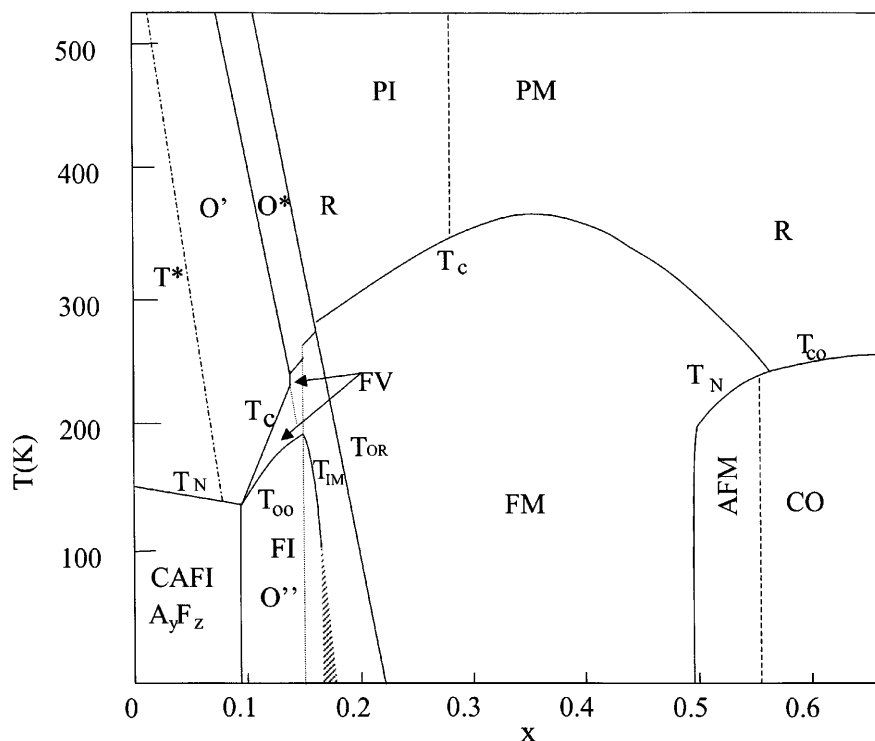
Fig. 38. Tentative phase diagram for the system $La_{1-x}Sr_xMnO_3$

The paramagnetic phase remains polaronic over the entire compositional range $0 < x \leq 0.3$, and locally cooperative J-T deformations persist into the R phase [204] even though rhombohedral symmetry is not compatible with a lifting of the e-orbital degeneracy. As in the $La_{1-x}Ca_xMnO_3$ system, we may anticipate a change from small polarons to Zener polarons with increasing x and decreasing temperature near $x = 0.1$. An optical absorption near 1.5 eV is characteristic of incoherent polaron behavior at temperatures $T > T_C$ in both the O^* and R phases; a strong incoherent-to-coherent cross-over occurs on cooling through T_C [205–209], but the conductivity remains low in the FV phase, becoming more characteristic of a strongly correlated metal in the FM phase [199]. In the compositional range $0.2 \leq x \leq 0.3$, the thermoelectric power $\alpha(T)$ changes sign from positive to negative [210], which we interpret to indicate that the charge carriers are two-manganese Zener polarons in the paramagnetic phase. Ferromagnetic alignment below T_C or by the application of a magnetic field shifts $\alpha(T)$ toward more positive values; a positive $\alpha(T)$ would be found for a narrow majority-spin σ^* band split by a correlation energy that restricts charge transfer to ferromagnetic e^1-O-e^0 interactions. Moritomo et al. [211] have argued that the characteristic optical transitions around 3 eV and 1 eV found below T_C for $x = 0.4$ are due, respectively, to interband and intraband transitions among electrons of e-orbital parentage; Shiba et al. [212] have argued that the orbital dependence of the transfer integrals makes the interband transitions allowed.

The magnetization M(T) in the FM phase near $x = 0.3$ decreases with increasing temperature in a manner consistent with spin-wave excitations [213], but the spin dynamics appear to be influenced near T_C by strong electron-lattice interactions [214]. The volume of an $x = 0.3$ sample showed a smooth contraction on cooling through T_C [215].

Several groups place the boundary between the FM and AFM phases beyond $x = 0.5$; this boundary varies sensitively with the method of sample preparation. We follow the report of Fujishiro et al. [216] and place it in the range $0.48 < x < 0.50$.

The application of a magnetic field stabilizes the FM phase, moving the O^*-R boundary to the left and suppressing the Type-A AFM phase at $x = 0.5$. Asamitsu et al. [217, 218] have measured a shift of the O^*-R transition temperature for $x = 0.17$ from 280 K to 220 K in an applied field of 7 T to produce a field-induced structural change from O^* to R symmetry in this temperature range. Campbell et al. [219] have confirmed the field-induced transition on a single-crystal $x = 0.165$ sample with neutron diffraction.

The FM phase is also stabilized by pressure. In an $x = 0.15$ sample, we [199] found a transition from vibronic to itinerant electronic behavior in the pressure range $5 < P < 6$ kbar and the temperature range $T_{co} < T < T_C$; it marks the FV-FM transition. A neutron-diffraction study [220] of an $x = 0.165$ sample showed that pressure stabilizes the R-rhombohedral phase relative to the O^* phase. We have also found that T_C jumps discontinuously by about 15−20 °C not only at the first-order O'—O^* transition, but also at the FV-FM and the O^*-R transitions [199, 220a]. In addition, the slope dT_C/dP drops discontinuously on crossing each transition.

Okuda et al. [221] have shown that the Debye temperature increases with x in the range $0.12 \leq x \leq 0.30$, saturating at a normal value for the perovskite structure above $x = 0.30$, which indicates that strong electron-lattice interactions persist in the FM phase out to $x = 0.30$. The electronic specific heat is only slightly enhanced as x decreases to $x = 0.17$, but it drops sharply to zero with decreasing x in the interval $0.15 < x < 0.17$ where there is a transition from itinerant to vibronic electronic behavior.

Of particular interest is the complex character of the phases that appear in the transitional compositional range $0.1 \leq x \leq 0.17$ of the phase diagram. Yamada et al. [222] identified a c-axis-modulated (O'') phase at $x = 1/8$; it is the same phase found in the $La_{1-x}Ca_xMnO_3$ system that we argued contained an ordering of Zener polarons with their axes parallel to the c-axis. Kawano et al. [223] showed that the magnetic order in the O'' phase is a canted-spin configuration with a Type-A antiferromagnetic component oriented along the b-axis and a large ferromagnetic component along the c-axis. The $x = 0.17$ sample was found to be ferromagnetic as was an $x = 0.185$ sample in which the FM easy axis was found to be tilted slightly from the c-axis [202]. According to the de Gennes [224] double-exchange model, the e electrons occupy itinerant states of a narrow σ^* band to give a c-axis ferromagnetic double-exchange interaction varying as $\cos(\theta/2)$, see Eq. (10) of Goodenough, this volume, whereas the antiferromagnetic t^3-O-t^3 superexchange interaction varies as $\cos\theta$, where θ is the angle between spins of adjacent (001) planes. Competition between these interactions can give a cant angle with a large ferromagnetic component that increases monotonically to full ferromagnetism ($\theta = 0$) as the strength of the double-exchange component increases. However, the transport properties below T_{oo} and the variation with x of the ratio T_C/D, where D is the spin-wave stiffness, rule out the de Gennes model in the O' phase. Khaliullin and Kilian [225] have developed a double-exchange model containing strong electron coupling to local J-T deformations to account for deviations of T_C/D from a universal constant; their model may be applicable to the FV phase, but it does not apply below T_{oo}. Nevertheless, it is apparent that, on cooling through T_C, a ferromagnetic e-orbital double-exchange interaction varying as $\cos(\theta/2)$ is introduced along the c-axis to compete with the antiferromagnetic t^3-O-t^3 c-axis superexchange interaction varying as $\cos\theta$. Moreover, the strength of this double-exchange interaction must increase as the temperature is lowered through T_{oo} even though the charge carriers appear to become trapped. We are therefore forced to consider a reorientation of two-manganese Zener polarons at T_{oo} so that the axes of the polarons are oriented along the c-axis. In the range $T_{oo} < T < T_C$, the local deformations at Mn(III) and the axes of the Zener polarons fluctuate to give isotropic ferromagnetic interactions. Pair formation can be accomplished within the context of in-plane orbital ordering at Mn(III) ions by an orthorhombic rather than a tetragonal deformation of the Mn(III)$O_{6/2}$ octahedra interacting with an Mn(IV) ion in a neighboring (001) plane. We [167] have noted that T_{oo} continues to increase with x until it reaches the O'—O^* phase boundary; it does not have a maximum value at $x = 1/8$ as predicted for ordering of Mn(IV) ions into and within alternate (001) planes. The principal driving force for the

transition appears to be an orbital ordering. Neutron-diffraction studies near x = 1/8 have found no long-range magnetic order above T_C; for x = 0.15, anisotropic damping of the larger-q spin waves increases dramatically with temperature [226]. The second-order transition at T_{oo} on cooling from the FV phase changes to a first-order transition at T_{IM} on cooling from the FM phase; T_{IM} decreases with increasing x until it terminates at an O'' + FM two-phase boundary. Under pressure, the Zener polarons are mobile below T_{IM}, but apparently retain their axes parallel to the c-axis [220a].

Uhlenbruck et al. [227] and Nojiri et al. [228] have shown that the CO phase is stabilized relative to the FV phase by an applied magnetic field and Senis et al. [229] have shown that it is stabilized by pressure as well as an applied field, which is consistent with a c-axis ordering of Zener polarons increasing the c-axis double-exchange component. Endoh et al. [230] used resonant X-ray scattering to demonstrate in an x = 0.12 sample that orbital ordering plays a critical role in the transition at T_{oo}. Darling et al. [231] have monitored the elastic moduli and Neumeier et al. [232] the thermal expansion of an x = 0.17 sample; a discontinuous change in the (Mn—O) bond lengths occurs at the first-order O^*-R transition at 285 K and a smooth transition at the second-order magnetic-ordering temperature T_C = 265 K, but no change in the $\langle$Mn—O$\rangle$ bond length occurs at T_{oo} = 252 K. Kiryukhin et al. [233] have demonstrated photoinduced disorder of the O'' phase in an x = 1/8 sample. The dielectric constant ε_1 and conductivity $\sigma_1 = \varepsilon_0 \varepsilon_2 \omega$ of all samples $0.1 \leq x \leq 0.175$ were found [234] to increase on cooling through T_C, and it was concluded that the charge carriers are polaronic in the paramagnetic phase and that they remain strongly coupled to the lattice on cooling through T_C even though the probability for electron transfer between neighboring sites is enhanced. Kawano et al. [198] used neutron scattering to identify a T_C = 150 K and a T_{oo} = 110 K in an x = 0.10 sample. On the other hand, Ghosh et al. [235] have observed that a magnetic field H increases T_{oo} and that the magnetization M increases at 108 K in three steps with increasing H in the range 1.6 < H < 4 T, which suggests that the magnetic field increases the cant angle in the O'' phase discontinuously. In all these studies, the phase boundaries are assumed to represent global transitions. However, we have argued in this paper that the CMR phenomenon is associated with a more conductive ferromagnetic phase within a matrix that is less conductive. In the $La_{1-x}Sr_xMnO_3$ system, the CMR phenomenon is found in the range $0.10 \leq x \leq 0.175$, but only above T_C for x = 0.175 [236]. The phenomenon extends below T_c in the range $0.10 \leq x \leq 0.15$ where the O'' phase is found below T_C; for the x = 0.10 sample, the maximum CMR does not occur at T_C, but at the 110 K anomaly. Thus the CMR phenomenon is clearly identified with the compositional range where competitive phases coexist and a more conductive, ferromagnetic phase is stabilized relative to the other phases by an applied magnetic field. Evidence for the coexistence of two phases between localized and itinerant electronic behavior has been reported for x = 0.15 with structural studies [237], for x = 1/8 with reflectivity spectra [238], and for x = 0.155 and 0.17 with thermal conductivity, which showed anoma-

lously strong phonon scattering near T_C due to spin fluctuations coupled to lattice instabilities [239].

2.5
The Ferrates

Preparation of stoichiometric $Ln_{1-x}A_xFeO_3$ perovskites of larger x requires high oxygen pressure and is more easily achieved with the more basic A cations La^{3+} and Sr^{2+}. Figure 39 is a tentative phase diagram for the system $La_{1-x}Sr_xFeO_3$. Like the system $La_{1-x}A_xMnO_3$, the t^3 configuration at every Fe atom remains localized with spin S = 3/2 and the e electrons undergo a transition from localized behavior in $LaFeO_3$ to itinerant in $SrFeO_3$.

Dann et al. [240] have provided structural data showing the system is O-orthorhombic (Pbnm) in the range $0 \leq x \leq 0.2$, R-rhombohedral (R$\bar{3}$c) in the range $0.4 \leq x \leq 0.7$, and cubic (Pm3m) in the range $0.8 \leq x \leq 1.0$. Although the volume per formula unit decreases linearly with x, the lattice parameters and individual Fe—O bond lengths change significantly on passing from the O to the R phase; it is the A—O bonds that change on passing from the R to the cubic phase. Their Mössbauer data showed a clear difference between the iron-atom valences below the antiferromagnetic Néel temperature in the R and cubic phases.

The high-spin Fe(IV)/Fe(III) couple forms an antibonding σ^* band at the top of the $O:2p^6$ valence band that contains a large $O-2p_\sigma$ component. Consequently the holes that are initially introduced into it by Sr^{2+} substitution
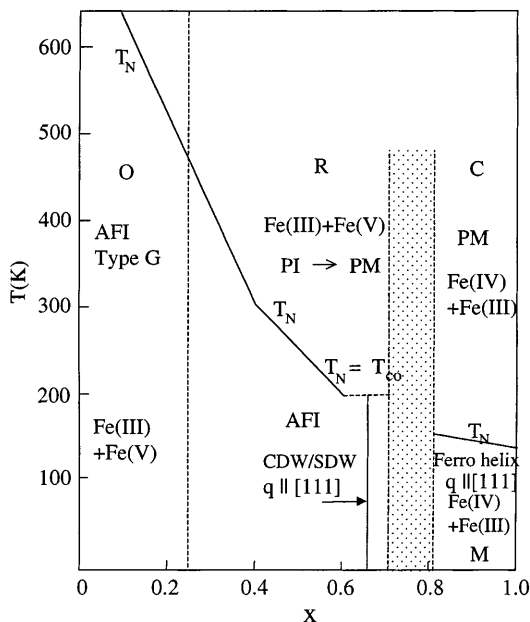
Fig. 39. Tentative phase diagram for the system $La_{1-x}Sr_xFeO_3$

for La^{3+} prefer to occupy molecular orbitals (MOs) rather than a localized e orbital; in fact, they tend to be trapped as pairs within an Fe(V)O$_6$ MO complex, which corresponds to a disproportionation reaction 2Fe(IV) = Fe(V) + Fe(III). Therefore, the orthorhombic phase is insulating and the Mössbauer spectra reveal the presence of Fe(V) as well as Fe(III) ions, but not Fe(IV). Trapping of the holes into Fe(V)O$_6$ complexes represents a clear phase segregation of delocalized, empty MO states of e-orbital parentage within a complex from the localized, high-spin Fe(III):t^{3}e^2 configurations of the matrix; trapping of two holes in MOs of an Fe(V)O$_6$ complex is strong enough to overcome the coulomb repulsion between them.

Whereas LaFeO$_3$ contains localized Fe(III):t^{3}e^2 configurations, SrFeO$_3$ contains Fe(IV):t$^3\sigma^{*1}$ configurations with itinerant σ^* electrons of e-orbital parentage. Consequently the initial electrons introduced into the σ^* band of SrFeO$_3$ by La^{3+} substitution for Sr^{2+} tend to be either itinerant or large polarons that repel one another by coulomb forces.

Therefore, the cubic phase is metallic below as well as above T$_N$, and the room-temperature Mössbauer spectra can be treated as an averaged charge state. At 4.2 K, in the AFM phase below T$_N$, Mössbauer parameters can distinguish Fe(III) from Fe(IV) ions, but the isomer shifts at the Fe(III) remain anomalously low [240]. The ferromagnetic-spiral spin configuration with q$\|$ [111] found [48, 49] below T$_N$ = 134 K in SrFeO$_3$ is probably retained throughout the cubic phase.

Of particular interest is a unique composition LaSr$_2$Fe$_3$O$_9$ (x = 2/3) within the R phase. Battle et al. [241] identified and Matsuno et al. [242] confirmed that, below a first-order transition at 198 K, the Fe(IV)O$_6$ complexes order into every third (111) plane to give rise to a CDW/SDW propagating along the [111] direction with a q$_{SDW}$ = 2q$_{CDW}$ in the formal-valence configuration $\cdots$353353 $\cdots$ with spin ordering $\cdots\uparrow\uparrow\uparrow\downarrow\downarrow\downarrow\cdots$, Fig. 40. This situation is analogous to the CDW/SDW found in LaNiO$_3$ except that the ferromagnetic slabs contain three (111) planes instead of two. The Fe(III)-O^{2-}-Fe(III) superexchange interaction between slabs is antiferromagnetic as in LaFeO$_3$; within a 353 slab the interactions are ferromagnetic Fe(III):e^2-O-Fe(V):e^0 superexchange interac-
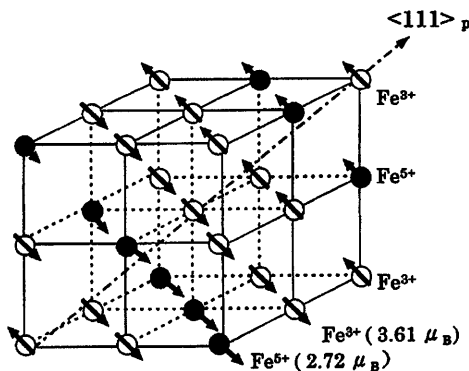
Fig. 40. Schematic structure of the CDW/SDW in LaSr$_2$Fe$_3$O$_9$

tions. The Fe(III) ions transfer a majority-spin electron to a same-spin e-orbital hole of the $Fe(V)O_6$ complex. The neutron-diffraction data of Matsuno et al. [242] have identified a moment of 0.07 μ_B on the oxygen atoms of a 353 slab and 0.00 μ_B on the oxygen between the slabs. Optical spectroscopy [243] has revealed the opening of an energy gap at $T_N = T_{co}$ that increases with decreasing temperature to $2\Delta \approx 0.13$ eV. Park et al. [244] have also shown that substitution of a smaller rare-earth in $LnSr_2Fe_3O_9$ lowers T_{co} to 165 K for Ln = Nd and suppresses the first-order character of the magnetic transition for Ln = Sm, lowering it to $T_N = 87$ K for Ln = Gd. The resistivity $\rho(T)$ exhibits a discontinuous change from a "bad metal" to a semiconductor on cooling through T_{co} for Ln = La, Pr, and Nd; the Ln = Sm and Gd samples remain semiconductive above T_N, which shows once again how sensitive the transport properties are to a decrease in the tolerance factor t near a transition from localized to itinerant electronic behavior. It is also significant that the first-order character of the transition at T_N is associated with a change from polaronic to itinerant carriers at T_N, but not with a polaronic to polaronic transition even though the optical gap 2Δ that opens up at T_N actually increases with decreasing width of the σ^* band as the tolerance factor decreases.

Mössbauer data reveal formation of $Fe(V)O_6$ clusters below T_N throughout the entire O and R phase fields [240]. We presume the spins of the $Fe(V)O_6$ complexes align parallel, not antiparallel, to their nearest-neighbor Fe(III) ions within a Type-G antiferromagnetic matrix so long as coulomb repulsions can keep the complexes isolated from one another, as could occur for x < 0.5. Higher concentrations of $Fe(V)O_6$ complexes can be expected to force the creation of planar clusters and complex magnetic order, complete ordering of the planar clusters into a CDW/SDW occurring at the x = 2/3 composition.

Sathe et al. [244a] have reported Type-G antiferromagnetic order at 10 K in a rhombohedral $La_{0.7}Sr_{0.3}FeO_3$ sample that was single-phase to neutron diffraction, which places the O-R transition in the range $0.2 \leq x \leq 0.3$. Their values of the mean iron moment are consistent with ferromagnetic coupling of the $Fe(V)O_6$ complexes to their six nearest neighbors. The T_N of $La_{1-x}Sr_xFeO_3$ varies continuously with x in the range $0.2 \leq x \leq 0.4$, which suggests the strength of the superexchange interaction does not change significantly across the O-R transition.

Chern et al. [245] have measured the complex dielectric constant for rhombohedral ceramic samples in the range 0.2 < x < 0.8. Above T_N, the activation energy of the mobility of the charge carriers decreases smoothly to zero with increasing x as x approaches 2/3. At lower values of x, a strong dipolar contribution to ε_1 at low frequencies can be interpreted by a Debye thermally activated process with an activation energy $E_a \approx 260$ meV similar to that of the charge-carrier mobility. As x increases, this dipolar contribution, which may be associated with $Fe(V)O_6$ complexes trapped at Sr^{2+} ions, becomes progressively replaced by another process characteristic of more loosely bound charge carriers within clusters, and the high-frequency conductivity within these clusters approaches that of the itinerant-electron conduction above T_N. Grenier et al. [246] have shown that T_N drops linearly

with increasing x throughout the O phase from above 700 K at x = 0 to about 500 K at x = 0.20, continuing to drop linearly through the O + R two-phase region.

2.6
The Cobaltates

Preparation of oxygen-stoichiometric, R-rhombohedral (R$\bar{3}$c) La$_{1-x}$Sr$_x$CoO$_3$ without high oxygen pressure is restricted to the compositional range $0 \leq x \leq 0.5$. The phase diagram of Fig. 41, which is adapted from [247], is complicated by changes with temperature of the spin states at the Co(III) ions. The antibonding σ^* band of low-spin LaCoO$_3$ lies ca. 1 eV above the top of the O:2p^6 valence band and contains a large O-2p$_\sigma$ component. However, only ca. 0.03 eV is required to excite a t electron of the low-spin (LS), diamagnetic Co(III):t$^6\sigma^{*0}$ configuration to a localized e orbital stabilized by a local J-T deformation of the octahedral site; the resulting intermediate-spin (IS) state
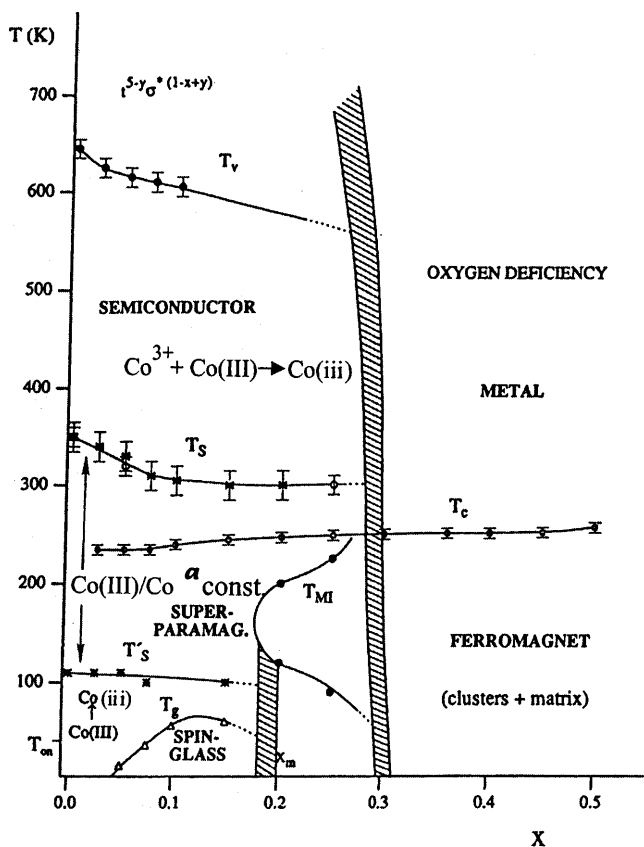
Fig. 41. Phase diagram of La$_{1-x}$Sr$_x$CoO$_3$ (0 = x = 0.50); adapted from [247]. Co(III) = low-spin; Co(iii) = intermediate-spin; Co^{3+} = high-spin

t^3e^1 has a spin S = 1. The IS state was first distinguished from the anticipated high-spin state t^4e^2 (S = 2) below 300 K in $LaCoO_3$ by NMR and Raman studies [56, 57, 248]. Louca et al. [249] have studied samples in the range $0 \leq x \leq 0.5$ with pair-density-function analysis of neutron-diffraction data; they observed that the IS cobalt population of $LaCoO_3$ increased from zero to 40% on raising the temperature to 100 K. However, local J-T deformations were increasingly suppressed in the range $100 < T < 200$ K, which we interpret to signal fast spin-configuration exchange associated with a further t-electron excitation that suppresses short-range order of LS, IS, and HS configurations; the excitations give a large thermal expansion of the lattice [62]. At higher temperatures, localized HS configurations appear to be stabilized by LS near-neighbor short-range fluctuations, and as the temperature is raised further, the HS ions transfer an e electron and t hole to neighboring LS sites to create itinerant σ^* electrons in a uniform intermediate-spin configuration $t^5\sigma^{*1}$ above 600 K.

Substitution of Sr^{2+} for La^{3+} introduces LS Co(IV) with empty MOs of e-orbital parentage at a $Co(IV)O_6$ complex. The strong Co(IV)-O covalent bonding of the complex stabilizes IS Co(III) at the nearest-neighbor cobalt, and ferromagnetic electron transfer from IS Co(III) to LS Co(IV) gives rise to superparamagnetic clusters below a magnetic-ordering temperature T_C of the cluster. Yamaguchi et al. [250] have estimated a cluster size of 5–8 Co atoms. For small x, these clusters are trapped at the Sr^{2+} ions that introduced the Co(IV) ions. The spin states of the Co(III) matrix change with temperature as in $LaCoO_3$: thermal excitation of IS states on alternate Co atoms below 100 K with a transition of the IS states to HS states in the range $100 < T \leq 300$ K, e-electron and t-hole transfer leading to a global intermediate-spin, metallic $t^5\sigma^{*1}$ paramagnetic state at high temperatures. The higher-spin states thermally excited in the Co(III) matrix are stabilized at higher temperatures by the spin entropy; the higher-spin states of a superparamagnetic cluster are stabilized by the strong covalent bonding in a $Co(IV)O_6$ LS complex.

In the range $0.05 \leq x \leq 0.15$, the superparamagnetic clusters interact through the Co(III) matrix to form a spin glass below T_g. For $x \geq 0.20$, the ferromagnetic clusters percolate through the matrix to give long-range ferromagnetic order below T_C, but metallic behavior at all temperatures is only established for $x > 0.3$. In the interval $0.2 \leq x \leq 0.30$, the paramagnetic phase is polaronic in the temperature range $T_C < T < T_v$, it becomes metallic below T_C where the Weiss molecular field stabilizes the conductive phase, increasing its volume fraction until it percolates through the Co(III) matrix. Below 100 K, stabilization of LS Co(III) in the matrix perturbs the periodic potential of the conductive phase to introduce variable-range hopping between clusters and a reentrant insulator phase. Itoh and Natori [251] have used ^{59}Co and ^{139}La NMR to confirm this evolution of properties with x; they place the critical concentration for percolation below T_C of the ferromagnetic phase at $x_c \approx 0.18$. Caciuffo et al. [252] found a phase with long-range ferromagnetic order in their samples for x = 0.10. The value of x_c appears to depend on sample preparation. In the range $0.3 \leq x \leq 0.5$, the volume fraction of the IS conductive phase grows with x to give a ferromagnetic matrix with localized t^5

and itinerant $\sigma^{*(1-y)}$ electrons coexisting on the same cobalt atoms [47]. However, the ferromagnetic matrix forms a "cluster glass"; within the ferromagnetic matrix, a volume fraction of all Co(III) ions, though shrinking as x increases, is still present at x = 0.5. Antiferromagnetic interactions through the Co(III) phase give rise to a cluster glass persisting to x = 0.5 [253–255].

Direct evidence of two electronic phases in what appears to X-ray diffraction to be a single crystallographic phase was also obtained with neutron diffraction, high-resolution microscopy, and magnetic susceptibility by Caciuffo et al. [252]. As in the manganese oxides, these authors showed that the volume fraction of the hole-rich, more conductive clusters grows in a magnetic field from below to beyond a percolation threshold to give rise to the large, negative magnetoresistance observed [256–258] in the range $0.15 \le x \le 0.25$. At x = 0.30, conductive ferromagnetic clusters are at the threshold for percolation above T_C, and on raising the temperature through T_C, the conductive volume transforms smoothly from a percolating to a cluster phase [259]. Ibarra et al. [260] have reported a huge anisotropic magnetostriction for x = 0.3 and 0.5, but little magnetostriction for x = 0.08. For x = 0.3 and 0.5, the magnetostriction is large and positive parallel to the applied field and negative perpendicular to the applied field. Optical microscopy [252] has shown that the two phases of different lattice parameter order into alternating slabs, and the huge anisotropic magnetostriction indicates that the slabs can orient themselves parallel to the direction of the applied field. Moreover, transmission electron microscopy on thin films of x = 0.5 deposited on a single-crystal $LaAlO_3$ substrate [261] as well as optical microscopy [252] have indicated an enrichment of the conductive slabs with Sr^{2+} and of the non-conductive slabs with La^{3+}. X-ray photoemission data show a high density of states at the Fermi energy ε_F of the x = 0.5 sample [262]. The density of states transferred to ε_F in the conductive, ferromagnetic phase increases with x; the density of states of ε_F does not decrease on lowering the temperature below T_C [263, 264], indicating that no antiferromagnetic or charge-ordered phase competes with the ferromagnetic phase.

2.7
$La_{2-x}Sr_xCuO_4$

The perovskite systems AMO_3 discussed in this paper all contain a first-row transition-metal atom M; they exhibit unusual physical properties at a first-order transition from localized to itinerant electronic behavior. A common feature of this transition is a dynamic phase segregation at lower temperatures into regions of itinerant electrons coexisting with regions of localized electrons that is made possible by locally cooperative displacements of the oxygen atoms. These displacements accommodate shorter equilibrium ⟨M—O⟩ bond lengths in the itinerant-electron regions and longer equilibrium ⟨M—O⟩ bond lengths in the localized-electron regions.

If the MO_3 array of the parent compound contains redox energies that are split by a finite energy gap, substitution of Sr^{2+} for La^{3+} introduces holes into

the lower redox band. Where there is a large O-2p component in the antibonding redox band into which the holes are introduced, the holes may occupy molecular orbitals or itinerant-electron states rather than localized 3d states at the M atoms. Where the Sr^{2+} concentration is small, the holes are confined to molecular orbitals of a cluster. The volume of a hole-rich cluster may be confined to a single $MO_{6/2}$ complex as in $La_{1-x}Sr_xFeO_3$ or include several M atoms as in the superparamagnetic clusters of $La_{1-x}Sr_xCoO_3$. The itinerant-electron clusters are hole rich and therefore positively charged. As the volume fraction of the hole-rich clusters increases, they may no longer repel one another by coulomb forces; greater elastic and magnetic-exchange energy may be gained than coulomb energy lost if the hole-rich and hole-poor regions organize themselves into alternating slabs of positive and negative charge. The most stable alternating-slab configuration would be periodic, which would correspond to a CDW of a given wavelength that may be commensurate or incommensurate with the crystal lattice. The commensurate CDWs tend to be pinned whereas the incommensurate CDWs may be mobile and therefore not readily detected by a diffraction experiment. Faster probes such as X-ray absorption fine structure (XAFS) or pair-density-function analysis of neutron data from a synchrotron source are needed to obtain the structural information of a travelling CDW.

In this final section, we show that these same considerations apply to the copper-oxide systems exhibiting high-temperature superconductivity. However, the copper-oxide superconductors all contain two-dimensional (2D) CuO_2 sheets in which the e-orbital degeneracy has been removed. The change from localized to itinerant electronic behavior occurs in atomically non-degenerate $x^2 - y^2$ orbitals that σ-bond to the bridging oxygen of the CuO_2 sheets; these oxygen atoms make $(180° - \phi)$ Cu—O—Cu bonds as in the (001) planes of a perovskite. In 2D sheets, the CDWs take the form of 1D stripes rather than 2D slabs. We restrict the discussion to the $La_{2-x}Sr_xCuO_4$ system since it spans the entire range of superconductive compositions from underdoped through optimally doped to overdoped. Moreover, the superconductive sheets of this system are in perovskite layers separated by rock-salt layers, and the oxidation state of the layers is unambiguously known once the chemical composition is determined.

The structure of the $La_{2-x}Sr_xCuO_4$ system is illustrated by the parent compound $La_2CuO_4 = LaO \bullet LaCuO_3$ illustrated in Fig. 42; perovskite layers alternate with rock-salt layers. The valence state of the copper is Cu(II), a J-T ion; the single hole in the d^9 configuration is ordered by the crystal symmetry into the σ-bonding $x^2 - y^2$ orbitals of the CuO_2 planes, which makes the apical Cu—O bonds longer than the Cu—O bonds in the CuO_2 planes. Nevertheless, the 2D tolerance factor remains $t_{2D} < 1$; and on lowering the temperature, the lattice adjusts to a $t_{2D} < 1$ by a cooperative rotation of the CuO_6 octahedra about a tetragonal [110] axis to give O-orthorhombic symmetry with $(180° - \phi)$ Cu—O—Cu bonds in the CuO_2 sheets. A $t_{2D} < 1$ also means that the Cu—O bonds in the CuO_2 sheets are under a compressive stress, and this compressive stress may be relieved by oxidation of the CuO_2 sheets. If prepared in air, La_2CuO_4 tends to accept interstitial oxygen within the
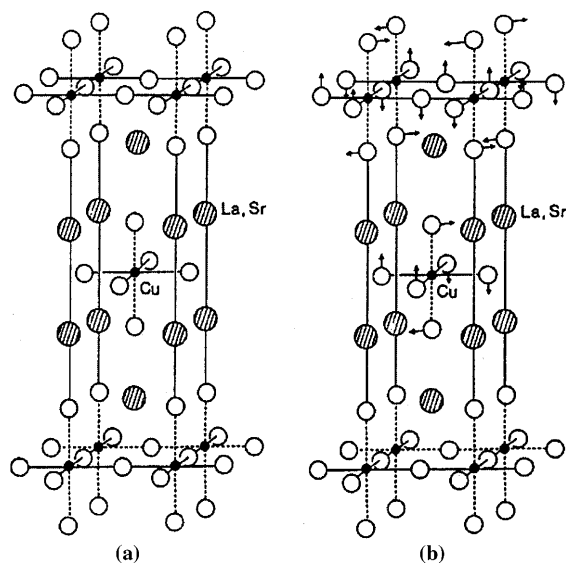
Fig. 42. The tetragonal intergrowth structure of high-temperature La_2CuO_4; *arrows* show cooperative rotations of CuO_6 octahedra in the orthorhombic phase ($T < T_t$)

tetrahedral sites of the rock-salt layers [265] to give $La_2CuO_{4+\delta}$. The transport and magnetic properties of this system have been reported and interpreted elsewhere [266]. We simply call attention here to the fact that the interstitial oxygen remain mobile down to 200 K, which allows for phase segregation between the parent compound ($\delta \approx 0$) on one side and a superconductive composition with $\delta \approx 0.05$ on the other. The phase segregation occurs below 300 K.

Figure 43 is a phase diagram for the system $La_{2-x}Sr_xCuO_4$. Substitution of a larger Sr^{2+} ion for La^{3+} is an alternate way to oxidize the CuO_2 sheets, and the larger size of the Sr^{2+} ion also increases t_{2D} to relieve the compressive stress on the CuO_2 sheets. As a result, the transition from O-orthorhombic to the high-temperature tetragonal (HTT) phase occurs at a temperature T_t that decreases sharply with increasing x, the tetragonal phase becoming stable to lowest temperatures for $x > 0.22$.

The parent compound La_2CuO_4 is an antiferromagnetic insulator with an energy gap $\Delta \approx 2$ eV between the empty $x^2 - y^2$ upper Hubbard band, which corresponds to the Cu(II)/Cu(I) redox energy, and the filled $x^2 - y^2$ band corresponding to the Cu(III)/Cu(II) redox energy. The highest occupied redox couple of the Cu(II) ion falls below the top of the $O:2p^6$ valence band in an ionic model, so the antibonding band becomes pinned at the top of the bonding valence band; it retains its $x^2 - y^2$ parentage, but with a strong $O-2p_\sigma$ component. The energy gap in the insulating parent compound is, in the language of the Zaanen, Sawatzky, Allen scheme, a charge-transfer gap rather than a Mott–Hubbard gap U, see Goodenough, this volume. The situation is
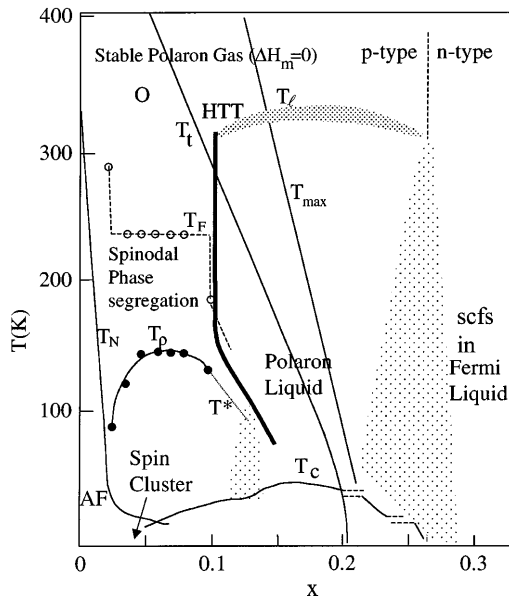
Fig. 43. Tentative phase diagram for the system $La_{2-x}Sr_xCuO_4$. scfs = strong-correlation fluctuations

analogous to the perovskites $LaFeO_3$ and $LaCoO_3$. Consequently, the initial holes introduced into the lower redox band by Sr^{2+} substitution occupy delocalized molecular orbitals (MOs) of a cluster. However, the cluster is not confined to a single copper atom, as proposed by Zhang and Rice [267], but to a non-adiabatic polaron containing about 5–6 copper atoms [268]. These multicenter polarons are analogous to the superparamagnetic clusters found in the perovskite system $La_{1-x}Sr_xCoO_3$; but in the absence of localized spins, these conductive clusters are not superparamagnetic. We deduce the size of the mobile clusters from measurements of the thermoelectric power $\alpha(T)$. In the underdoped compositions $0 \leq x \leq 0.1$, $\alpha(T)$ is temperature-independent and large above a temperature T_F, Fig. 44 [269]. This behavior is typical of polaronic conduction in which the statistical term, Eq. (11), dominates. In this case, the spin-degeneracy factor in Eq. (11) is $\beta = 2$. The temperature independence above T_F means that all the holes are mobile for $T > T_F$ and contribute independently to α. Therefore, it is possible to determine the fraction of available sites c that are occupied by charge carriers as was done to identify the presence of two-manganese Zener polarons in the manganese-oxide perovskites. The number of Cu centers in a polaron is given by N/N^*, where N is the number of Cu centers per unit volume and N^* is obtained from the measured $c = xN/N^*$. Figure 45 shows the measured $\alpha(300 \text{ K})$; the dotted line is a fit for $N/N^* = 5.3$. Why the polarons do not collapse to a small-polaron Zhang–Rice singlet is an open question. An LS Cu(III) may undergo a pseudo J-T deformation from square-coplanar to rhomboidal Cu—O bonding.
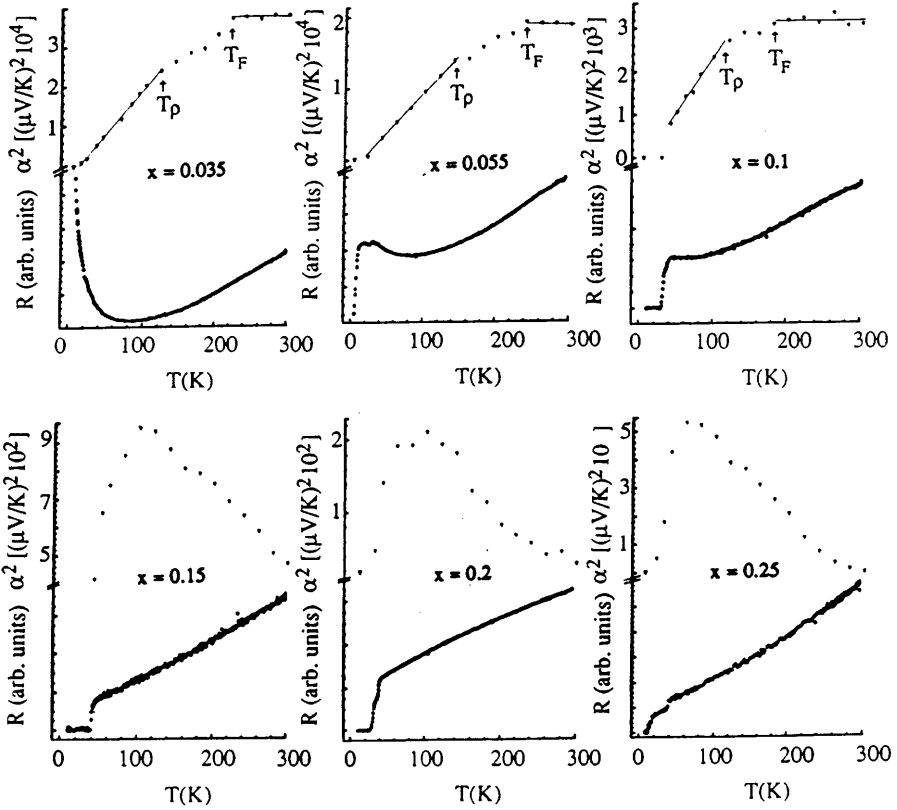
Fig. 44. Temperature dependence of resistance R(T) and the square of the thermoelectric power $[\alpha(T)]^2$ for several compositions x of $La_{2-x}Sr_xCuO_4$; after [269]

Therefore, one possibility is a gain in elastic energy associated with cooperative pseudo J-T distortions of several Cu centers from square to rhomboidal Cu—O bonding within the polarons. A model calculation [270] that included pseudo J-T deformations gave a stable polaron size of six to seven copper centers and an amoeba-like motion of the polaron that reduced the motional enthalpy ΔH_m to a small value. The calculation reproduced the normal-state resistance R(T) of Fig. 44: the up-turn in R(T) with decreasing temperature below T_ρ is caused by the small motional enthalpy of the multicenter polarons; a 61-T pulsed magnetic field suppressed superconductivity in an x = 0.16 sample to reveal an R(T) like that for x = 0.035 in Fig. 44 [271]. At higher temperatures, a $kT \gg \Delta H_m$ makes the polaron mobility approach a limit $\mu_p = eD_0/kT$, so the resistance has a linear temperature dependence that extends to high temperatures.

Within a cluster, a $\langle Cu-O \rangle_{itin}$ bond length is smaller than the $\langle Cu-O \rangle_{loc}$ bond length of the matrix within which it moves. Therefore, we refer to the
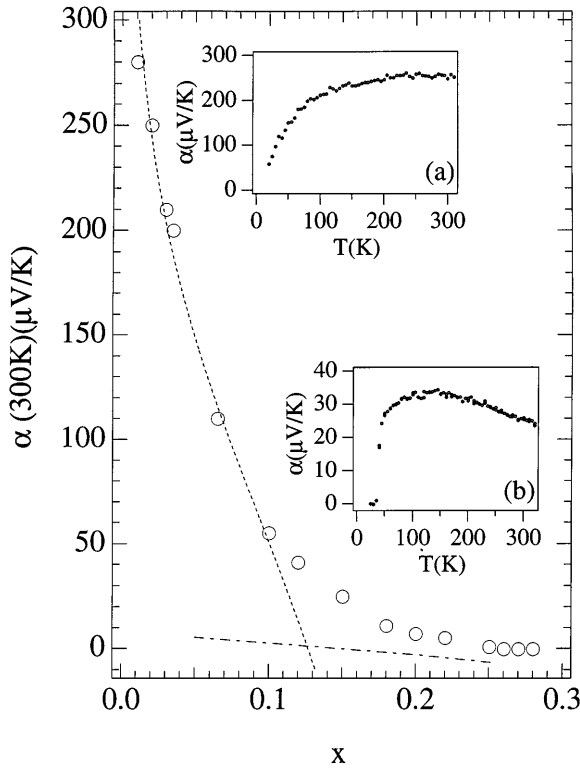
Fig. 45. Room-temperature thermoelectric power α(300 K) for $La_{2-x}Sr_xCuO_4$. *Dashed line* = fit to logarithmic plot with $N/N^* = 5.3$. *Dot and dash line* = result of band calculation. *Insets* (a) and (b) are $\alpha(T)$ for x = 0.02 and 0.15, respectively; after [268]

mobile clusters as "correlation bags" within which single or multiple holes are trapped in order to distinguish them from conventional dielectric small polarons or bipolarons. At small Sr^{2+} concentrations (x < 0.10) and temperatures $T > T_F$, the bags contain a single hole; but at larger values of x, the bags interact to form, below room temperature, two-hole bags or multihole itinerant-electron stripes along Cu—O—Cu rows. At values of x > 0.25, the inverse situation is found; holes are excluded from strong-correlation fluctuations of larger $\langle Cu—O\rangle_{loc}$ bond length in a Fermi-liquid matrix with a $\langle Cu—O\rangle_{itin}$ bond length. The high-temperature superconductive phase condenses with decreasing temperature from a polaron-liquid (vibronic) state in which, with increasing x, there is a transition from fluctuating two-hole bags in a localized-electron matrix to strong-correlation fluctuations in a Fermi-liquid matrix. Moreover, below T_F in the range 0 < x < 0.1, there is a spinodal phase segregation into the parent antiferromagnetic phase and the superconductive phase; the superconductive phase percolates for $x \geq 0.05$.

In the polaron-liquid state, there is a transition with increasing x from fluctuating two-hole bags in a localized-electron matrix to strong-correlation

fluctuations in a Fermi-liquid matrix. In the region of x = 1/8, ordering of the holes into itinerant-electron stripes in every fourth Cu—O—Cu row competes with the superconductive phase, which we would argue occurs at an $x \approx 1/6$ with holes ordered into alternate Cu—O—Cu rows.

Bozin et al. [271a] have used pair-distribution function analysis of pulsed neutron data to demonstrate the coexistence of two different equilibrium ⟨Cu—O⟩ bond lengths in the superconductive compositions, one corresponding to that of the parent antiferromagnetic phase with $\langle Cu—O \rangle_{loc}$ and the other to that of the overdoped phase with $\langle Cu—O \rangle_{itin}$. Hunt et al. [272] have demonstrated the presence of a phase consisting of alternating hole-rich and hole-poor stripes in the entire underdoped compositional range $1/16 \leq x \leq 1/8$ where superconductivity is observed. Formation of alternating stripes gains coulomb and magnetic-exchange energy without undue sacrifice of elastic energy, and superconductivity occurs in a thermodynamically distinguishable phase where the stripes order into a travelling charge-density wave (CDW) [269]. A low-temperature segregation in the oxidized samples $La_2CuO_{4+\delta}$ into an antiferromagnetic parent ($\delta \approx 0$) and a superconductive phase ($\delta \approx 0.05$) mirrors the underdoped samples $0 < x \leq 0.1$ of $La_{2-x}Sr_xCuO_4$ since each interstitial oxygen introduces two holes into the CuO_2 sheets.

The long-range antiferromagnetic ordering temperature T_N drops precipitously from near room temperature at x = 0 to zero at x = 0.02 [273]. This rapid drop reflects a dilution of the parent phase by the introduction of a second phase of relatively large volume fraction. The volume of the antiferromagnetic phase is decreased at lower temperatures $T < T_F$ by a spinodal phase segregation into the parent and superconductive phases. Formation of the superconductive phase breaks the parent phase into isolated spin clusters [274]. Cho et al. [275] have argued convincingly for the existence of quasistatic fluctuations of mesoscopic antiferromagnetic domains in the range $0.02 \leq x \leq 0.08$. Julien et al. [276] have studied an x = 0.06 sample with ^{63}Cu and ^{139}La NMR/NQR to show that, on cooling, the CuO_2 sheets progressively separate into two phases, one of them having enhanced antiferromagnetic correlations in clusters and the other giving rise to superconductivity below T_c = 8 K. Similar measurements in the lightly doped region $0 < x \leq 0.02$ have suggested the polarons form 1D stripes at quite low values of x; these hole-rich stripes separate and uncouple undoped antiferromagnetic domains of the parent phase [277]. For x = 0.02, these 1D stripes become progressively trapped below ca. 30 K. Kochelaev et al. [278] have identified with electron paramagnetic resonance (EPR) another type of polaron in $La_{2-x}Sr_xCuO_4$ with $0 < x \leq 0.02$; it consists of an O-2p_σ hole in a three-copper polaron that couples ferromagnetically the spins S = 1/2 at the three copper atoms to give a superparamagnetic S = 3/2 cluster. This observation highlights the strong O-2p_σ hybridization in the (x^2-y^2) σ^* band.

The paramagnetic susceptibility has its maximum value at a $T_{max} > T_N$, typical of a 2D antiferromagnet with short-range antiferromagnetic fluctuations. Torrance et al. [279] have reported the variation of T_{max} with x that is shown in Fig. 43. The localized spins within the normal state of the superconductive phase must contribute to T_{max} since compositions 0.14 ≤

$x \leq 0.22$ are bulk superconductors. As the width of the non-conductive stripes decreases with increasing x, T_{max} decreases.

Interpretation of T_F and T_ρ of Figs. 43 and 44 and the temperature T^* below which a pseudogap appears in the spectral weight at ε_F is more tentative. Loeser et al. [280] have shown with angle-resolved photoemission spectroscopy (ARPES) that the pseudogap below T^* is anisotropic with the same size and symmetry as the superconductive gap, which has led to speculation that it represents superconductive fluctuations. However, the decrease in T^* with increasing x and its suppression in a magnetic field [281] indicate that the pseudogap is related to a splitting of bonding and antibonding states in bipolarons that open up regions of the Fermi surface at $(\pm\pi, 0)$ and $(0, \pm\pi)$. As x increases, stabilization of bipolarons becomes weaker and T^* decreases. Onufrieva and Pfenty [282] have argued that the pseudogap opens up at a 2D quasiparticle topological transition having an electron-hole asymmetry with respect to the composition of the superconductive phase; they assumed the existence of a quantum critical point at this composition. On the underdoped side, we suggest the pseudogap is associated with two-hole bags of four copper centers having a gap between occupied bonding and empty antibonding states. On the overdoped side, where bipolarons cannot form, the pseudogap may reflect superconductive fluctuations. We believe that $T^* \approx T_\rho$ represent the same phenomenon on the underdoped side; T^* remains close to T_c on the overdoped side. Figure 44 shows that there is no anomaly in R(T) at T_F for our ceramic specimens whereas single-crystal studies have shown a decrease in the small c-axis conduction on cooling through $T^* \approx T_\rho$ where $\rho(T)$ departs from a linear relationship. Based on transport data for single-crystal $YBa_2Cu_4O_8$ and $YBa_2Cu_3O_{7-\delta}$ [283], we propose that the 2D phase segregation below T_F occurs independently in different CuO_2 sheets.

Figure 44 reveals an additional small anomaly; it can be seen in the R(T) curves at a temperature T_d that is independent of x and corresponds to the maximum T_c in the optimally doped samples. The fact that it is independent of x indicates that any changes at this temperature are driven by elastic rather than electronic energies. Nevertheless, T_d could represent a change in the electron-lattice coupling needed to give coherence to the superconductive pairs.

Figure 44 also shows that the character of the thermoelectric power $\alpha(T)$ changes dramatically between the underdoped composition x = 0.10 and the bulk superconductor x = 0.15. Figure 46 shows that $\alpha(T)$ for x = 0.15 is nearly temperature-independent above a critical temperature T_l. At low temperatures it exhibits an unusual enhancement with a maximum value near 140 K; a phonon-drag enhancement would have its maximum near 70 K. We have shown that this unusual enhancement is a characteristic and unique feature of all the superconductive copper oxides [284–286].

Since the superconductive phase contains itinerant charge carriers and a well-defined Fermi surface, interpretation of the enhancement of $\alpha(T)$ must begin with the general expression of Eq. (5). It follows from Eq. (5) that the enhancement implies an increasing asymmetry of the electronic dispersion curve on crossing ε_F and therefore an increased flattening of the dispersion
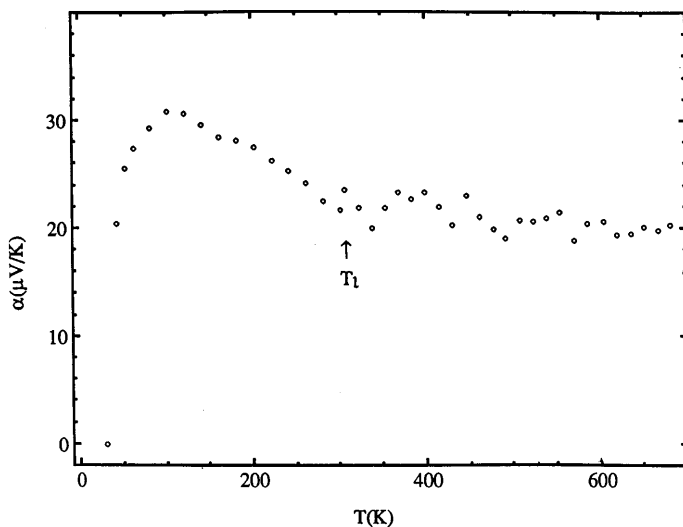
Fig. 46. Temperature dependence of the thermoelectric power $\alpha(T)$ for $La_{1.85}Sr_{0.15}CuO_4$ showing a transition at $T_l \approx 300$ K; after [269]

curve just above ε_F as the temperature is decreased. Direct evidence that this indeed is what is happening comes from angle-resolved photoemission spectroscopy (ARPES) [287–292]. These experiments show a dramatic transfer of spectral weight from the (π, π) to the $(\pm\pi, 0)$ and $(0, \pm\pi)$ directions in reciprocal space, which correspond to the Cu—O—Cu bond directions in the CuO_2 sheets.

In 1993, we pointed out that the superconductive phase is a distinguishable thermodynamic state that condenses from a polaron gas above T_l to a polaron liquid below T_l [269]. We did not specify at that time the nature of the polaron liquid, but it now appears to be a dynamic fluctuation of two-hole or multihole bags in the range $0.10 < x < 0.10 + \Delta x$ that progressively changes to purely vibronic states as the stabilization of bags decreases with increasing x. Although the spinodal phase segregation between the antiferromagnetic parent phase and the polaron-liquid phase below T_F may be largely driven by magnetic interactions, condensation of the polaron gas into a polaron liquid is relatively independent of magnetic-exchange interactions. The holes of the polaron-liquid phase progressively order with decreasing temperature into alternating hole-rich and hole-poor Cu—O—Cu stripes. With a maximum of one hole for every three Cu centers in the hole-rich stripes, the fully ordered phase would correspond to an $x_c = 1/6$ for the superconductive phase. As the holes become more ordered, there appears to be a transition from localized to itinerant vibronic states [293]. Vibronic states are hybridized electronic states and vibrational modes of the same symmetry. Hybridization of itinerant electronic states of wave vector **k** with an optical phonon of wave vector **q** propagating along a Cu—O—Cu bond axis of the CuO_2 sheets would have a

momentum vector $\mathbf{k}' \sim \mathbf{q}(\cos\theta + i\sin\theta)$, where θ is the angle between $\mathbf{k}$ and $\mathbf{q}$. The energies of these heavy electrons would be

$$E_{\mathbf{k}'} \sim \mathbf{k}'^2 \sim (\cos^2\theta - \sin^2\theta) + i\sin 2\theta \tag{13}$$

Formation of heavy-electron Cooper pairs would give a superconductive gap symmetry $d_{x^2-y^2} + id_{xy}$, a symmetry deduced by Deutscher et al. [293a] from tunneling experiments. Shen et al. [289] have pointed out that their ARPES data indicate a transfer of spectral weight by a momentum vector $|Q| \approx 0.45\pi$ directed along $(\pi, 0)$. Evidence for vibronic states is manifest in thermal-conductivity anomalies [294] and a dependence of T_c on the Cu—O—Cu bond angle, which we have seen influences the period ω_O^{-1} of locally cooperative oxygen vibrations in the perovskites. Figure 47 shows that T_c increases as pressure straightens the Cu—O—Cu bond angle of orthorhombic $La_{2-x}Sr_xCuO_4$ samples, but $dT_c/dP = 0$ in the tetragonal phase with $180°$ Cu—O—Cu bond angles [295].

Figure 43 shows a weak suppression of T_c near $x = 1/8$. Complete suppression of superconductivity at $x = 1/8$ in $La_{2-x}Ba_xCuO_4$ was first reported by Moodenbaugh et al. [296], and a similar suppression was found in the Nd-doped composition $La_{1.48}Nd_{0.4}Sr_{0.12}CuO_4$ [297]. These compositions undergo, on cooling, a transition to a low-temperature tetragonal (LTT) phase in which the CuO_6 octahedra tilt around [100] and [010] axes in alternate (001) CuO_2 sheets [298, 299]. This change of tilt direction pins bag stripes into a static, commensurate CDW, which has allowed the stripes to be studied by neutron diffraction [300, 301]. The structure may pass through an interme-diate phase [299] and also a temperature range where the O and LTT phases coexist. Incommensurate, mobile stripes have been found in superconductive samples [302–304]. We have used pressure to induce superconductivity in $La_{2-x}Ba_xCuO_4$ samples by depinning a static CDW [305]. Based on XAFS data, Bianconi et al. [306, 307] pioneered the idea of mobile stripes in the superconductive cuprates. Returning to the $La_{2-x}Sr_xCuO_4$ system, Suzuki et al.
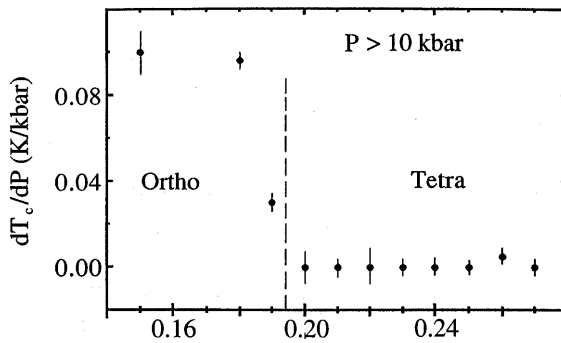
Fig. 47. Variation with x of the pressure dependence of T_c for P > 10 kbar in the system $La_{2-x}Sr_xCuO_4$; after [314]

[308, 309] have presented evidence for a lattice instability toward the LTT structure at x = 0.12; this instability pins partially an incommensurate CDW, thereby lowering T_c without suppressing it completely. Thus there is mounting evidence that the high-temperature superconductivity of the copper oxides is a mobile-stripe phase containing itinerant vibrons that is condensed from a vibronic state and that pinning of the stripes suppresses superconductivity. However, the metallic-stripe bags found for x = 1/8 every fourth Cu—O—Cu row may represent an order that is competitive with the superconductive phase which appears to occur at an x ≈ 1/6.

Further support for mobile stripes comes from the system $La_{1.6-x}Nd_{0.4}Sr_xCuO_4$, which is superconductive over the entire compositional range $0.07 \leq x \leq 0.25$. However, unlike $La_{2-x}Sr_xCuO_4$, the Nd-doped system undergoes a transition to the LTT phase below about 60 K over the entire solid-solution range. Singer et al. [310] have shown that ^{63}Cu NQR data can provide an order parameter for the formation of mobile stripes. Their systematic ^{63}Cu NQR study of the $La_{1.6-x}Nd_{0.4}Sr_xCuO_4$ system shows that mobile stripes exist in the normal state throughout the entire superconductive compositional range; the striped phase segregated at x ≈ 1/8 is the most sharply defined. These authors also point out that the charge ordering precedes spin ordering in the stripes and that despite evidence [311] for local LTT tilts in $La_{2-x}Sr_xCuO_4$, the LTT distortion tends to pin the stripes, but does not cause their formation. Substitution of additional Nd pins the stripes. Noda et al. [312] have used resistivity and Hall-effect data as a function of x on $La_{1.4-x}Nd_{0.6}Sr_xCuO_4$ single crystals containing static stripes every fourth Cu—O—Cu row to deduce a change from 1D charge transport for x < 1/8 to 2D transport for x > 1/8.

Inelastic neutron-scattering measurements [313] of the bulk superconductor $La_{1.85}Sr_{0.15}CuO_4$ have shown the development at low temperatures, but above the superconductive critical temperature T_c, of a discontinuity in the dispersion of the highest longitudinal optical-phonon branch that is indicative of dynamic, short-range cell doubling parallel to the Cu—O—Cu bond axes. A doubling of the periodicity along a Cu—O—Cu bond direction distinguishes this phenomenon from the stripe charge ordering at x = 1/8, which quadruples the periodicity. An unusual flatness of the phonon dispersion from (0.25, 0, 0) to (0.50, 0, 0) was also noted. The best fit to the data corresponded to a charge modulation of period 2a (a is the tetragonal lattice parameter) on the oxygen atoms, which would correspond to condensation of holes into alternate Cu—O—Cu rows as envisaged for a superconductive x ≈ 1/6 phase. Moreover, Egami et al. [313a] have identified the presence of 5 Cu-center clusters, which may also be 4 Cu-center clusters and 5 oxygen atoms, in the hole-rich Cu—O—Cu rows. These clusters appear to be the anticipated two-hole bags, so the experimental picture favors a superconductive phase at x ≈ 1/6 with one hole per three copper in alternate Cu—O—Cu rows. These mobile stripes are to be distinguished from the metallic stripes appearing every fourth row in the x = 1/8 compositions. The metallic stripes are stripe bags with one hole per two copper atoms, which corresponds to filled bonding and empty antibonding states in the stripes.

Thus far we have considered charge transport only in the *a-b* planes; that along the *c*-axis is also instructive. Figure 48 shows ρ(T) data of Ito et al. [314] on single crystals of $La_{2-x}Sr_xCuO_4$ taken for x = 0.08, 0.20, and 0.34. In the underdoped x = 0.08 sample, the *c*-axis resistivity is incoherent (activated) for all temperatures T > T_c. A transition from a metallic to a semiconductive temperature dependence of ρ_c(T) occurs near 150 K on cooling the bulk superconductor x = 0.20, and ρ(T) has a metallic temperature dependence to lowest temperatures in the overdoped, non-superconductive sample x = 0.34. These and similar measurements on other copper-oxide superconductors have shown that the *c*-axis electrical transport between CuO_2 planes is not described by conventional band theory. A subsequent, more systematic study of the *c*-axis optical spectra and charge dynamics of the $La_{2-x}Sr_xCuO_4$ system by Uchida et al. [315] has led to the conclusion that the superconductive compositions are found at a cross-over from the underdoped regime in which the *c*-axis transport is incoherent to the overdoped regime in which there is three-dimensional itinerant-electron (coherent) behavior. Charge transport in the bulk superconductors is not strictly three-dimensional above T_c; two-dimensional conductivity persists. Hussey et al. [316] have measured the
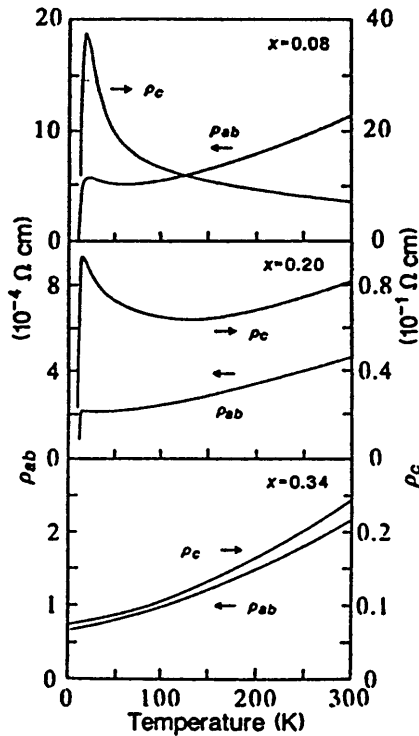
Fig. 48. Temperature dependence of ρ_{ab} and ρ_c for three compositions of $La_{2-x}Sr_xCuO_4$; after [314]

out-of-plane magnetoresistance of single-crystal La$_{2-x}$Sr$_x$CuO$_4$ (x = 0.09, 0.14, 0.15, 0.25) with the field applied parallel and perpendicular to the CuO$_2$ planes. They confirm that the c-axis transport above T$_c$ in the superconductive samples is an incoherent process involving multiple scattering events within an a-b plane before a hole hops to an adjacent layer.

What appear to be the common features of the optical spectra in all the copper-oxide superconductors are the following. Upon doping holes into the CuO$_2$ sheets of the parent compound, a transfer of spectral weight takes place in the out-of-plane spectrum from a 5–6-eV region to a region near 2 eV while the in-plane transferred spectral weight forms a Drude peak at $\omega = 0$ and a mid-infrared peak near 0.5 eV that softens on passing from the underdoped regime to the bulk superconductors. The c-axis peak near 2 eV does not soften with increasing x, so the low-energy c-axis spectral weight remains smaller than expected from band calculations and, into the superconductive region, is spread over a wide energy range rather than forming a Drude peak at $\omega = 0$; the c-axis conductivity forms a Drude peak at $\omega = 0$ only in the overdoped samples. However, a sharp Josephson c-axis tunneling appears below T$_c$ in the low-frequency region. The c-axis spectrum of La$_{2-x}$Sr$_x$CuO$_4$ is only weakly gapless for x = 0.16; it becomes strongly gapless for larger x with a Drude-like peak at $\omega = 0$ even at T $\ll$ T$_c$, which indicates the appearance at higher x of a non-superconductive overdoped phase coexisting with the superconductive phase. We [295] have shown that the transition to the overdoped phase does not give a smooth decrease with x in T$_c$; it occurs in steps characteristic of a two-phase segregation, see Fig. 43.

Holes in the O:2p bands would transfer along the c-axis. Therefore, the c-axis charge transfer would involve excitation of holes to the O:2p bands, which would require less energy as x increases. Moreover, strong electron-lattice coupling would introduce elastic excitations, and the data of McQueeny et al. [313] indicate the presence of vibrational modes with holes located on the oxygen atoms in a superconductor. We [268] have noted that, for a given value of x, the low-temperature enhancement of the thermoelectric power, which appears to be a measure of the transfer of spectral weight from (π, π) and $(\pi, 0)$ reciprocal axes, is larger where the c-axis conductivity is greater. If the transfer of spectral weight is due to the formation of itinerant vibronic states, as we have proposed [293], this observation would indicate that the c-axis conductivity is enhanced by the formation of vibronic states in the a-b planes; the formation of vibronic sates would promote elastic excitation of the holes to the O:2p bands.

The mechanism responsible for the formation of Cooper pairs in the superconductive state remains unsolved. Extensive spin-polarized inelastic neutron-scattering experiments have revealed a 41 meV resonance in the spin-excitation spectrum of the superconductive copper oxides that has caught theoretical attention [317]. Carbotte et al. [318] have noted that if these spin excitations are strongly coupled to the charge carriers, they should also be seen as a peak in the optical conductivity. They therefore calculated $\sigma(\omega)$ for a d-wave superconductor with inelastic scattering from the neutron data. Comparison with a-axis optical-conductivity data [319] showed that the

41 meV peak in the spin-excitation spectrum corresponds to a clearly resolved peak at about 69 meV in the $\sigma_a(\omega)$ data. They concluded that the coupling is strong enough to account for the high-T_c superconductivity. But what is not established is whether the coupling of the charge carriers to the spins is a result of strong coupling of the charge and spin to the lattice with the spin excitations going along for the ride rather than driving the formation of the superconductive pairs.

An alternative view is to consider pairing of itinerant vibronic states. The periodicity of the travelling CDW to which the electrons are coupled would introduce a pairing of electrons of momentum $\mathbf{k} + \mathbf{q}$ and $-(\mathbf{k} + \mathbf{q})$ to open a gap at the Fermi surface that has d-wave symmetry with a maximum in the $(\pm\pi, 0)$ and $(0, \pm\pi)$ directions. This approach, which has been considered by Seibold and Varlamov [320] is more consistent with the massive evidence now available for strong electron-lattice interactions in the copper oxides, as in the perovskites, at the cross-over from localized to itinerant electronic behavior.

3
References

1. Campet G, Dare-Edwards MP, Hamnett A, Goodenough JB (1980) Nouveau Journale de Chimie 4: 501
2. Megaw HD (1945) Nature 155: 484; Kay HF, Vousden P (1949) Phil Mag 40: 1019; Vousden P (1951) Acta Cryst 4: 373
2 a. Itoh M, Wang R, Inaguma Y, Yamaguchi T, Shan Y-J, Nakamura T (1999) Phys Rev Lett 82: 3540
3. Goral JP, Greedan JE, MacLean DA (1982) J Solid State Chem 43: 244
4. Okimoto Y, Katsufuji T, Okada Y, Arima T, Tokura Y (1995) Phys Rev B 51: 9581
5. Greedan JE (1985) J Less Common Metals 111: 335
6. Fujimori A, Hase I, Namatome H, Fujishima Y, Tokura Y, Eisaki H, Uchida S, Takegahara K, De Groot FMF (1992) Phys Rev Lett 69: 1796
6. a. Itoh M, Tsuchiya M, Tanaka H, Motoya K (1999) J Phys Soc Japan 68: 2783
7. Okada Y, Arima T, Tokura Y, Murayama C, Mori N (1993) Phys Rev B 48: 9677
8. Onoda M, Ohta H, Nagasawa H (1991) Solid State Commun 79: 281; Chamberland BL, Danielson PS (1971) J Solid State Chem 3: 243
9. Dougier P, Fan JCC, Goodenough JB (1975) J Solid State Chem 14: 247
10. Iga F, Nishihara Y (1992) J Phys Soc Japan 61: 1867
11. Morikawa K, Mizokawa T, Kobayashi K, Fujimori A, Eisaki H, Uchida S, Iga F, Nishihara Y (1995) Phys Rev B 52: 13,711
12. Inoue IH, Hase I, Aiura Y, Fujimori A, Haruyama Y, Maruyama T, Nishihara Y (1995) Phys Rev Lett 74: 2539
13. Zhou J-S, Goodenough JB (1996) Phys Rev B 54: 13,393
14. Brinkman WF, Rice TM (1970) Phys Rev B 2: 4302
15. MacDonald DKC (1962) Thermoelectricity: an introduction to the principles. Wiley, New York
16. Fukushima A, Murata K, Morikawa K, Iga F, Kido G, Nishihara Y (1994) Physica B 194/196: 1161

17. Howson MA, Gallagher BG (1988) Phys Rev 170: 265
18. Zubkov VG, Berger IF, Pesina ZM, Bazuev GV, Shveiken GP (1986) Sov Phys Dokl 31: 459
19. Zubkov VG, Bazuev GV, Perelyaev VA, Shveiken GP (1973) Sov Phys Solid State 15: 1079
20. Nguyen HC, Goodenough JB (1995) Phys Rev B 52: 8776
20. a. Nguyen HC, Goodenough JB (1994) CR Acad Sci Paris Ser II 319: 1285
21. Goodenough JB (1968) Phys Rev 171: 466
22. Borukhovich AS, Bazuev GV, Shveiken GP (1974) Sov Phys Solid State 15: 1467; 16: 181
23. Borukhovich AS, Zubkov VG, Bazuev GV (1978) Sov Phys Solid State 20: 1049
24. Shirakawa N, Ishikawa M (1991) Jpn J Appl Phys 30: L 755
25. Mahajan AV, Johnston DC, Torgeson DR, Borsa F (1991) Physica C 185/189: 1095; (1992) Phys Rev B 46: 10,966
26. Dougier P, Hagenmuller P (1974) J Solid State Chem 11: 177
27. Zubkov VG, Bazuev GV, Shveiken GP (1980) Sov Phys Crystallogr 25: 103
28. Ren Y, Palstra TTM, Khomskii DI, Pellegrin E, Nugroho AA, Menovsky AA, Sawatzky GA (1998) Nature 396: 441
29. Kawano H, Yoshizawa H, Ueda Y (1994) J Phys Soc Japan 63: 2857
30. Zubkov VG, Bazuev GV, Shveiken GP (1976) Sov Phys Solid State 18: 1165
30. a. Noguchi M, Nakazawa A, Oka S, Arima T, Wakabayashi Y, Nakao H, Murakami Y (2000) Phys Rev B 62: R9271
31. Bordet P, Chaillot C, Marezio M, Huang Q, Santoro A, Cheong S-W, Takagi H, Oglesby CS, Batlogg B (1993) J Solid State Chem 106: 253
32. Goodenough JB, Longo JM (1970) In: Hellwege KH (ed) Landolt-Börnstein Tabellen, New Series III/4a, Springer, Berlin Heidelberg New York, p 228
33. Goodenough JB, Longo JM, Kafalas JA (1968) Mat Res Bull 3: 471
34. Zhou J-S, Goodenough JB (1999) Phys Rev B 60: R15,002
35. Van Vleck JH (1939) J Chem Phys 7: 72
36. Wollan EO, Koehler WC (1955) Phys Rev 100: 545
37. Goodenough JB (1955) Phys Rev 100: 564
38. Rodríguez-Carvajal J, Hennion M, Moussa F, Moudden AH, Pinsard L, Revcolevschi A (1998) Phys Rev B 57: R3189
39. Murakami Y, Hill JP, Gibbs D, Blume M, Koyama I, Tanaka M, Kawato H, Arima T, Hirota K, Endoh Y (1998) Phys Rev Lett 81: 582
40. Dzialoshinskii IE (1958) J Phys Chem Solids 4: 214
41. Kanamori J (1960) J Appl Phys 31: 14S
42. Mizokawa T, Khomskii DI, Sawatzky GA (1999) Phys Rev B 60: 7309
43. Jonker GH, van Santen JH (1950) Physica 16: 337
44. Goodenough JB, Wold A, Arnott RJ, Menyuk N (1961) Phys Rev 124: 373
45. J Töpfer, Goodenough JB (1997) Europ J Solid State Inorg Chem 34: 481
46. van Roosmalen JAM, Cordfunke EHP (1994) J Solid State Chem 110: 106
47. Goodenough JB (1971) Mater Res Bull 6: 967
48. Gallagher PK, McChesney JB, Buchanan DNE (1964) J Chem Phys 41: 2429
49. Takeda T, Komura S, Fugii H (1983) J Magn Magn Mater 31/34: 797
50. Takano M, Nasu S, Abe T, Yamamoto K, Endo S, Takeda Y, Goodenough JB (1991) Phys Rev Lett 67: 3267
51. Takano M, Nakanishi N, Takeda Y, Naka S, Takada T (1977) Mater Res Bull 12: 923
51. a. Takeda Y, Naka S, Takano M (1979) J Phys (Paris) Colloque 40, C2: 331
52. Takeda T, Kanno R, Kawamoto Y, Takano M, Kawasaki S, Kamiyama T, Izumi F (unpublished)
52. a. Woodward PM, Cox DE, Moshopoulu E, Sleight AW, Morimoto S (2000) Phys Rev B 62: 844
52. b. Inami T, Kawasaki S, Takano M (unpublished)
53. Potze R, Sawatzky GA, Abbate M (1995) Phys Rev B 51: 11,501
54. Richter L, Bader SD, Brodsky MB (1980) Phys Rev B 22: 3059

55. Senarís-Rodríguez MA, Goodenough JB (1995) J Solid State Chem 116: 224
56. Yamaguchi S, Okimoto Y, Taniguchi H, Tokura Y (1996) Phys Rev B 53: R2926
57. Yamaguchi S, Okimoto Y, Tokura Y (1997) Phys Rev B 55: R8666
58. Asai K, Yokukura O, Suzuki M, Naka T, Matsumoto T, Takahashi H, Mori N, Kohn K (1997) J Phys Soc Japan 66: 967
59. Mehta A, Berliner R, Smith RW (1997) J Solid State Chem 130: 192
60. Raccah PM, Goodenough JB (1967) Phys Rev 155: 932
61. Bhide VG, Rajoria DS, Rao GR, Rao CNR (1972) Phys Rev B 6: 1021
62. Asai K, Yoneda A, Yokokura O, Tranquada JM, Shirane G, Kohn K (1998) J Phys Soc Japan 67: 290
62. a. Abbate M, Fuggle JC, Fujimori A, Tjeng LH, Chen CT, Potze R, Sawatzky GA, Eisaki H, Uchida S (1993) Phys Rev B47: 16,124
63. Arumarkavalli T, Kulkarni GU, Rao CNR (1993) J Solid State Chem 107: 299
64. Saitoh T, Mizokawa T, Fujimori A, Abbate M, Takeda Y, Takano M (1997) Phys Rev B 55: 4259
65. Goodenough JB, Raccah PM (1965) J Appl Phys 36: 1031
66. Demazeau G, Marbeuf A, Pouchard M, Hagenmuller P (1971) J Solid State Chem 3: 582
67. Vassiliou J, Hornbostel M, Ziebarth R, Disalvo FJ (1991) J Solid State Chem 90: 168
68. Lacorre P, Torrance JB, Pannetier J, Nazzal AI, Wang P, Huang TC (1991) J Solid State Chem 91: 225
69. Torrance JB, Lacorre P, Nazzal AI, Ansaldo EJ, Niedermayer C (1992) Phys Rev B 45: 8209
70. Medarde ML (1997) J Phys, Cond Matter 9: 1679
71. García-Muñoz JL, Rodríguez-Carvajal J, Lacorre P (1992) Europhys Lett 20: 241
72. Rodríguez-Carvajal J, Rosenkranz S, Medarde M, Lacorre P, Ferandez-Díaz MT, Fauth F, Trounov V (1998) Phys Rev B 57: 456
73. Goodenough JB (1996) J Solid State Chem 127: 126
74. Alonso JA, García-Muñoz JL, Ferández-Díaz MT, Aranda MAG, Martínez-Lope MJ, Casais MT (1999) Phys Rev Lett 82: 3871
75. Obradors X, Paulius LM, Maple MB, Torrance JB, Nazzal AI, Fontcuberta J, Granados X (1993) Phys Rev B 47: 12,353
76. Massa NE, Alonso JA, Martínez-Lope MJ, Rasines I (1997) Phys Rev B 56: 986
77. Mroginski MA, Massa NE, Salva H, Alonso JA, Martínez-Lope MJ (1999) Phys Rev B 60: 5304
78. Medarde M, Lacorre P, Conder K, Fauth F, Furrer A (1998) Phys Rev Lett 80: 2397
79. Zhou J-S, Goodenough JB, Dabrowski B (1999) In: Barnes SE, et al. (eds) CP483, High temperature superconductivity (AIP 1-56396-880-0/99), p 388; (2000) Phys Rev B 61: 4401
80. Sreedhar K, Honig JM, Darwin M, McElfresh M, Shand PPM, Xu J, Crooker BC, Spalek J (1992) Phys Rev B 46: 6382
81. Xu XQ, Peng JL, Li ZY, Ju HL, Greene RL (1993) Phys Rev B 48: 1112
82. Alonso JA, Martínez-Lope MJ, Rasines I (1995) J Solid State Chem 120: 170
83. Vobornik I, Perfetti L, Zacchigna M, Grioni M, Margaritondo G, Mesot J, Medarde M, Lacorre P (1999) Phys Rev B 60: R8426
84. Granados X, Fontcuberta J, Obradors X, Torrance JB (1992) Phys Rev B 46: 15,683
85. Zhou J-S, Goodenough JB, Dabrowski B, Klamut PW, Bukowski Z (2000) Phys Rev Lett 84: 526
86. Mott NF (1990) Metal-insulator transitions. Taylor & Francis, Cambridge, London
87. Moriya T (1985) Spin fluctuations in itinerant electron magnetiism. Springer, Berlin, Heidelberg, New York
88. Ghosh A, Raychaudhuri AK, Sreekala R, Rajeswari M, Venkatesan T (1998) Phys Rev B 58: R14,665
89. Demazeau G, Parent C, Pouchard M, Hagenmuller P (1972) Mater Res Bull 7: 913
90. Darracq S, Matar S, Demazeau G (1993) Solid State Commun 85: 961
91. Bringley JF, Scott BA, LaPlaca SJ, McGuire TR, Mehran F (1993) Phys Rev B 47: 15,269

92. Goodenough JB, Mott NF, Pouchard M, Demazeau G, Hagenmuller P (1973) Mater Res Bull 8: 647
93. Zhou J-S, Archibald W, Goodenough JB (1998) Phys Rev B 57: R2017
94. Zhou J-S, Archibald W, Goodenough JB (2000) Phys Rev B 61: 3196
95. Fujishima Y, Tokura Y, Arima T, Uchida S (1992) Phys Rev B 46: 11,167
96. Kumagai K, Suzuki T, Taguchi Y, Okada Y, Fujishima Y, Tokura Y (1993) Phys Rev B 48: 7636
97. Tokura Y, Taguchi Y, Okada Y, Fujishima Y, Arima T, Kumagai K, Iye Y (1993) Phys Rev Lett 70: 2126
98. Furukawa Y, Okamura I, Kumagai K, Goto T, Fukase T, Taguchi Y, Tokura Y (1999) Phys Rev B 59: 10,550
99. Hays CC, Zhou J-S, Markert JT, Goodenough JB (1999) Phys Rev B 60: 10,367
100. Taguchi Y, Tokura Y, Arima T, Inaba F (1993) Phys Rev B 48: 511
101. Pen HF, Abbate M, Fujimori A, Tokura Y, Eisaki H, Uchida S, Sawatzky GA (1999) Phys Rev B 59: 7422
102. Reuter B, Wollnik M (1963) Naturwissenschaften 50: 569
103. Dougier P, Deglane D, Hagenmuller P (1976) J Solid State Chem 19: 135
104. Nguyen HC, Goodenough JB (1995) Phys Rev B 52: 8776
105. Dougier P, Hagenmuller P (1975) J Solid State Chem 15: 158
106. Mahajan AV, Johnston DC, Torgesen DR, Borsa F (1992) Phys Rev B 46: 10,973
107. Kasuya M, Tokura Y, Arima T, Eisaki H, Uchida S (1993) Phys Rev B 47: 6197
108. Webb JB, Sayer M, Mansingh A (1977) Can J Phys 55: 1725
109. Grenier J, Ea N, Pouchard M, Abon-Sekkina MM (1984) Mater Res Bull 19: 1301
110. Bansal KP, Kumari S, Das BK, Jain GC (1983) J Mater Sci 18: 2095
111. Karim DP, Aldred AT (1979) Phys Rev B 20: 2255
112. Sarma DD, Maiti K, Vascovo E, Carbone C, Eberhardt W, Rader O, Gudat W (1996) Phys Rev B 53: 13,369
113. Hwang HY, Cheong S-W, Radaelli PG, Marezio M, Batlogg B (1995) Phys Rev Lett 75: 914
114. Archibald W, Zhou J-S, Goodenough JB (1996) Phys Rev B 53: 14,445
114 a. Goodenough JB, Zhou J-S (1998) Mat Res Soc Symp Proc 494: 335
115. Mira J, Rivas J, Rivadulla F, Vázquez-Vázquez C, López-Quintela MA (1999) Phys Rev B 60: 2998
116. McIlroy DN, Waldfried C, Zhang J, Choi J-W, Foong F, Lion SH, Dowben PA (1996) Phys Rev B 54: 17,438
117. Chechersky V, Nomura K, Nath A, Ju H, Greene RL (1997) Low Temp Phys B 23: 549
118. Chechersky V, Nath A, Isaac I, Franck JP, Ghosh K, Ju H, Greene RL (1999) Phys Rev B 59: 497
119. Lanzara A, Saini NL, Brunelli M, Natali F, Bianconi A, Radaelli PG, Cheong S-W (1998) Phys Rev Lett 81: 878
120. Zener C (1951) Phys Rev 82: 403
121. Goodenough JB (1997) J Appl Phys 81: 5330
122. Quijada M, Cerne J, Simpson JR, Drew HD, Ahn KH, Millis AJ, Shreekala R, Ramesh R, Rajeswari M, Venkatesan T (1998) Phys Rev B 58: 16,093
123. Kim KH, Jung JH, Noh TW (1998) Phys Rev Lett 81: 1517
124. Zhao YG, Li JJ, Sheekala R, Drew HD, Chen CL, Cao WL, Lee CH, Rajeswari M, Ogale SG, Ramesh R, Baskaram G, Venkatesan T (1998) Phys Rev Lett 81: 1310
125. Sakaie KE, Slichter CP, Lin P, Jaime M, Salamon MB (1999) Phys Rev 59: 9382
126. Lu Q, Chen C-C, deLozanne A (1997) Science 276: 2006
127. Fäth M, Freisem S, Menovsky AA, Tomioka Y, Aarts J, Mydosh JA (1999) Science 285: 1540
128. De Teresa JM, Ibarra MR, Algarabel PA, Ritter C, Marquina C, Blasco J, García J, del Moral A, Arnold Z (1997) Nature 386: 256
129. Goodenough JB (1996) Mat Res Symp Proc 401: 515; (1999) Aust J Phys 52: 155
130. Nagaev EL (1996) Physics-Uspekhi 39: 781
131. Emin D (1998) In: Hundley M, Nickel J, Ramesh R, Tokura Y (eds) Science and technology of magnetic oxides. Mat Res Soc, Pittsburgh, p 163

132. Dagotto E, Yunoki S, Malvezzi AL, Moreo A, Hu J, Capponi S, Poilblanc D, Furukawa N (1998) Phys Rev B 58: 6414
133. Moreo A, Yunoki S, Dagotto E (1999) Science 283: 2034
134. Alexandrov AS, Bratkovsky AM (1998) Phys Rev Lett 82: 141
135. Alexandrov AS, Bratkovsky AM (1999) Condens Matt 2: 8183
136. Radaelli PG, Iannone G, Marezio M, Hwang HY, Cheong S-W, Jorgensen JD, Argyriou DN (1997) Phys Rev B 56: 8625
137. De Teresa JM, Blanco J, Ibarra MR, García J, Marquina C, Algarabel P, del Moral A (1996) J Appl Phys 79: 5175
138. Neumeier JJ, Hundley MF, Thompson JD, Heffner RH (1995) Phys Rev B 52: R7006
139. Laukhin V, Fontcuberta J, García-Muñoz JL, Obradors X (1997) Phys Rev B 56: R10,009
140. Fontcuberta J, Laukhin V, Obradors X (1998) Appl Phys Lett 72: 2607
141. De Teresa JM, Ibarra MR, Blasco J, García J, Marquina C, Algarabel PA (1996) Phys Rev B 54: 1187
142. Jaime M, Salamon MB (1999) In: Kaplan TA, Mahanti SD (eds) Physics of manganites. Khver Academic, Plenum, New York, p 243
143. Zhou J-S, Archibald W, Goodenough JB (1996) Nature 381: 770
144. Overend N, Zhou J-S, Goodenough JB (unpublished)
145. Zhao G-M, Conder K, Keller H, Müller KA (1996) Nature 381: 676
146. Zhao G, Hunt MB, Keller H (1997) Phys Rev Lett 78: 955
147. Zhao G, Keller H, Hofer J, Shengelaya A, Müller KA (1997) Solid State Commun 104: 57
148. Zhou J-S, Goodenough JB (1998) Phys Rev Lett 80: 2665
149. Chechersky V, Nath A, Isaac I, Franck JP, Ghosh K, Ju H, Greene RL (1999) Phys Rev B 60: 3005
150. Franck JP, Isaac I, Chen W, Chrzanowski J, Homes CC (1999) J Supercon 12, 364
151. Uehara M, Kim TH, Cheong S-W (private communication)
152. Dabrowski B, Klamut PW, Bukowski Z, Dybzinski R, Siewenie JE (1999) J Solid State Chem 144: 461
153. Dabrowski B, Dybzinski R, Bukowski Z, Chmaissem O (1999) J Solid State Chem 146: 448
154. Croft M, Sills D, Greenblatt M, Lee C, Cheong S-W, Ramanujachary KV, Tran D (1997) Phys Rev B 55: 8726
155. Dyson TA, Qian Q, Kao C-C, Rueff J-P, De Groot FMF, Cheong S-W, Greenblatt M, Sabramanian MA (1999) Phys Rev B 60: 4665
156. Wold A, Arnott RJ (1959) J Phys Chem Solids 9: 176
157. Faaland S, Knudsen KD, Einarsrud MA, Rormark L, Hoier R, Grande T (1998) J Solid State Chem 140: 320
158. Radaelli PG, Marezio M, Hwang HY, Cheong S-W, Batlogg B (1996) Phys Rev B 54: 8992
159. García-Muñoz JL, Suaaidi M, Fontcuberta J, Rodríguez-Carvajal J (1997) Phys Rev B 55: 34
160. Subías G, García J, Blasco J, Proietti MG (1998) Phys Rev B 57: 748
161. Jung JH, Kim KH, Noh TW, Choi EJ, Yu J (1998) Phys Rev B 57: R11,043
162. Worledge WC, Miéville L, Geballe TH (1998) Phys Rev B 57: 15,267
162 a. Matsumoto G (1970) IBM J Res Develop 14: 258
163. Hennion M, Moussa F, Rodríguez-Carvajal J, Pinsard L, Revcolevschi A(1997) Phys Rev B 56: R497
164. Moussa F, Hennion M, Biotteau G, Rodríguez-Carvajal J, Pinsard L, Revcolevschi A (1999) Phys Rev B 60: 12,299
165. Fujishiro H, Fukase T, Ikebe M, Kikuchi T (1999) J Phys Soc Japan 68: 1469
166. Yamada Y, Hino O, Nohdo S, Kanao R, Inami T, Katano S (1996) Phys Rev Lett 77: 904
167. Zhou J-S, Goodenough JB (2000) Phys Rev B 62: 3834
168. Allodi G, DeRenzi R, Guidi G, Lucci F, Pieper MW (1997) Phys Rev B 56: 6036
169. Allodi G, DeRenzi R, Guidi G (1998) Phys Rev B 57: 1024
170. Papavassiliou G, Fardis M, Belesi M, Pissas M, Panagiotopoulos I, Kollias G, Narchos D, Dimitropoulos C, Dolinsek J (1999) Phys Rev B 59: 6390

171. Dho J, Kim J, Lee S, Kim KH, Lee HJ, Jung JH, Noh TW (1999) Phys Rev B 59: 492
172. Radaelli PG, Cox DE, Marezio M, Cheong S-W (1997) Phys Rev B 55: 3015
173. Ahn KH, Millis AJ (1998) Phys Rev B 58: 3697
174. Kuwahara H, Tomioka Y, Asamitsu A, Moritomo Y, Tokura Y (1995) Science 270: 961
175. Moritomo Y (1999) Phys Rev B 60: 10,374
176. Shimomura S, Tajima K, Wakabayashi N, Kobayashi S, Kuwahara H, Tokura Y (1999) J Phys Soc Japan 68: 1943
177. Kawano H, Majimoto R, Yoshizawa H, Tomioka Y, Kuwahara H, Tokura Y (1997) Phys Rev Lett 78: 4253
178. Llobet A, García-Muñoz JL, Fontera C, Ritter C (1999) Phys Rev B 60: R9889
179. Tomioka Y, Asamitsu A, Moritomo Y, Kuwahara H, Tokura Y (1995) Phys Rev Lett 74: 5108
179 a. Wang R, Makesh R, Itoh M (1999) Phys Rev B 60: 14,513
180. Yunoki S, Hotta T, Dagotto E (2000) Phys Rev Lett 84: 3714
181. Fontcuberta J, Laukhin V, Obradors X (1999) Phys Rev B 60: 6266
182. Fujishiro H, Fukase T, Ikebe M (1998) J Phys Soc Japan 67: 2582
183. Papavassiliou G, Fardis M, Milia F, Simopoulos A, Kallias G, Pissas M, Niarchos D, Ioannidis N (1997) Phys Rev B 55: 15,000
184. Allodi G, De Renzi R, Licci F, Pieper MW (1998) Phys Rev Lett 81: 4736
185. Yoshimori Y, Hammel PC, Thompson JD, Cheong S-W (1999) Phys Rev B 60: 9275
186. Roy M, Mitchell JF, Ramirez AP, Schiffer P (1998) Phys Rev B 58: 5185
187. Chen CH, Cheong S-W (1966) Phys Rev Lett 76: 4042
188. Smolyaninova VN, Ghosh K, Greene RL (1998) Phys Rev B 58: R14,725
189. Zhao G, Ghosh K, Keller H, Greene RL (1999) Phys Rev B 59: 81
190. Mahesh R, Itoh M (1999) J Solid State Chem 144: 232
191. Granado E, Moreno NO, García A, Sanjuro JA, Rettori C, Torriani I, Oseroff SB, Neumeier JJ, McClellan KJ, Cheong S-W, Tokura Y (1998) Phys Rev B 58: 11,435
192. Uehara M, Mori S, Chen CH, Cheong S-W (1999) Nature 399: 560
193. Kajimoto R, Kakeshita T, Oohara Y, Yoshizawa H, Tomioka Y, Tokura Y (1998) Phys Rev B 58: R11,837
194. Mori S, Chen CH, Cheong S-W (1998) Phys Rev Lett 81: 3972
195. Mori S, Chen CH, Cheong S-W (1998) Nature 392: 473
196. Radaelli PG, Cox DE, Capogna L, Cheong S-W, Marezio M (1999) Phys Rev B 59: 1440
197. Urushibara A, Moritomo Y, Arima T, Asamitsu A, Kido G, Tokura Y (1995) Phys Rev B 51: 14,103
198. Kawano H, Kajimoto R, Yoshizawa H (1996) Phys Rev B 53: R14,709
199. Zhou J-S, Goodenough JB, Asamitsu A, Tokura Y (1997) Phys Rev Lett 79: 3234
200. Moritomo Y, Asamitsu A, Tokura Y (1997) Phys Rev B 56: 12,190
201. Dabrowski B, Xiong X, Bukowski Z, Dybzinski R, Klamut PW, Siewenie JE, Chmaissem O, Shaffer J, Kimball CW, Jorgensen JD, Short S (1999) Phys Rev B 60: 7006
202. Xiong X, Dabrowski B, Chmaissem O, Bukowski Z, Dybzinski R, Kimball CW, Jorgensen JD (1999) Phys Rev B 60: 10,186
203. Kumagai K, Iwai A, Tamioka Y, Kuwahara H, Tokura Y, Yakubovskii A (1999) Phys Rev B 59: 97
204. Louca D, Egami T, Brosha LL, Röder H, Bishop AP (1997) Phys Rev B 56: R8475
205. Okimoto Y, Katsufuji T, Ishikawa T, Uruhibara A, Arima T, Tokura Y (1995) Phys Rev Lett 75: 109
206. Okimoto Y, Katsufuji T, Ishikawa T, Arima T, Tokura Y (1997) Phys Rev B 55: 4206
207. Machida A, Moritomo Y, Nakamura A (1998) Phys Rev B 58: R4281
208. Takenaka K, Iida K, Sawaki Y, Sugai S, Moritomo Y, Nakamura A (1999) J Phys Soc Japan 68: 1828
209. Takenaka K, Sawaki Y, Sugai S (1999) Phys Rev B 60: 13,011
210. Asamitsu A, Moritomo Y, Tokura Y (1996) Phys Rev B 53: R2952
211. Moritomo Y, Machida A, Matsua K, Ichida M, Nakamura A (1997) Phys Rev B 56: 1
212. Shiba H, Shiina R, Takanashi A (1997) J Phys Soc Japan 66: 941

213. Smolyaninova VN, Hamilton JJ, Greene RL, Mukovskii YM, Karabashev SG, Balbashov AM (1997) Phys Rev B 55: 5640
214. Fernandez-Baca JA, Dai P, Hwang HY, Kloc C, Cheong S-W (1998) Phys Rev Lett 80: 4012
215. Martin MC, Shirane G, Endoh Y, Hirota K, Moritomo Y, Tokura Y (1996) Phys Rev B 53: 14,285
216. Fujishiro H, Ikebe M, Konno Y (1998) J Phys Soc Japan 67: 1799
217. Asamitsu A, Moritomo Y, Tomioka Y, Arima T, Tokura Y (1995) Nature 373: 407
218. Asamitsu A, Moritomo Y, Kamai R, Tomioka Y, Tokura Y (1996) Phys Rev B 54: 1716
219. Campbell AJ, Balakrishnan G, Lees MR, Paul D McK, McIntyre GJ (1997) Phys Rev B 55: R8622
220. Kamenev KV, McIntyre GJ, Paul D Mck, Lees MR, Balakrishnan G (1998) Phys Rev B 57: R6775
220. a. Zhou J-S, Goodenough JB, Phys Rev B (in press)
221. Okuda T, Asamitsu A, Tomioka Y, Kimura T, Taguchi Y, Tokura Y (1998) Phys Rev Lett 81: 3203
222. Yamada Y, Hino O, Nohdo S, Kanao R (1996) Phys Rev Lett 77: 904
223. Kawano H, Kajimoto R, Kubota M, Yoshizawa H (1996) Phys Rev B 53: 2202
224. De Gennes P-G (1960) Phys Rev 118: 141
225. Khaliullin G, Kilian R (2000) Phys Rev B 61: 3494
226. Vasiliu-Duloc L, Lynn JW, Moudden AH, de Lern-Guevara AM, Revcolevschi A (1998) Phys Rev B 58: 14,913
227. Uhlenbruck S, Teipen R, Klingeler R, Büchner B, Friedt O, Hücker M, Kierspel H, Niemöller T, Pinsard L, Revcolevschi A, Gross R (1999) Phys Rev Lett 82: 185
228. Nojiri H, Kaneko K, Motokawa M, Hirota K, Endoh Y, Takahashi K (1999) Phys Rev B 60: 4142
229. Senis R, Laukhin V, Martinez B, Fontcuberta J, Obradors X, Arsenov AA, Mukovskii YM (1998) Phys Rev B 57: 14,680
230. Endoh Y, Hirota K, Ishihara S, Okamoto S, Murakami Y, Nishizawa A, Fukuda T, Kimura H, Nojiri H, Kaneko K, Maekawa S (1999) Phys Rev Lett 82: 4328
231. Darling TW, Migliori A, Moshopoulou EG, Trugman SW, Neumeier JT, Sarrao JL, Bishop AR, Thompson JD (1998) Phys Rev B 57: 5093
232. Neumeier JJ, Andres K, McClellan KJ (1999) Phys Rev B 59: 1701
233. Kiryukhin V, Wang YJ, Chou FC, Kastner MA, Birgeneau RJ (1999) Phys Rev B 59: R6581
234. Pimenov A, Hartinger C, Loidl A, Mukhin AA, Ivanov VY, Balbashov AM (1999) Phys Rev B 59: 12,419
235. Ghosh K, Greene RL, Lofland SE, Bhagat SM, Karabasher SG, Shulyater DA, Arsenov AA, Mukovskii Y (1998) Phys Rev B 58: 8206
236. Anane A, Dupas C, LeDang K, Renard JP, Veillet P, de Leon-Guevara AM, Millot F, Pinsard L, Revcolevschi A (1995) J Phys: Condens Matter 7: 7015
237. Itoh M, Nishi K, Yu JD, Inaguma Y (1997) Phys Rev B 55: 14,408
238. Jung JH, Kim KH, Lee HJ, Ahn JS, Hur NJ, Noh TW, Kim MS, Park J-G (1999) Phys Rev B 59: 3793
239. Ikebe M, Fujishiro H, Konno Y (1998) J Phys Soc Japan 67: 1083
240. Dann SE, Durrie DB, Weller MT, Thomas MF, Al-Rawwas AD (1994) J Solid State Chem 109: 134
241. Battle PD, Gibb TC, Nixon S (1989) J Solid State Chem 79: 75
242. Matsuno J, Mizokawa T, Fujimori A, Mamiya K, Takeda Y, Kawasaki S, Takano M (1999) Phys Rev B 60: 4605
243. Ishikawa T, Park SK, Katsufuji T, Arima T, Tokura Y (1998) Phys Rev B 58: R13,326
244. Park SK, Ishikawa T, Tokura Y, Li JQ, Matsui Y (1999) Phys Rev B 60: 10,788
244. a. Sathe VG, Paranjpe SK, Siruguri V, Pimpale AV (1998) J Phys: Condens Matter 10: 4045
245. Chern G, Hsieh WK, Tai MF, Hsung KS (1998) Phys Rev B 58: 1252

246. Grenier J-C, Ea N, Penchard M, Abon-Sekkina MM (1984) Mat Res Bull 19: 1301
247. Señarís-Rodríguez MA, Goodenough JB (1995) J Solid State Chem 118: 323
248. Yamaguchi S, Okimoto Y, Taniguchi H, Tokura Y (1996) Phys Rev B 53: R2926
249. Louca D, Sarrao JL, Thompson JD, Röder H, Kwei GH (1999) Phys Rev B 60: 10,378
250. Yamaguchi S, Okimoto Y, Taniguchi H, Tokura Y (1996) Phys Rev B 53: 2926
251. Itoh M, Natori I (1995) J Phys Soc Japan 64: 970
252. Caciuffo R, Rinaldi D, Barucca G, Mira J, Rivas J, Señarís-Rodríguez MA, Goodenough JB (1999) Phys Rev B 59: 1068
253. Itoh M, Natori I, Kubota S, Motoya K (1994) J Phys Soc Japan 63: 1486
254. Makherjee S, Ranganathan R, Anilkumar PS, Joy PA (1996) Phys Rev B 54: 9267
255. Nam DNH, Jonason K, Nordblad P, Khiem NV, Phuc NX (1999) Phys Rev B 59: 4189
256. Yamaguchi S, Taniguchi H, Takagi H, Arima T, Tokura Y (1995) J Phys Soc Japan 64: 1885
257. Mahendrin R, Roychaudhuri AK (1996) Phys Rev B 54: 16,044
258. Golovanov V, Mihaly L, Moodenbaugh AR (1996) Phys Rev B 53: 8207
259. Caciuffo R, Mira J, Rivas J, Señarís-Rodríguez MA, Radaelli PG, Carsughi F, Fiorani D, Goodenough JB (1999) Europhys Lett 45: 399
260. Ibarra MR, Mahendrin R, Marquina C, García-Landa B, Blasco J (1998) Phys Rev B 57: R3217
261. Wang ZL, Zhang J (1996) Phys Rev B 54: 1153
262. Vasquez RP (1996) Phys Rev B 54: 14,938
263. Saitoh T, Mizokawa T, Fujimori A, Takeda Y, Takano M (1996) J Electron Spectros Relat Phenom 78: 195
264. Saitoh T, Mizokawa T, Fujimori A, Abbate M, Takeda Y, Takano M (1997) Phys Rev B 55: 4257
265. Jorgensen JD, Dabrowski B, Pei S, Hinks DF, Soderholm L, Morosin B, Schirber JE, Venturini EL, Ginley DS (1988) Phys Rev B 38: 11,337
266. Grenier JC, Lagueyte N, Wattiaux A, Doumerc J-P, Dordor P, Etourneau J, Pouchard M, Goodenough JB (1992) Physica C 202: 209
267. Zhang FC, Rice TM (1988) Phys Rev B 37: 3759
268. Zhou J-S, Goodenough JB (1996) Phys Rev B 54: 12,488
269. Goodenough JB, Zhou J-S, Chan J (1993) Phys Rev B 47: 5275
270. Bersuker GI, Goodenough JB (1997) Physica C 274: 267
271. Boebinger GS, Ando Y, Passner A, Kimura T, Okuya M, Shimoyama J, Kishio K, Tamasaku K, Ichikawa N, Uchida S (1996) Phys Rev Lett 77: 5417
271. a. Bozin ES, Kwei GH, Takagi H, Billinge SJL (2000) Phys Rev Lett 84: 5856
272. Hunt AW, Singer PM, Thurber KR, Imai T (1999) Phys Rev Lett 82: 4300
273. Weidinger A, Niedermayer C, Golnik A, Simon R, Recknagel E, Budnick JI, Chamberland B, Baines C (1988) Phys Rev Lett 62: 102
274. Cannelli G, Canali M, Cantelli R, Cordero F, Ferraro S, Ferretti M, Traquattrini F (1992) Phys Rev B 45: 931
275. Cho JH, Borsa F, Johnston DC, Torgeson DR (1992) Phys Rev B 46: 3179
276. Julien M-H, Borsa F, Caretta P, Horvatic M, Berthier C, Liu CT (1999) Phys Rev Lett 83: 604
277. Borsa F, Carretta P, Cho JH, Chou FC, Hu Q, Johnston DC, Lascialfari A, Torgeson DR, Gooding RJ, Salem NM, Vos KJE (1995) Phys Rev B 52: 7334
278. Kochelaev BI, Sichelschmidt J, Elschner B, Lemor W, Loidl A (1997) Phys Rev Lett 79: 4274
279. Torrance JB, Bezinge A, Nazzal AI, Huang TC, Parkin SSP, Keane DT, LaPlaca SJ, Horn PM, Held GA (1989) Phys Rev B 44: 8872
280. Loeser AG, Shen Z-X, Dessau DS, Marshall DS, Park CH, Fournier P, Kapitulnik A (1996) Science 273: 325
281. Fan YF, Matl P, Harris JM, Ong NP (1995) Phys Rev B 52: R751
282. Onufrieva F, Pfenty P (1999) Phys Rev Lett 82: 3136
283. Zhou J-S, Goodenough JB (1996) Phys Rev B 54: 11,997
284. Zhou J-S, Goodenough JB (1995) Phys Rev B 51: 3104
285. Zhou J-S, Goodenough JB (1996) Phys Rev Lett 77: 151
286. Goodenough JB, Zhou J-S (1997) J Supercond 10: 309

287. Campuzano JC, Jennings G, Faiz M, Beaulaigue L, Veal BW, Liu JZ, Paulikas AP, Vandervoort K, Claus H, List RS, Arko AJ, Bartlett RJ (1990) Phys Rev Lett 64: 2308
288. Saini NL, Avila J, Bianconi A, Lanzara A, Asensio MC, Tajima S, Gu GD, Koshizuka N (1997) Phys Rev Lett 79: 3467
289. Shen Z-X, White PG, Feng DL, Kim C, Gu GD, Ikeda H, Yoshizaki R, Koshizuka N (1998) Science 280: 259
290. Norman MR, Ding H, Randeria M, Campuzano JC, Yokoya T, Takeuchi T, Takahashi T, Mochiku T, Kadowski K, Gutasarma P, Hinks DG (1998) Nature 392: 157
291. Chuang Y-D, Gronko AD, Dessau DS, Aiura Y, Yamagueli Y, Oka Y, Arko AJ, Joyce J, Eisaki H, Uchida SI, Nakamua K, Ando Y (1999) Phys Rev Lett 83: 3717
292. Mizokawa T, Kim C, Shen Z-X, Ino A, Fujimori A, Goto M, Eisaki H, Uchida S, Tagami M, Yoshida K, Rykov AI, Siohara Y, Tomimoto K, Tajima S (1999) Phys Rev B 60: 12,335
293. Goodenough JB, Zhou J-S (2000) J Supercond (in press); (1999) In: Fukuyama H, Nagaosa N (eds) Proc 29th Taniguchi Symposium, Springer Solid-Sate Sciences 125, Springer, Berlin Heidelberg New York, p 9
293. a. Deutscher G, Dagon Y, Kohen A, Kupke R (2000) J Supercond (in press)
294. Baberski O, Lang A, Maldonado O, Hücker M, Büchner B, Freimuth A (1998) Europhys Lett 44: 335
295. Zhou J-S, Chen H, Goodenough JB (1994) Phys Rev B 49: 9084
296. Moodenbaugh AR, Xu Y, Suenaga M, Flokerts TJ, Shelton RN (1988) Phys Rev B 38: 4596
297. Crawford MK, Harlow RL, McCarron EM, Farneth WE, Herron N (1993) Phys Rev B 47: 11,623
298. Moodenbaugh AR, Wu L, Zhu Y, Lewis LH, Cox DE (1998) Phys Rev B 58: 9549
299. Sakita S, Nakamura F, Suzuki T, Fujita T (1999) J Phys Soc Japan 68: 2755
300. Tranquada JM, Sternlieb BJ, Axe JD, Nakamura Y, Uchida S (1995) Nature 375: 561
301. Tranquada JM, Ichikawa N, Uchida S (1999) Phys Rev B 59: 14,712
302. Cheong S-W, Aeppli G, Mason TE, Mook H, Hayden SM, Canfield PC, Fisk Z, Clausen KN, Martinez JL (1991) Phys Rev Lett 67: 1791
303. Yamamoto K, Kasufuji T, Tanabe T, Tokura Y (1998) Phys Rev Lett 80: 1493
304. Tranquada JM, Axe JD, Ichikawa N, Moodenbaugh AR, Nakamura Y, Uchida S (1997) Phys Rev Lett 78: 338
305. Zhou J-S, Goodenough JB (1997) Phys Rev B 56: 6288
306. Bianconi A, Della Longa S, Missori M, Pettiti I, Pompa M, Soldator A (1993) Jpn J App Phys 32 (suppl 32–3): 578
307. Bianconi A, Saini NL, Lanzara A, Missori M, Rossetti T, Oyanagi H, Yamaguchi H, Oka K, Ito T (1996) Phys Rev Lett 76: 3412
308. Suzuki T, Goto T, Chiba K, Shinoda T, Fukase T, Kimura H, Yamada K, Ohashi M, Yamaguchi Y (1998) Phys Rev B 57: R3229
309. Suzuki T, Oshima Y, Chiba K, Fukase T, Goto T, Kimura H, Yamada K (1999) Phys Rev B 60: 10,500
310. Singer PM, Hunt AW, Cederström AF, Imai T (1999) Phys Rev B 60: 15,345
311. Bozin ES, Billinge SJL, Kwei GM, Takagi H (1999) Phys Rev B 59: 4445
312. Noda T, Eisaki H, Uchida S (1999) Science 286: 265
313. McQueeny RJ, Petrov Y, Egami T, Yethiraj M, Shirane G, Endoh Y (1999) Phys Rev Lett 82: 628
313. a. Egami T, Petrov Y, Louca D, J Supercond (in press)
314. Ito T, Takagi H, Ishibashi S, Ido T, Uchida S (1991) Nature 350: 596
315. Uchida S, Tamasuku K, Tajima S (1996) Phys Rev B 53: 14,558
316. Hussey NE, Cooper JR, Kodama Y, Nishihara Y (1998) Phys Rev B 58: R611
317. Demler E, Zhang SC (1995) Phys Rev Lett 75: 4126
318. Carbotte JP, Schachinger E, Basov DN (1999) Nature 401: 354
319. Basov DN, Liang R, Dabrowski B, Bonn DA, Hardy WN, Timusk T (1990) Phys Rev Lett 77: 4090
320. Seibold G, Varlamov S (1999) Phys Rev B 60: 13,056

Local Atomic Structure of CMR Manganites and Related Oxides

T. Egami

Department of Materials Science and Engineering, University of Pennsylvania, Philadelphia, PA 19104-6272, USA
E-mail: egami@seas.upenn.edu

The crystal structure determined by diffraction analysis is usually used as a basis for explaining the properties of a solid in terms of the nature of the atomic bonding. However, in many transition-metal oxides the actual atomic structure can be slightly different from the crystal structure due to substitutional disorder or strong electron-lattice coupling. In order to understand the properties of such a system, it is more important to determine the local atomic structure than the average crystal structure since the properties tend to reflect more strongly the local structure than the average structure. Recently local structural determination became much easier and more accurate due to the advent of synchrotron-based radiation sources. In this chapter we describe one of the methods of local structural determination, the pulsed neutron atomic pair-density function (PDF) analysis, and demonstrate how it helps us to understand the microscopic interactions in the colossal magnetoresistive (CMR) manganites, ferroelectric oxides, and superconductive cuprates. In particular, we show how the knowledge of the local structure leads to the concept of a critical stability of lattice polarons that controls the CMR phenomenon and possibly the high-temperature superconductivity.

Keywords: Local atomic bonding, PDF analysis, CMR manganites, Polarons, Ferroelectrics, Superconducting cuprates

1
Introduction

Determining the crystal structure is usually one of the first steps when one attempts to explain the properties of a crystalline solid in terms of the atomic bonding in the solid. The crystallographic analysis that is used in determining the crystal structure, however, assumes periodicity of the structure while the structure of many technologically useful solids is not perfectly periodic. For instance, the local atomic structure of mixed-ion oxides, in which the same crystal site is occupied by a mixture of two or more elements, depends upon which element is occupying the site; consequently the actual interatomic distances and atomic displacements vary from site to site. In such a case, estimating the bond length from the crystallographic structure can lead to erroneous results. For instance, if two isostructural oxides AO$_n$ and BO$_n$ are mixed into a pseudo-binary solid solution A$_{1-x}$B$_x$O$_n$, the lattice constant of the solid would change nearly linearly with x, following Vegard's law. However, the local bond lengths A—O and B—O usually remain largely unchanged from those in the unmixed state, and the lattice constant merely represents the weighted average of the two. The crystal structure, on the other hand, gives only the average (A, B)—O distance, which is equal to neither A—O nor B—O distances. Usually chemical intuition is used in such a case to conjecture the magnitude of local displacements and hence the real bond lengths inferred

from crystallographic data. But instead of guessing the bond lengths, it is possible, and better, to determine the actual local structure of the solids directly by local structural probes.

At present the most commonly used local probe is X-ray absorption fine structure (XAFS) analysis [1]. The X-ray absorption coefficient of a solid shows small oscillations as a function of the energy of the X-ray. This effect occurs because a virtual photoelectron emitted at the absorption of a photon is reflected by neighboring atoms and interferes with the absorption process. By analyzing these oscillations, the distances to the neighboring atoms can be determined. The greatest merit of this technique is that local atomic distances from a specific element can be determined. This is an important advantage in studying complex materials. However, since the basis of the XAFS is the scattering of local photoelectrons, the data analysis is complex, involving many parameters, and the procedure of analysis is not completely established. In particular where the structure is disordered, the XAFS signal becomes strongly damped, resulting in unrealistically small coordination numbers. In general the effect of disorder is exaggerated by the XAFS method. An attractive alternative to the XAFS method is the atomic pair-density function (PDF) analysis of diffraction data using neutrons, X-rays, or electrons as a probe [2, 3]. In particular, since the physics of neutron and X-ray scattering is very well understood, the PDF analysis using neutrons or X-rays has many advantages over the XAFS method. In this chapter we introduce this method and show how this method helped us to understand the atomic bonding and interactions in some transition metal oxides including the colossal magnetoresistive (CMR) manganites, ferroelectrics, and superconductive cuprates.

2
Analysis of Local Atomic Structure
by the Pulsed Neutron Atomic Pair-Density Function (PDF) Method

2.1
Limitation of Crystallographic Methods

When the need to determine the atomic structure of a solid arises, most researchers rely upon crystallographic analysis using diffraction of X-rays or neutrons, even when it is suspected that the solid has some internal disorder due to defects or alloying. However, the limitation of such analysis is not well-recognized, often resulting in misleading or even erroneous interpretation. In this section we examine the limitation of the crystallographic methods in examining crystalline solids with extensive disorder.

Usually structural disorder is described by crystallographic methods of structural analysis through two parameters [2, 3]:

1. Large Debye–Waller (DW) factor
2. Partial occupation of lattice sites

In some limited cases these two can correctly characterize the extent of local disorder in a crystalline solid, but in many cases they provide false information on the nature of local disorder.

2.1.1
Large Debye–Waller (DW) Factor

Local atomic displacements due to phonons are well-described by the DW factor, $e^{-\langle u^2 \rangle Q^2}$, where u is the local atomic displacement from the average atomic position and Q is the diffraction vector, $4\pi \sin \theta / \lambda$ (θ is the diffraction angle and λ is the wavelength of the probe). This method is usually extended to describe other kinds of local disorder than lattice vibration. However, this extension has serious limitations that are too often insufficiently recognized. The DW approximation is inaccurate at least in the following cases:

1. Strong anharmonicity: if the local potential for an atom is a double-well, the atomic distribution will be bimodal. However, in the DW approximation this appears simply as a widely distributed atom density in a soft potential.
2. Uneven distribution of the magnitudes of displacements: if a relatively small number of atoms have larger amplitudes of displacement while others remain normal, fitting one DW factor results in a significant underestimate of the displacements. Atoms with very large displacements are practically ignored.
3. Correlated atomic displacements: if two atoms move in the same direction, the change in the interatomic distance is smaller than the displacements of each, and the DW factor overestimates the relative displacements of the atoms. On the other hand, if the motions are anti-correlated, the DW factor underestimates the relative displacements.

Point 2 can be illustrated by the following example. Let us assume that the vibrational amplitude of 60% of the atoms is 0.05 Å while the rest of the atoms have a larger amplitude of 0.2 Å. The r.m.s. value of the vibrational amplitude, $\langle u^2 \rangle^{1/2}$, is equal to 0.132 Å. If we fit a single DW factor for this case, the estimated amplitude of 0.062 Å is barely 1/2 of the correct value, as is shown in Fig. 1. This serious underestimate occurred because large atomic displacements result in a Debye–Waller factor that decreases sharply with Q and contributes relatively little to the overall fitting by a single DW factor. It is often believed that the DW factor provides at least the correct r.m.s. value of displacements while it neglects correlation among them. This example demonstrates that such a belief is completely unfounded. The example above can, of course, be modeled by assuming two kinds of lattice sites with different DW factors. However, it takes an unusually keen insight to come up with such a model just by looking at the diffraction data.
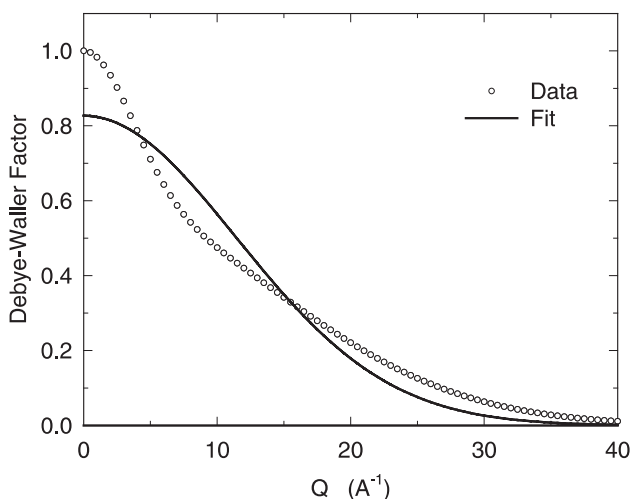
Fig. 1. Debye–Waller envelope when 60% of the atoms have the vibrational amplitude of 0.05 Å while others have a larger amplitude of 0.2 Å (*circles*). The r.m.s. value of amplitudes is then 0.132 Å. A fit by a single Debye–Waller envelope (*solid line*) results in the r.m.s. value of 0.062 Å, an underestimate by more than 50%. This illustrates a danger of trusting the Debye–Waller approximation in describing disorder

2.1.2
Partial Occupation of Lattice Sites

The density of lattice vacancies can be determined, usually accurately, by the site occupation parameter. Thus if the local atomic potential is bifurcated and atoms are locally displaced, it may appear that partial occupation of the displaced site describes the system quite well. However, in such cases there is usually strong coupling between the occupation parameter and the DW factor during the process of refinement. Also, local displacement of an atom is usually accompanied by a lattice relaxation around the displaced atom and a much increased DW factor of the displaced site. Thus, in practice, it is very difficult to describe anharmonic local displacements through partial occupation of two closely spaced sites.

The arguments above highlight severe compromises made in trying to describe local disorder by simply extending the crystallographic methods. It is much preferred to determine the local structure directly by local probes. In the following we describe the method of pulsed neutron PDF analysis and some of the results obtained by this method that help to understand the properties of electronic ceramics.

2.2
Experimental Technique

In the crystallographic methods of structural study all the analyses culminating in the fitting of the data are done in reciprocal (Q) space. This practice is

followed because the diffraction data are displayed in Q space and, owing to Bragg's law, the position and intensity of the Bragg peaks can be directly related to the periodic structure. We, on the other hand, live in real space, and most of us cannot operate effectively in reciprocal space except for well trained crystallographers. Furthermore, crystallographic intuition may not be useful in dealing with disordered systems. Thus there is much to be gained by transposing the data to real space before analysis. The idea of real-space analysis is to carry out the data analysis completely in real space by Fourier-transforming the diffraction data, including both the Bragg and diffuse scattering intensities, into a PDF as described below and fitting it to the model in real space.

The pulsed neutron diffraction measurement is carried out with a powder sample that is uniformly and isotropically packed in a container, usually made of vanadium or aluminum. The data are collected in the time-of-flight (TOF) method. The TOF gives the velocity of the neutron, and thus the value of Q for elastic scattering. The first step of the analysis is to subtract the background intensity from the measured intensity. This requires an accurate measurement of the true background, as discussed below. Then corrections are made for absorption, multiple scattering, spectrum of the incident beam, and inelastic scattering (Plazcek correction [5]) to obtain the normalized structure function S(Q) that approaches unity at the large-Q limit.

The PDF is obtained by the Fourier-transformation of S(Q) [2, 3]:

$$\rho_0 g(r) = \rho_0 + \frac{1}{2\pi^2 r} \int_0^\infty [S(Q) - 1] \sin(Qr) Q \, dQ \tag{1}$$

where ρ_0 is the number density of the sample. The PDF, $\rho_0 g(r)$, describes the probability of finding a pair of atoms at a separation r. The integration limits in Eq. (1) should theoretically be from 0 to ∞. However, because of the Debye–Waller factor S(Q) approaches unity at large Q. Thus S(Q)−1 becomes sufficiently small at large enough values of Q, and the integration can be terminated there. A premature termination results in spurious oscillations, called the termination error. The error in S(Q), $\Delta S(Q)$, can be propagated to the PDF by

$$\Delta g(r) = \frac{1}{2\pi^2 r \rho_0} \left[\sum_v [\Delta S(Q_v) \sin(Q_v r) Q_v \, dQ_v]^2 \right]^{1/2} \tag{2}$$

where v indexes the data points [4]. Note that the summation in Eq. (2) is nearly independent of r, so that the error actually decreases as 1/r. Thus, contrary to common belief, the PDF is more accurate at large distances.

The process of measurement for the PDF analysis is very similar to that for the usual powder diffraction analysis. The main differences from the conventional powder diffraction experiments in obtaining the data are the following:

1. The diffraction data must be taken up to very high values of Q to minimize the termination errors. The recommended cutoff value of Q is $\sim 3/\langle 2u^2 \rangle^{1/2}$.

2. The definition of the background is different from that in the crystallographic analysis. In crystallographic analysis such as the Rietveld refinement, diffuse scattering from the sample is a part of the background to be removed by fitting; but in the PDF analysis it is an important, integral part of the data. The background in the PDF analysis consists purely of the unwanted scattering intensities external to the sample, such as those coming from the sample container. Therefore the background has to be *measured*, rather than *fitted*, in the process of data analysis.

In crystallographic analysis, the atomic structure of the sample is assumed to be perfectly periodic and to be specified by a finite number of parameters. Then, by measuring the position and the intensity of a sufficient number of Bragg peaks, they can be completely determined. On the other hand, if the structure is not periodic, the number of parameters required to specify the structure is 3N, where N is the number of atoms in the system, which is practically infinite. Therefore it becomes necessary to obtain as much information as reasonably attainable, by collecting the data over the entire Q space where data exist. Fortunately or unfortunately, because of the Debye–Waller factor, the data in reciprocal space attenuates with Q, so that beyond a certain limit the Q-space does not contain any meaningful data and the measurement can be terminated there. Conversely, the measurement has to be made up to a Q value high enough to make the Debye–Waller factor negligibly small. The limit of $3/\langle 2u^2 \rangle^{1/2}$ was derived from this consideration [4]. The maximum attainable Q value is determined by the wavelength of the scattering probe since $Q < 4\pi/\lambda$. Normally, a Q space up to 30–40 Å^{-1} is required for successful PDF analysis. This translates to $\lambda = 0.3$–0.4 Å, or 500–900 meV for neutrons and 30–40 keV for X-rays. Such high-energy neutrons are best obtained from pulsed spallation neutron sources that provide strong epithermal neutrons, such as the Intense Pulsed Neutron Source (IPNS) of the Argonne National Laboratory or the Lujan Center, Los Alamos Neutron Science Center (LANSCE), of the Los Alamos National Laboratory.

The second point above marks the most important difference between the PDF method and crystallographic analysis. In the crystallographic analysis, diffuse scattering intensities are discarded as background while they are fully retained in the PDF analysis. The trouble is that measuring the real background is difficult. In fact, measuring the background introduces further noise, so that superficially the PDF method suffers from more noise than the crystallographic methods. However, suffering from noise by retaining important information is obviously superior to having less noise by ignoring them. In many cases one has to worry about the sample-dependent background produced by double scattering from the sample and the environment. This background can be determined by measuring two standard samples with large and small scattering cross sections.

The coordination number, N_C, can be obtained by integrating the radial distribution function, $\rho_0 r^2 g(r)$ over the range from r_1 to r_2 that defines the nearest-neighbor peak [6]:

$$N_C = 4\pi\rho_0 \int_{r_1}^{r_2} g(r)r^2 \, dr \tag{3}$$

For a multi-element system, the total PDF is made of compositionally resolved partial PDFs:

$$g(r) = \sum_{\alpha,\beta} c_\alpha c_\beta g_{\alpha\beta}(r) \tag{4}$$

where α and β denote elements that can be determined either by isotopic substitution for neutrons or anomalous scattering for X-rays [7].

Since the PDF is obtained from powder diffraction data, it is a one-dimensional quantity averaged over all orientations of a crystal, and the orientational information is lost. It is often suggested that, in order to recover the orientational information, the PDF analysis should be extended to single-crystal diffraction. While this is true, it is extremely difficult to carry out such a measurement since $S(\mathbf{Q})$ has to be determined over the three-dimensional Q space up to large values of Q. This determination would necessitate collecting and storing a huge amount of data, easily tens or hundreds of Gbyte. However, by using an area detector, such a measurement is not out of reach and will be attempted in the near future.

2.3
Standard Samples

As an example, the S(Q) of f.c.c. Ni is shown in Fig. 2 and the PDFs of Ni and $SrTiO_3$ are shown and compared to the calculated PDF in Figs 3 and 4 [8]. The method to calculate the model PDF is explained in the next section. Ni
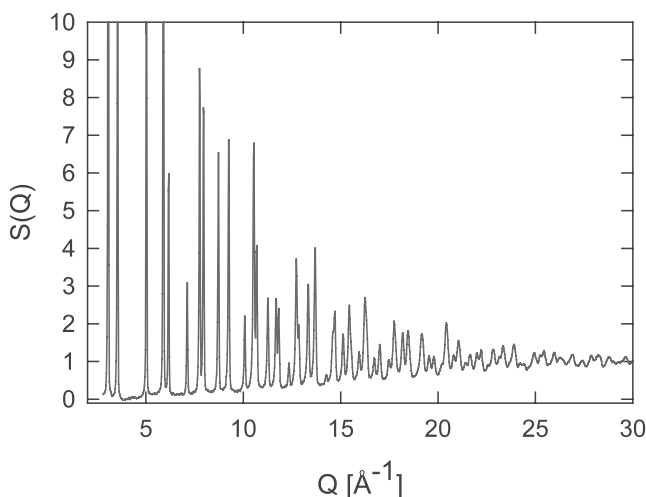
Fig. 2. Structure function S(Q) of f.c.c. Ni powder obtained by pulsed neutron scattering
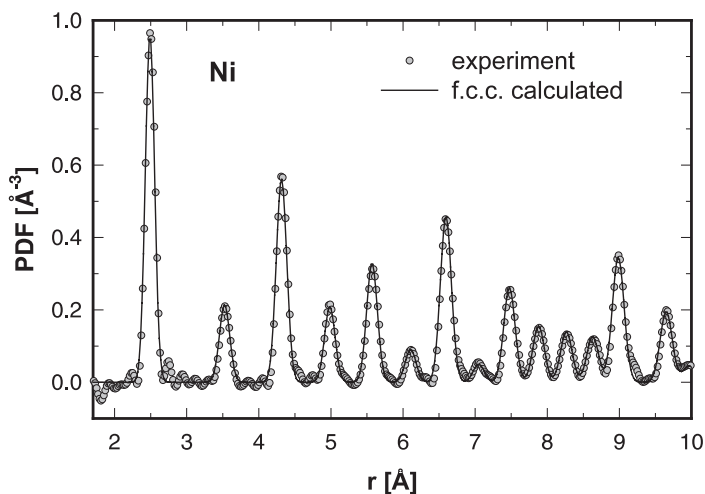
Fig. 3. Pulsed neutron PDF of polycrystalline Ni compared to the PDF of a model
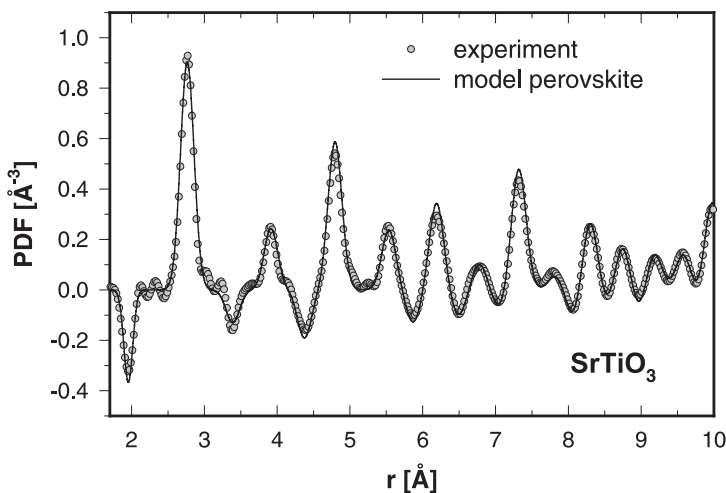
Fig. 4. Pulsed neutron PDF of polycrystalline $SrTiO_3$ compared to the calculated PDF

represents the case of a large b (b = 1.03×10^{-12} cm), while $SrTiO_3$ is a case of a relatively small $\langle b \rangle$ because of the negative b value for Ti ($\langle b \rangle = 0.420 \times 10^{-12}$ cm for $SrTiO_3$). Oscillations of the PDF seen at small values of r within the distance to the nearest neighbor are noise due to various errors. When the integration in Eq. (1) is carried out up to 30 Å^{-1}, termination errors typically represent only 1/3 of the total noise. Most of the noise is white noise in the integration in Eq. (1) and thus decreases as 1/r with increasing

distance as mentioned above. The peak position and coordination number determined by the integration in Eq. (3) are listed in Table 1.

2.4
Real-Space Modeling

The PDF of a model structure is calculated first by counting the interatomic distances in the model:

$$g(\mathbf{r}) = \frac{1}{4\pi r^2 N} \sum_{i,j} \delta(\mathbf{r} - |\mathbf{r_i} - \mathbf{r_j}|) \tag{5}$$

where $\mathbf{r_i}$ and $\mathbf{r_j}$ are the positions of the i-th and j-th atoms. This will be convoluted by a Gaussian function to describe the atomic vibration, $\exp(-(r - r')^2/2\sigma_{ij}^2)$, where

$$\sigma_{ij}^2 = \left\langle (u_i - u_j)^2 \right\rangle = \left\langle u_i^2 \right\rangle + \left\langle u_j^2 \right\rangle - 2\langle u_i u_j \rangle \tag{6}$$

and u_i and u_j are the vibrational amplitudes of the i-th and j-th atoms in the direction parallel to the vector between them. This process is similar to using the Debye–Waller approximation, but unlike the DW approximation it is possible to include atomic correlations. Since close neighbor atoms tend to vibrate in phase, usually for close neighbors $\langle u_i u_j \rangle > 0$ and consequently σ_{ij} is small. It is actually possible to determine the phonon dispersion knowing the value of $\langle u_i u_j \rangle$ for various pairs [9]. In the modeling, different values of σ_{ij} should, in principle, be used for each pair, but in practice it is often sufficient to use just a few values, for instance for the nearest neighbors and beyond.

The agreement between the model and experimental PDFs can be evaluated by the agreement factor A defined by

$$A^2 = \int_{r_1}^{r_2} \frac{\left[g_{exp}(r) - g_{mod}(r) \right]^2 dr}{\int_{r_1}^{r_2} dr} \tag{7}$$

Table 1. Atomic distance and number of neighbors in Ni and $SrTiO_3$ determined from the PDF analysis compared to the expected values [8]

Compound	Coordination shell	Peak position [Å]		Number of neighbors	
		Expected	Measured	Expected	Measured
Ni	First	2.49	2.49	12	11.995
	Second	3.53	3.53	6	6.022
	Third	4.32	4.32	24	23.875
	Fourth	4.98	4.98	12	11.974
	Fifth	5.57	5.57	24	23.818
$SrTiO_3$	First (Ti—O)	1.95	1.95	6	5.97
	Second (O—O, Sr—O)	2.77	2.77	36	36.87

where r_1 and r_2 define the range over which the structural refinement is made. This agreement factor is equivalent to the R factor in crystallographic analysis [10]. The structural model can be improved by minimizing the A-factor, usually by the steepest decent method or the Monte-Carlo simulated annealing procedure. In the latter, a small random change in the structure is applied, resulting in a change in the A factor of ΔA, and the change will be adopted with the probability

$$f = \frac{1}{e^{\Delta A/kT} + 1} \tag{8}$$

where T represents a fictitious temperature used in the modeling and controls the rate of convergence.

For crystalline $PbZrO_3$, which has tetragonal (*Imma*) symmetry and 40 atoms per unit cell, the real-space refinement method resulted in a practically identical structure as the Rietveld method did [11] (Fig. 5). The only difference was that the thermal parameter of Pb refined by the PDF method was appreciably smaller and more realistic than that by the Rietveld method. Thus for a perfectly periodic system, the PDF method is at least equivalent to the Rietveld method. While it is obviously more convenient to use the Rietveld method for determining the lattice constants, the atomic position within the
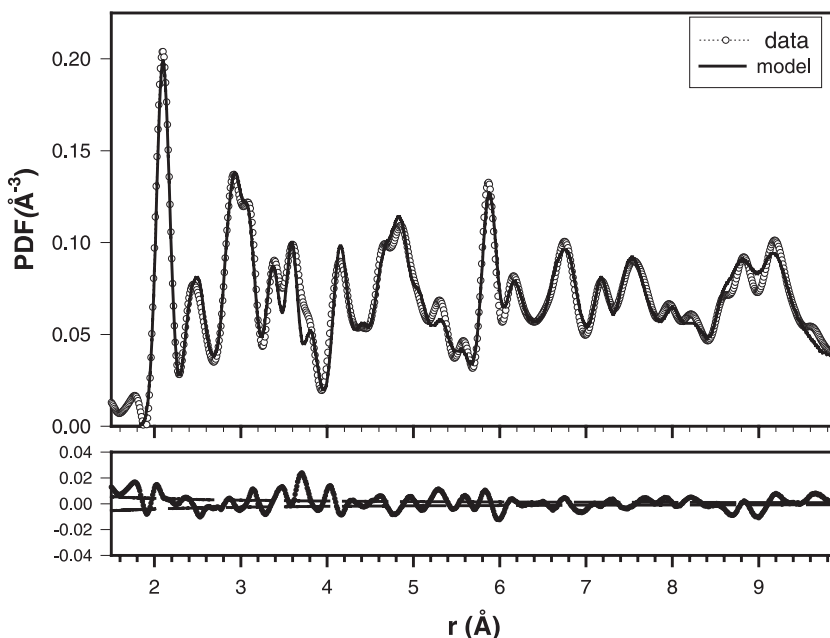
Fig. 5. The pulsed neutron PDF of $PbZrO_3$ compared to the model PDF refined by the real-space method [11]. The lower inset shows the difference between the experimental and model PDFs and the error ($\pm\sigma$) of the PDF due to statistical noise

unit cell of a complex material may well be better determined by the PDF method. If the system is disordered, only the PDF method can distinguish the local structure from the average structure. Usually the PDF at large values of r is well fitted with the average structure determined by the Rietveld method, but deviations are seen at short distances. By carrying out the modeling of the PDF for different ranges of distances, it is possible to determine the short-, medium- and long-range structure separately.

A typical process of modeling crystalline solids with disorder is as follows [10]:

1. Carry out the Rietveld analysis to determine the average long-range crystal structure.
2. Calculate the PDF based upon the result of the Rietveld analysis.
3. Observe differences between the experimentally determined PDF and the Rietveld-derived PDF.
4. Model the short-range local structure, typically below 5 Å, usually with a lower symmetry.
5. Determine the spatial extension (correlation length) of the local structure, by modeling the PDF over various sections, for instance, 0–10 Å, 10–20 Å, etc.

If the local structure deviates from the average structure, the crystal symmetry is usually broken and the symmetry is lowered. For instance, the local symmetry may be rhombohedral or tetragonal; but if the direction of the axes vary randomly from site to site, the system would appear cubic as a whole. Then, even though the crystal structure is cubic, the solid would have many properties reflecting the lower local symmetry, such as the mixing of the Raman and IR active modes and non-cubic crystal-field effects. Many high-symmetry solids are of this type as we will see later.

3
CMR Manganites

3.1
Background

In the manganites $(R_{1-x}A_x)_{n+1}Mn_nO_{3n+1}$ (R = La, Pr, or Nd, A = Sr, Ba, Ca, or Pb), a colossal magnetoresistive (CMR) behavior is observed near the ferromagnetic transition temperature, T_C [12–14], as is discussed in detail in other chapters of this book. This effect is most pronounced in the compositional range in which T_C changes rapidly as hole doping (x) is increased, or as the average atomic radius of the A-site ions (rare earth and alkali ions), $\langle r_A \rangle$, is increased [13–15]. The two phase diagrams, where T_C is plotted against x [16] or $\langle r_A \rangle$ [15], appear similar. Understanding the physics behind such phase diagrams is a major step toward understanding the CMR phenomenon itself.

The electronic mechanism to produce a ferromagnetic metallic phase in manganites was discussed long ago by Zener [17], Goodenough [18],

Hasegawa and Anderson [19], and de Gennes [20] in terms of the double-exchange (DE) mechanism. Parallel Mn spins make it easy for doped holes to hop from site to site, so that if there is a sufficient density of doped holes, their contribution wins over the superexchange interaction, converting the system to a ferromagnetic metal. Recently, however, Millis et al. [21] pointed out that the DE interaction is insufficient to explain the details of the electrical resistivity; it yields too small a magnitude and a wrong temperature dependence. They suggested that strong electron-lattice interactions provide the missing resistivity via polaron formation. Various direct and indirect experimental methods have been mobilized to test this prediction; they have successfully confirmed the spatially inhomogeneous nature of the spin and charge states that could be interpreted in terms of spin-lattice polarons in the insulating phase [22–32]. The PDF analysis played a major role in this process and also provided further insight into the physics of CMR phenomenon [8, 22, 32].

The central question is how and why localized doped holes become suddenly delocalized by a modest applied magnetic field. In the paramagnetic insulating phase, doped holes are localized as spin-lattice polarons; they become more delocalized as polarons become unstable at the metal-insulator (M-I) transition. The sharper this transition, the more dramatic is the CMR effect, since a small magnetic field can create a large change in the conduction mechanism. Thus the polaron stability is at the heart of the problem. Another crucial question is the nature of the interaction among the charges. A repulsive interaction (coulomb interaction) leads to charge ordering, while an attractive interaction (DE interaction, elastic interaction) results in phase segregation. Experimentally, charge ordering in the insulator phase has been observed [33]; in the metallic phase a tendency for phase segregation appears to exist. Thus, the balance between the repulsive and attractive forces must be very delicate.

Currently the standard explanation of the ionic-size effect on polaron stability is that as the atomic size $\langle r_A \rangle$ is reduced, and the electron bandwidth is decreased because of the increased bending of the Mn—O—Mn bond, leading to the formation of polarons and localization of holes [9, 21]. However, the reduction in the bandwidth estimated from the bond angle is very small [24, 33]. Furthermore, recent data indicate that even as the value of $\langle r_A \rangle$ is reduced, the spin-wave stiffness is unchanged [34]. Since the spin-wave stiffness is related to the exchange constant and the bandwidth, this explanation of the relation between $\langle r_A \rangle$ and x through the bandwidth is much in doubt. Recently we proposed an alternative explanation involving the structural dependence of the elastic energy to form polarons that controls the stability of the lattice polarons [35]. This concept is based upon knowledge of the local atomic structure of the solids determined by the PDF analysis of the pulsed neutron powder diffraction data. In this section we first summarize some experimental results and then discuss the stability of the polarons. Finally, a brief discussion is given on the nature of the mutual interaction and self-organization of the charges.

3.2
Perovskite La$_{1-x}$A$_x$MnO$_3$

3.2.1
Crystallographic Data

In LaMnO$_3$ the Mn ion is trivalent with four electrons in the d-shell that are fully spin-polarized due to the strong Hund coupling. The nearly cubic crystal-field splits the d-level into t$_{2g}$ (triplet) and e$_g$ (doublet) levels. The four electrons fill the triplet t$_{2g}$ level and singly occupy the doublet e$_g$ orbital. This promotes the splitting of the doubly-degenerate e$_g$ level into two by the Jahn–Teller (JT) distortion, which elongates the MnO$_6$ octahedra and splits the Mn—O bond lengths into four short (1.92 Å and 2.05 Å) and two long (2.16 Å) bonds. Consequently nearly stoichiometric LaMnO$_3$ is an antiferromagnetic insulator and has the monoclinic ($P2_{1/c}$) or orthorhombic (*Pnma*) structure, depending upon a slight change in oxygen stoichiometry [36–38]. In this structure, the occupied e$_g$ orbital, and thus the axis of the JT distortion, is oriented in the *a-b* plane with alternating directions ("antiferromagnetic" orbital ordering). With excess of oxygen, which creates vacancies at the cation sites, the structure changes to rhombohedral R$\bar{3}$ symmetry. With the replacement of La by a divalent ion such as A = Ca, Sr, Ba, and Pb, the JT distortion in the crystal lattice becomes progressively smaller. The orbital ordering is lost with about 12% doping, rendering the system an orbital-glass with an orthorhombic structure [39]. With about 16% of doping, the JT distortion in the lattice disappears and the structure becomes rhombohedral [40]. La$_{1/2}$A$_{1/2}$MnO$_3$ is a charge ordered compound that is an antiferromagnetic insulator [41]. If the doping exceeds 50%, the system remains an antiferromagnetic insulator with occasional charge ordering being observed at rational values of the amount of doping [33].

Millis et al. [21] suggested that the evidence of lattice involvement in charge transport may be observed in the Debye–Waller (DW) factor. Indeed Dai et al. [25] reported an anomalous temperature dependence of the DW factor and concluded that polarons must be formed. However, the evidence provided by the DW factor is qualitative as we discussed earlier. The DW approximation assumes a harmonic (Gaussian) distribution of atomic displacements. If only a small number of atoms deviate significantly from the average positions, the DW approximation greatly underestimates the actual displacements.

3.2.2
Local Structure and Lattice Polarons

In mixed-ion oxides such as La$_{1-x}$A$_x$MnO$_3$, the local structure is expected to deviate from the average because of the ionic size difference between La and A. In addition, if charges are localized as polarons, the atomic environment inside and outside of the polarons would be appreciably different. The local structure

of this system was studied by the XAFS method by several groups [26, 27, 42, 43]. In the XAFS experiment, the split in the Mn—O bond lengths due to the JT distortion can be detected only by modeling since the intrinsic peak broadening of the PDF due to the lifetime effect of the photoelectrons is significant. This photoelectron effect introduces an ambiguity that is model dependent. Consequently the amount of split reported by the XAFS measurements varied widely, from 0.1 Å [27] to 0.5 Å [26]. However, the results of the XAFS studies on the Mn—O distances could be semi-quantitatively correct. For instance, the observation of a correlation between the split in the Mn—O distances deduced from the XAFS results and the magnetization [43] is important since it demonstrates directly the connection between the structure and magnetism. However, the logarithmic relation found between them in [43] could be the result of Debye–Waller distortion, and the true relationship could well be linear.

A more direct determination of the local structure was made by Billinge et al. [22] with the pulsed neutron PDF method. They studied the temperature dependence of the PDF for $La_{1-x}Ca_xMnO_3$ and noted that the peak height at 2.75 Å changes anomalously with temperature as shown in Fig. 6. Below T_C, the height of this peak rises much more sharply with decreasing temperature for the samples with x = 0.2 and 0.3 than is expected from the normal thermal effect.

This peak in part includes the O—O distances in the MnO_6 octahedra. Without the JT distortion, each octahedron has 12 O—O bonds that are 2.8 Å long; with the JT distortion, 8 of them become 3.0 Å long. Consequently the PDF peak height is reduced where there are local JT distortions. Thus their results are consistent with having polarons above T_C that are annihilated below T_C.

Billinge et al., however, assumed that their polarons are of the conventional breathing type where anions are attracted isotropically toward a hole. On the other hand, Louca et al. [8, 31, 32] showed that the nature of the polarons is closely connected to the local JT distortion. The PDF of $LaMnO_3$ (Fig. 7) has a negative peak at 1.97 Å with a shoulder at 2.2 Å. This peak represents the Mn—O distances and is negative because the neutron scattering length b of Mn is negative. They showed for the $La_{1-x}Sr_xMnO_3$ that the positions of these first two sub-peaks of the PDF are nearly independent of the amount of hole doping, x, as shown in Fig. 8. Thus locally the JT distortion remains unchanged in magnitude while the average JT distortion decreases sharply with composition. In particular, the local JT distortions are found even in the rhombohedral phase where all the Mn—O distances are equal in the crystal structure as shown in Fig. 9. This discrepancy between the local and average structure can be explained only with the loss of alignment of the local JT distortions and the local orbital moments. If the local JT distortions and orbital moments are randomly oriented in all x, y, and z directions with equal proportions (orbital paramagnetism), the local distortions cancel each other and the total JT distortion is absent. In this way the decreasing JT distortion in the average structure can be explained by the gradual loss of JT or orbital order with hole concentration.
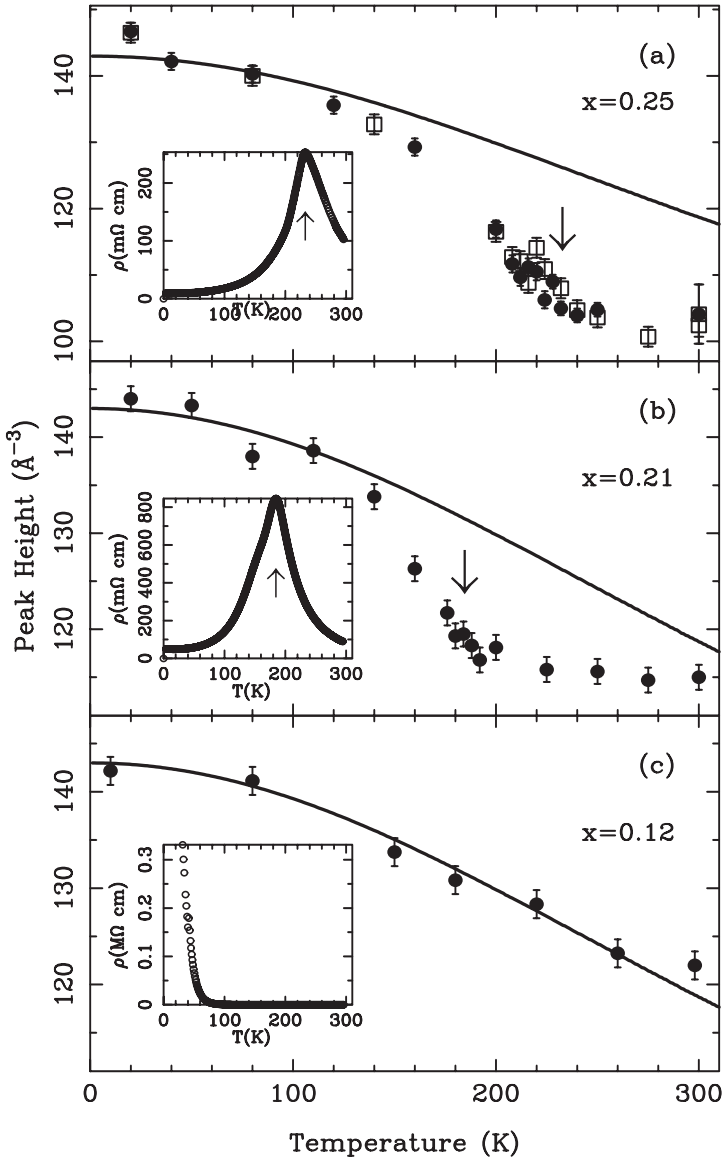
Fig. 6. Temperature dependence of the PDF peak height at 2.75 Å for $La_{1-x}Ca_xMnO_3$ compared to the expected temperature dependence (*solid line*) [22]. Anomalous depression near and above T_C indicates formation of lattice polarons

While hole doping does not change the Mn—O peak positions, their intensity is modified by doping. The JT-distorted MnO_6 octahedron of a Mn^{3+} has four short ($\sim$1.97 Å) and two long ($\sim$2.2 Å) Mn—O bonds while that of Mn^{4+} without the JT distortion has six short Mn—O bonds. Thus, by counting
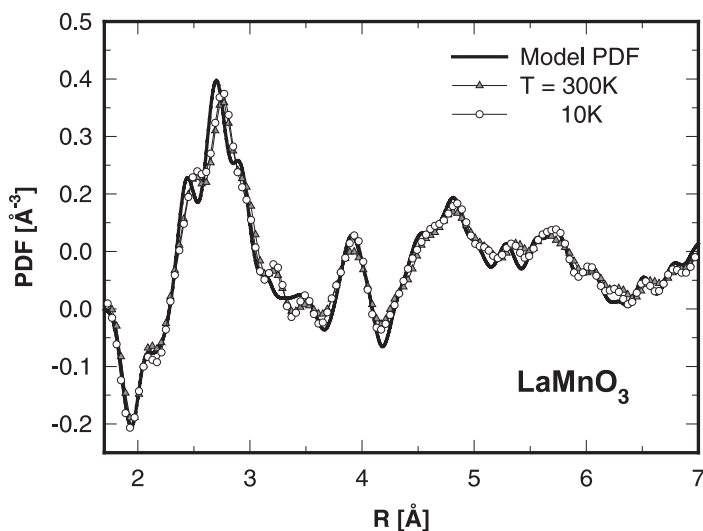
Fig. 7. Pulsed neutron PDF of LaMnO$_3$ compared to the model PDF calculated for the crystal structure [32]
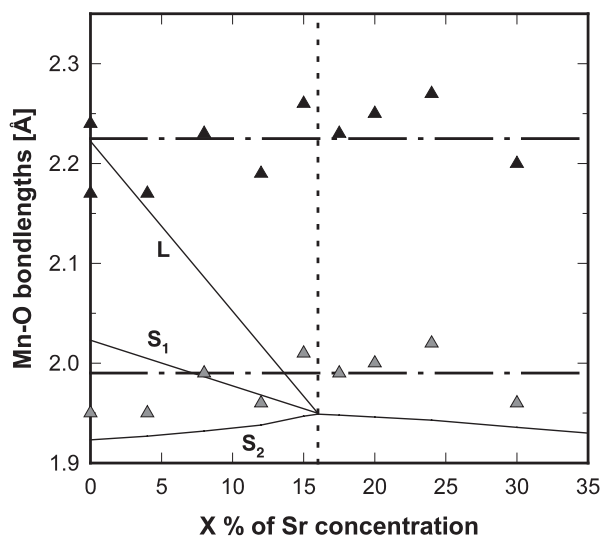
Fig. 8. The positions of the first two sub-peaks of the PDF for La$_{1-x}$Sr$_x$MnO$_3$ as a function of x at T = 10 K, compared to the Mn—O bond lengths determined from the crystal structure [32]

the number of short bonds per Mn ion, the number of Mn sites with a JT distortion can be determined. This can be done with Eq. (3) by integrating the first sub-peak of the PDF. The second sub-peak overlaps with the La—O peak at 2.56 Å, and its area cannot be reliably assessed. Figure 10 shows such data
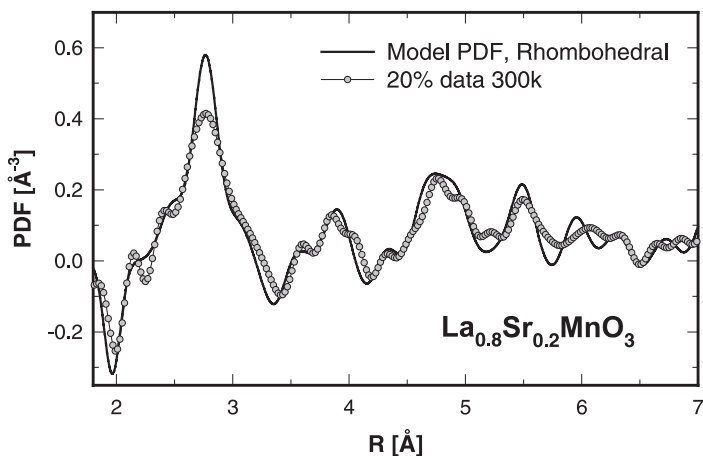
Fig. 9. The PDF of $La_{0.8}Sr_{0.2}MnO_3$ compared to the model PDF calculated for the average crystal structure [8]. Note that the experimental PDF has a sub-peak around 2.2 Å, but the calculated PDF does not. Furthermore the peak of the model PDF at 2.75 Å is much taller than the corresponding peak of the experimental PDF
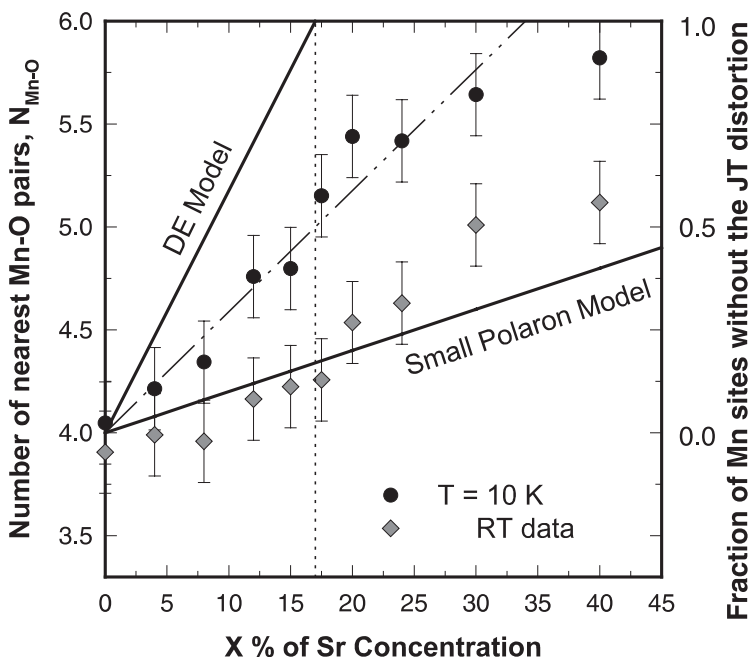
Fig. 10. The number of short Mn—O bonds per Mn ion for $La_{1-x}Sr_xMnO_3$ determined by integrating the PDF, as a function of x for T = 10 K and 300 K (above T_C), except for x = 0.2 (320 K), 0.24, 0.3 (350 K). The line named small polaron line connects $N_{Mn—O} = 4$ for x = 0 and $N_{Mn—O} = 6$ for x = 1 [32]

[32], where $N_{Mn-O} = 4$ corresponds to the state where every site has the local JT-distortion as in Mn^{3+}, and 6 to all sites without the JT-distortion as in Mn^{4+}. The fraction of the Mn sites without the local JT-distortion can be defined as $X_{aJT} = (N_{Mn-O} - 4)/2$, shown as the right hand scale of Fig. 10. At room temperature, the data lie on the straight line connecting $N_{Mn-O} = 4$, or $X_{aJT} = 0$, for x = 0, and $N_{Mn-O} = 6$, or $X_{aJT} = 1$, for x = 1 (small polaron line), representing the mixture of Mn^{3+} and Mn^{4+}. In other words, above T_C the charge is localized on one Mn site, forming a small single-site polaron. This is the most direct evidence of the polaron represented by the local absence of the JT distortion. We may call this an anti-JT polaron.

It should be noted that the results in Fig. 10 alone would not be enough to differentiate the Mn-centered polaron from the oxygen-centered polaron as envisaged by Zener [17]. However, in $LaMnO_3$ the filled z^2 orbitals of neighboring Mn ions are oriented perpendicular to each other because of the antiferromagnetic orbital ordering. Thus, these two orbitals cannot resonate through an oxygen ion as in the Zener polaron, except at high charge densities where the orbital ordering ceases.

At T = 10 K, the data of N_{Mn-O} are well above the small-polaron line. It extrapolates to 6 at x $\sim$ 0.35, with the slope about three times that of the small-polaron line. It indicates that on average each hole kills a JT distortion at three Mn sites; a polaron is extended over three sites. This could be a consequence of antiferromagnetic spin correlation. If three spins are antiferromagnetically coupled ($\uparrow\downarrow\uparrow$) by flipping the central spin they will become ferromagnetically aligned ($\uparrow\uparrow\uparrow$), allowing a hole to move easily through the three sites. Thus a polaron would become extended over three sites. It is interesting to note that N_{Mn-O} is continuous through the metal-insulator (M-I) transition at x = 0.16, and is substantially below 6 even in the metallic phase up to x $\sim$ 0.35. The implications of this finding will be discussed later.

As the temperature is increased, N_{Mn-O} decreases continuously as shown in Fig. 11. This observation implies that the total volume over which the local JT distortion is suppressed becomes reduced as the polarons become more localized. The PDF peak height at 2.75 Å follows this closely since it also quantifies the same thing. Thus, the results in Fig. 11 provide a clear explanation of the observation in Fig. 6 in terms of the temperature dependence of the fraction of JT-distorted sites.

3.3
Layered $La_{2-x}Sr_{1+x}Mn_2O_7$

Among the perovskite-related layered manganites $(La/A)_{n+1}Mn_nO_{3n+1}$, known as the Ruddlesden–Popper phases, the n = 2 and n = ∞ (perovskite) compounds show the CMR phenomenon while the n = 1 compound is insulating [44, 45]. The two-layered (n = 2) manganite, $La_{2-2x}Sr_{1+2x}Mn_2O_7$ or equivalently $(La_{1-x}Sr_xMnO_3)_2SrO$, is made of two layers of perovskite structure and a single rock-salt layer of SrO. The perovskite layer has an almost cubic structure and shows a very small average JT distortion at low temperatures [46]. For instance in perovskite $R_{Mn-O}(long) - R_{Mn-O}(short)$ it is $\sim$0.2 Å,
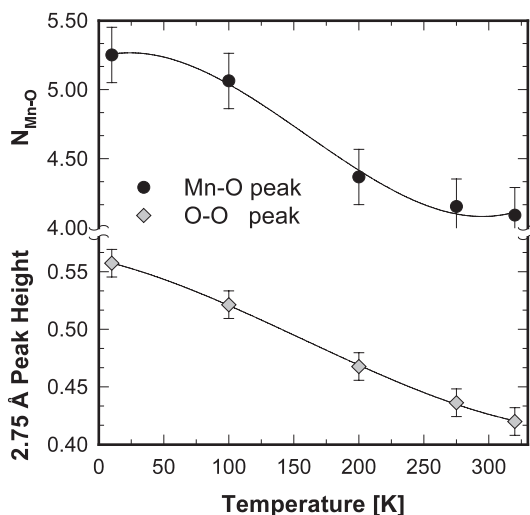
Fig. 11. Temperature dependence of the number of short Mn—O bonds per Mn site (*above*) and the PDF peak height at 2.75 Å (*below*) for $La_{0.825}Sr_{0.175}MnO_3$ [8]

while in $La_{1.2}Sr_{1.8}Mn_2O_7$ it is only 0.024 Å. This observation appears to suggest that a very different mechanism is at work. However, the pulsed-neutron PDF determined by Louca et al. [47] shows that, locally, the MnO_6 octahedra are JT distorted in a way very similar to that of the perovskite manganites. Figure 12 compares the PDF of the two-layered compound ($La_{1.2}Sr_{1.8}Mn_2O_7$) with that of
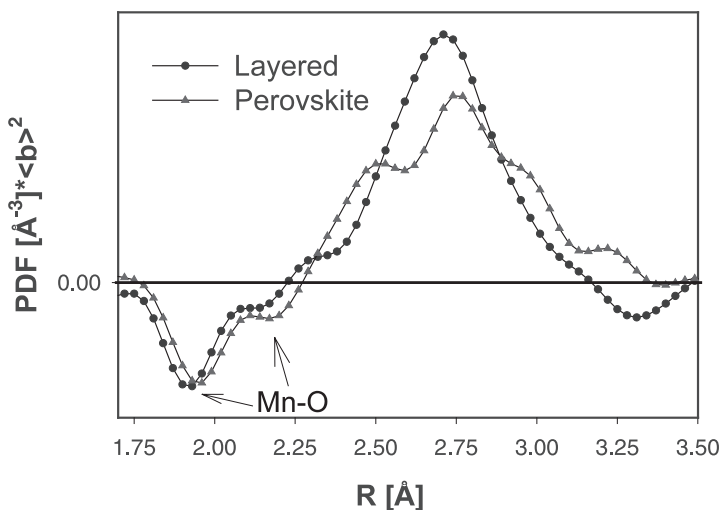
Fig. 12. The PDF of $La_{1.6}Sr_{1.4}Mn_2O_7$ compared to the PDF of $LaMnO_3$. In order to compare the intensity of the Mn—O peak correctly the PDFs are multiplied through $\langle b^2 \rangle$ [47]

the perovskite $LaMnO_3$. The shape of the Mn—O peak is very similar between the two. This means that many of the Mn ions are locally JT distorted in the layered compounds in the same way as in the perovskites.

Then why are the local JT distortions not reflected to the average crystal structure? The answer clearly is the ionic size effect. The ionic radii of La and Sr are 1.36 Å and 1.44 Å [48], so that in $La_{1.2}Sr_{1.8}Mn_2O_7$ the average distance between the A-site ions (La, Sr) and oxygen is $R_{AO} = 2.808$ Å. In the crystal structure of $La_{1.2}Sr_{1.8}Mn_2O_7$ the A-site ions form a rock-salt type sheet. If one tries to match the MnO_2 layer to the AO rock-salt layer, the Mn—Mn distance should be $\sqrt{2}R_{AO} = 3.972$ Å. As Fig. 12 shows in this compound the Mn—O distances in the JT distorted MnO_6 octahedron are $R_{Mn—O}(short) = 1.92$ Å and $R_{Mn—O}(long) = 2.12$ Å. Thus if the axes of the JT distorted octahedra are aligned, the Mn—Mn distance should be $2 \times R_{Mn—O}(short) = 3.82$ Å, and would not fit the AO rock-salt layer. On the other hand if the axes of the JT distortion are not aligned and pointing in the x, y, and z directions equally, the average Mn—Mn distance would be $(4/3) R_{Mn—O}(short) + (2/3)R_{Mn—O}(long)$ $= 3.972$ Å, which happens to be the ideal distance to match the AO rock-salt layer. For this reason $La_{1.2}Sr_{1.8}Mn_2O_7$ has almost no JT distortion in the average structure.

It is also noteworthy that $N_{Mn—O}$, determined in the same way as in the perovskite, changes completely smoothly through T_C (=117 K) and, instead, shows anomalous changes around 250 K, as shown in Fig. 13. The measurement of spin excitation indicates that the magnitude of the exchange constant within the perovskite layer is similar to that in the three-dimensional perovskite [49], which suggests that a strong two-dimensional ferromagnetic correlation develops well above T_C. It is thus possible that the conduction
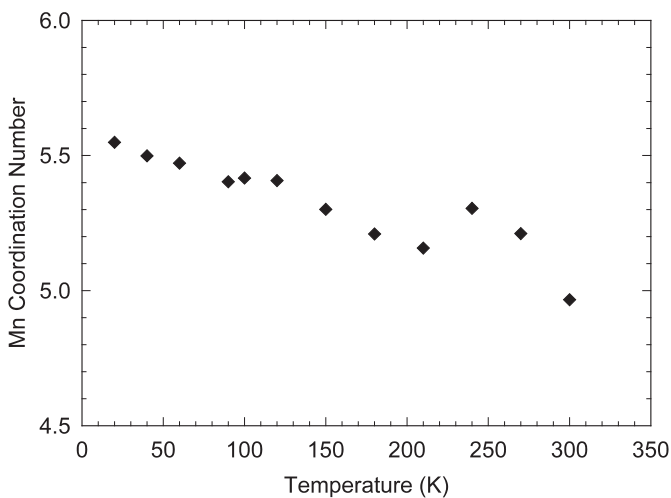
Fig. 13. Temperature dependence of the number of short Mn—O bonds in $La_{1.6}Sr_{1.4}Mn_2O_7$ [47]. Note that the data are continuous through T_C (=117 K)

paths made of Mn sites without the local JT distortion are already formed above T_C, but show no overall metallic conduction because of the poor c-axis conduction. The temperature of 250 K, which is similar to the T_C of the three-dimensional perovskite, may signal the onset of such two-dimensional ferromagnetic correlation.

3.4
Polaron Stability and Local Structure

As mentioned above, at the heart of the CMR physics is the question of the stability of the polarons. We will now turn to this question and demonstrate how the knowledge of the local structure helps to elucidate the phenomenon. While the CMR phenomenon in manganites is complex, involving magnetic and orbital ordering, in this discussion we focus on the electron-lattice interaction alone to simplify the argument. Within this scope, the stability of lattice polarons is dictated by the competition between the kinetic energy that tends to *delocalize* the carrier and the electron-lattice coupling that tends to *localize* it. The electron-lattice (Jahn–Teller) energy is [21, 50]

$$H^{JT} = -g \sum_i q_i n_i + \frac{K}{2} \sum_i q_i^2 \tag{9}$$

where q_i is the ionic displacement parameter and n_i is the excess charge density of the i-th ion; g characterizes the strength of the electron-lattice coupling and K is the elastic modulus. Minimizing H^{JT} with respect to q gives

$$H^{JT} = \sum_i \left[\frac{K}{2} \left(q_i - \frac{g n_i}{K} \right)^2 - \frac{g^2 n_i^2}{2K} \right] \tag{10}$$

Thus the polaron binding energy is given by

$$E_{JT} = -\langle H^{JT} \rangle / N = \frac{g^2 \langle n^2 \rangle}{2K} - \frac{K}{2} \langle u^2 \rangle \tag{11}$$

where $u = q - \langle q \rangle$, and $\langle q \rangle$ is the JT displacement = $g\langle n \rangle / K$. This competes against the double-exchange energy, which can be simplified in the limit of the strong Hund coupling as

$$H^{DE} = -t \sum_{\langle i,j \rangle \sigma} \sigma_{ij} \left(c_{i\sigma}^+ c_{j\sigma} + c_{j\sigma}^+ c_{i\sigma} \right) \tag{12}$$

where summation is made for the interacting neighbors, σ denotes spin, and σ_{ij} describes the spin correlation between i-th and j-th spins which is proportional to $\cos(\theta/2)$, where θ is the angle the spins S_i and S_j make. The critical parameter for polaron formation is [21, 50]

$$\lambda = \frac{g^2}{Kt \cos(\theta/2)} \tag{13}$$

By simulation, it is known that $\lambda = \lambda_C \sim 1$ marks the crossover point; where $\lambda_C > 1$, polarons are stable. Usually one focuses on the structure dependence

of **t** through the bending of the Mn—O—Mn bond. However, K can also be structure-dependent, and in our view this is much more important [35].

The structure dependence of K comes not from the dependence of the elastic constant itself on the ionic radius of the A-site ion, which is small, but from the change in the phonon mode associated with the polaron. Thus the *relevant* elastic constant changes greatly with the structure. When $LaMnO_3$ is doped with a divalent ion, and thus with a hole, an anti-JT polaron is created as shown above. At the polaron site, the two long Mn—O bonds of the JT-distorted MnO_6 octahedron are shortened to become two short Mn—O bonds. If the Mn—O—Mn bond is straight, this local bond contraction produces tensile strains in the bonds nearby, where Mn—O bonds have to be stretched (*longitudinal* accommodation, Fig. 14a). On the other hand, if the Mn—O—Mn bond is strongly buckled, the local bond contraction can be accommodated by straightening the buckled bond (*transverse* accommodation, Fig. 14b). Thus the phonon mode involved in the polaron changes with the amount of bond bending or buckling, which is determined by the ionic size of the A-site ion. Now the energy for longitudinal accommodation is high, since the Mn—O bond is a very strong bond and stretching it is costly in energy, while the transverse accommodation is far less costly in energy. Therefore the effective elastic constant K depends strongly on the ionic size, and becomes much reduced as the size of the A-site ion is reduced. Since the energy cost of stretching the Mn—O bond is so high that we may assume that the polarons will not be produced at all if the longitudinal accommodation is involved. A similar argument was used successfully in explaining the polarons in linear chain compounds that show Peierls distortion [51].

The condition for the crossover from longitudinal to transverse accommodation can be readily derived based upon the knowledge of the local structure. In $LaMnO_3$, the Mn—O—Mn bond in the plane is made of a combination of

(a)   (b)
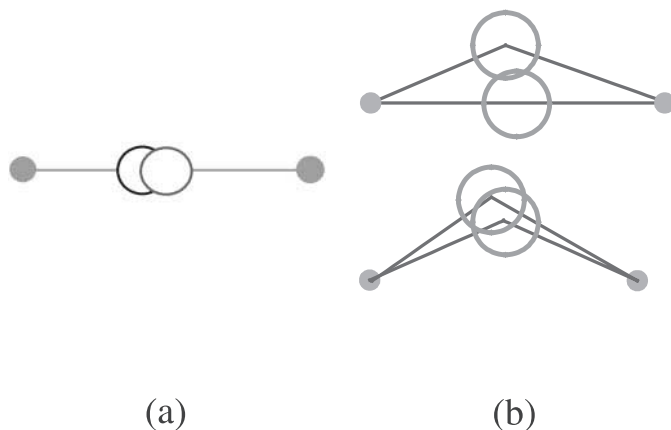
Fig. 14. a Longitudinal accommodation of the strain to eliminate the JT distortion locally when the Mn—O—Mn bond is straight. **b** Transverse accommodation when the Mn—O—Mn bond is buckled [35]

long and short Mn—O bonds. When a polaron is created, the long bond becomes a short bond, and the Mn—O—Mn bond is made of two short Mn—O bonds. The lattice has to be able to accommodate this shortened Mn—O—Mn bond. If we define the tolerance factor as

$$\tau = \frac{R_{A-O}}{\sqrt{2}\, R_{Mn-O}} \qquad (14)$$

where R_{A-O} and R_{Mn-O} are the distances between the A-site ion and oxygen and between Mn and oxygen, respectively; the crossover condition is that $\tau = 1$ for the shortened Mn—O—Mn bond. If τ is larger than unity, the Mn—O bonds *within the polaron* in $La_{1-x}A_xMnO_3$ are in tension. From Fig. 8 we obtain $R_{Mn-O} = 1.97$ Å, and thus $R_{A-O} = 2.786$ Å for $\tau = 1$. Since the covalent radius of oxygen is 1.40 Å [48], the crossover condition is that

$$\langle r_A \rangle_{CR} = 1.386 \text{ Å} \qquad (15)$$

This value is larger than the 12-coordinated ionic radii of La (1.36 Å) and Ca (1.34 Å), but is smaller than the ionic radius of Sr (1.44 Å) [48]. Thus the La—Sr system will cross this boundary at x = 0.325 while the La—Ca system will never cross this boundary at any value of x. Note that we use the 12-coordinated ionic radii, while some in the field (for instance [15]) use the 9-coordinated ionic radii. In our argument we start from the ideal, undeformed perovskite, and ask whether the structure is stable or not. That is why the 12-coordinated ionic radii are used here.

On the other hand, if the radius of the A-site ion is too small, the polaron will become too stable, and the system will become an antiferromagnetic or ferromagnetic insulator. The condition for such high stability can be determined from the data for the $La_{0.7-x}(Pr/Y)_xCa_{0.3}MnO_3$ system [16]. If the radius of the A-site ion is below 1.34 Å, the system is a ferromagnetic insulator. Thus, if $\langle r_A \rangle$ is greater than 1.386 Å, the polarons will not form and we have a homogeneous regular metal. If $\langle r_A \rangle$ is smaller than 1.34 Å, we have an insulator. In the crossover regime

$$1.34 \text{ Å} < \langle r_A \rangle < 1.386 \text{ Å} \qquad (16)$$

the polarons are marginally stable and are influenced easily by external factors such as the applied magnetic field, producing the CMR phenomena.

It should be noted that this argument on the upper limit of the ionic size requires no adjustable parameter, and the critical ionic size is obtained directly from the observed Mn—O bond length. The prevailing theory based upon the band narrowing, on the other hand, cannot give the ionic size that corresponds to the critical value of λ without numerical calculations.

This argument explains quite well the dependence of T_C on the A-site ion size observed by Hwang et al. [15] and reproduced in Fig. 15. The value of T_C declines sharply when the A-site ionic radius $\langle r_A \rangle$ becomes smaller than 1.25 Å $(La_{0.7}Sr_{0.3})$, and saturates at 1.18 Å $(Pr_{0.7}Ca_{0.3})$. Here Hwang et al. used the 9-coordinated ionic radius, and in our definition they correspond to 1.39 Å and 1.34 Å, respectively. Above $\langle r_A \rangle = 1.386$ Å the system is metallic and T_C

Fig. 15. The Curie temperature of $A_{0.7}A'_{0.3}MnO_3$ system. $\langle r_A \rangle$ is the average ionic radius of the A-site ions in the 9-coordination [15]

changes only gradually with the ionic radius. Below $\langle r_A \rangle = 1.34$ Å the system is insulating and the charges are localized as polarons. Where T_C changes rapidly with $\langle r_A \rangle$, the system is marginally stable. Thus external stimuli, such as the applied magnetic field, can strongly influence the system, creating the CMR effect.

The discussion so far assumed hole doping into $LaMnO_3$. If we start from the other side, $AMnO_3$, and replace A with a trivalent ion, the situation is very different. In this case we are doping an electron that produces a local JT distortion and a JT-polaron in the matrix that is free of the JT distortion. Since the local JT distortion increases the Mn—O bond length, which can easily be accommodated by buckling the Mn—O—Mn bond, a JT polaron is always stable. Thus the system is always an insulator for x > 0.5, resulting in the asymmetry between the hole doping and electron doping. In this case, polarons often order forming a polaron lattice, or charge ordering, at doping levels that are rational fractions.

It is instructive to consider the phase diagram shown in Fig. 16 that was constructed according to the discussion above [35]. Here the axes are $\langle r_A \rangle$ and the concentration of the divalent ions, x. First of all, this phase diagram is asymmetric, since the x field greater than 0.5 (electron doping) is always insulating. Also, at small doping levels of holes, the system is insulating due to localization as discussed later. The CMR phenomenon is expected to be observed only in the crossover region indicated in the diagram. The polaron stability increases as $\langle r_A \rangle$ is reduced, including the crossover region. This phase diagram is in excellent agreement with the experimental phase diagram

Fig. 16. Phase diagram of the ionic radius of the A-site ion vs the concentration of the divalent ion, x. The CMR behavior is observed in the crossover regime where polarons are marginally stable and are influenced easily by external forces [35]

shown in Fig. 17 [14] if we note that the radius of La (1.34 Å in Fig. 16) corresponds to the covalent radius of 1.7 Å in Fig. 17.

Fig. 17 suggests that the value of T_C is strongly suppressed near x = 0.5, and the constant T_C line is not horizontal. This is most likely related to the tendency of charge ordering [32, 41]. The configuration of orbital moments at x = 0.5 includes alternating long-short and short-short Mn—O bond combinations; and for this pattern to be stable, the short-short Mn—O bond combination has to be either free of strain or bent, but not in tension. This agrees with the crossover condition above (Eq. 14) and suggests that charge ordering at x = 0.5 will not take place when $\langle r_A \rangle$ is larger than $\langle r_A \rangle_{CR}$. However, where the value of $\langle r_A \rangle$ is reduced below this value, charge ordering will take place, localizing the carriers and depressing or eliminating T_C. Where the value of x is close to 0.5, apparently charges still can order locally, thus pulling down T_C. This tendency is clearly shown in the experimental result of Fig. 18. Thus a theory of a finer scale has to be developed to account for the actual values of T_C within the crossover regime in Fig. 16.

Another phenomenon worth mentioning here is the isotope effect [29]. It is particularly interesting that the sample with ^{18}O has a lower T_C than that with ^{16}O, and the difference increases with a decreasing A-site ionic size. Usually ^{18}O
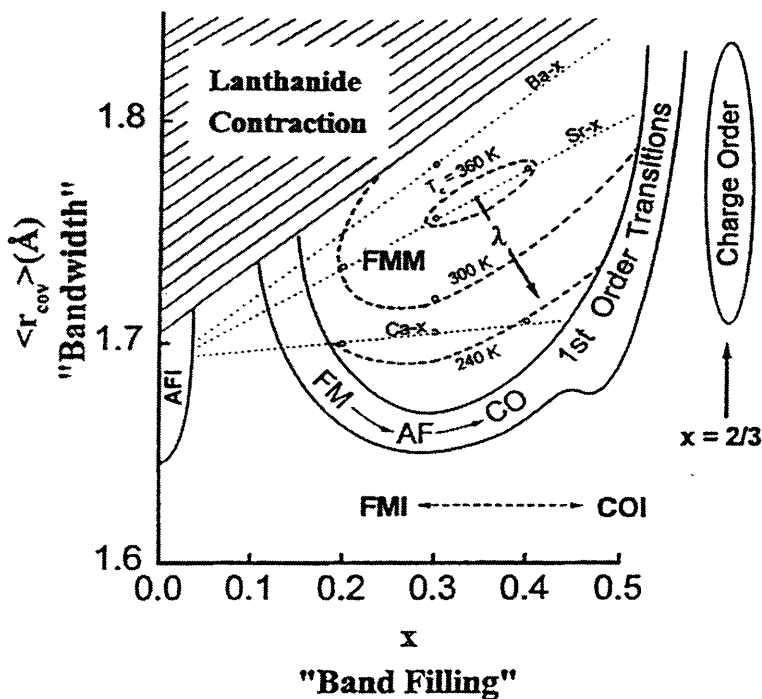
Fig. 17. The experimentally determined diagram of T_C as a function of the "covalent radius" representing $\langle r_A \rangle$ and the hole density, x [14]. This phase diagram corresponds well to Fig. 16 if the vertical axis is rescaled so that the position of La (1.34 Å in Fig. 16 and 1.7 Å in Fig. 17) is adjusted accordingly

has a smaller vibrational amplitude than ^{16}O does, resulting in a smaller zero-point vibrational energy (the second term in Eq. 11) and a larger polaron binding energy. Thus polarons should be more stable, lowering the value of T_C. This is more convincing evidence of the polaron formation in this system. The dependence on the size of the A-site ion may be explained in the following way. When the vibrational amplitude $\langle u^2 \rangle$ is reduced, the A—O distance becomes shorter due to anharmonic effects, increasing the amount of buckling. This will increase the stability of the polarons in the line of argument above, and the effect is more pronounced if the A-site ionic radius is close to the critical value. This will explain the dependence of the isotope effect on the ionic radius.

3.5
Lattice Involvement in Metal-Insulator Transition and CMR Effect

3.5.1
Metal-Insulator Transition as a Function of Charge Density at Low Temperatures

As shown in Fig. 10, the data for $N_{Mn—O}$ as a function of doping, x, are continuous through the M-I transition, and the value of $N_{Mn—O}$ is significantly
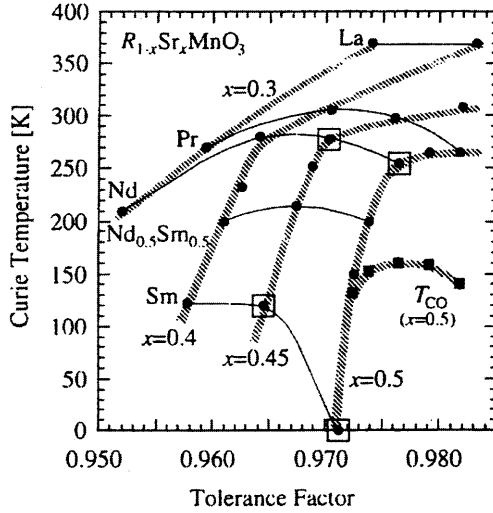
Fig. 18. Curie temperature of $R_{1-x}Sr_xMnO_3$ system as a function of the A-site atomic size expressed in terms of the tolerance factor [52]. At x = 0.5 as the size decreases T_C is quickly suppressed below t = 0.976 ($Nd_{0.5}Sr_{0.5}MnO_3$) which corresponds to $\langle r_A \rangle$ = 1.384 Å in our definition (XII coordination)

below 6 even in the metallic phase up to x $\sim$ 0.35 [8, 32]. A similar result was also obtained recently for the La—Ca system [53]. Since it is now well established that the carriers form polarons in the insulating phase, these data appear to indicate that the polarons survive in the metallic phase. This, however, is a very strange notion since the tendency of localization by forming polarons and metallic conductivity are not mutually compatible. Usually the high dielectric constant of the metallic phase reduces the polaron binding energy and delocalizes the carriers.

Part of the answer to this conundrum came from the knowledge of the lattice dynamics. The pulsed neutron powder diffraction spectrometer used in determining the PDF does not have an explicit energy discrimination mechanism, but has an effective energy transfer window of about 20 meV. This is because of the special neutron dynamics involving the so-called Placzek shift. If the energy transfer of neutron scattering is large, the true momentum transfer differs significantly from the assigned momentum transfer calculated assuming elastic scattering. This difference is the Placzek shift. For elastic scattering the magnitude of Q is given by

$$Q = 2k\sin\theta \tag{17}$$

where k is the momentum of the neutron. For inelastic scattering, however,

$$Q = \sqrt{k_i^2 + k_f^2 - 2k_ik_f\cos 2\theta} \tag{18}$$

where k_i and k_f are the initial and final momenta of the neutron in the scattering process. If $k_i = k_f$, Eq. (18) is reduced to Eq. (17). In the TOF

measurement, only the average velocity of the neutron is measured. Since for most of the TOF spectrometers the primary path from the source to the sample is much longer than the secondary path from the sample to the detector, k_i may be approximated by the average momentum:

$$k_i \approx k = m\frac{L}{\hbar\tau} \tag{19}$$

where m is the neutron mass, L is the total flight path length, and τ is the time of flight. The energy transfer in the scattering is

$$\hbar\omega = \frac{\hbar^2}{2m}\left(k_i^2 - k_f^2\right) \approx -\frac{\hbar^2}{m}\,k\Delta k \tag{20}$$

where $\Delta k = k_f - k_i$. Thus Eq. (18) becomes

$$Q = 2\,k\sin\theta\left(1 - \frac{m\omega}{\hbar k^2} + \cdots\right) = 2\,k\sin\theta\left(1 - \frac{4\,m\omega\sin^2\theta}{\hbar Q^2} + \cdots\right) \tag{21}$$

which represents the Placzek shift. If this shift is caused by phonons, the effect can be corrected by the process proposed by Placzek [5]. On the other hand, if it is caused by local lattice vibrations and the magnitude of the energy transfer is 10–20 meV, the shift depends upon the scattering angle and the calculated PDF varies irregularly with the detector angle [54] as shown in Fig. 19 [8]. If the energy transfer is much smaller, the PDF is independent of the detector angle as shown in Fig. 20 [8]. If the energy transfer is larger, the scattering information is lost during the Fourier-transform process.

It was found that the variation in the PDF with the detector angle was appreciable only for x = 0.15, less for x = 0.175, and insignificant for other compositions [8]. Thus, the local lattice vibration associated with the local JT-
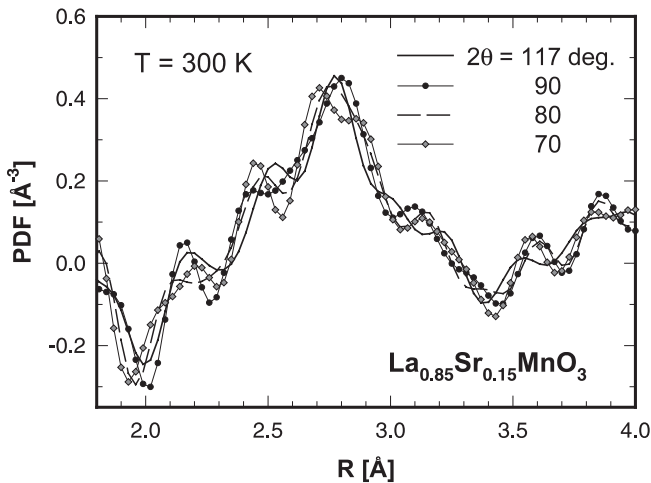
Fig. 19. The dependence of the PDF on the detector angle for $La_{0.85}Sr_{0.15}MnO_3$ at T = 10 K. The PDF was calculated with the detectors up to the detector angle shown [8]
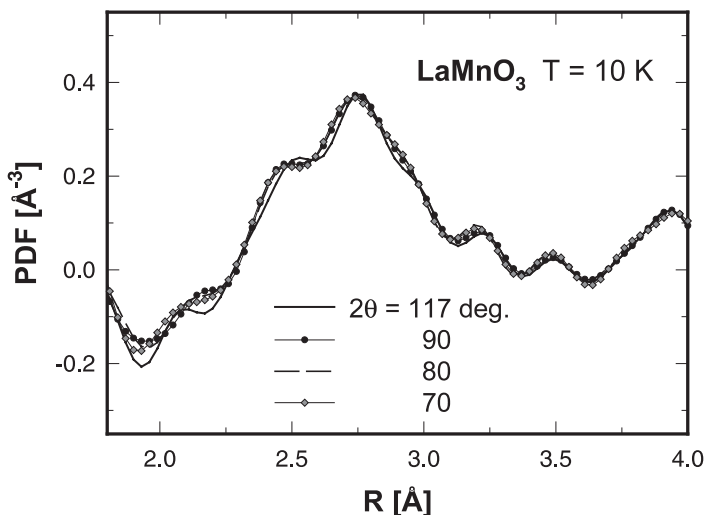
Fig. 20. The dependence of the PDF on the detector angle for $LaMnO_3$ at T = 10 K. Virtually no angle dependence is seen [8]

distortion is in the range of 10–20 meV *only in the close vicinity of the M-I transition*; it is slower at compositions above or below the M-I transition. Since the conductivity increases by many orders of magnitude at the M-I transition, we have to conclude from this observation that in the metallic phase the dynamics of the local distortions are decoupled from the dynamics of charge carriers and are not following them. Then the carriers are no longer trapped by the local distortion and they are not in the polaronic state anymore (Fig. 21). The local lattice distortion in such a state does not follow an individual carrier any more, but responds to the charge density fluctuations which have much slower dynamics.

A *percolative* picture emerges from these results [8, 30, 32, 35, 55, 56]. As the density of polarons is increased, they start to become in contact. If the polarons are single-site polarons, charges will remain localized even if two polarons are in contact because of the high coulomb repulsion to place two carriers on the same site (Hubbard U). However, if the polarons are more extended over several sites, as is the case for $(La/Sr)MnO_3$ shown above, charge carriers will become mobile within the connected network of the polarons. If the size of the network of the connected polarons reaches a macroscopic scale, metallic conduction commences. At the M-I transition the number of short Mn—O bonds is about 5, as shown in Fig. 10, indicating that the volume fraction of the undistorted, metallic sites is 50%. This is consistent with the percolation in a two-dimensional square lattice [57].

In this picture the carriers in the connected pathways are not localized, but flow through the channels within which the JT distortion is locally suppressed. In-between the channels, however, the JT distortion is locally alive, the charge density is low, and conductivity is very low. We may call these regions
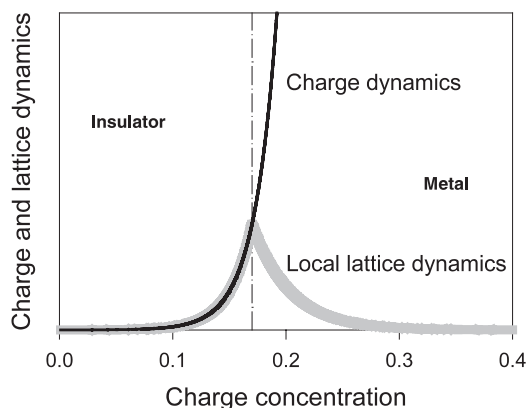
Fig. 21. Schematic diagram of the dynamics of the lattice and charge as a function of the charge concentration, x. As x is increased the polaron dynamics accelerates, but at the M-I transition (x = 0.175) they become decoupled, and the lattice dynamics slows down

"insulating" islands. This picture is consistent with the phase segregation model [58–60] and the "two-fluid" model [61, 62]. The detailed state of the conducting pathways in the metallic phase remains controversial and will be discussed later. The magnetic coupling within the islands could either be antiferromagnetic or ferromagnetic, depending upon details of geometry and temperature. In particular, if the orbital moments are ordered in the zig-zag manner as in the layers of $LaMnO_3$, the superexchange interaction is ferromagnetic. Since the metallic samples are reported to be fully magnetized at low temperatures [63], ferromagnetic interaction appears to win over the antiferromagnetic interaction.

This picture explains quite well the observed antiferromagnetic fluctuation near T_C [41, 48], the central peak in spin excitation [64], strong spin wave softening and damping [65, 66], relatively low conductivity [39], smeared Fermi edge [67], and small thermopower [61, 62, 68]. In particular the ARPES studies show that the electronic dispersion is well defined only up to about 1 eV below the Fermi level, and near the Fermi level it becomes totally smeared [67]. This smearing could be evidence of scattering by the split e_g levels. Where the JT distortion is locally present, the e_g level should be locally split and the potential locally lowered by $\Delta/2 = 0.7$ eV. This distortion will scatter electrons within $\Delta/2$ from the Fermi surface, as is observed.

3.5.2
Metal-Insulator Transition at T_C

It is interesting to note that the local lattice behavior near T_C is fundamentally different between the perovskite and the layered compounds. In the perovskites the density of the Mn sites with the local JT distortion changes sharply at T_C indicating rapid changes in the volume of metallic conduction

(Figs. 1 and 11). The magnetic transition is achieved by a catastrophic collapse of polarons into a metallic volume, indicating that the nature of the transition is of the first-order. On the other hand, in the layered compound the density of the Mn sites with the JT distortion changes smoothly through T_C (Fig. 10), just as in the case of the metal-insulator transition as a function of x (Fig. 13). The magnetic transition is achieved by coherence of spin and local JT distortion, or in other words orbital ordering, while the metallic volume changes continuously. This is indicative of a second-order transition.

3.5.2.1
Perovskite

As temperature is decreased through T_C in the perovskite, the fraction of the volume in which the JT distortion is suppressed, $X_{aJT} = (N_{Mn—O} − 4)/2$, is increased sharply as shown in Fig. 11. This increase must be indicating partial, but not total, delocalization of the carriers through the DE interaction. Indeed, an increase in conductivity is accompanied by the increase in X_{aJT} as indicated in Fig. 6 in terms of the PDF peak height at 2.75 Å. Thus, it is expected that the volume without the local JT distortion is metallic and ferromagnetic since the DE interaction should be dominant there. The sharp change in the conducting volume at T_C must be indicative of a first-order phase transition, as suggested by the temperature dependence of the magnetization [13, 14]. However, X_{aJT} remains less than unity except at T = 0 for x > 0.35 for $La_{1−x}Sr_xMnO_3$ (Figs. 10 and 11), leading to a two-phase picture and the percolative view of the transport phenomena [8, 30, 32, 35, 55, 56, 58–62, 68, 69]. Details of the morphology of the two phases require a separate discussion given below.

3.5.2.2
Layered Compound

The temperature dependence of X_{aJT} of the perovskite through T_C is in strong contrast to the behavior of $N_{Mn—O}$, and thus of X_{aJT}, through the M-I transition as shown in Fig. 10 and that of $La_{1.4}Sr_{1.6}Mn_2O_7$ as shown in Fig. 13. In $La_{1.4}Sr_{1.6}Mn_2O_7$, the metallic volume changes smoothly through T_C while the lattice constant undergoes a discontinuous change. Such behavior is typical of an order/disorder-type second-order ferroelastic phase transition in which the local units of distortion that are randomly oriented at high temperatures become aligned at T_C [70]. At high temperatures (>250 K), the axis of distortion of MnO_6 octahedra is randomly oriented, and carriers appear to be in the single-site polaronic state. Below 250 K carriers become more delocalized, resulting in two-dimensional local metallic islands. The presence of strong in-plane spin correlation above T_C and the absence of its divergence at T_C support this view [71]. These islands are not fully connected, and c-axis conduction is very poor. Consequently conductivity is low even in the a-b plane. At T_C, the local JT distortions (orbital moments) start to align along the c-axis, and three-dimensional metallic conduction commences. For that

reason it is possible that the driving force for this transition is not only the spin correlation, but the orbital ordering as well.

It is not quite clear whether the local JT distortion in the layered compounds is the same as in the perovskite, producing an elongated octahedron with four short and two long Mn—O bonds, or different, resulting in a pyramid with five short and one long M—O bonds. The axial symmetry of the layered compounds appears to prefer the second. However, the magnitude of the local JT distortion is as large as the one in the perovskite. Note that the total JT distortion is an order of magnitude smaller than the local JT distortion even at low temperatures. As was discussed above this implies that the local JT distortions are nearly randomly oriented. Almost 2/3 of the local JT distortions are in the plane, with the distortion along the *c*-axis slightly exceeding 1/3. Thus the total symmetry is not as important as it might appear, and it is most likely that the local chemistry produces an environment very similar to that in the perovskite, with two long and four short M—O bonds around an Mn^{3+} ion. In this scenario, the local M-I transition within the plane takes place around 250 K where the number of short Mn—O bonds is about 5.0 (Fig. 13), which is consistent with the density of the JT-distorted sites at T_C for the perovskite as shown in Fig. 10. Thus the transition around 250 K must be percolative, while the transition at T_C is due to the three-dimensional ordering of the spin and orbital moment.

3.5.3
Spatial Distribution of Charge Carriers

As we have shown above, the metallic state just above the critical charge density for the M-I transition is in a two-phase state. It has not been clear, however, how these two phases are mixed in space. One extreme is totally random distribution, while the other extreme is macroscopic phase separation. The second is very unlikely because of the hefty electrostatic energy price for charge segregation. The spatial distribution of charge carriers depends upon the interaction among them. A repulsive interaction leads to a charge ordered (CO) state, while an attractive interaction results in a phase segregated (PS) state. If the interaction is very weak or absent the spatial distribution will be random. The coulomb repulsion is the main component of the repulsive interaction, while the DE interaction and the elastic interaction provide an attractive force.

The CO state has been observed for various rational values of x, typically for x = 0.5 [33, 72], forming stripes of charges [73]. The structure of $La_{1/2}Ca_{1/2}MnO_3$ [74, 75] indicates that the ordered charges are in the polaron lattice state. It should be noted, however, that in real samples the degree of charge ordering is less than perfect, possibly disturbed by the distribution of La and Ca ions. Thus the distortion of the MnO_6 octahedra in the average structure [74] is much smaller than that of the real local structure. The PDF measurement [75] suggests the magnitude of the JT distortion is again as large as in the undoped $LaMnO_3$. The CO state can be disrupted by the application of electric or magnetic fields resulting in a metallic state [76], indicating that

the CO state is only marginally stable. Interestingly, the stability increases as $\langle r_A \rangle$ decreases [76, 77], as expected from the preceding discussion.

The presence of the CO state suggests that the repulsive interaction among the charges is considerable. At the same time the marginal stability of the CO state indicates that the repulsive and attractive forces among the charges are nearly balanced. This argues against the possibility of large-scale phase separation. Large ferromagnetic droplets were detected by small angle neutron scattering [78] which is often cited as the evidence of large-scale phase segregation. However, in the presence of orbital ordering, superexchange is positive as observed in the plane of $LaMnO_3$. Thus the size of the ferromagnetic droplets does not necessarily correspond to the size of the charge segregation region.

It is instructive to compare the PDF of $La_{0.8}Sr_{0.2}MnO_3$ [20%] and that of $La_{0.6}Sr_{0.4}MnO_3$ [40%] at $T = 10$ K as shown in Fig. 22. Here the r-axis of the 40% sample is scaled by 0.6% so that the lattice constants of the two samples match. At $T = 10$ K the 40% sample is metallic without JT distortion whereas some local JT distortions are left in the 20% sample. Indeed the PDF of the
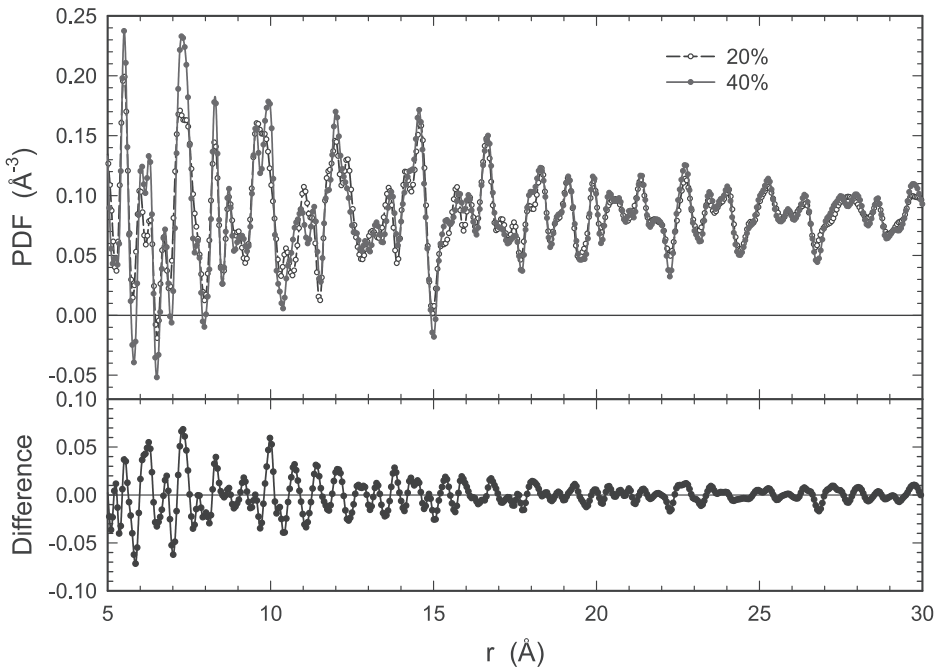
Fig. 22. The PDF of $La_{1-x}Sr_xMnO_3$ ($x = 0.2$, 0.4) determined by pulsed neutron scattering. The r-axis of the PDF of 40% sample is scaled by 0.6% so that the lattice constants match. The difference after scaling (*below*) shows that the two structures are very similar in the length-scale larger than 15 Å. Thus the local JT distortions in the 20% sample are uncorrelated beyond 15 Å, suggesting that the charge correlation length may be of the order of 15 Å

40% sample is very close to the PDF calculated for the average crystal structure, while that of the 20% sample deviates considerably from the PDF of the average structure. The two experimental PDFs in Fig. 22 differ considerably at short distances, while the difference becomes smaller beyond about 15 Å, and falls to the level of noise. This observation implies that the local JT distortions in the 20% sample are uncorrelated in orientation and magnitude beyond $3 \sim 4$ times the lattice constant, a. Should the phase segregation exist, this length-scale of 15 Å must be the correlation length of the two phases. For three-dimensional correlation, this correlation domain includes only $30 \sim 60$ Mn ions, and in two-dimensions only 15 Mn ions. Such an object can barely be called a phase. This result suggests that the large-scale charge segregation is highly unlikely in this system, mainly because of the electrostatic repulsion effect. On the other hand, the correlation length of 15 Å is not short either, suggesting that the polarons self-organize themselves locally to some extent. For instance, the strong correlation at 5.5 Å ($= \sqrt{2}a$) indicates a local short-range ordering of orbital moments in the 20% sample. It is also interesting to note that the correlation length of 15 Å is close to the periodicity of the charge stripes expected for this composition. It is possible that the charges are ordered in the short range into local stripes.

4
Ferroelectric Oxides

Ferroelectric oxides are another class of materials for which the knowledge of the local structure has played a major role in understanding the properties of solids. In particular, the pulsed neutron PDF has shown that the local structure of relaxor ferroelectric oxides such as $Pb(Mg_{1/3}Nb_{2/3})O_3$ (PMN) is completely different from the average structure, and demonstrated that their properties cannot be explained without a detailed knowledge of the local structure.

4.1
Antiferroelectric $PbZrO_3$ (PZ) and Ferroelectric $Pb(Zr_{1-x}Ti_x)O_3$ (PZT)

As mentioned earlier, the structure of PZ at low temperature was determined consistently both by the Q-space method (the Rietveld refinement) and the real-space method (PDF refinement) [11]. However, as the temperature is increased, local disorder develops, and thus the real-space method becomes more advantageous. As shown in Fig. 23, the changes in the PDF with temperature are not uniform with respect to interatomic distances, some peaks changing much more than others [11]. The real-space analysis shows that the displacement of Pb ions along the c-axis becomes very anharmonic, developing a double-well potential with increasing temperature. This displacement results in locally correlated fluctuations along the c-axis, which explains the observed high c-axis permittivity [79]. The real-space analysis also succeeded in determining the structure of the intermediate phase that appears over the very narrow temperature range of 501–510 K [11].
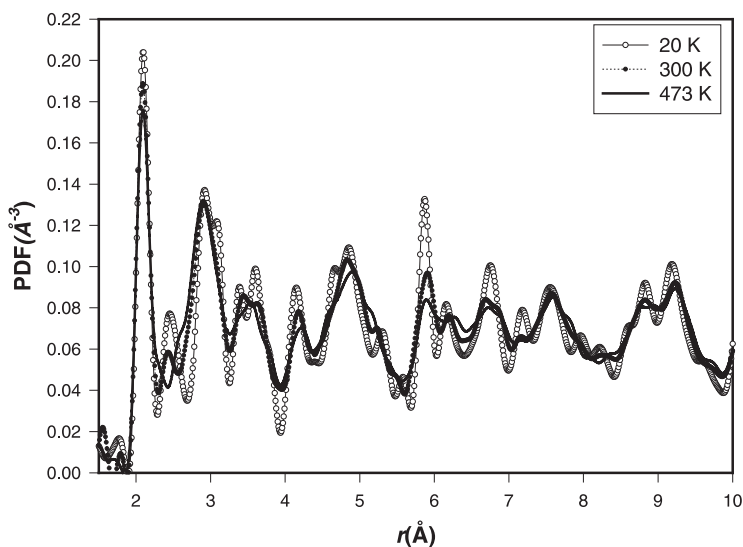
Fig. 23. Pulsed neutron PDF of PbZrO$_3$ at various temperatures. Note that the temperature dependence is not uniform, with some peaks changing more with temperature than others

It is interesting that the PDF hardly changes through the antiferroelectric transition at 501 K [11]. This appears to suggest that the system is already polarized at the atomic level even above the transition temperature, and the phase transition merely brings about the long-range phase coherence of the displacements. Such a picture is that of the order/disorder model. The local structures determined by the XAFS or PDF [80, 81] often appear to lend support to this model, rather than the soft-mode model, of the phase transition [70]. In the soft-mode model, the phase transition is brought about by softening of particular phonon modes. However, one has to be careful about the dynamics of measurement. If the time-scale of the measurement is shorter than the relevant soft-mode, the soft-mode appears frozen, and the system appears to be locally polarized. Since the energy scale of the EXAFS measurement is several hundreds of eV, it is a fast measurement and the local structure appears always polarized. In the case of the neutron PDF measurement, the energy scale is about 10 meV as we discussed above. If the energy of the soft-mode is below this range, as is usually the case near the transition temperature, the PDF shows local polarization. This, however, is not a disproof of the soft-mode model.

If only 5% of Zr is replaced by Ti in PZ, making it PZT, the structure changes from orthorhombic to rhombohedral and antiferroelectricity is replaced by ferroelectricity [82]. It is rather surprising that such a small amount of substitution can produce so drastic an effect. The study of the local structure by pulsed neutron PDF analysis gave an answer to this question. The situation is rather similar to the case of manganites discussed above. As shown in Fig. 24, in spite of the phase change the PDF of Pb(Zr$_{1-x}$Ti$_x$)O$_3$ changes
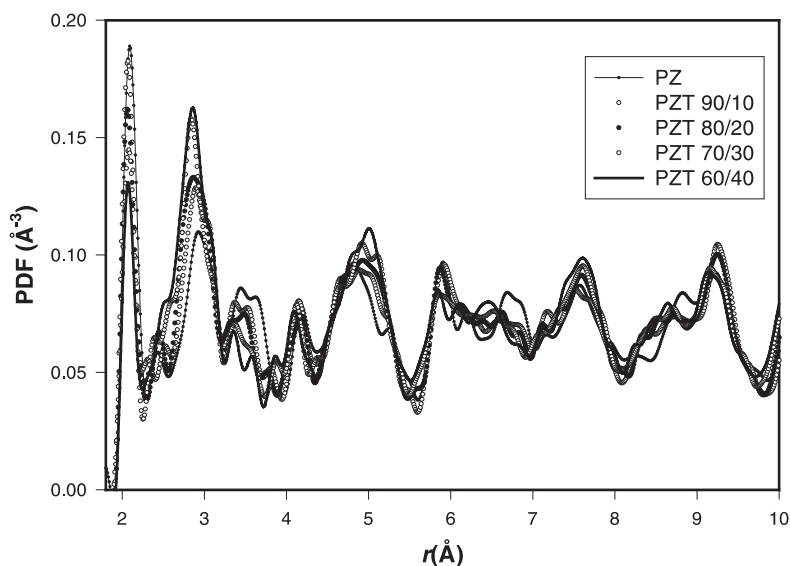
Fig. 24. Pulsed neutron PDF of $Pb(Zr_{1-x}Ti_x)O_3$ (PZT) for various Zr/Ti ratios [83]. Since Ti has a negative neutron scattering length the peak height changes with composition, but the basic position and features remain unchanged

rather little with x [82]. In other words, even where the average structure is rhombohedral locally, the structure retains the orthorhombic atomic arrangement. The rhombohedral symmetry results from averaging of local orthorhombicity with random orientation, just as the local JT distortion with random orientation resulted in the rhombohedral structure for manganites.

4.2
Relaxor Ferroelectric $Pb(Mg_{1/3}Nb_{2/3})O_3$ (PMN) and $Pb(Mg_{1/3}Ta_{2/3})O_3$-$PbZrO_3$ (PMT-PZ)

In most applications of ferroelectricity, high permittivity is the desired property. However, in regular ferroelectrics the permittivity depends strongly on temperature with a maximum at the Curie temperature. Since such a strong temperature dependence presents a major problem in application, many of the ferroelectric materials used today are relaxor ferroelectrics in which the ferroelectric transition is smeared and broad, resulting in a permittivity that changes only slowly with temperature. $Pb(Mg_{1/3}Nb_{2/3})O_3$ (PMN) is one of the most widely studied relaxor ferroelectrics [84]. Its structure is close to the ideal cubic perovskite, with Pb on the A-site and Mg/Nb on the B-site. Since Mg is divalent while Nb is pentavalent, it is difficult to imagine that Mg and Nb occupy the B-site randomly. Indeed electron diffraction detected broad, but strong, superlattice diffraction peaks of the 1/2 [111] type indicating chemical ordering into the NaCl structure on the B-sites [85]. The dark-field imaging of the superlattice diffraction peak by transmission electron microscopy (TEM) showed formation of numerous nano-domains. These nano-domains do not

grow even with annealing. It was then postulated that the superparaelectric behavior of these nano-domains results in the relaxor behavior [85].

It is interesting that this ordering into two sublattices is not readily compatible with the composition with 1/3 Mg and 2/3 Nb. It was proposed earlier that within these nano-domains, the two sublattices of the NaCl structure are taken by Mg and Nb, with the remaining matrix becoming rich in Nb. In this model, charge is not balanced within and outside the domain. The idea is that the charge imbalance prevents the domain from growing further because of the self-energy due to charging [86]. However, with the domain size approaching 50 Å, the amount of charge build-up is huge, making this model difficult to accept. Indeed, in this model a strong density fluctuation of Nb is expected, but the small-angle X-ray scattering did not detect such local compositional variations [87]. Also, it was found that the relaxor ferroelectric behavior is retained even after a similar long range chemical order has developed in a very similar system, $Pb(Mg_{1/3}Ta_{2/3})O_3$-$PbZrO_3$ (PMT-PZ) [88]. Thus, the chemically ordered nano-domains have little to do with the origin of relaxor ferroelectricity.

The pulsed-neutron PDF of PMN shown in Fig. 25 is completely different from the PDF calculated for the crystal structure [89]. In particular, the measured PDF has a prominent peak around 2.45 Å, while the model PDF has no peak in that neighborhood. It is interesting to note that the PDF of PMN strongly resembles the PDF of PZT as shown in Fig. 26 [91]. It is also similar to the PDF of PMT-PZ as shown in Fig. 27 [90]. Since the PDF of PZT resembles
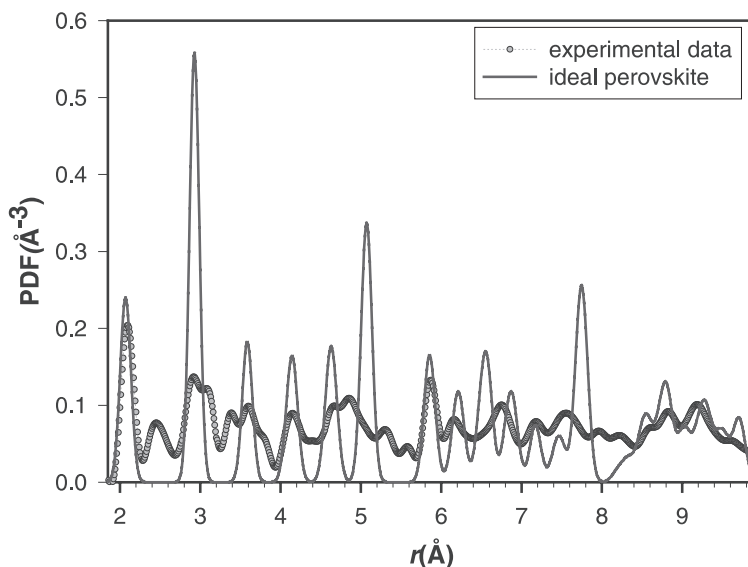
Fig. 25. Pulsed neutron PDF of $Pb(Mg_{1/3}Nb_{2/3})O_3$ (PMN) (*circles*) compared to the PDF calculated for an ideal perovskite structure (*solid line*). Except for the first peak, they differ completely, with peaks in the experimental PDF appearing at places where there is no corresponding peak in the calculated PDF, for instance at 2.45 Å [89]
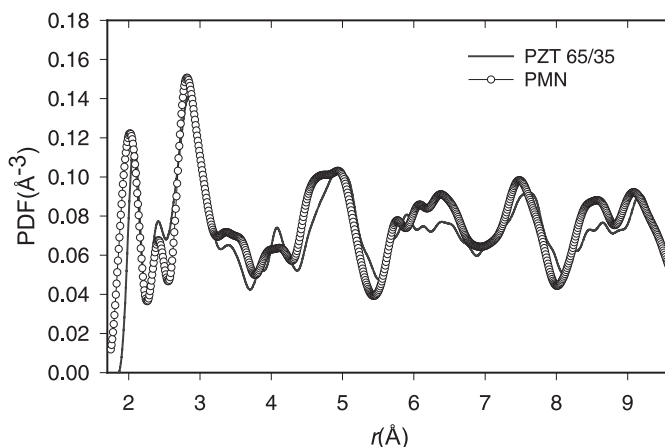
Fig. 26. Pulsed neutron PDF of PMN compared to that of PZT 65/35 [91]

the PDF of PZ having a structure that is now accurately known [11], it is possible to identify the PDF peaks by comparison. It was found that the peak at 2.45 Å is due to short Pb—O bonds that are created because of the strong off-centering of the Pb ion in the O_{12} cage by about 0.5 Å as shown in Fig. 28 [11]. Such a large displacement produces a strong dipolar moment for PbO_{12}.

Apparently this local polarization is nearly independent of composition as shown in Figs. 25–28. The system can then be described in terms of the interacting dipolar moments. Disorder comes into play via the interaction parameter and also the local potential for reorientation of the dipolar moment with random preferred axis [91, 92]. The local polarization of the PbO_{12} is
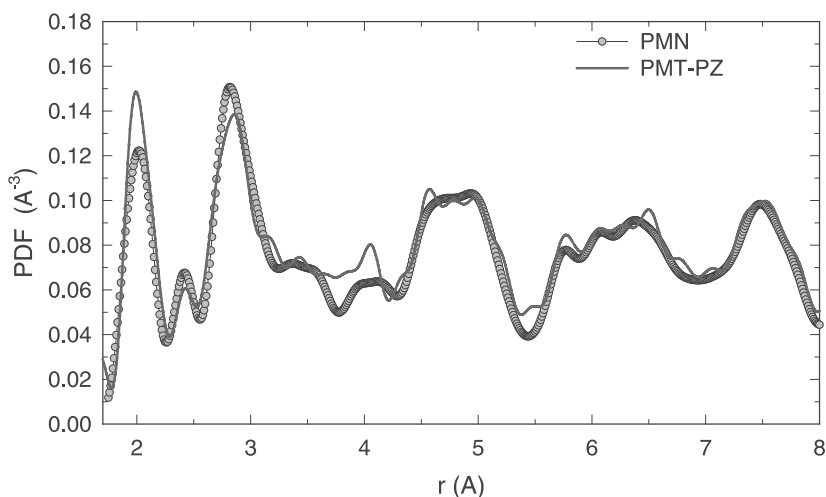
Fig. 27. Pulsed neutron PDFs of PMN and PMT-PZ [90]
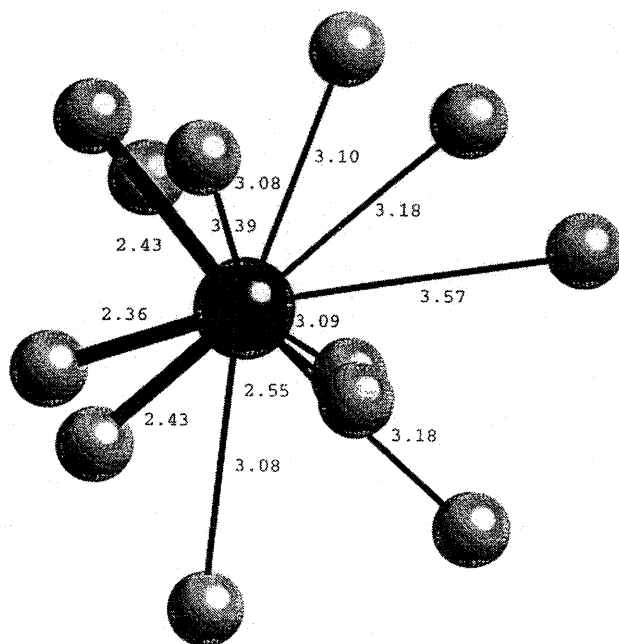
Fig. 28. Local environment of Pb in $PbZrO_3$ [11]

accommodated by local displacements of oxygen ions resulting in local rotations of BO_6 octahedra [91, 92]. Thus the polarization of one PbO_{12} cluster is connected to the polarization of neighboring PbO_{12} clusters through the rotation of BO_6 octahedra. This provides local elastic interaction among the Pb polarizations in addition to the electronic dipolar interaction. This example demonstrates that the knowledge of the local structure has greatly extended our understanding of this complex system.

5
Superconducting Cuprates

Superconducting cuprates are yet another system for which the PDF method provided novel information that could not have been attained by other methods. Since detailed discussions have been published elsewhere [93, 94], in this article we summarize just several observations as examples and relate them to the recent experiments of the lattice effects.

5.1
Dynamic Local Structural Anomaly Near T_C and T_{PG}

While there is practically no change in the average crystal structure of cuprates at the superconducting transition temperature, the pulsed neutron PDF of

$Tl_2Ba_2CaCu_2O_8$ showed small, but reproducible changes near T_C. The change is particularly significant for a sub-peak at 3.2 Å, as shown in Fig. 29 [4]. Interestingly, this anomaly is definitely dynamic, since it depends strongly on the detector angle, just as we discussed for manganites. The modeling suggests that this peak corresponds to the distance between the apical oxygen (O1) and the in-plane oxygen (O2). The equilibrium O1-O2 distance is 3.0 Å, but around T_C this separation splits into two distances at 2.8 Å and 3.2 Å. Our conjecture is that such a split exists all along, but the oscillation is too fast to be observed by the PDF, and only in the vicinity of T_C does the dynamics slow down enough to become observable [95]. This split is caused probably by the out-of-plane motion of O2 rather than the c-axis motion of O1. In either case, this observation demonstrates a major response of the lattice to the superconducting transition.

Another example of a lattice anomaly is the observation involving $Yba_2Cu_4O_8$. It was found that the chain oxygen O2 in this compound is dynamically displaced in the direction perpendicular to the chain but parallel to the CuO_2 plane, forming a ferroelectric domain of about 8×20 Å, below the spin-gap or pseudo-gap temperature, T_{PG} [96]. This is indicative of a local response to slowly moving charged particles that could well be related to the formation of the CDW-SDW state discussed below.

5.2
Electron-Lattice Coupling in Cuprates

Since it is apparent that the high temperature superconductivity of cuprates cannot be explained by the Bardeen–Cooper–Schrieffer (BCS) mechanism that explained the low temperature superconductors so beautifully, the role of the
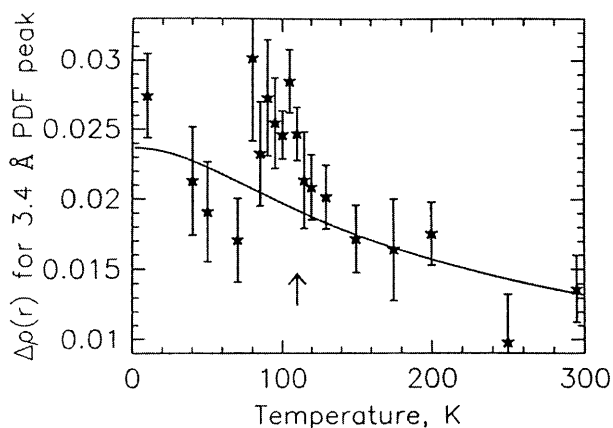
Fig. 29. Peak height of the pulsed neutron PDF of $Tl_2Ba_2CaCu_2O_8$ at 3.2 Å as a function of temperature. The *solid line* is the temperature dependence calculated from the phonon density of states. The *arrow* indicates the superconducting transition [4]

lattice (phonon) has been all but ignored in this field. However, there are many observations of anomalous lattice behaviors that suggest either unconventional mechanism involving the lattice, or at least the unconventional nature of the superconductivity in the cuprates. For instance, the two observations above suggest that at least some of the charge dynamics in the superconducting cuprates are as slow as the lattice dynamics. When we compare these and other results to the observations in manganites, the parallelism is rather striking.

It is very interesting that, just as in the case of manganites, increased Cu—O—Cu bond bending suppresses superconductivity [35, 97]. At the same time the Cu—O—Cu bond is always bent, at least locally, even when it is straight in the average structure [98, 99]. This suggests that again, just in the case of CMR manganites, superconductivity may be observed where the polarons are marginally stable; either a high stability or a total instability of polarons would be damaging to the superconductivity. It was found for the manganites that, in the crossover regime, the local lattice (Jahn–Teller) distortion exists even in the metallic phase. In the case of cuprates this could translate to the presence of a dynamic charge-density-wave (CDW) instability [100].

Indeed, recent phonon measurements suggest the presence of such a dynamic CDW at low temperatures in superconductive $La_{1.85}Sr_{0.15}CuO_4$ [101]
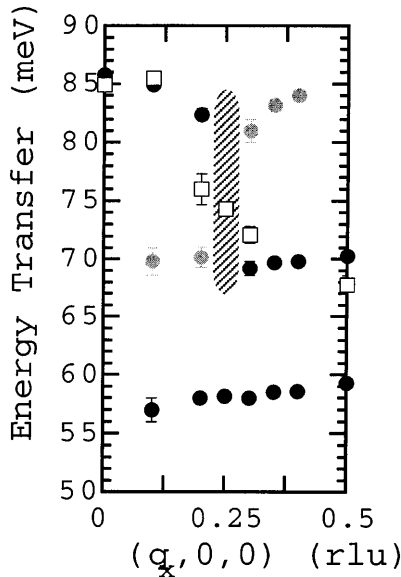
Fig. 30. The dispersion of the LO phonons in $La_{1.85}Sr_{0.15}CuO_4$ along the (100) direction (along the Cu—O bond in the plane) [101]. At T = 300 K (*squares*) the dispersion is continuous and agrees with the earlier measurement [103]. At low temperatures, however, the dispersion (*filled circles*) becomes discontinuous at q = 0.25. Weak peaks (*gray circles*) suggest that the branch has split into two separate branches

and $YBa_2Cu_3O_7$ [102]. The dispersion of the high-energy LO phonon mode develops a discontinuity at q = 0.25 at low temperatures as shown in Fig. 30. This suggests an underlying periodicity of 2a, where a is the Cu—Cu distance in the CuO_2 plane. One possibility is that this is due to a dynamic CDW. On the other hand, the magnetic periodicity is 8a, which can be interpreted in terms of the antiferromagnetic stripe domains of 4a wide. Since the antiferromagnetic domain boundary attracts doped holes, the magnetic correlation would impose a potential for charge with the 4a periodicity. It is possible that this conflict between the CDW and SDW prevents the formation of either static CDW or SDW and keeps the system in the dynamic state. Also, such a strong electron-phonon interaction as evidenced in the large phonon renormalization must have some relevance to the pairing mechanism. Several scenarios are possible, including phonon resonantly coupling the two CDW states. In either case recent experimental results suggest that the phonon mechanism is far from dead in high temperature superconductivity, and has to be carefully re-addressed.

6
Concluding Remarks

In this chapter we have shown how critical the local structure is to the elucidation of the properties of mixed-ion oxides such as the CMR manganites, ferroelectric titanates, and superconducting cuprates. The effect of local structure is more pronounced for oxides than for free-electron metals since the local structure tends to be better defined in oxides due to their covalent bonding, relatively open structure, and the tendency for charge localization. In metals, on the other hand, small local effects are smeared out because of delocalized charge, strong screening, and densely packed structure.

In the three families of oxides discussed here, local deviations from the lattice structure are caused by electron-lattice interaction. Where the electron-lattice coupling is relatively weak, it merely causes electron-phonon scattering; but where it is strong, non-linear phenomena such as polaron formation take place, causing the lattice to distort locally. For a long time we have mainly dealt with weak interactions by linear response theory based upon a periodic lattice. However, phenomena of recent interest such as the CMR behavior and high temperature superconductivity are based upon strong interactions, and in such a case we have to consider non-linear local interactions. By determining the local structure accurately, it has become possible to describe many of these local electronic interactions.

7
References

1. Stern EA, Sayers DE, Lytle FW (1975) Phys Rev B 11: 4836
2. Warren BE (1969, 1990) X-ray diffraction. Dover Publication, New York
3. Klug HP, Alexander LE (1968) X-ray diffraction procedures for polycrystalline and amorphous materials. Wiley, New York
4. Toby BH, Egami T, Jorgensen JD, Subramanian MA (1990) Phys Rev Lett 64: 2414
5. Placzell G (1952) Phys Rev 86: 377
6. Cargill GS III (1975) Solid State Physics 30: 227
7. Suzuki K (1987) In: Price DL, Skold K (eds) Methods of experimental physics, vol 23, pt b, Neutron scattering. Academic Press, San Diego, p 243
8. Louca D, Egami T (1999) Phys Rev B 59: 6193
9. Dimitrov D, Louca D, Röder H (1999) Phys Rev B 60: 6204
10. Egami T (1995) J Phys Chem Solids 56: 1407
11. Teslic S, Egami T (1998) Acta Cryst B 54: 750
12. Jin S, Tiefel TH, McCormack M, Fastnacht RA, Ramesh R, Chen LH (1994) Science 264: 413
13. Ramirez AP (1997) J Phys: Condens Matter 9: 8171
14. Tokura Y (ed) (1999) Colossal magnetoresistance oxides. Gordon & Breach, London (in press)
15. Hwang HY, Cheong S-W, Radaelli, Marezio M, Batlogg B (1995) Phys Rev Lett 75: 914
16. Jonker GH, Van Santen JH (1950) Physica 16: 337; Van Santen JH, Jonker GH (1950) Physica 16: 599
17. Zener C (1951) Phys Rev 81: 440
18. Goodenough JB (1955) Phys Rev 100: 564
19. Anderson PW, Hasegawa H (1955) Phys Rev 100: 675
20. DeGennes PG (1960) Phys Rev 118: 141
21. Millis AJ, Littlewood PB, Shairman BI (1995) Phys Rev Lett 74: 5144
22. Billinge SJL, DiFrancesco RG, Kwei GH, Neumeier JJ, Thompson JD (1996) Phys Rev Lett 77: 715
23. Radaelli PG, Cox DE, Marezio M, Cheong S-W, Schiffer PE, Ramirez AP (1995) Phys Rev Lett 75: 4488
24. Radaelli PG, Marezio M, Hwang HY, Cheong S-W, Batlogg B (1996) Phys Rev B 54: 8992
25. Dai P, Zhang J, Mook HA, Liou S-H, Dowben PA, Plummer EW (1996) Phys Rev B 54: R3694
26. Tyson TA, Mustre de Leon J, Conradson SD, Bishop AR, Neumeier JJ, Zang J (1996) Phys Rev B 53: 13,985
27. Booth CH, Bridges F, Snyder GJ, Geballe TH (1996) Phys Rev B 54: R15,606
28. Zhao G-M, Conder K, Keller H, Müller KA (1996) Nature (London) 381: 676
29. Hundley MF, Neumeier JJ (1997) Phys Rev B 55: 11,511
30. Louca D, Egami T (1997) J Appl Phys 81: 5484
31. Egami T, Louca D, McQueeney RJ (1997) J Superconductivity 10: 323
32. Louca D, Egami T, Brosha EL, Röder H, Bishop AR (1997) Phys Rev B 56: R8475
33. Cheong S-W, Hwang HY (1999) In: Tokura Y (ed) Colossal magnetoresistance oxides. Gordon & Breach, London (in press)
34. Fernandez-Baca JA, Dai P, Hwang HY, Kloc C, Cheong S-W (1998) Phys Rev Lett 80: 4012
35. Egami T, Louca D (1998) J Superconductivity 12: 23
36. Mitchell JF, Argyriou DN, Potter CD, Hinks DG, Jorgensen JD, Bader SD (1996) Phys Rev B 54: 6172
37. Huang Q, Santoro A, Lynn JW, Erwin RW, Borchers JA, Peng JL, Greene RL (1997) Phys Rev B 55: 14,987

38. Louca D, Egami T (2000) Phys Rev B 61: 1351
39. Murakami Y, Endoh Y (2000) J Superconductivity (in press)
40. Urushibara A, Moritomo Y, Arima T, Asamitsu A, Kido G, Tokura Y (1995) Phys Rev B 51: 14,103
41. Wollan EO, Koehler WC (1955) Phys Rev 100: 545
42. Lanzara A, Saini NL, Brunelli M, Natali F, Bianconi A, Radaelli PG, Cheong S-W (1998) Phys Rev Lett 81: 878
43. Booth CH, Bridges F, Kwei GH, Lawrence JM, Cornelius AL, Neumeier JJ (1998) Phys Rev Lett 80: 853
44. Moritomo Y, Asamitsu A, Kuwahara H, Tokura Y (1996) Nature (London) 380: 141
45. Kimura T, Asamitsu A, Tomioka Y, Tokura Y (1996) Science 274: 1698; (1997) Phys Rev Lett 79: 3720
46. Mitchell JF, Argyriou DN, Jorgensen JD, Hinks DG, Potter CD, Bader SD (1997) Phys Rev B 55: 63
47. Louca D, Kwei GH, Mitchell JF (1998) Phys Rev Lett 80: 3811
48. Shannon RD (1976) Acta Crystal A 32: 751
49. Perring TG, Aeppli G, Hayden SM, Carter SA, Remeika JP, Cheong S-W (1997) Phys Rev Lett 78: 3197
50. Röder H, Zang J, Bishop AR (1996) Phys Rev Lett 76: 1356
51. Batistik I, Huang XZ, Bishop AR, Saxena A (1993) Phys Rev B 48: 6065
52. Tomioka A, Kuwahara H, Asamitsu A, Kasai M, Tokura Y (1997) Appl Phys Lett 70: 3609
53. Billinge SJL (1999) (private communication)
54. McQueeney RJ (1998) Phys Rev B 57: 10,560
55. Egami T (1996) J Low Temp Phys 105: 791
56. Egami T, Louca D, McQueeney RJ (1997) J Superconductivity 10: 323
57. Zallen R (1983) The physics of amorphous solids. Wiley, New York
58. Yunoki S, Hu J, Malvezzi AL, Moreo A, Furukawa N, Dagotto E (1998) Phys Rev Lett 80: 845
59. Yunoki S, Moreo A, Dagotto E (1998) Phys Rev Lett 81: 5612
60. Moreo A, Yunoki S, Dagotto E (1999) Science 283: 2034
61. Zhou J-S, Archibald W, Goodenough JB (1996) Nature 381: 676
62. Jaime M, Lin P, Salamon MB, Han PD (1998) Phys Rev B 58: R5901
63. Tokura Y (1998) (private communication)
64. Lynn JW, Erwin RW, Borchers JA, Huang Q, Santoro A, Peng J-L, Li ZY (1996) Phys Rev Lett 76: 4046
65. Lynn JW, Erwin RW, Borchers JA, Santoro A, Huang Q, Peng J-L, Greene RL (1997) J Appl Phys 81: 5488
66. Hwang HY, Dai P, Cheong S-W, Aeppli G, Tennant DA, Mook HA (1998) Phys Rev Lett 80: 1316
67. Dessau DS, Saitoh T, Park C-H, Shen Z-X, Villela P, Hamada N, Morimoto Y, Tokura Y (1998) Phys Rev Lett 81: 192
68. Archibald W, Zhou J-S, Goodenough JB (1996) Phys Rev B 53: 14,445
69. Gor'kov LP, Kresin VZ (1998) JETP Lett 67: 985
70. Salje EKH (1990) Phase transitions in ferroelastic and co-elastic crystals. Cambridge Press, Cambridge
71. Osborn R, Rosenkranz S, Argyriou DN, Vasiliu-Doloc L, Lynn JW, Sinha SK, Mitchell JF, Gray KE, Bader SD (1998) Phys Rev Lett 81: 3964
72. Ramirez AP, Schiffer P, Cheong S-W, Chen CH, Bao W, Palstra TM, Zegarski B, Gammel PL, Bishop DJ (1996) Phys Rev Lett 76: 3188
73. Chen CH, Cheong S-W (1996) Phys Rev Lett 76: 4042
74. Radaelli PG, Cox DE, Marezio M, Cheong S-W (1997) Phys Rev 55: 3015
75. Billinge SJL, DiFrancesco RG, Hundley MF, Thompson JD, Kwei GH (1999) (unpublished)
76. Asamitsu A, Moritomo Y, Tomioka A, Arima T, Tokura Y (1995) Nature 373: 407

77. Tokunaga M, Muira N, Tomioka Y, Tokura Y (1998) Phys Rev B 57: 5259
78. Hennion M, Moussa F, Biotteau G, Rodriguez-Carvajal J, Pinsard L, Revcolevschi A (1998) Phys Rev Lett 81: 1957
79. Dai X, Li J-F, Viehland D (1995) Phys Rev B 51: 2651
80. Stern EA, Yacoby Y (1996) J Phys Chem Solids 57: 1449
81. Kwei GH, Billinge SJL, Cheong S-W, Saxton JG (1995) Ferroelectrics 164: 57
82. Jaffe B, Cook WR, Jaffe H (1971) Piezoelectric ceramics. Academic Press, London
83. Teslic S, Egami T, Viehland D (1996) J Phys Chem Solids 57: 1537
84. Cross LE (1987) Ferroelectrics 76: 241
85. Husson E, Chubb M, Morell A (1988) Mat Res Bull 23: 357
86. DeMathan N, Husson E, Gaucher P, Morell A (1990) Mat Res Bull 25: 427
87. Egami T, Teslic S, Davies PK, Chen I-W, Chen H (1998) Ferroelectrics 206/207: 231
88. Akbas M, Davies PK (1997) Commun Amer Ceram Soc 80: 2933
89. Egami T, Rosenfeld HD, Toby BH, Bhalla A (1991) Ferroelectrics 120: 11
90. Rosenfeld HD, Egami T (1993) Ferroelectrics 150: 183
91. Egami T, Teslic S, Dmowski W, Davies PK, Chen I-W, Chen H (1998) J Korean Phys Soc 32: S935
92. Egami T, Dmowski W, Akbas M, Davies PK (1998) AIP Conf Proc 436: 1
93. Egami T, Billinge SJL (1994) Prog Mater Sci 38: 359
94. Egami T, Billinge SJL (1996) Lattice effects in high-T_C superconductors. In: Ginsberg DM (ed) Physical properties of high temperature superconductors V. World Scientific, p 265
95. Egami T, Toby BH, Dmowski W, Billinge S, Davies PK, Jorgensen JD, Subramanian MA, Gopalakrishnan J, Sleight AW (1989) Physica C 162/164: 93
96. Sendyka TR, Dmowski W, Egami T, Seiji N, Yamauchi H, Tanaka S (1995) Phys Rev B 51: 6747
97. Büchner B, Breuer M, Freimuth A, Kampf AP (1994) Phys Rev Lett 73: 1841
98. Billinge SJL, Davies PK, Egami T, Catlow CRA (1991) Phys Rev B 43: 10,340
99. Andersen OK, Jepsen O, Leichtenstein AI, Mazin II (1994) Phys Rev B 49: 4145
100. Perali A, Castellani C, Di Castro C, Grilli M (1996) Phys Rev B 54: 16,216
101. McQueeney RJ, Petrov Y, Egami T, Yethiraj M, Shirane G, Endoh Y (1998) Phys Rev Lett 82: 628
102. Egami T, McQueeney RJ, Petrov Y, Yethiraj M, Shirane G, Endoh Y (1999) AIP Conf Proc 483: 231
103. Pintschovius L, Pyka N, Reichardt W (1991) Physica C 185/189: 156

Optical Spectroscopic Studies of Metal-Insulator Transitions in Perovskite-Related Oxides

S.L. Cooper

Department of Physics, Frederick Seitz Materials Research Laboratory,
and Science and Technology Center for Superconductivity,
University of Illinois at Urbana-Champaign, Urbana, IL 61801, USA
E-mail: slcooper@uiuc.edu

This article examines metal-insulator transitions observed in perovskite-like Ti-, V-, Mn-, Fe-, Co-, Ni-, Cu-, Bi-, and Ru-oxide systems using optical spectroscopies, particularly infrared reflectance and Raman scattering. The rich phenomena examined in these materials include bandfilling- and bandwidth-induced metal-insulator transitions, mass renormalization effects, metal-insulator transitions involving charge-, spin-, and orbital-ordering, colossal magnetoresistance, polaronic effects, double exchange ferromagnetism, and electronic phase separation. In addition to describing the optical spectroscopic signatures of these remarkable phenomena, this article will examine theoretical models of this diverse behavior, and will explore some of the outstanding questions confronting the physics of these materials.

Keywords: Metal-Insulator transitions, Optical spectroscopy, Raman scattering, Perovskite materials

1
Introduction and Overview

In spite of their structural and chemical similarities, perovskite-type 3d transition oxides such as $A_{1-x}A'_xMO_3$ and $A_{2-x}A'_xMO_4$ (A = trivalent rare-earth ion, A' = divalent cation, and M = 3d transition metal ion) exhibit a remarkably broad range of phenomena, including antiferromagnetism, "colossal" magnetoresistance behavior, double-exchange ferromagnetism, coexisting metallic and insulating phases, and charge- and orbital-ordering. This diversity is largely a consequence of the strong coupling among the spin-, charge-, and lattice-degrees of freedom in these systems, which causes the delicate balance among the Coulomb (U), charge-transfer (Δ_{CT}), magnetic exchange (J), and carrier hopping (t_{pd}) energies to be modified substantially by subtle changes in temperature, composition, magnetic field, and pressure. Although it is not yet completely understood how these interactions combine to drive the various transitions and ground states observed in the ternary transition metal oxides, there are several important effects whose complex interplay contributes to the myriad properties observed in these materials.

1.1
Electronic Properties of Transition Metal Perovskites

One of the most important factors governing the electronic structure of the parent compounds AMO_3, $A'MO_3$, A_2MO_4, and A'_2MO_4, and therefore the optical and transport properties of the doped phases, is the relationship among the three fundamental energy scales common to these materials [1]: the charge transfer gap, Δ_{CT}, between the occupied oxygen 2p state and the unoccupied 3d or 4d metallic state; the energy separation, U, between singly- and doubly-occupied 3d or 4d states; and the bandwidths W of the oxygen and metal states. Within the ionic Zannen-Sawatzky-Allen (ZSA) model, which ignores details such as the effects of covalency and the polarizability of the lattice, the conduction properties of the transition metal oxides are primarily associated with differences in the ionization potential of the transition metal cations, and can be organized into four categories [2]:

1. Charge-transfer insulators, $W < \Delta_{CT} < U$, such as La_2CuO_4, $LaMnO_3$, $LaFeO_3$, and La_2NiO_4
2. Mott–Hubbard insulators, $W < U < \Delta_{CT}$, such as $LaTiO_3$, V_2O_3, and La_2NiO_4
3. Low-Δ_{CT} metals, in which the lowest lying metal conduction band overlaps the O-2p valence state, $\Delta_{CT} < W$
4. Low-U metals, $U < W$, in which the two metal orbitals overlap.

It is worth noting two important trends in the electronic properties of ternary transition metal oxides of the form AMO_3 (A = rare earth, M = transition metal) as a function of increasing transition metal atomic number. First, there is a systematic reduction in the size of the 3d wavefunction of the transition metal ion from the left to the right side of the "iron group" row of the periodic

table, Ti $\rightarrow$ Cu, which results in a systematic increase in the Hubbard U; this is associated with a concomitant increase in the electron affinity of the transition metal ion from the left to the right side of the 3d row, which causes a systematic reduction of the charge transfer energy, Δ_{CT}, between the O(2p) and metal 3d states. As a result of these two effects, transition metal oxides with metal ions from the left side of the periodic table have Mott–Hubbard type gaps, while metal ions from the right side of the row tend to have charge-transfer-type gaps. The crossover point occurs roughly at M = Mn in binary (MO) transition metal oxides, and slightly earlier in the periodic row, M = Cr, in the perovskite RMO_3 systems due to a reduction of Δ_{CT} by the higher valence of the rare earth ion R in the perovskites [3, 4]. Second, the specific d-orbitals comprising the unfilled bands (with bandwidth W) important for low energy excitations and transport properties in the ternary transition metal oxide system $A_{1-x}A'_xMO_3$ depend upon the transition metal element M. In particular, the three-dimensional $A_{1-x}A'_xMO_3$ system exhibits both a large Hund's rule exchange energy J_H and a crystal field splitting 10Dq between the t_{2g} triplet ground state and e_g doublet excited state of the M(3d) levels. Consequently, the t_{2g} band is the relevant band for charge transport in transition metal perovskites with lighter transition elements, such as the titanates, $ATi^{3+}O_3$, which have a single electron in the t_{2g} band, $(t_{2g})^1$, and the vanadates, $AV^{3+}O_3$, which have two electrons in the t_{2g} band, $(t_{2g})^2$. On the other hand, the higher e_g band comprises the unfilled band in many of the heavier transition metal perovskites, such as the manganites $AMn^{3+}O_3$ $[(t_{2g})^3e_g^1]$, nickelates $ANi^{3+}O_3$ $[(t_{2g})^6e_g^1]$, and high T_c cuprates.

1.2
Doping and Bandwidth Control in the TM Perovskites

There are, in principal, two independent paths to a metal $\rightarrow$ insulator transition in Mott–Hubbard systems [5], both of which are characterized by the disappearance of the squared plasma frequency associated with the free carriers, $\omega_p^2 \sim n/m^*$:

1. *Doping-induced (or "filling-controlled") MI transitions*, resulting from the disappearance of the carrier density n
2. *Bandwidth-controlled MI transitions*, reflecting the divergence of the carrier effective mass m^*

In view of the importance of these two routes to achieving MI transitions in Mott–Hubbard transitions, it is worth examining how doping and bandwidth can be more or less independently controlled in ternary TM oxide systems.

1.2.1
Doping (Bandfilling) Control

Doping in the ternary transition metal perovskites AMO_3 is accomplished via substitution of divalent cations A' = Ca, Sr, Ba for trivalent rare earth ions A, $A_{1-x}A'_xMO_3$, which has the effect of changing an equivalent number of

transition metal (M) ions from M^{3+} to M^{4+}. The principal influence of this substitution is to dope the system by changing the filling of the 3d band away from an integer value. Notably, there are also several important peripheral consequences of this substitution that contribute to the rich phenomena observed in these systems: First, chemical substitution influences the size and sign of the M-M magnetic exchange interaction, and hence the magnetic ordering behavior of the ground state, by altering the M-M distance [6–8]. Second, as discussed in more detail below, chemical substitution effectively creates an inhomogeneous mixed-valent system $A^{3+}_{1-x}A'^{2+}_xM^{3+}_{1-x}M^{4+}_xO_3$ in the "doped" regime, making conditions favorable for various forms of electronic inhomogeneity, including polaronic distortions and charge-ordering.

1.2.2
Bandwidth Control

Control of the 3d bandwidth W in the ternary transition metal perovskites $A_{1-x}A'_xMO_3$, is principally governed by variations in the rare earth (A) site. The perovskite-like AMO_3 transition metal oxides have a distorted $GdFeO_3$-type structure (Fig. 1), in which the MO_6 octahedra are rotated so that the
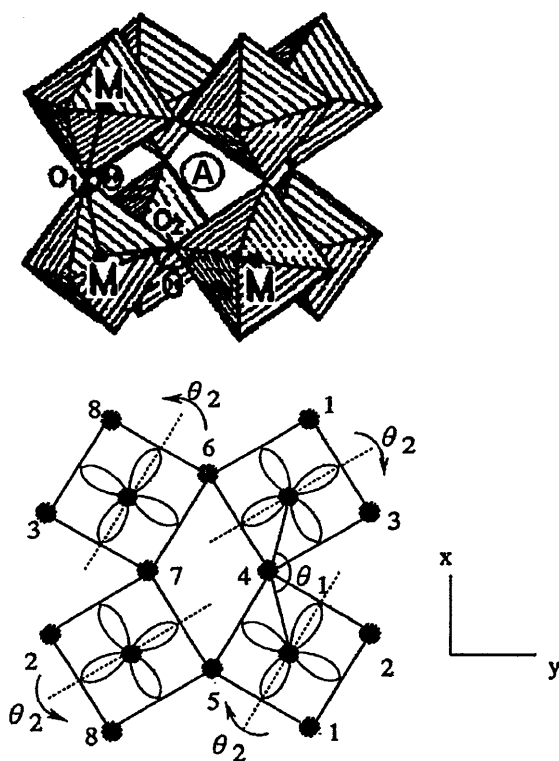
Fig. 1. (*top*) AMO_3 structure. (*bottom*) The tilted MO_6 octahedra, as illustrated for the particular case of the t_{2g} orbital at the M site [74]

MOM bond angle deviates from the ideal perovskite angle of 180°. This rotation of the MO_6 octahedra is caused by the incomplete filling of space in the unit cell by the rare earth element, A, and is typically quantified by the so-called "tolerance factor", $t \equiv (d_{R-O})/\sqrt{2}(d_{M-O})$, which relates the size of the rare-earth-oxygen bond length, d_{R-O}, to that of the transition-metal-oxygen bond length, d_{M-O} ($t = 1$ in the ideal perovskite structure). Due to the "lanthanide contraction" of the rare earth ionic radius from the left to the right side of the periodic table, perovskite transition metal oxides with rare-earth elements from the left side of the row tend to have larger tolerance factors than those with A elements from the right side. The principal effect of decreasing the M—O—M bond angle from 180° (i.e., decreasing the tolerance factor from 1) is to increase the splitting (U-W) between upper and lower Hubbard bands, both by increasing the Coulomb energy, U, and by reducing the M(3d)—O(2p)—M(3d) overlap that governs the 3d conduction bandwidth, W. Thus, transition metal perovskites with larger rare-earth ions at the A site tend to exhibit smaller gaps than those with smaller rare earth ions. However, there are also important collateral effects of the changing bandwidth that contribute to additional complexity in the physical properties of these systems, including an increased propensity in the more distorted (smaller bandwidth) TM perovskite systems for electronic localization, strong electron-lattice coupling, and charge and/or orbital ordering.

1.3
Inhomogeneous Electronic Phases in the TM Perovskites

The substitution of divalent cations $A' =$ Ca, Sr, Ba for trivalent rare earth ions A in the transition metal perovskite system $A_{1-x}A'_x MO_3$ has the effect of changing an equivalent number of transition metal (M) ions from M^{3+} to M^{4+}, effectively creating the mixed-valent system $A^{3+}_{1-x}A'^{2+}_x M^{3+}_{1-x}M^{4+}_x O_3$ in the "doped" regime. In addition to other interesting effects described above, the inhomogeneous mixed-valent character of the doped 3d transition metal oxides is conducive to the development of various forms of electronic phase separation involving the coexistence of metallic and insulating meso-scale regions [9]. Indeed, the remarkable propensity for electronic phase separation in certain complex oxides is evolving into one of the most significant problems in condensed matter physics for two reasons. First, there is growing evidence that electronic phase separation and charge inhomogeneity may be at the root of some of the most remarkable phenomena observed in condensed matter systems, including the unusual normal and superconducting state properties of the high T_c cuprates [10], colossal magnetoresistance behavior in the manganese perovskites [11–13], and charge-"stripe" formation in the cuprates, manganites, and nickelates [14, 15]. Second, this electronic inhomogeneity may represent a truly novel state of matter on the cusp between metallic, semiconducting, and insulating phases, its elucidation demanding a new paradigm for describing the solid state. Below, we focus on two particularly interesting and prevalent forms of electronic inhomogeneity observed in the ternary transition metal oxides.

1.3.1
Charge-Ordering Behavior

At commensurate bandfillings (i.e., those for which the carrier concentration is a rational fraction of the transition-metal site density), many of the perovskite-type 3d transition metal oxides exhibit interesting charge-ordering phenomena involving the formation of ordered domain walls between spin and charge degrees of freedom: In three-dimensional $La_{1-x}Sr_xFeO_3$ (x = 0.67) [16–18], charge-ordering has been observed with domain walls oriented perpendicular to the (1, 1, 1) direction, while in three-dimensional $(La,Pr)_{1-x}Ca_xMnO_3$, charge-stripe domain walls form perpendicular to the (1, 1, 0) direction [19–21] for commensurate concentrations of x = 1/8, 4/8, 5/8, and 7/8 [22]. Charge-ordering is also observed in layered transition-metal oxides such as $La_{2-x}Sr_xNiO_4$ (x ∼ 0.135–0.5) [23–25] and $La_{2-x}Sr_xMnO_4$ (x = 0.5) [26], where the charge domain walls are oriented along the (1, 1, 0) directions, and in the layered $La_{1.6-x}Nd_{0.4}Sr_xCuO_4$ (x = 0.125) system, where charge domain walls have been observed along the (1,0,0) direction [27, 28]. The stability of charge-ordered states in transition metal oxides is supported by numerous Hartree-Fock calculations of single- and multi-band Hubbard models [29–33], which indicate that while the Coulomb interaction plays an important role in localizing the charge carriers, both the superexchange interaction [34] and electron-lattice coupling [30] are influential in stabilizing the charge-ordered state. Importantly, charge ordering is by no means unique to transition metal perovskites, and indeed has also been reported in such diverse systems as $Bi_{1-x}K_xBiO_3$ [35], Fe_3O_4 [36], and Ti_4O_7 [36].

1.3.2
Small Polaron Formation

Even away from "commensurate" values of the bandfilling, x, the combination of strong electronic correlations and mixed-valence in the $A^{3+}_{1-x}A'^{2+}_xM^{3+}_{1-x}M^{4+}_xO_3$ system is conducive to the development of random "dynamical" charge and spin disorder in the form of polaronic distortions. This occurs, for example, in specific instances where one of the transition metal species is "Jahn–Teller-active", and hence susceptible to Jahn–Teller distortions; such is the case for the Mn^{3+} ion in the doped manganites, $A_{1-x}A'_xMnO_3$, and the Co^{3+} ion in its intermediate spin configuration in $LaCoO_3$, which have $(t_{2g})^3e_g^1$ and $(t_{2g})^5e_g^1$ configurations, respectively. However, "breathing mode"-type distortions may be even more generally anticipated in the $A^{3+}_{1-x}A'^{2+}_xM^{3+}_{1-x}M^{4+}_xO_3$ family due to the large difference in the ionic size of the M^{3+} and M^{4+} ions. Notably, in cases where a large exchange coupling also exists between the itinerant and localized spins, this intrinsic disorder also favors the formation of magnetic polarons (or magneto-elastic polarons) [13], as has been observed in colossal magnetoresistance (CMR) systems $A_{1-x}A'_xMnO_3$ (x < 0.5) [37–39], $La_{1-x}Sr_xCoO_3$ [40], and EuB_6 [41].

It is the complex interplay among the many properties described above that spawns the diversity of phenomena observed in the 3d transition metal oxides.

In the following we describe the insights that optical spectroscopies, most particularly infrared reflection and Raman scattering, convey about this interplay and the rich phase behavior exhibited by these materials.

2
Optical Spectroscopic Probes of Strongly-Correlated Systems

Infrared and Raman spectroscopies are extremely effective probes of the metal-insulator transitions in transition metal oxides. Infrared spectroscopy provides a measure of the optical spectral weight, $\sim \omega_p^2$ ($\sim n/m^*$), which is the natural order parameter for the Mott transition [5] as it approaches a zero value for either of the two paths by which a Mott transition is achieved, a diminution of the carrier density n or a divergence of the carrier effective mass m^*. On the other hand, Raman scattering is useful for simultaneously studying the evolution of electronic, phonon, and spin excitations, and most particularly the carrier scattering rate, through various metal-insulator transitions. Below, we provide some of the salient experimental details regarding these techniques.

2.1
Reflectance Spectroscopy

2.1.1
Basic Results

One of the most important quantities in the study of materials is the frequency-dependent complex dielectric response:

$$\varepsilon(\omega) = \varepsilon_1(\omega) + \frac{4\pi i}{\omega}\,\sigma_1(\omega) \tag{1}$$

where $\varepsilon_1(\omega)$ is the real part of the dielectric function and $\sigma_1(\omega)$ is the frequency-dependent conductivity, which reflects the rate at which particle-hole pairs are created by photons of frequency ω. The common method for obtaining the dielectric response of a material is to measure the frequency-dependent reflectivity $R(\omega)$ of a material, calculate the imaginary part of the optical reflectance, i.e., the phase shift function $\Theta(\omega)$, from a Kramers–Kronig transformation of $R(\omega)$, then use the complex reflectance to compute other fundamental optical constants such as the optical conductivity, $\sigma_1(\omega)$, loss function, $\mathrm{Im}(\frac{-1}{\varepsilon(\omega)})$, and the dielectric function $\varepsilon_1(\omega)$ using standard constitutive relations [42].

2.1.2
Sum Rules

In addition to important optical constants, it is often useful to examine the integrated spectral weight associated with various optical transitions. The optical conductivity is constrained by the f-sum rule [42]:

$$\int_0^\infty \sigma(\omega)\mathrm{d}\omega = \frac{\pi n e^2}{2\,m} = \frac{\omega_p^2}{8} \tag{2}$$

where n is the total electron density in the material, e is the electronic charge, m is the free electron mass, and ω_p is the plasma frequency. In situations where intra- and inter-band electronic transitions are well-separated in energy, it is convenient to define a partial sum rule for the integrated spectral weight below a frequency ω:

$$N_{eff}(\omega) = \frac{2\,m V_{cell}}{\pi e^2} \int_0^\infty \sigma_1(\omega')\mathrm{d}\omega' \tag{3}$$

where $(m/m^*)N_{eff}(\omega)$ is the number of carriers contributing to the optical conductivity below a frequency ω, m/m^* is the ratio of the free electron mass to the effective mass of the partially-filled bands, and V_{cell} is the unit cell volume. Importantly, $N_{eff}(\omega)$ can be related to an effective plasma frequency, $\omega_p^2 = \frac{4\pi e^2}{m^*}\frac{N_{eff}}{V_{cell}}$, and to an effective kinetic energy, $K(\omega) = \frac{a_0}{m V_{cell}}N_{eff}(\omega)$, and hence is a sensitive indicator of either bandwidth- or bandfilling-controlled metal-insulator transitions [43, 44].

2.1.3
Drude Model

The simplest description of the dielectric function of the mobile carriers in a metal is the Drude model, which assumes that carriers relax in response to an electric field via elastic scattering with a rate $\tau^{-1} = \frac{v_F}{l}$, where v_F is the Fermi velocity and l is the carrier mean free path. The corresponding real parts of the dielectric function $\varepsilon_1(\omega)$ and optical conductivity $\sigma_1(\omega)$ in the Drude model are:

$$\varepsilon_1(\omega) = \varepsilon_\infty - \frac{\omega_p^2 \tau^2}{(1 + \omega^2\tau^2)} \quad \text{and} \quad \sigma_1(\omega) = \frac{\omega_p^2}{4\pi}\frac{\tau}{(1 + \omega^2\tau^2)} \tag{4}$$

Consequently, in the Drude approximation, for the usual case when $\omega_p \gg 1/\tau$, one expects the following behaviors:

1. The dielectric response is large and negative for $\omega < \omega_p/\sqrt{\varepsilon_\infty}$, is zero at $\omega = \omega_p/\sqrt{\varepsilon_\infty}$, and approaches ε_∞ at high frequencies.
2. The energy loss function has a peak at $\omega = \omega_p/\sqrt{\varepsilon_\infty}$.
3. The optical conductivity in Eq. (4) has a characteristic width of τ^{-1} and a maximum of $\sigma_{dc} = \frac{\omega_p^2\tau}{4\pi} = \frac{ne^2\tau}{m^*}$ at $\omega = 0$.

2.1.4
Correlation Effects: The Extended Drude Model

The simple Drude model assumes that the sole relaxation channel of the carriers arises from elastic scattering, and hence ignores correlation and inelastic scattering effects. In an analysis of the optical response of strongly correlated materials, the latter can be incorporated by considering an "extended" Drude model [45] in which the frequency-dependence of the

effective carrier mass m^* and scattering rate $\gamma^*=1/\tau^*$ is taken into account. The frequency dependence of these quantities can be deduced from the measured real and imaginary parts of the dielectric function ($\varepsilon_1(\omega)$ and $\varepsilon_2(\omega) = \frac{4\pi}{\omega}\sigma_1(\omega)$, respectively) with the relations

$$m^* = \frac{4\,\pi n e^2 \gamma^*}{\varepsilon_2 \omega(\omega^2 + \gamma^{*2})} \quad \text{and} \quad \gamma^* = \frac{\omega \varepsilon_2}{(\varepsilon_\infty - \varepsilon_1)} \tag{5}$$

2.2
Raman Spectroscopy

2.2.1
Basic Results

Raman scattering is a two photon process in which a photon changes its frequency ω, wavevector $\mathbf{k}$, and polarization ε via scattering from the values (ω_I, $\mathbf{k}_I$, ε_I) to the values (ω_S, $\mathbf{k}_S$, ε_S) while the scattering material experiences a transition from $|i\rangle$ to $|f\rangle$. The associated photon differential scattering cross section for this process is [46]:

$$\frac{d^2\sigma}{d\Omega d\omega_S} = \frac{V^2 \omega_I \omega_S^3}{c^4}\left(\frac{n_S}{n_I}\right)\sum_f \langle\langle|\langle f|\chi_{IS}|i\rangle|^2\rangle\rangle\delta(\omega_I - \omega_S - \omega) \tag{6}$$

where $\langle\langle\ldots\rangle\rangle$ represents a thermodynamic average over the initial states of the scattering material. The transition susceptibility tensor χ in Eq. (6) is the quantum mechanical analogue of the classical susceptibility, and has the matrix elements

$$\langle f|\chi_{IS}|i\rangle = \frac{e^2}{V\omega_S\omega_I}\sum_m\left[\frac{\langle f|\varepsilon_S\cdot\mathbf{j}_{kS}|m\rangle\langle m|\varepsilon_I\cdot\mathbf{j}_{-kI}|i\rangle}{[E_m - E_i - \hbar\omega_I]} + \frac{\langle f|\varepsilon_S\cdot\mathbf{j}_{-kI}|m\rangle\langle m|\varepsilon_I\cdot\mathbf{j}_{kS}|i\rangle}{[E_m - E_i + \hbar\omega_S]}\right]$$
$$-\frac{e^2}{m\omega_S\omega_I}\varepsilon_I\cdot\varepsilon_S\langle f|\rho_{-q}|i\rangle \tag{7}$$

where $\vec{\mathbf{j}}_q = \sum_j e^{-iq\cdot r_j}\left(\vec{\mathbf{p}}_j - \frac{\hbar\vec{q}}{2}\right)\cdot m^{-1}$ is the qth Fourier component of the particle current density operator, and $\rho_q = \sum_j e^{-iq\cdot r_j}$ is the qth Fourier component of the particle density operator. Thus, the Raman scattering cross section for a particular excitation is associated with the correlation function of the dynamical susceptibility at the wavevector $\mathbf{q}$ and frequency ω of the excitation. There are two important features to note about the scattering cross section in Eq. (6) – kinematic and symmetry constraints.

2.2.1.1
Kinematical Constraint

Wavevector conservation in a translationally invariant crystal requires $\mathbf{q} = \mathbf{k}_I - \mathbf{k}_S$ (Stokes scattering), which for the usual experimental conditions,

$\omega \ll \omega_I$ and $|\mathbf{k}_I| \approx |\mathbf{k}_S|$, can be written $|\mathbf{q}| = 2|\mathbf{K}_I|\sin\frac{\theta}{2}$ to a good approximation. Consequently, because the range of excitation wavevectors that light scattering experiments typically probe, $0 < |\mathbf{q}| < 3 \times 10^{-3}$ Å^{-1} [46], is generally several orders of magnitude smaller than the size of the Brillouin zone boundary, $|\mathbf{k}_{ZB}| \sim 2\pi/a \sim 1$ Å^{-1}, Raman scattering typically probes only excitations very near the Brillouin zone center, i.e., $|\mathbf{q}| \approx \mathbf{0}$. This limitation is circumvented when wavevector conservation is lost due to disorder, or in two-phonon or two-magnon scattering, in which the $|\mathbf{k}| \approx \mathbf{0}$ photons create two single (phonon or magnon) excitations of equal and opposite momenta, $\mathbf{q}$ and $-\mathbf{q}$.

2.2.1.2
Symmetry Constraint

The Raman scattering cross section is also constrained by the selection rules imposed by the susceptibility tensor in Eq. (6). For example, the transition susceptibility matrix element $\langle f|\chi_{ab}|i \rangle$ is nonzero only if the decomposition of the direct product $\Gamma_f^* \otimes \Gamma_\chi \otimes \Gamma_i$ contains the totally symmetric representation, Γ_1, where Γ_i and Γ_f, are the irreducible representations of the initial and final states of the scattering medium, respectively. Additionally, the induced polarization $\mathbf{P}$, the susceptibility tensor χ, and the incident field $\mathbf{E}_I$, $\mathbf{P} = \chi\mathbf{E}$, must be covariant under all spatial transformations of the scattering medium, and hence an excitation must have a symmetry contained in the decomposition of $\Gamma_{PV}^* \otimes \Gamma_{PV}$ (PV = polar vector) to be "Raman–active".

2.2.2
Phonon Scattering and Resonance Effects

When considering light scattering from phonons or spins, one generally treats the electron-phonon or electron-spin interaction as a perturbation and calculates the relevant scattering cross sections using third- or higher-order perturbation theory [46].

Note also that the second- and higher-order terms in the scattering cross section (Eqs. 6 and 7) involve transitions to virtual intermediate states that contribute energy denominators of the form $(E_m - E_i - \hbar\omega_I)$ and $(E_m - E_i + \hbar\omega_S)$. As a result, "resonant enhancements" of the scattering cross section occur when the incident photon energy hω_I approaches the energy difference between initial and intermediate states due to the vanishing of the energy denominator. In particular, the low temperature phonon Raman scattering intensity is given by $S_{ph}(\omega) \sim \left(\frac{\omega}{c}\right)^4 \left|\frac{\delta\varepsilon}{\delta Q}\right|^2$ [47], and thus the phonon Raman intensity reflects the degree to which the phonon mode's atomic displacement Q modulates the dielectric response ε at the laser frequency ω. Consequently, studies of the resonant Raman intensity of various excitations can be particularly useful for exploring the coupling between these excitations and the electronic bands in complex oxides [47–49].

2.2.3
Raman Scattering from Conduction Electrons

Raman scattering from conduction electrons has evolved as a powerful probe of metal-insulator transitions in strongly correlated systems, as evidenced by recent studies of charge gap development in "Kondo Insulators" [50–52] and charge-ordering systems [53], and of scattering rate changes across insulator (or semiconductor/semimetal) to metal transitions in bandfilling-controlled [54] and "colossal magnetoresistance" [39, 41, 55] systems. Electronic Raman scattering distinguishes itself from more conventional optical probes of metal-insulator transitions such as infrared reflectivity in that it (a) affords a means of simultaneously probing changes in the spin-, lattice-, and electronic-degrees-of-freedom, (b) provides a means of studying changes in the scattering rate associated with different scattering channels, (c) is sensitive to low carrier density phases, which is of particular utility in mixed-phase regimes of various complex oxides, and (d) lends itself to sophisticated techniques useful for exploring the low frequency charge dynamics across metal-insulator transitions, including pressure, magnetic-field, and time-resolved (pump-probe) studies.

Raman scattering from conduction electrons is associated with the correlation function for an *effective density* $\tilde{\rho}$:

$$\frac{d^2\sigma}{d\Omega d\omega_S} = \frac{r_o^2}{2\pi}\left(\frac{\omega_S}{\omega_I}\right)\left(\frac{n_S}{n_I}\right)\int_{-\infty}^{\infty} dt\, e^{i\omega t}\langle\tilde{\rho}_q^\dagger(t)\tilde{\rho}_q(0)\rangle \tag{8}$$

where

$$\tilde{\rho}_q = \sum_{n,\mathbf{k},\sigma}\gamma_{n\mathbf{k}}c_{n\mathbf{k}+q,\sigma}^\dagger c_{n\mathbf{k},\sigma} \tag{9}$$

$c^\dagger$ and c are the electron creation and annihilation operators, respectively, $r_o = e^2/mc^2$ is the Thomson radius of the electron, n is a band index, and $\gamma_{n\mathbf{k}}$ is the electron-photon Raman scattering "vertex". Importantly, when the incident and scattered photons are non-resonant, i.e., far from a real electronic transition, the Raman scattering vertex $\gamma_{n\mathbf{k}}$ in Eq. (9) is related to the inverse effective mass tensor $\boldsymbol{\mu}^{-1}$:

$$\gamma_{n\mathbf{k}} = \varepsilon_I \cdot \frac{m}{\mu} \cdot \varepsilon_S = m\sum_{i,j}\varepsilon_{Si}\frac{d^2 E_{n\mathbf{k}}}{\hbar^2 dk_i dk_j}\varepsilon_{Ij} \tag{10}$$

Within this "effective mass approximation", the electronic Raman scattering cross section in Eq. (8) can be associated with effective mass fluctuations around the Fermi surface, the different symmetry components of which can be experimentally selected by varying the scattering geometry (ε_I and ε_S) in the Raman experiment.

Absent Fermi surface anisotropy or an appreciable contribution from interband transitions, the Raman scattering cross section in Eq. (8) corresponds to scattering from ordinary density fluctuations, and consequently is proportional to the dielectric loss function [56], $\frac{d^2\sigma}{d\Omega\, d\omega_S} \sim [n(\omega) + 1]$

$q^2 \text{Im} \left[\frac{1}{\varepsilon(q,\omega)}\right]$. Because the long-range Coulomb interaction pushes most of the spectral weight associated with density fluctuations up to the plasma frequency, in an isotropic electron gas one expects a significant Raman response at ω_p due to plasmon scattering, but a very weak low frequency (intraband) electronic scattering response. On the other hand, in materials with a complex Fermi surface (such as the transition metal perovskites), for example due to an anisotropic or multi-sheeted Fermi surface, the intraband electronic Raman scattering intensity can be quite strong, as it is dominated in this case by mass fluctuations that do not involve a net change in the charge density, and hence are not screened by the long-range Coulomb interaction. Kosztin and Zawadowski [57] have also noted that strong intraband electronic Raman scattering in complex metals requires impurity scattering, inelastic scattering, or strong electron-electron interactions to take up the momentum in the electronic scattering process. Ipatova et al. [58] first pointed out that in the presence of such strong scattering, the electronic mean free path is generally shorter than the optical penetration depth, $l < \delta \sim q^{-1}$; consequently, the intraband electronic Raman scattering cross section in this case does not have a cutoff at $\hbar\omega = qv_F$, but is instead described by a "collision-dominated" response [59]:

$$S_L(\omega) \sim [n(\omega) + 1]|\gamma_L|^2 \frac{\omega \Gamma_L}{\omega^2 + \Gamma_L^2} \tag{11}$$

where $S_L(\omega)$ is the scattering response in channel L, Γ_L is the carrier scattering rate in channel L, and the amplitude factor $|\gamma_L|^2$ is the square of the Raman scattering vertex projected onto that channel. Note that this Raman spectral response is quite similar to the Drude optical conductivity in Eq. (4) – however, while the prefactor in the latter is a scalar quantity related to the plasma frequency, the prefactor in Eq. (11) is a symmetry-dependent factor related to the effective mass tensor. Consequently, by measuring the intraband Raman scattering response in different scattering geometries, one can isolate the carrier scattering rates associated with different scattering "channels", L. There is, on the other hand, no sum rule on the intraband Raman scattering response.

In the absence of strong electron-electron correlations or inelastic scattering, the carrier scattering rate is generally taken to be frequency-independent, $\Gamma = 1/\tau + Dq^2$, where τ is the carrier scattering time and D is the diffusion constant [58, 60]. However, for strongly-correlated systems, the scattering response in Eq. (11) can be "extended" in a manner analogous to the "extended Drude model" by using a frequency-dependent scattering rate, $\Gamma \sim \Gamma(\omega, T)$ in Eq. (11). Typical examples in which this has been done have included the electronic Raman scattering response in $Sr_xLa_{1-x}TiO_3$ [54], the "colossal magnetoresistance" manganese perovskites [39], and EuB_6 [41], all of which have been described by the response function in Eq. (11) with a "Fermi liquid" scattering rate given by $\Gamma(\omega, T) = \Gamma_o(T) + \alpha\omega^2$, and the electronic scattering response in the cuprates, which is commonly described using Eq. (11) with a scattering rate given by the Marginal Fermi liquid form, $\Gamma(\omega, T) = \alpha\sqrt{\omega^2 + \beta^2 T^2}$ [61, 62].

3
Metal-Insulator Transitions in the Perovskite-Related Oxides

3.1
Doping-Induced Metal-Insulator Transitions

3.1.1
$A_{1-x}A'_xTiO_3$ and $A_{1-x}A'_xVO_3$

The optical properties of several V—O and Ti—O perovskites have been investigated as a function of bandfilling, including $La_{1-x}Sr_xTiO_3$ [63], $A_{1-x}Ca_xTiO_3$ where A=La, Pr, Nd, Sm, and Y [64, 65], $La_{1-x}Sr_xVO_3$ [66], $La_{1-x}TiO_3$ [67], and $Y_{1-x}Ca_xVO_3$ [68]. All of these compounds have end-members that are simple band metals or insulators for x = 1 (with $3d^0$ $(t_{2g})^0$ in $SrTiO_3$ and $CaTiO_3$, and with $3d^1$ $(t_{2g})^1$ in $SrVO_3$ and $CaVO_3$), but are correlation-gap systems for x = 0. Due to their more extended 3d wavefunctions and smaller electron affinities, the V—O and Ti—O systems have larger $O(2p) \rightarrow Ti/V[3d(t_{2g})]$ charge-transfer energies than Mott–Hubbard energies, $U < \Delta_{CT}$, and hence are Mott–Hubbard systems. Typical energy scales reported for some of these compounds are listed in Table 1.

3.1.1.1
Spectral Response

The optical response of the $ATiO_3$ family (A = rare earth) is characterized by [69]: a low frequency gap in the optical conductivity; a strong optical absorption near 4 eV in $ATiO_3$, associated with $O(2p) \rightarrow Ti(3d)$ charge transfer transitions; and a mid-infrared absorption near 2 eV in $ATiO_3$ that systematically increases in energy as the bandwidth W decreases. The latter has been attributed to an optical transition between the filled lower and empty upper Hubbard subbands [67], which increases in energy $\sim(U - W)$ with decreasing bandwidth W. With increased doping into the metallic phase, the low frequency optical conductivity develops a Drude-like response that can be reasonably fit using an "extended" Drude model. This Drude-like response can be alternatively described with the sum of a small Drude contribution near $\omega = 0$, and a dominant incoherent contribution that extends to high frequencies ($\sim$1 eV) with a frequency dependence that scales roughly like $1/\omega$ [70].

Table 1. Electronic parameters for various titanium and vanadium perovskite systems

Material	U	Δ_{CT}	W	References
$LaTiO_3$	$\sim$0.2 eV	$\sim$4.3 eV	2.45 eV	63–65, 67
$YTiO_3$	$\sim$0.8 eV	$\sim$4.3 eV	2.04 eV	64, 65
$La_{0.4}Y_{0.6}TiO_3$	$\sim$1 eV	$\sim$4.3 eV	2.2 eV	74
$Y_{0.4}Ca_{0.6}TiO_3$	$\sim$1 eV	$\sim$4.3 eV	–	64, 65
YVO_3	$\sim$1.5 eV	$\sim$4.3 eV	–	68

In the $Ca_{1-x}Sr_xVO_3$ system, Makino et al. report several noteworthy optical features observed at all values of x [71]. First, the O(2p) $\rightarrow$ V(3d) charge transfer absorption band is observed near $\sim$4 eV. Second, *two* mid-infrared optical features are observed below the charge-transfer band, one near $\sim$1.7 eV, which is identified as the transition between the quasiparticle band and the upper and lower Hubbard bands at U/2, and a second near $\sim$3.5 eV, which is identified as the transition between upper and lower Hubbard bands, U. This interpretation is consistent with the spectral features predicted in calculations of the infinite-dimensional Hubbard model [72], and also with a recent interpretation of the optical data of (Ca,Sr)RuO$_3$ [73]. Finally, the low energy optical response of the $Ca_{1-x}Sr_xVO_3$ system is dominated by a Drude-like response, which can be fitted using an "extended" Drude model with $m^*/m_o \sim$ 3–4.

3.1.1.2
Spectral Weight Redistribution

One of the most dramatic consequences of increased bandfilling (i.e., increasing x) on the optical response of Mott–Hubbard perovskites such as $Y_{1-x}Ca_xVO_3$ [68], $La_{1-x}Sr_xVO_3$ [66], $Y_{1-x}Ca_xTiO_3$ [65], $LaTiO_{3+\delta}$ [74], $La_{1-x}TiO_3$ [67], and $A_{1-x}Ca_xTiO_3$ [64], is the rapid transfer of spectral weight from above the Mott–Hubbard gap to low frequencies (Fig. 2), which causes low frequency spectral weight below the Mott–Hubbard gap (N$_{eff}$) to develop much more rapidly as a function of x (= p = 1 − n, in Fig. 2a) than one expects in a simple doped semiconductor, N$_{eff} \sim$ x. This remarkable behavior reflects two related effects of increased doping (x) away from the Mott–Hubbard insulating phase: (i) a systematic decrease in the mass enhancement factor λ(x) (=F) = m^*/m − 1 (right bottom panel, Fig. 2) of the carriers, and a corresponding increase in the effective number of carriers, N$_{eff} \sim (4\pi ne^2/m^*\varepsilon_\infty)$ (left bottom panel, Fig. 2), as one dopes away from the insulating phase, and (ii) a systematic reduction of spectral weight well above the Mott–Hubbard gap, reflecting a collapse of the gap with increased doping. Importantly, the suppression of low frequency optical spectral weight, and its concomitant transfer above the Mott–Hubbard gap, is well-described by numerous calculations of the optical conductivity for the two-dimensional t-J and Hubbard models [75–82], which predict not only a spectral weight transfer with doping, but also a substantial incoherent contribution to the optical conductivity which may be related to an ubiquitous "mid-infrared" absorption observed in the cuprates, titanates, and vanadates. It should also be noted that the anomalous spectral weight redistribution is not unique to Mott–Hubbard-type perovskites, as similar behavior has also been observed in optical measurements of charge-transfer systems such as the high T$_c$ cuprates [83–88] and $La_{1-x}Sr_xCoO_3$ [89].

Two additional interesting features of spectral weight redistribution specific to the Ti and V perovskites should be mentioned. First, the spectral weight
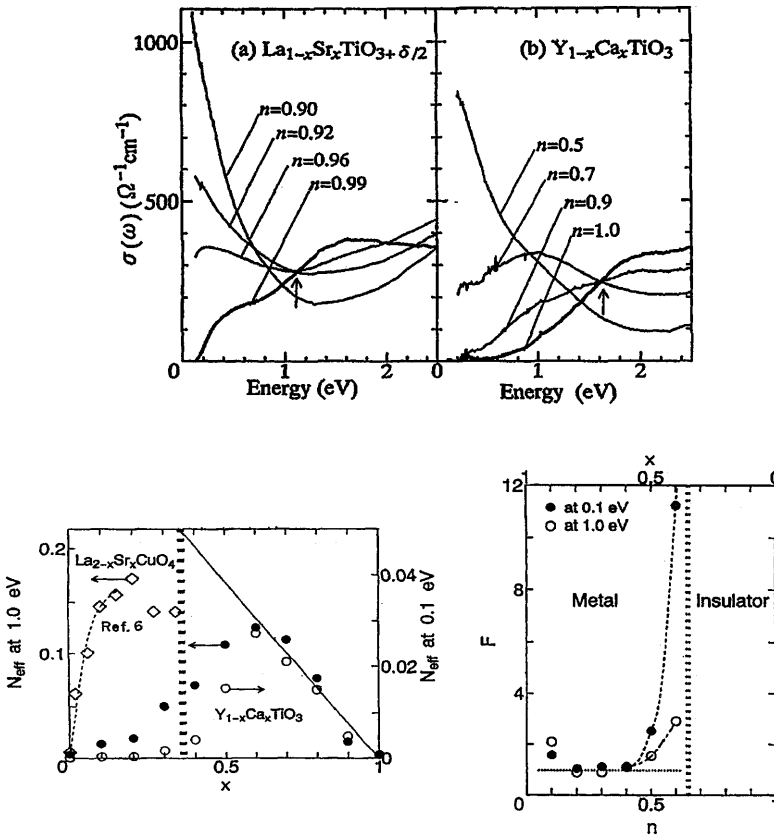
Fig. 2. (*top*) Optical conductivity spectra of $La_{1-x}Sr_xTiO_3$ and $Y_{1-x}Ca_xTiO_3$ as a function of changing bandfilling n (=1 − x) (from [74]). (*bottom*) Effective number of carriers N_{eff} as a function of x for $Y_{1-x}Ca_xTiO_3$ (*left*) and effective mass parameter $F = m^*/m − 1$ as a function of bandfilling (*right*) [65]

redistribution in the titanates occurs across a fixed point just above 1 eV in the optical conductivity (i.e., an "isosbetic point"), suggesting that low frequency spectral weight in these systems evolves with doping at the expense of spectral weight associated with Mott–Hubbard gap excitations. By contrast, no such fixed point is observed in the vanadates, suggesting that spectral weight is transferred from higher energies near the CT gap region [70]. The origin of this difference is not well-explained in Hubbard model calculations. Second, the spectral weight below the isosbetic point increases linearly with doping in the titanates [64], in agreement with predictions of the infinite-dimensional Hubbard model [70, 90] for the Drude weight. However, as discussed above, the low frequency spectral response is not strictly Drude, and indeed may be dominated by an incoherent charge response, and hence a meaningful comparison of the data with model calculations demands more theoretical and experimental investigation.

Interestingly, the enhancement of electronic correlation effects with increased electron doping in the titanates is also manifest in the evolution of the carrier response as $x \rightarrow 0$. For example, fits of the low frequency Drude response of $La_{1-x}Sr_xTiO_3$ using an extended Drude model illustrate that the effective carrier mass m^* and scattering rate γ^* acquire an increasingly strong frequency dependence with increased electron doping (i.e., as $x \rightarrow 0$), reflecting an increase in electronic correlations [63]. This trend is also apparent in Raman scattering measurements of $La_{1-x}Sr_xTiO_3$ [54], which exhibit an electronic Raman scattering response consistent with a "collision-limited" response function (Eq. 11) and a doping-dependent frequency-dependent rate, $\Gamma(\omega, T) = \Gamma_o(T) + \alpha\omega^2$ (Fig. 3). In the band metal $La_{0.1}Sr_{0.9}TiO_3$, the electronic Raman response is characterized by a diffusive response with a single, frequency-independent scattering rate ($\alpha = 0$). However, as additional La is added toward the Mott–Hubbard end-member $LaTiO_3$, there is an increased flattening of the electronic scattering spectrum that is attributable to a systematic increase in carrier effective mass m^* (i.e., the "correlation parameter" α), similar to that inferred from measurements of the Pauli paramagnetic susceptibility, the T^2 coefficient of the resistivity, and the specific heat [91] (bottom, Fig. 3).

3.1.1.3
Phonon Effects

Katsufuji and Tokura have reported that the enhancement of the carrier effective mass with hole doping in the titanates is also reflected in the Raman active optical phonons [92], which show a dramatic increase in intensity through the insulator to metal transitions of both $La_{1-x}Sr_xTiO_3$ and $Y_{1-x}Ca_xTiO_3$. This behavior was attributed to an enhanced dynamical modulation of the dielectric response, $d\varepsilon/dQ$, by the A_{1g} bending mode above the insulator $\rightarrow$ metal transition [92]. However, it should be noted that in another study of the $RTiO_3$ system, Reedyk et al. find no evidence for a diminution of phonon intensity in the insulating phase [93]. Thus, the impact of the MI transition on the phonons in bandfilling systems such as the titanates and vanadates remains uncertain, and further investigation and clarification of this issue is needed.

3.1.1.4
Electronic Inhomogeneity

The presence of electronically inhomogeneous phases near the MI transition of the titanates and vanadates has not been as carefully explored as in other perovskite systems, particularly the manganites, although there are some suggestive results that motivate a more complete investigation in these systems. For example, both the titanates and vanadates exhibit an increase in optical spectral weight as a function of increased doping that presages the MI transition measured via the d.c. conductivity [64]. This behavior appears to be
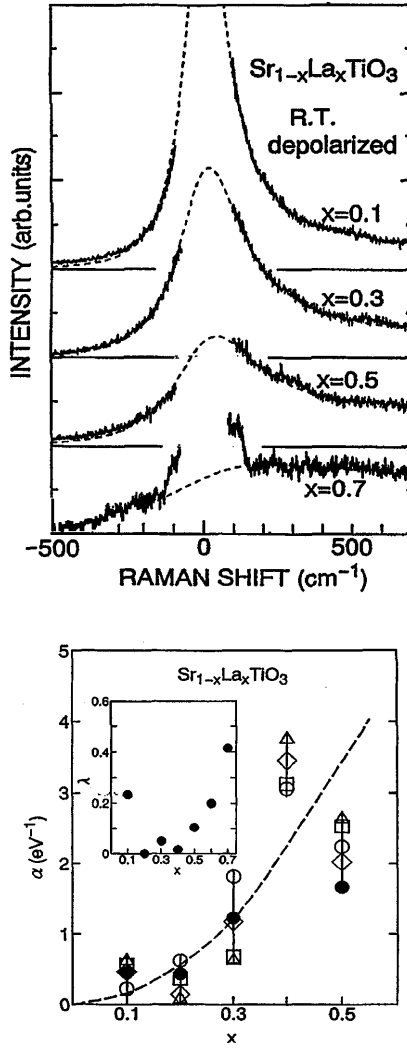
Fig. 3. (*top*) Electronic Raman scattering spectra of $Sr_{1-x}La_xTiO_3$ as a function of bandfilling x. (*bottom*) The ω^2 coefficient, α, of the scattering rate Γ as a function of bandfilling x, reflecting the increasing effective mass enhancement with x [54]

indicative of multiphase behavior on the insulating side of the MI transition, wherein small metallic domains nucleate in the insulating background as precursors to the bulk MI transition. Interestingly, Choi et al. also reported evidence that metallic domains develop, and eventually percolate, in the insulating phase VO_2 films as the temperature is increased toward the MI transition [94], suggesting further that multiphase behavior may be a common feature of MI transitions in vanadium- and titanium-oxide systems. More detailed investigation is needed to better examine this issue.

3.1.2
High T_c Cuprates

It is now well known that high T_c cuprate perovskites such as $La_{2-x}Sr_xCuO_4$ and $YBa_2Cu_3O_7$ exhibit a rich phase diagram as a function of doping (top, Fig. 4), including [95]: (i) a spin = 1/2 antiferromagnetic charge-transfer insulator phase ($T_N \sim 300$ K) with the spins localized primarily on the Cu^{2+} ions, and with
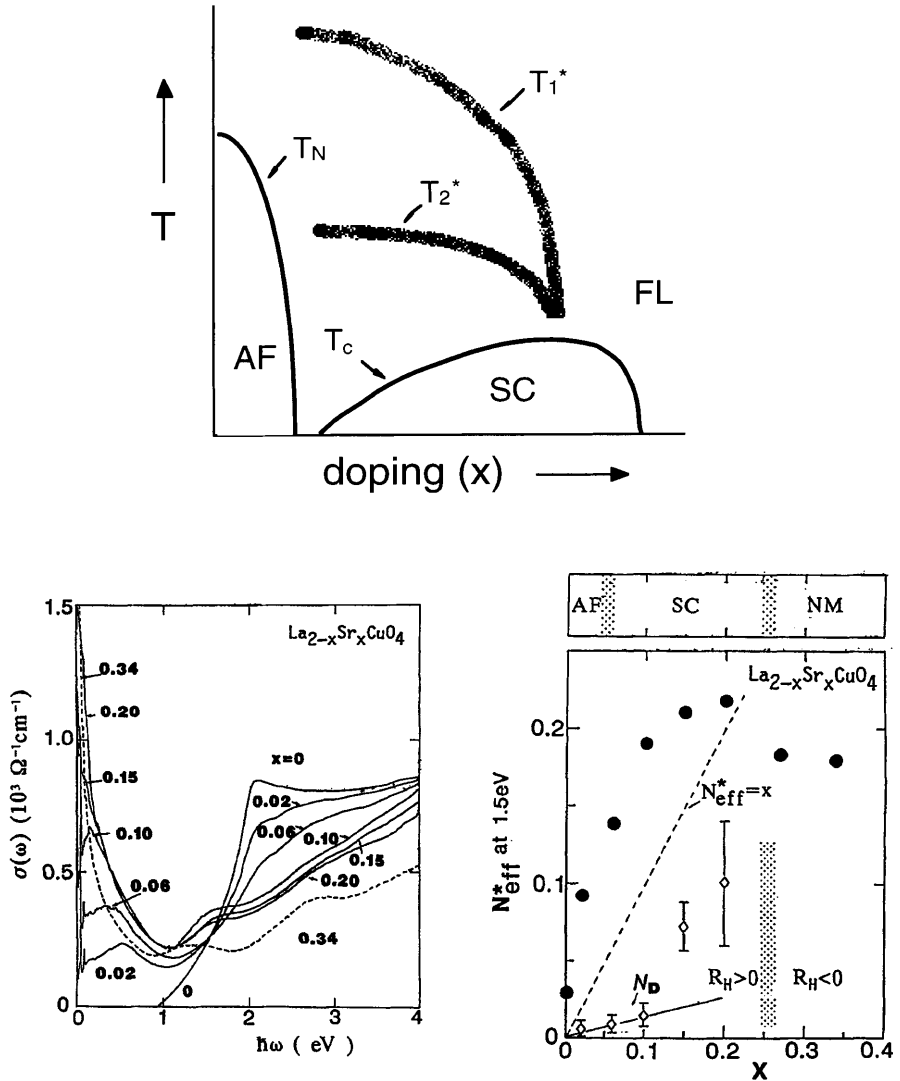
Fig. 4. (*top*) Phase diagram for high T_c cuprates. (*bottom*) Optical conductivity spectra (*left*) and effective number of carriers N_{eff} (*right*) of $La_{2-x}Sr_xCuO_4$ for various x [84]

Table 2. Electronic parameters for various cuprate systems

Material	U	Δ_{CT}	J	References
La_2CuO_4	8–10 eV	~2 eV	136 meV	84, 97
$YBa_2Cu_3O_6$	8–10 eV	1.75 eV	120 meV	83, 96

a charge transfer gap of $\Delta_{CT} \sim 1.75$ eV [83, 84, 96] and a Cu-Cu superexchange coupling of $J \sim 120$–140 meV [97–101] (Table 2); (ii) an underdoped "metallic" phase, which includes a temperature regime in which short range antiferromagnetic fluctuations, and perhaps even charge "stripes", develop in the CuO_2 planes, and a lower temperature regime characterized by the presence of a pseudogap in the charge and spin density of states; (iii) an optimally-doped superconductor region; and (iv) an overdoped region which exhibits Fermi liquid (FL) low temperature properties. In this section we will be primarily interested in the optical properties characteristic of the first two regimes. Optical measurements of the high T_c cuprates reveal several interesting consequences of doping away from the Mott–Hubbard insulator phase:

3.1.2.1
Spectral-Weight Transfer

In both electron-doped compounds $Pr_{2-x}Ce_xCuO_4$ [83] and $Nd_{2-x}Ce_xCuO_4$ [84] and hole-doped compounds $La_{2-x}Sr_xCuO_4$ [84] and $YBa_2Cu_3O_{6+x}$ [96], doping results in a dramatic redistribution of spectral weight from high frequencies (~1.5–3 eV, i.e., the charge-transfer gap region, in the case of the cuprates) to the far- and mid-infrared regions, similar to that observed in other complex oxide systems such as $Y_{1-x}Ca_xVO_3$ [68], $Y_{1-x}Ca_xTiO_3$ [65], and $La_{1-x}Sr_xCoO_3$ [89]. As shown in Fig. 4 (bottom) for the case of $La_{2-x}Sr_xCuO_4$, the collapse of the charge transfer band with doping causes low frequency spectral weight, N_{eff}, in the cuprates to develop much more rapidly than expected from the dopant concentration x, similar to the behavior in the titanates and vanadates (see Sect. 3.1.1). An anomalous transfer of spectral weight is also evident in electron-energy-loss (EELS) [85], X-ray absorption (XAS) [86, 87], and resonant photoemission [88] measurements of high T_c cuprates.

As discussed in Sect. 3.1.1, the anomalous increase of low frequency spectral weight in the optical conductivity with doping is not expected in a simple semiconductor; it reflects the diminution of electronic correlations and the associated effective mass enhancement with doping in these systems [75–80]. One interesting point to note is the similarity between the doping-induced spectral weight transfers observed in electron- and hole-doped cuprates [83]. Electron-doped charge-transfer systems are expected to exhibit a transfer of spectral weight with doping akin to that predicted in calculations of MH systems, since the electrons are doped primarily onto the Cu site (i.e., the upper Hubbard band). However, as holes introduced by doping are known to have chiefly oxygen character in the cuprates, and hence have little influence on the upper Hubbard band in the absence of O(2p)-Cu(3d) hybridization, the

anomalous spectral weight transfer observed in hole-doped cuprates appears to defy this picture. However, calculations by Eskes et al. conclude from this [77] that there is substantial O(2p)-Cu(3d) hopping in these systems which cause the spectral weight transfer in hole-doped charge-transfer systems to mimic that in electron-doped systems.

3.1.2.2
Evidence for Charge/Spin Inhomogeneity Near the MI Transition

A second interesting consequence of doping across the MI transition in the high T_c cuprates appears to be the development of some form of charge- and spin-inhomogeneity just above the MI transition, i.e., in the "bad" metal phase. The former is suggested by the appearance of a mid-IR band that is distinct from the Drude-like response in the optical conductivity, which appears to be indicative of some form of strong charge-localization in the "bad" metallic phase of the cuprates. However, the specific nature of the mid-IR band is still controversial [102, 103], and has been variously attributed to a "shake-off" type process involving carriers dressed with spin-fluctuations [79, 81, 104, 105], excitations out of a shallow impurity band [96], and photoionization of small-polarons [106].

Importantly, there is now significant evidence from neutron diffraction studies of $La_{1.6-x}Nd_{0.4}Sr_xCuO_4$ (x ~ 0.15, 0.2) [107], as well as from neutron scattering [108] and nuclear magnetic resonance [109] measurements of overdamped spin fluctuations in the underdoped cuprates, that spin-stripe order persists into the "bad" metal phase of the cuprates and indeed may coexist with superconductivity. Raman scattering studies of two-magnon spectra as a function of doping in several high T_c cuprates also appear to suggest that antiferromagnetic correlations with a spatial extent of several lattice constants survive into the underdoped metallic phase [110–112], perhaps revealing additional evidence for some form of short-range spin-ordering; however, due to the ephemeral nature of charge- and spin-stripe order in the cuprates, optical and Raman scattering measurements of ordering phenomena in these systems are currently inconclusive on this issue. A **q**-dependent optical probe such as inelastic X-ray scattering, however, holds more promise for investigating ordering phenomena in the high T_c cuprates as well as in other charge- and spin-ordering systems such as the manganites, ferrites, and nickelates.

3.1.2.3
Evolution of the Strongly Correlated Carrier Response

At large doping values, i.e., for the highest T_c values, the mid-IR and Drude-like responses of the high T_c cuprates eventually merge into what appears to be a single Drude-like response (Fig. 4b). Under the assumption that this response is comprised of only a "single-component" response, an extended Drude model is necessary to fit the data. This assumption, in turn, leads to the conclusion that the carrier mass is frequency-dependent, and that the carrier

scattering rate has a linear-in-ω frequency-dependence that is consistent with various models [113, 114] of the unconventional normal metallic state of the cuprates [84, 96, 103, 115]. Notably, however, one cannot rule out the possibility that this Drude-like response near optimal doping is actually comprised of "two-components": a Drude-band and some remnant of the mid-IR response [96].

3.1.2.4
Incoherent $\rightarrow$ Coherent c-axis Transport Crossover

The layered high T_c superconductors are among the most anisotropic materials known, exhibiting resistivity ratios ρ_c/ρ_{ab} in the range $\sim 10^2$–10^5 [116]. By comparison, the anisotropies of layered dichalcogenides such as $2H$-NbSe$_2$, $4Hb$-TaS$_2$, and $2H$-NbS$_2$ range from $\rho_c/\rho_{ab} \sim 10^1$ to 10^3. Most remarkably, while ab-plane transport and optical measurements of high T_c superconductors are indicative of metallic behavior above the in-plane metal-insulator transition, the c-axis transport and optical response are characterized by non-metallic charge transport throughout most of the phase diagram. Of particular interest to an examination of metal-insulator transitions in complex oxides is the fact that the transport [117, 118], electronic Raman scattering [96], and optical [96, 116] measurements of La$_{2-x}$Sr$_x$CuO$_4$ and perhaps YBa$_2$Cu$_3$O$_{6+x}$ demonstrate a crossover from incoherent to coherent c-axis charge transport at a doping level well above the in-plane MI transition, reflecting a crossover from quasi-two-dimensional to three-dimensional metallic behavior. Significantly, quasi-two-dimensional metallic behavior at high temperatures, and a *temperature-induced* crossover between incoherent $\rightarrow$ coherent c-axis transport below $T_M \sim 130$ K, is observed in the layered ruthenate system Sr$_2$RuO$_4$ [119] (see Sect. 3.2.3); however, the high T_c cuprates are distinguished by the fact that two-dimensional metallic behavior is observed essentially over the entire temperature range, at least in the underdoped metallic phases. A more detailed discussion of c-axis properties in high T_c cuprates is beyond the scope of this article, but it should be noted that a number of open questions regarding c-axis crossover behavior in the high T_c cuprates remain, including the nature of the relationship between the incoherent c-axis response of the high T_c cuprates and (a) high T_c superconductivity and (b) the unconventional normal state properties (e.g., pseudogap behavior [120]).

3.1.3
Ba$_{1-x}$K$_x$BiO$_3$ and BaPb$_y$Bi$_{1-y}$O$_3$

The optical properties of bismuthates such as Ba$_{1-x}$K$_x$BiO$_3$ and BaPb$_y$Bi$_{1-y}$O$_3$ provide an interesting comparison to those of complex transition metal oxides because they exhibit many spectral features similar to those observed in transition metal perovskites, including a broad redistribution of spectral weight through the doping-induced MI transition [121, 122], and a possible real-space ordering of holes in the insulating phase [35].

The normal-state phase diagram of the bismuth perovskites, $Ba_{1-x}K_xBiO_3$ and $BaPb_yBi_{1-y}O_3$, is characterized by a doping-induced metal-insulator transition near $x = 0.35$ [123] and $y = 0.70$ [124], respectively, which coincides with a tetragonal-to-orthorhombic structural change. There are several unresolved questions concerning this system. First, while the undoped material $BaBiO_3$ has one electron per unit cell, and hence is naively expected to be a metal, optical measurements show that the parent compound is in fact insulating [121, 125, 126]. Early tight-binding calculations suggested that the insulating behavior at half-filling ($x = y = 0$) is associated with the near-perfect nesting of the electron and hole Fermi surfaces in these systems, which favors a commensurate three-dimensional charge-density wave (CDW), and a consequent opening of an insulating gap at the Fermi surface [127–129]. However, more recent band structure calculations indicate that the observed breathing-mode lattice distortions [123, 130] are by themselves not sufficient to cause the measured gap in the density of states, suggesting that electronic correlations must also be taken into account. Second, the observed persistence of semiconducting behavior away from half-filling is not explained by tight-binding models, which instead predict metallic behavior in the doped phase due to the lifting of the nesting degeneracy and the resulting destabilization of the CDW state. Several explanations have been proposed to account for the persistence of insulating behavior away from half-filling, including chemical ordering waves [131], site potential differences [132], real-space electron pairing (small bipolarons) [133–135], and ordering of localized holes [35].

3.1.3.1
Doping Dependence of the Optical Response

Optical and Raman scattering measurements of $Ba_{1-x}K_xBiO_3$ and $BaPb_yBi_{1-y}O_3$ reveal several interesting features as a function of doping. The insulating phases are dominated by a broad peak in the optical conductivity near $\omega_o \sim 1$ eV in $Ba_{1-x}K_xBiO_3$ and $\omega_o \sim 2$ eV in $BaPb_yBi_{1-y}O_3$, associated with excitations across the fundamental charge gap (top, Fig. 5). Gap development and the doping dependence of the optical spectra in the bismuthates have been variously interpreted in terms of bipolaron formation [136–138], Peierls-type "bond-order" CDW formation associated with the development of inequivalent Bi—O bonds [121], and "site-diagonal" CDW formation associated with the development of inequivalent Bi^{3+} and Bi^{5+} sites [126]. These low temperature "charge ordered" states are reminiscent in certain respects of charge ordering phenomena observed in certain transition metal perovskites (see Sect. 3.4); however, it should be noted that, in contrast with the case of the bismuthates, magnetic interactions appear to play a key role in charge ordering behavior of the latter [34, 70]. All of these interpretations are consistent with Raman scattering studies showing that the intensity of the 570 cm^{-1} Bi—O breathing mode phonon increases dramatically (i.e., is "resonantly enhanced") as the excitation wavelength is tuned through the charge gap energy in $BaBiO_3$ [49, 125], illustrating that breathing mode distortions play an important role in the insulating behavior.
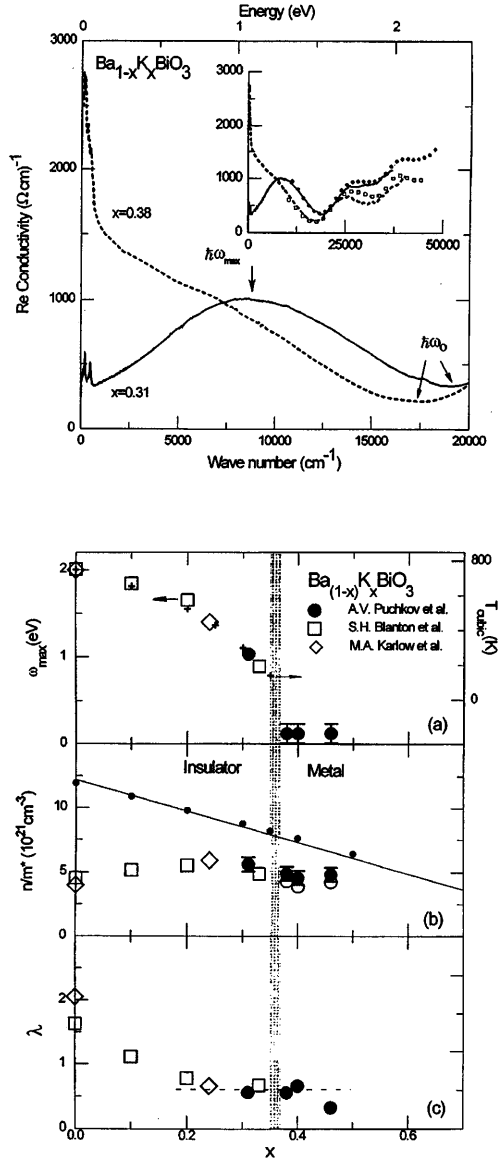
Fig. 5. (*top*) Optical conductivity spectra. (*bottom*) Absorption maximum, ω_{max}, n/m* ($\sim N_{eff}$), and mass enhancement factor, λ, of $Ba_{1-x}K_xBiO_3$ for various x [136]

Figure 5 (top) shows that adding carriers to the insulating phase leads to a doping-induced MI transition near x ∼ 0.35 in $Ba_{1-x}K_xBiO_3$, as evidenced in the optical data by [121, 125, 126, 136, 137, 139–141]: (i) the development of a Drude-like response, (ii) the dramatic decrease of the peak energy of the fundamental absorption ω_o, (iii) a decrease in the low frequency optical

spectral weight N$_{eff}$, and (iv) a decrease in the mass enhancement factor $\lambda = m^*/m - 1$ (bottom, Fig. 5). It has been argued recently [136] that a substantial amount of optical spectral weight appears to be tied-up in an incoherent spectral contribution, which militates against a conventional CDW description, and favors instead a bipolaronic (local CDW) description of gap formation in the bismuthates, wherein pairs of charge carriers strongly localize on a single site due to their strong interaction with the lattice. It is interesting to note in this regard that studies of the attractive-U Hubbard model by Eskes and Oles [122], which is argued to be appropriate for the bismuthates, has several features consistent with the bipolaron picture and with the observed spectral response of the bismuthates: a strong redistribution of spectral weight with doping, similar to that predicted by the negative-U Hubbard model (and observed also in the bismuthates, cuprates, titanates, and vanadates), a large incoherent contribution to the spectral response, and a proclivity for local pairing interactions. More theoretical investigation is needed to explore the compatibility of these interpretations.

3.2
Bandwidth-Controlled Metal-Insulator Transitions

As discussed previously, metal-insulator transitions can be induced by controlling the bandwidth, as well as the bandfilling, and a number of studies of perovskite-related oxides have examined the nature of metal-insulator transitions achieved via this route.

3.2.1
$A_{1-x}A'_x TiO_3$ and $A_{1-x}A'_x VO_3$

3.2.1.1
Spectral Weight Redistribution

Numerous optical studies have examined the influence of electronic correlations, U/W, on the metal-insulator transitions of Ti- and V-based Mott–Hubbard systems by varying the bandwidth W at fixed values of the bandfilling. For example, photoemission and optical studies have examined the effects of decreasing bandwidth (increasing electron correlations U/W) on the spectral response of the $YTiO_3 \rightarrow LaTiO_3 \rightarrow SrVO_3$ [142] and $SrVO_3 \rightarrow CaVO_3$ [71, 143, 144] series. The principal result of these studies is that spectral weight is systematically transferred from the coherent quasiparticle part of the spectral response near E$_F$ to the incoherent contribution of the spectral response (associated with transitions across the Hubbard gap) as a function of increasing electronic correlations, U/W. As in the case of bandfilling-controlled Mott transitions, this trend reflects an increase in the effective mass m* as the system approaches the Mott transition from the metallic side [145], and is in agreement with the results of dynamical mean-field calculations of the Hubbard model [70, 146]; importantly, however, the experimental results do not show a narrowing

of the quasiparticle band with increasing U/W that is also predicted in these calculations.

The remarkable doping-induced redistribution of optical spectral weight discussed previously has also been investigated in both the (La,Y)TiO$_3$ [74] and A$_{1-x}$Ca$_x$TiO$_3$ (A = La, Pr, Nd, Sm, and Y) [64] systems as a function of the electronic correlation strength, U/W. Two interesting effects of increasing the electronic correlation strength on the optical spectra of Mott–Hubbard systems were noted in these studies. First, the optical gap 2Δ in A$_{1-x}$Ca$_x$TiO$_3$ was found to increase linearly with increasing U/W [64], which is a trend similar to that observed in optical studies of La$_x$Y$_{1-x}$TiO$_3$ [74] and V$_2$O$_3$ [147, 148]. Second, the rate at which spectral weight is transferred from above the Hubbard gap to low frequencies as a function of doping (see discussion, Sect. 3.1.1) decreases with increasing electronic correlation strength (U/W): dN$_{eff}$/dp = 0.93 in La$_{1-x}$Sr$_x$TiO$_3$ and dN$_{eff}$/dp = 0.21 in Y$_{1-x}$Ca$_x$TiO$_3$ [74] (Fig. 6), where N$_{eff}$ is the integrated optical spectral weight below $\sim$1–1.5 eV
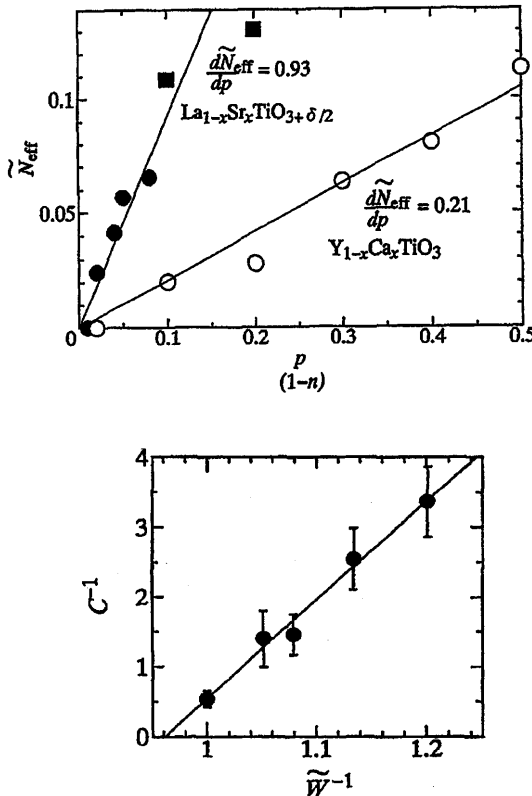
Fig. 6. (*top*) Hole-concentration p (=1 − x) dependence of the effective number of carriers N$_{eff}$ for La$_{1-x}$Sr$_x$TiO$_3$ and Y$_{1-x}$Ca$_x$TiO$_3$ [74]. (*bottom*) The parameter C^{-1} as a function of the electron correlation strength, $\widetilde{W}^{-1}$, where C is the rate at which the Drude-like response changes with bandfilling [64]

and p is the hole concentration (by comparison, the rate of change in the cuprate system $La_{2-x}Sr_xCuO_4$ is much larger [84], $dN_{eff}/dp = 1.6$, possibly reflecting the two-dimensional nature or the charge-transfer type gap of the cuprates). Interestingly, in the $A_{1-x}Ca_xTiO_3$ (A = La, Pr, Nd, Sm, Y) system, the rate (C) at which this doping-induced transfer occurs diverges as U/W approaches the critical value for the Mott–Hubbard transition, $(U/W)_c$ (Fig. 6) [64], presumably reflecting the divergence of the (normalized) carrier effective mass m^* with doping as the MI transition is approached [5, 73]:

$$\frac{1}{m^*} = 1 - \frac{(U/W)^2}{(U/W)_c^2} \tag{12}$$

Katsufuji et al. used their results to estimate the critical value of the bandwidth-controlled Mott–Hubbard transition, $(U/W)_c \sim 0.97$, in the $A_{1-x}Ca_xTiO_3$ system. This value is below that estimated from quantum Monte Carlo simulations of the half-filled single band Hubbard model [72], $(U/W)_c \sim 1.5$; however a proper comparison between theory and experiment requires more careful consideration of both orbital degeneracy [149], which increases the critical value $(U/W)_c$, and the deviation of the system from half-filling [150]. It is also worth noting for comparison that Ahn et al. estimate a value $(U/W)_c \sim 2.7$ from their measurements of the $(Ca,Sr)RuO_3$ system [73].

3.2.1.2
Phonon Effects

Recent Raman scattering studies of the $RTiO_3$ (R = rare earth) series by Reedyk et al. [93] also found that certain optical phonons, particularly the Ti—O bending mode near 300 cm^{-1}, exhibit a dramatic increase in energy and asymmetry with decreasing bandwidth. Interestingly, this trend in the phonon response appears to be correlated with an increase in the observed electronic Raman continuum intensity, a fact which appears to suggest that both features are connected to the systematic increase in the orthorhombic distortion. However, more detailed analysis of both the electronic (in particular, the Raman scattering vertex (Eq. 10)) and phononic scattering response (e.g., phonon self-energy effects) is necessary to determine to what extent these trends reflect enhanced electronic correlation effects as opposed to mere changes in electronic structure.

3.2.2
ANiO$_3$

One of the best examples of a bandwidth-controlled MI transition is that exhibited by the $ANiO_3$ series (A = rare earth). As shown in Fig. 7, the $ANiO_3$ compounds with A = Sm, Eu, Nd, Pr are low-Δ_{CT} metals with temperature-induced MI transitions: $ANiO_3$ compounds with intermediate values of the tolerance factor (t), i.e., A = Sm, Eu, have MI transitions that are substantially
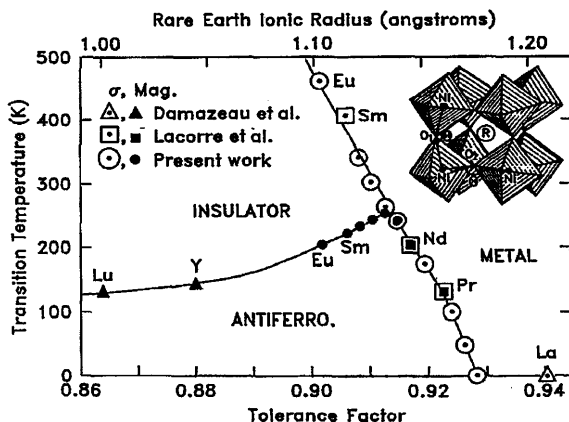
Fig. 7. Phase diagram for $ANiO_3$ (A = R = rare earth) as a function of tolerance factor and ionic radius of the rare earth ion [151]

higher than their respective antiferromagnetic ordering temperatures, while the transition to the AF insulating phase coincides with the MI transition in large-t $ANiO_3$ materials, A = Nd and Pr. The bandwidth-controlled MI transition in the $ANiO_3$ system has been attributed to the straightening of the Ni—O—Ni bond, and the consequent closing of the charge transfer gap, as a function of increasing rare-earth ionic radius (i.e., increasing tolerance factor, t), decreasing temperature [151], and increasing pressure [152, 153]. Indeed, neutron scattering studies have shown that the MI transition in this system is accompanied by an increased tilt of the NiO_6 octahedra, and an associated $\sim 0.5°$ decrease in the Ni—O—Ni bond angle [154]. Furthermore, optical studies by Arima and Tokura [155] reveal a clear gap in the optical conductivity for low-t materials $YNiO_3$ and $SmNiO_3$, but a finite (albeit non-Drude) low frequency conductivity in the high-t materials $NdNiO_3$ and $LaNiO_3$. Notably, the $ANiO_3$ series has the low-spin S = 1/2 configuration $t_{2g}^6 e_g^1$, and hence the AF insulating phase of some $ANiO_3$ compounds may involve orbital ordering associated with the orbital degeneracy of this state [156]; however, no evidence for Jahn–Teller distortions has been reported for these systems thus far [70].

3.2.2.1
Optical Response

The optical response of both $LaNiO_3$ [4] and $NdNiO_3$ [157] have been reported. For reasons discussed above, the former is a paramagnetic metal at all temperatures while the latter transforms from a paramagnetic metal phase at high temperatures to an antiferromagnetic insulating phase below $T_N \sim 200$ K. The high temperature optical conductivity of both compounds is characterized by three key features (Table 3): (i) a high frequency peak near ~ 10 eV which has been attributed to O(2p) $\rightarrow$ A(5d/4f) transitions (A = rare

Table 3. Electronic parameters for the nickel perovskite system

Material	Δ_{CT}	$2\Delta_{SDW}$	W	References
(La/Nd)NiO$_3$	=1 eV	~0.3 eV	–	4, 157

earth); (ii) a constant conductivity between 1–5 eV, which is likely attributable to O(2p) $\rightarrow$ Ni(3d) charge transfer excitations [4]; and (iii) a Drude-like response below 1 eV. Importantly, the Drude-like response in NdNiO$_3$ is not described well by a simple Drude response (Eq. 4) [157]; nor is a fit of the measured response using a "single-component", extended Drude model (Eq. 5) satisfactory, as such a fit requires the frequency-dependent scattering rate $\Gamma(\omega)$ to have values for which the quasiparticles are not well-defined, i.e., $\Gamma > \omega$. Instead, the non-Drude low frequency response may reflect a strong overlap between the intraband response of the itinerant 3d carriers and the broad conductivity associated with the O(2p) $\rightarrow$ Ni(3d) CT excitations, i.e., a "two-component" optical response, which derives from the strong hybridization of the Ni(3d) and O(2p) states.

3.2.2.2
Temperature-Induced MI Transition

As a function of decreasing temperature below the MI transition ($T_N \sim 200$ K) in NdNiO$_3$, the optical conductivity exhibits both a transfer of spectral weight from below ~0.3 eV to higher frequencies ($0.3 < \omega < 2$ eV) and the development of a peak in the optical conductivity near 0.4 eV (Fig. 8). The dramatic optical spectral weight redistribution is noteworthy in several respects. First, it is remarkably similar to that observed in bandfilling-controlled MI transitions in other Mott–Hubbard systems, including the cuprates [83, 84], titanates [65], vanadates [68], and cobaltites [89], in that it involves a rapid transfer of spectral weight over a wide energy range. Katsufuji et al. [157] estimates the amount of spectral weight, $\sim 4\pi Ne^2/m^*$, transferred from below 0.3 eV through the MI transition to be ~0.058, which corresponds to an effective mass enhancement of the carriers in the metallic phase of $m^*/m \sim 17$, assuming that each Ni site contributes one conduction electron. A similar mass enhancement due to strong correlation effects was also suggested by the large electronic specific heat coefficient observed in LaNiO$_3$, $\gamma \sim 13.8$ mJ/K^{2}mol [158]. Second, the integrated spectral weight below 0.3 eV, N_{eff}(0.3 eV), changes gradually over a rather broad temperature range (~50 K), and indeed appears to track the temperature-dependence of the magnetic moment; this indicates that the large scale changes in electronic structure that accompany the MI transition are strongly correlated with the magnetic transition in NdNiO$_3$. On the other hand, Katsufuji et al. found that the lattice parameter of NdNiO$_3$ changes relatively abruptly, i.e., in a range of 10 K, suggesting that the electron-lattice coupling is not primarily responsible for the changes in electronic structure through the MI transition. Notably, the
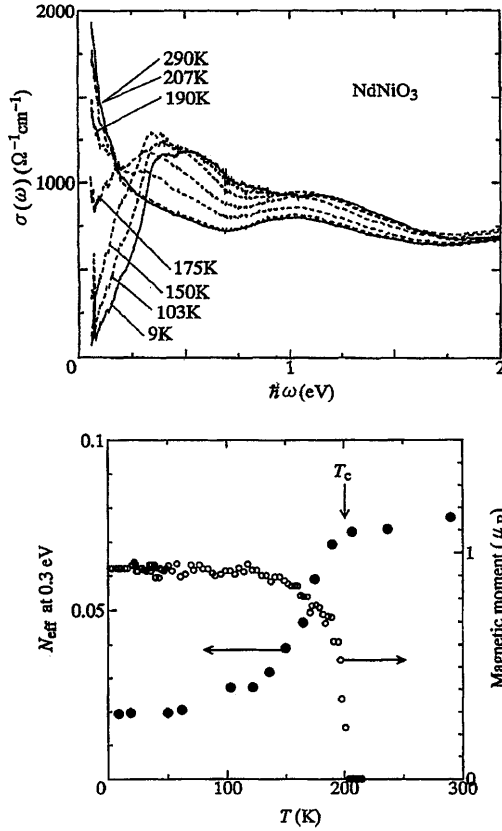
Fig. 8. (*top*) Optical conductivity spectra for $NdNiO_3$ at various temperatures. (*bottom*) Effective number of carriers N_{eff} and the magnetic moment as a function of temperature [157]

latter result differs from the case of the "charge-ordering" transition in the manganese perovskites, in which a close correspondence among the temperature-dependences of the charge (N_{eff}), spin (χ), *and* lattice responses is observed through the MI transition [159]; this difference likely derives from the stronger electron-lattice coupling in the manganese perovskite system. Katsufuji et al. conclude from their results that the charge gap in $NdNiO_3$ is associated with a spin-density-wave (SDW), rather than a charge-density-wave (CDW) gap. However, they note that while the optical gap energy, 2Δ, exhibits a temperature-dependence consistent with a BCS-type gap function, i.e., the prediction of a simple mean-field theory, the magnitude of the gap is far in excess of the BCS gap value ($2\Delta_{BCS} \sim 3.5k_BT_N$), i.e., $2\Delta \sim 20k_BT_N$, possibly as a consequence of strong electron-correlation effects. Interestingly, Cr [160], NiS [161], and (Bi,Ca)MnO_3 [159] also exhibit gap parameters $2\Delta/k_BT_N$ with larger-than-mean-field values.

3.2.2.3
Phonon Effects

There is a dearth of information regarding the influence of the MI transition on phonons in the $NdNiO_3$ system, either from Raman scattering or optical techniques. This is surprising, particularly in view of evidence for structural changes at the MI transition [151, 154], and of the orbitally-degenerate $t_{2g}^6 e_g^1$ configuration of the $ANiO_3$ system, which makes conditions favorable for the development of Jahn–Teller polarons and other forms of electronic inhomogeneity. Much greater effort in this area of investigation is clearly merited.

3.2.3
$(Sr_{1-x}Ca_x)_{n+1}Ru_nO_{3n+1}$ and $Sr_{1-x}Ca_xRuO_3$

Ruthenium oxide compounds with perovskite-type structures have attracted a great deal of recent interest: $SrRuO_3$ is noteworthy because it exhibits magnetic order below $T_C \sim 160$ K [162], an unusual feature for a 4d-based system, while the layered system Sr_2RuO_4 exhibits superconductivity below $T_C \sim 1$ K [163]. Optical studies of the effects of electron correlation strength (bandwidth) on both three-dimensional $Sr_{1-x}Ca_xRuO_3$ [73] and layered $(Sr_{1-x}Ca_x)_2RuO_4$ and $(Sr_{1-x}Ca_x)_3Ru_2O_7$ [164] systems have been reported recently (Table 4). Both studies exploited the fact that the replacement of Sr by Ca causes a reduction in bandwidth W, and hence an increase in the electron correlation strength, U/W, while maintaining a constant carrier doping.

3.2.3.1
$Sr_{1-x}Ca_xRuO_3$

The $Sr_{1-x}Ca_xRuO_3$ system exhibits both a non-Drude low frequency optical conductivity, $\sigma(\omega) \sim 1/\omega$, and a broad electronic Raman continuum [165–167], similar to that seen in the high T_c cuprates [62] (see Sect. 3.1.2). Several noteworthy features have been observed in photoemission and optical spectra of $Sr_{1-x}Ca_xRuO_3$ as a function of bandwidth. First, Ahn et al. observe *two* mid-infrared optical features below ~ 5 eV: a peak near ~ 1.5 eV, which the authors attribute to transitions between the quasiparticle band and the upper and lower Hubbard bands ($\sim U/2$), and a peak near ~ 3 eV, which the authors identify as the transition between upper and lower Hubbard bands, U. This interpretation of the data is consistent with the spectral features predicted in calculations of the infinite-dimensional Hubbard model [72], and also with a recent interpretation of the optical data for the $Sr_{1-x}Ca_xVO_3$ system [71]. Strong electronic correlation effects are also apparent in photoemission

Table 4. Electronic parameters for various ruthenium perovskite systems

Material	U	Δ_{CT}	W	References
$(Ca,Sr)RuO_3$	~ 3 eV	~ 5 eV	–	73
Ca_2RuO_4	~ 1 eV	>3 eV	–	164

spectra of $Sr_{1-x}Ca_xRuO_3$ [168, 169], both in a suppression of spectral weight near E_F compared to band structure predictions [170] and in the systematic transfer of spectral weight from the incoherent to coherent parts of the spectral response with decreasing electronic correlations U/W. The latter trend in particular is quite similar to that observed in the titanate and vanadate systems (see Sect. 3.2.1). Second, the ratio of the effective mass m^* to the band mass m_b was found by Ahn et al. to increase systematically from $m^*/m_b \sim 2.2$ in $SrRuO_3$, to $m^*/m_b \sim 3.2$ in $Ca_{0.5}Sr_{0.5}RuO_3$, and finally to $m^*/m_b \sim 4$ in $CaRuO_3$ [73]. While these values are less than those estimated from specific heat measurements ($m^*/m_b \sim 3.2$ in $SrRuO_3$ [169] and $m^*/m_b \sim 8$ in $CaRuO_3$ [171]), the observed trend in the effective mass is nevertheless indicative of a system approaching a Mott-type transition from the metallic side as a function of increasing U/W. Finally, Ahn et al. found that the quantity $(U/W)^2$ varies linearly with $1/m^*$, as expected from Eq. (12), with a critical value of the Mott–Hubbard transition $(U/W)_c \sim 2.7$. This estimated value is substantially larger than that estimated from quantum Monte Carlo simulations of the half-filled single band Hubbard model [72], $(U/W)_c \sim 1.5$, although a better comparison of model calculations with experiment requires consideration of the effects of doping away from half-filling.

We note finally that Raman scattering measurements of $SrRuO_3$ by Kirillov et al. [167] and Iliev et al. [172] show that the paramagnetic $\rightarrow$ ferromagnetic phase transition is accompanied by dramatic optical phonon anomalies, particularly a dramatic hardening of several O modes [172]. While these phonon anomalies have been generally attributed to changes in spin-phonon coupling below T_C in $SrRuO_3$ [167, 172], a more definitive assessment of these results requires more careful consideration of how the phonons are influenced by changes in carrier density [173] and lattice parameter through the ferromagnetic transition.

3.2.3.2
$(Sr_{1-x}Ca_x)_{n+1}Ru_nO_{3n+1}$

Recent optical and angle-resolved photoemission (ARPES) studies of the layered $(Sr_{1-x}Ca_x)_{n+1}Ru_nO_{3n+1}$ system [164] also found a trend toward increasing carrier effective mass as a function of increasing correlation strength U/W, similar to that observed in the three-dimensional ruthenates $(Sr,Ca)RuO_3$ [73], the vanadates [71], and the titanates [67, 91]. This trend is revealed in the low frequency optical measurements as a change from a Drude-like response in the "good" metal $Sr_3Ru_2O_7$, to a dominant mid-infrared band response in the "bad" metal $Ca_3Ru_2O_7$, and finally to the presence of a Mott–Hubbard insulating gap at $\Delta \sim 0.2$ eV, and a peak near 1.2 eV associated with the Hubbard U, in the Mott–Hubbard insulator Ca_2RuO_4 (Fig. 9). A similar trend is observed as a function of increasing Ca concentration in ARPES measurements of the $(Sr_{1-x}Ca_x)_3Ru_2O_7$ system.

In the intermediate correlation strength system, $Ca_3Ru_2O_2$, Raman Scattering results reveal a metal-insulator transition to an antiferromagnetic phase below $T_m \sim 50$ K, as evidenced by the development of a large charge gap
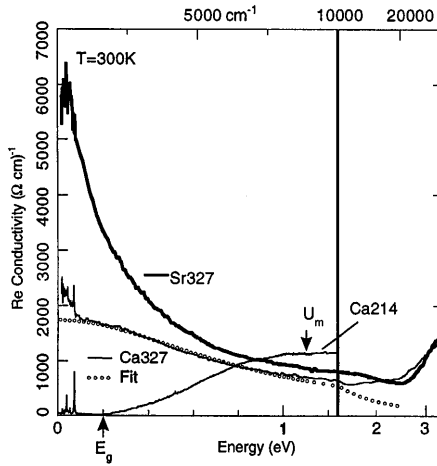
Fig. 9. Optical conductivity spectra of Ca_2RuO_4 (Ca214), $Ca_3Ru_2O_7$ (Ca327), and $Sr_3Ru_2O_7$ (Sr327) [164]

$2\Delta_c \sim 760$ cm^{-1} ($2\Delta_c/K_BT_M \sim 23$), by the softening of the 438 cm^{-1} out-of-phase c-axis O mode, and by the evolution of a two-magnon resonance near 58 cm^{-1}, from which an antiferromagnetic exchange coupling of $J \sim 8.7$ cm^{-1} was estimated [254].

At the low correlation strength end of the series, on the other hand, the in-plane transport and optical responses of Sr_2RuO_4 are characteristic of metallic behavior at all temperatures. However, the c-axis d.c. and optical [174] conductivities demonstrate that there is a change from non-metallic transport to metallic transport with a highly renormalized carrier effective mass below $T_M \sim 130$ K. While this behavior is clearly indicative of a crossover from quasi-two-dimensional to three-dimensional metallic behavior below T_M, there is as yet no satisfactory theoretical understanding of the nature of this crossover. Note also that a similar crossover from incoherent to coherent c-axis transport is also observed as a function of doping in the layered high T_c cuprates $La_{2-x}Sr_xCuO_4$ and (perhaps) $YBa_2Cu_3O_{6+x}$ [116] (see Sect. 3.1.2). However, c-axis transport behavior in the high T_c cuprates is clearly distinguished from that observed in the layered ruthenates in that there is no evidence for a temperature-induced incoherent $\rightarrow$ coherent crossover at high temperatures, suggesting that there may be something special in the nature of the in-plane charge dynamics of the cuprates that promotes incoherent c-axis transport.

3.3
Colossal Magnetoresistance and Metal-Insulator Transitions to DE Ferromagnetism

3.3.1
$A_{1-x}A'_xMnO_3$

There has been renewed interest in the past few years in the manganese perovskite series, $A_{1-x}A'_xMnO_3$ (A is a trivalent rare earth ion such as La, Pr, or

Nd, and A′ is a divalent alkali earth cation such as Ca, Sr, or Ba), due to the particularly rich phase diagram of this system [21, 175, 176]. With regard to *doping-induced changes* – the end members of $A_{1-x}A'_x MnO_3$, i.e., for $x = 0$ or 1, are antiferromagnetic or spin-canted insulators, but in the doping $0.2 \leq x \leq 0.5$, most of the $A_{1-x}A'_x MnO_3$ materials have a ferromagnetic metal ground state with a transition to a paramagnetic insulator high temperature phase above a doping-dependent Curie temperature, T_C (see, for example, top, Fig. 13). At still higher doping, $(x \geq 0.5)$ these systems generally exhibit "charge- and orbital-ordered" antiferromagnetic insulating ground states in which the charges and orbital configurations exhibit various periodic patterns (see Sect. 3.4.1). With regard to *bandwidth-controlled changes* – as the ionic radius of the A′ site in $A_{1-x}A'_x MnO_3$ is decreased (i.e., decreasing tolerance factor t) from the $La_{1-x}Sr_x MnO_3$ system to the $Nd_{1-x}Sr_x MnO_3$ system and finally to the $La_{1-x}Ca_x MnO_3$ system, there is an increase in the orthorhombic distortion, and a concomitant decrease in the bandwidth W, which results generally in an enhancement of electron-lattice coupling and charge/orbital ordering effects [70].

The novel transport and optical properties of the $A_{1-x}A'_x MnO_3$ system are influenced by two key features of the electronic structure (Table 5). The first is *strong Hund's rule exchange coupling*: the $A_{1-x}A'_x MnO_3$ system contains $(4 - x)$ Mn d electrons, three of which occupy the t_{2g} levels, d_{xy}, d_{yz}, and d_{zx}, providing a strongly localized core spin of $S_c = 3/2$, while the remaining $(1 - x)$ electron occupies the e_g level with its spin oriented parallel to the core spin due to a large Hund's rule exchange coupling, J_H, in this system. In the "double-exchange" description [6, 177–179], charge transport in $A_{1-x}A'_x MnO_3$ occurs via hopping of the spin-polarized e_g electron between Mn^{3+} and Mn^{4+} sites. The resulting spin-dependent hopping largely accounts for the dramatic "colossal magnetoresistance" behavior observed in the $A_{1-x}A'_x MnO_3$ system. The second is *Jahn–Teller distortion*: the $t_{2g}^3 e_g^1$ configuration of the Mn^{3+} ion in $A_{1-x}A'_x MnO_3$, favors a symmetry-breaking Jahn–Teller distortion that lifts the twofold degeneracy of the $Mn[3d(e_g)]$ level. Millis et al. have argued that Jahn–Teller distortions in $A_{1-x}A'_x MnO_3$ strongly influence transport by localizing the carriers in polaronic states [180–182], although the importance of "breathing mode" distortions in these materials has also been stressed [13]. Indeed, there is now substantial evidence that the charge dynamics in the paramagnetic phase of the lower T_C $A_{1-x}A'_x MnO_3$ materials is dominated by the hopping of small magnetoelastic polarons [37, 38], and that the strongly field-dependent sizes of small magnetoelastic polarons contribute to colossal magnetoresistance behavior in the low doped regime of the

Table 5. Electronic parameters for various manganese perovskite systems

Material	E_{JT}	Δ_{CT}	J_H	W	References
$LaMnO_3$	∼1 eV	∼4 eV	∼3 eV	2.45 eV	188–192
$La_{0.7}Sr_{0.3}MnO_3$	∼1 eV	∼4 eV	3 eV	2.2 eV	188–192

manganites. Notably, pure spin polaron formation near T_C is observed in other metallic ferromagnets exhibiting large negative magnetoresistance, including EuB_6 [41], EuO [183], the Mn pyrochlores $Tl_2Mn_2O_7$ [184–186], and $La_{1-x}Sr_xCoO_3$ [89, 187], but the CMR manganites are distinguished by the substantial enhancement of magnetoresistivity due to strong electron-lattice coupling [187].

3.3.1.1
Key Optical Features in $A_{1-x}A'_xMnO_3$ (x < 0.5)

The electronic structure of the $A_{1-x}A'_xMnO_3$ system for x < 0.5 has been investigated in a number of optical studies [39, 188–192], although there remains some disagreement as to the key energy scales associated with this system. Several optical features have been reported below ∼5 eV: (i) an absorption peak observed near ∼4 eV, which is generally agreed to be the $O(2p) \rightarrow Mn[3d(e_g)]$ charge transfer gap energy, Δ_{CT} [188–192]; (ii) a peak observed between 1 eV and 1.5 eV, generally attributed to a "parallel spin" $e_g \rightarrow e_g$ transition in which an electron makes a transition from the lower Jahn–Teller-split e_g level of one Mn^{3+} site to the upper Jahn–Teller-split e_g level of another Mn^{3+} site, with its spin *parallel* to the core spins of the two sites [188–191]. The energy of this transition is expected to be $U + E_{JT}$, where U is the Hubbard repulsion between two e_g electrons on the same final site and E_{JT} is the Jahn–Teller distortion energy; however, Quijada et al. have argued that the effective U describing the low energy physics (<4 eV) of the e_g band is small [191], suggesting that the 1–1.5 eV absorption peak represents reasonably well the Jahn–Teller distortion energy E_{JT} in these materials; (iii) Quijada et al. have identified a weak optical transition observed near ∼3 eV with the "antiparallel spin" $e_g \rightarrow e_g$ transition, in which an electron is excited from the lower Jahn–Teller-split e_g level of one Mn^{3+} site to the upper Jahn–Teller-split e_g level of another Mn^{3+} site, such that the final state electron spin is *antiparallel* to the core spin of the second site [191]. This transition has a non-zero optical matrix element above T = 0 in the ferromagnetic phase due to thermal disordering of the core spins, and has an energy $\sim U + E_{JT} + J_H$, where J_H is the Hund's exchange energy; (iv) finally, Jung et al. have reported a ∼0.5 eV absorption in the optical conductivity of $La_{0.7}Ca_{0.3}MnO_3$, which they attribute to a transition from one e_g orbital to another e_g orbital *on the same site* [188, 189]. However, this interpretation has been questioned, as such an intra-site e_g transition is dipole-forbidden and should therefore have a much smaller oscillator strength than is actually observed for the 0.5 eV absorption band [191].

Interestingly, an analysis of the measured integrated spectral weights associated with the "parallel" (N_{eff}^{par}) and "antiparallel" (N_{eff}^{anti}) transitions by Quijada suggests a spectral weight ratio of roughly $N_{eff}^{anti}/N_{eff}^{par} \sim 1/3$, which is consistent with a theoretical estimate of this ratio using a double-exchange model, absent electron-electron and electron-phonon interactions [191]. This appears to suggest that the effects of these two interactions on the carrier kinetic energy are weak. Quijada et al. also note that the spin-stiffness constant D associated with magnon dispersion ($\hbar\omega_{magnon} = Dq^2$) should be related to

the optical spectral weight N_{eff} in double-exchange ferromagnets, since D influences the intersite hopping amplitude for the carriers in the double-exchange (DE) model. These authors are able to obtain reasonable estimates of D, using both an estimate of the e_g carrier kinetic energy K ($\sim N_{eff}$) from their optical measurements and a simple relationship between the spin-stiffness and carrier kinetic energy that ignores electron-electron and electron-phonon interaction effects [191]:

$$D = \frac{Ka_o^2}{4S_c}\left[1 - \frac{\alpha t^2}{J_H S_c K}\right] \tag{13}$$

where a_o is the lattice parameter, S_c is the core spin (=3/2 in the manganites), J_H is the Hund's rule exchange coupling, and $\alpha = 1.04$.

The temperature induced ferromagnetic metal $\rightarrow$ paramagnetic insulator transition in $A_{1-x}A'_x MnO_3$ (0.2 < x < 0.5) is characterized in the optical response by [190–193] (top, Fig. 10): (a) a gradual suppression of the electronic contribution to the optical conductivity below $\omega \sim 1.5$ eV, revealing the presence of an optical gap; (b) a concomitant redistribution of low frequency electronic spectral weight to frequencies above the optical gap; and (c) the appearance of sharp phonon features inside the optical gap due to the dramatic reduction in screening charges. Similar properties are observed in the temperature-induced MI transitions of V_2O_3 [147, 148, 194, 195], VO_2 [94, 196, 197], $NdNiO_3$ [157], $LaCoO_3$ [89], and $BaPb_{0.67}Bi_{0.33}O_3$ [126]. The suppression of the low frequency optical conductivity as a function of increasing T (and decreasing H) in $A_{1-x}A'_x MnO_3$ primarily reflects two competing effects: (a) a gradual misalignment of the core spins, and the consequent reduction in carrier kinetic energy $K(\omega)\left(\frac{a_o}{mV_{cell}}N_{eff}(\omega)\right)$ via the double-exchange mechanism, with increasing temperature above T = 0; and (b) an increase in the electron-phonon coupling with decreasing K, which results in additional decreases in the carrier kinetic energy (and N_{eff}) [181]. Recent calculations have also stressed the influence of orbital fluctuations on the optical conductivity in the manganites [198–200]. Importantly, a spectral weight redistribution in the optical response of $A_{1-x}A'_x MnO_3$ can also be induced by increasing the magnetic field, confirming that the optical spectral weight changes that betray the MI transition are correlated with the changing spin polarization of the system [190]. The effects of magnetic field on DE transport are also manifest in the electronic Raman scattering spectrum of $A_{1-x}A'_x MnO_3$, which exhibits a collision-dominated scattering response (Eq. 11) in the paramagnetic phase [39, 55] that is strongly field-dependent near T_C in certain scattering geometries [55], reflecting the strong field-dependence of the carrier-spin scattering rate for carrier hopping along the Mn—O bonds.

3.3.1.2
Polaron Effects and the Inhomogeneous FM Metal State

There is substantial transport, optical, and Raman scattering evidence that the charge dynamics in the paramagnetic phase of the $A_{1-x}A'_x MnO_3$ system
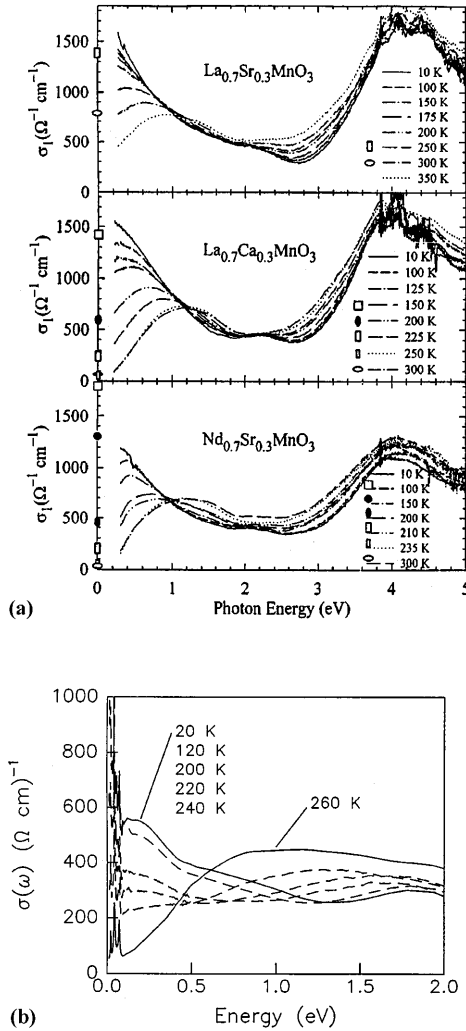
Fig. 10. (*top*) Optical conductivity spectra of $La_{0.7}Sr_{0.3}MnO_3$, $La_{0.7}Ca_{0.3}MnO_3$, and $Nd_{0.7}Sr_{0.3}MnO_3$ as a function of temperature [191]. (*bottom*) Optical conductivity of $La_{0.7}Ca_{0.3}MnO_3$ as a function of temperature [203]

is dominated by small polarons, and that the paramagnetic insulator → ferromagnetic metal transition in $A_{1-x}A'_xMnO_3$ (x ≤ 0.5) is associated with a crossover from small- to large-polaron behavior [39, 191]. For example, small- to large-polaron crossover is manifest in electronic Raman scattering measurements of several $A_{1-x}A'_xMnO_3$ materials as a change from a collision-limited electronic scattering response (see Eq. 11) in the PM phase, reflecting incoherent hopping of the carriers, to a flat continuum response in the FM phase typical of carrier scattering in a strongly-correlated metal [39, 55] (Fig. 11a). Also, optical measurements of several $A_{1-x}A'_xMnO_3$ materials with
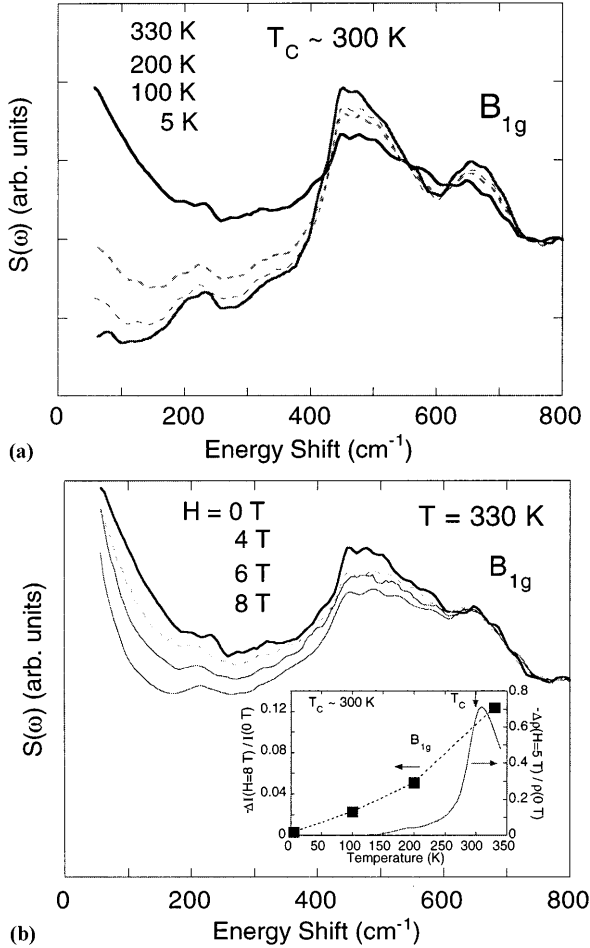
Fig. 11. Electronic Raman scattering spectra of La$_{1.63}$Sr$_{0.37}$MnO$_3$ as a function of (*top*) temperature and (*bottom*) magnetic-field. (*inset*) field-dependence of electronic Raman scattering intensity (*solid squares*) compared to the magnetoresistivity [55]

x ≤ 0.5 materials reveal a gradual merging of the ∼1 eV "Jahn–Teller polaron" peak into a Drude-like response with decreasing temperature [191, 201] (Fig. 10a) which has been attributed to incoherent → coherent (i.e., small polaron → large polaron) crossover of the charge dynamics as these systems transit into the ferromagnetic metal state. We note, finally, that Kim et al. observe an abrupt hardening of infrared-active Mn—O phonon modes below T$_C$, which they attribute to the effects of small- to large-polaron crossover [202]. However, Raman scattering measurements do not show any evidence for anomalous hardening of phonons below T$_C$ in the doped materials [39, 203]; on the other hand, these Raman studies do reveal an abrupt narrowing of the Mn—O bending and stretch modes below T$_C$, which is attributed to

the increased ordering of the MnO_6 octahedra observed in other measurements [204, 205] below the MI transition (Fig. 11a). On the other hand, an abrupt softening of the ~ 600 cm^{-1} B_{1g} mode is observed by Raman scattering at the paramagnetic insulator to canted-antiferromagnet transition ($T_N \sim 140$ K) in undoped $LaMnO_3$ [206].

Significantly, the formation of small magnetic polarons near the metal-insulator transition, and small- to large polaron crossover behavior, is not unique to the manganese perovskites, as similar behavior has been reported in low T_C ferromagnetic metals such as the Mn pyrochlores [185], EuO [183], and EuB_6 [41]; indeed, it is likely that giant magnetoresistance behavior near T_C in many ferromagnetic metals derives in part from the presence of such polarons, due to the strong sensitivity of magnetic polaron size and overlap to magnetic field and temperature near T_C. However, polarons in the manganites are distinguished by the large lattice component, which amplifies the magnetoresistivity effects [187], and appears to expand greatly the doping range over which polarons are stable. Indeed, perhaps the most interesting feature of double-exchange ferromagnetism in $A_{1-x}A'_xMnO_3$ materials is experimental evidence that the polaronic distortions which nucleate in the PM phase persist well into the ferromagnetic state [39, 207, 208], indicating a novel low temperature phase in these materials that consists of coexisting metallic and insulating meso-scale regions. These results are consistent with recent analytical [209] and numerical [9, 210, 211] studies showing that double-exchange systems are unstable towards electronic phase separation over a wide range of doping.

Several optical results support evidence for an inhomogeneous ferromagnetic phase in $A_{1-x}A'_xMnO_3$ systems, involving the coexistence of hole-rich and hole-poor regions. For example, the electronic Raman scattering response of $A_{1-x}Sr_xMnO_3$ ($x \sim 0.37$) exhibits a noticeable magnetic-field dependence well below the MI transition measured by d.c. transport (Fig. 11b) [55], suggesting that small insulating regions persist into the ferromagnetic metallic phase. Furthermore, both Raman scattering [39] and infrared reflectivity studies [203, 212] (Fig. 10b) show a clear signature in their respective optical responses that small polaron absorption near 0.2 eV persists well into the ferromagnetic metal phase of the $A_{1-x}(Sr,Ca)_xMnO_3$ system. These results suggest that the paramagnetic insulator to ferromagnetic metal transition of the smaller bandwidth manganese perovskites may involve a percolation transition of metallic clusters that coexist at low temperatures with remnant insulating regions. In support of this picture, measurements of the critical behavior in the $A_{1-x}A'_xMnO_3$ system indicates that the ferromagnetic transition becomes increasingly first-order in lower T_C materials [213].

The nature and origin of phase separation behavior in the FM state of the manganites, and its relationship to similar phase separation behavior observed in the charge-ordered regime of the manganites (see Sect. 3.4.1), remain important unresolved theoretical and experimental issues. Computational studies observe clear "phase separation" regimes in the phase diagram of manganese perovskites where the electronic compressibility diverges; these studies also show that phases proximate to phase separation regimes, such as the DE ferromagnetic phase, also exhibit a propensity towards charge clustering

due to an enhancement of charge-fluctuations in these phase regimes [9]. It is also interesting to note that the dramatic electronic inhomogeneity observed in the ferromagnetic phase of the manganites appears to differ from that observed in ferromagnetic metals with weak electron-lattice coupling such as EuB_6 [41], EuO [183], and the Mn pyrocholores $Tl_2Mn_2O_7$ [185], suggesting that strong electron-lattice coupling may also be important for stabilizing the inhomogeneous ferromagnetic phase. More experimental and theoretical investigation is clearly needed to examine these important issues.

3.3.2
$La_{2-2x}Sr_{1+2x}Mn_2O_7$

The layered manganese oxide system $La_{2-2x}Sr_{1+2x}Mn_2O_7$ also exhibits a rich phase diagram which depends sensitively on doping x [70]. For example, $La_{1.2}Sr_{1.8}Mn_2O_7$ exhibits a number of interesting properties, including a large transport anisotropy [214], a paramagnetic insulating state above $T_C \sim 126$ K [215] that is characterized by a mixture of fluctuating ferromagnetic and antiferromagnetic meso-scale regions [214], magnetic polaron formation [216] and colossal magnetoresistance behavior [215] in the vicinity of T_C, and a paramagnetic insulator to ferromagnetic metal transition below T_C. There has been little optical study of this interesting system, but three recent investigations reporting evidence for strong electron-phonon coupling and polaronic effects in these layered manganese oxides should be noted. First, photoemission measurements by Dessau et al. [217] found that the observed energy band dispersions and Fermi surface crossings in $La_{1.2}Sr_{1.8}Mn_2O_7$ agree reasonably well with local spin density approximation (LSDA) predictions, but that there was a strong suppression of spectral weight near the Fermi energy that the authors attributed to strong electron-phonon coupling effects. Second, X-ray absorption spectroscopy measurements of $La_{2-2x}Sr_{1+2x}Mn_2O_7$ (x = 0.35, 0.40) show that the temperature-dependent insulator to metal transition involves an increase in the density of states at the Fermi energy due to a transfer of spectral weight to the absorption threshold [218]. As discussed in Sect. 3.1, similar behavior is observed in bandfilling-controlled metal-insulator transitions of the high T_c cuprates [83, 84], titanates [64, 65, 67], and vanadates [66, 68]. However, an interesting difference in the $La_{2-x}Sr_{1+2x}Mn_2O_7$ system is that the charge-carriers appear to have both out-of-plane and in-plane character, reflecting the strong competition between the tetragonal lattice distortion and the charge dynamics in this material [218]. Finally, Raman scattering measurements of $La_{1.2}Sr_{1.8}Mn_2O_7$ by Romero et al. [219] revealed two interesting features: (a) the energy of the ~ 325 cm^{-1} B_{1g} symmetry O phonon mode increases with decreasing temperature in the paramagnetic insulator phase, in a manner reminiscent of the activated temperature-dependence of the resistivity, but begins to soften abruptly below the MI transition at T_C – the authors attribute this behavior to direct coupling of the B_{1g}-symmetry mode to polaronic charge fluctuations; however, another interpretation is that the large hardening of the phonon mode reflects the large temperature-dependent changes observed in both the Mn—O_z bond length [220] and the c-axis magnetostriction [221] above

and below T_C (associated with the stabilization of the $d_{3z^2-r^2}$ orbital state [221]), to which the out-of-phase c-axis B_{1g} mode frequency should be highly sensitive; (b) also, Romero et al. observe a broad scattering response near 450 cm^{-1} that is strongly suppressed both with increasing magnetic field near T_C and upon entering the ferromagnetic phase, which they attribute to some form of magnetic scattering [219]. However, the rather structured lineshape associated with the observed scattering response suggests a phononic origin for this peak; indeed, one interesting possibility is that this feature is "defect"-induced phonon scattering above T_C caused by spin-disorder, an interpretation which also accounts for the observed strong suppression of scattering both in the ferromagnetic phase and as a function of increasing field near T_C. We note, finally, that ESR evidence for magnetic polarons near the metal-insulator transition of $La_{1.35}Sr_{1.65}Mn_2O_7$ suggests that a direct optical signature for polaron formation might be observable. Such signatures would include spin-flip Raman scattering, similar to that observed for magnetic polarons in EuB_6 [41], or polaron photoionization, similar to that observed in $A_{1-x}A'_xMnO_3$ via optical reflectivity [203] and Raman scattering [39].

3.4
Charge-Ordering Transitions

Among the most interesting phenomena exhibited by the 3d transition metal perovskites is the real-space ordering of charge, i.e., charge-ordering (CO), which arises primarily due to a combination of strong electron-electron correlations, exchange interactions, electron-phonon coupling, and the commensurability of the carrier concentration with the periodicity of the lattice [23, 222, 223]. Among the significant issues which need to be better understood in these systems include:

1. What is the process by which individual small polarons in more electronically-disordered phase regions organize to form charge-"stripes"
2. What are the dynamics of charge "stripes"
3. How do these dynamics influence the nature of the ground state in doped antiferromagnetic insulators [224]

Optical investigations have only recently begun to address these and other related issues.

3.4.1
$A_{1-x}Ca_xMnO_3$

A particularly interesting example of CO behavior is observed in Mn—O systems such as $Pr_{1-x}Ca_xMnO_3$ ($0.3 < x < 0.5$) [20] and $(La,Bi)_{1-x}Ca_xMnO_3$ ($0.5 < x < 0.7$) [225], as the orbital degree of freedom associated with the Mn^{3+} sites results in a rich interplay between orbital and charge ordering as a function of bandwidth.

Several optical investigations of charge ordering transitions in Ca-based manganese perovskites have been performed. Okimoto et al. performed
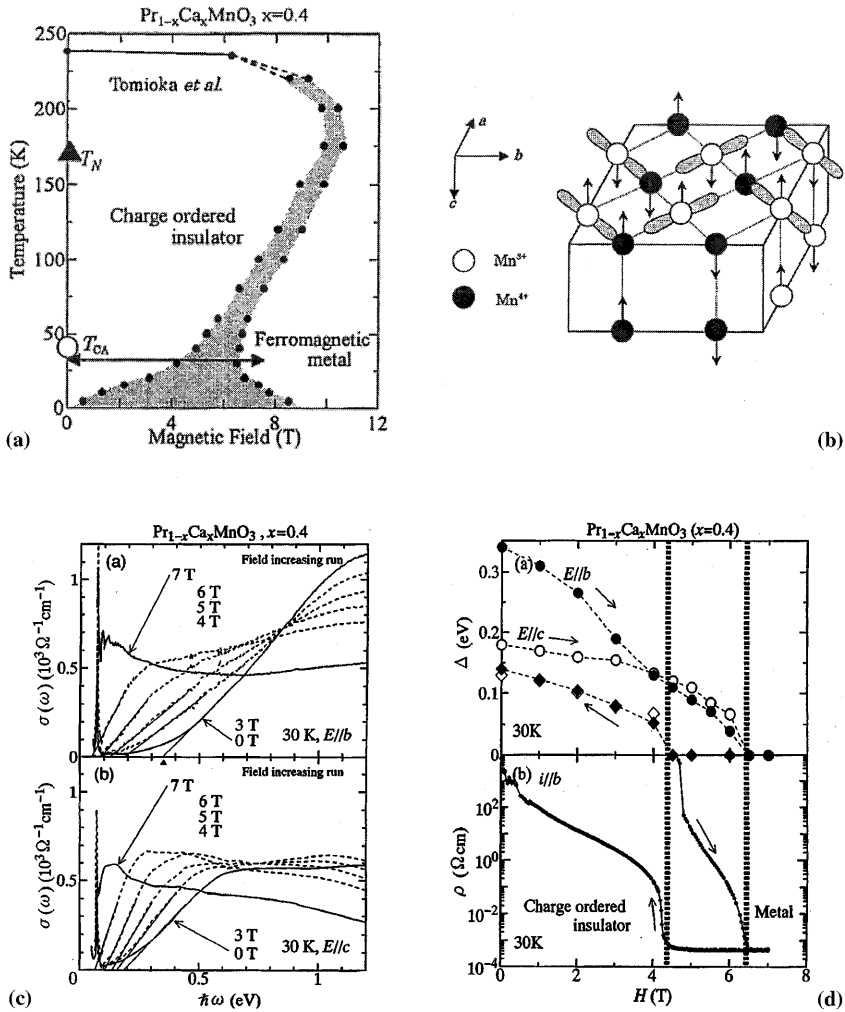
Fig. 12. (*top*) Phase diagram for $Pr_{1-x}Ca_xMnO_3$ (x = 0.4) (*left*) and CE-type ordering (*right*). (*bottom*) Optical conductivity spectra of $Pr_{1-x}Ca_xMnO_3$ (x = 0.4) for light polarized along the b- (E||b) and c- (E||c) axis (*left*), and charge gaps (Δ_b, Δ_c) and resistivity ρ as a function of magnetic field (*right*) [225]

temperature- and field-dependent optical measurements of the $Pr_{1-x}Ca_xMnO_3$ system for 0.3 < x < 0.5 [226, 227]. This material exhibits an antiferromagnetic *CE*-type [6, 228] ordered ground state (Fig. 12a, b) in this phase regime, in which the Mn^{3+} and M^{4+} species are regularly arranged on the lattice, and the $d_{3x^2-r^2}$ and $d_{3y^2-r^2}$ orbitals at the Mn^{3+} site are alternately ordered in the ab-plane. The optical results of Okimoto et al. indicate three key features [226, 227] (Fig. 12c, d). First, there is a suppression of low frequency spectral weight in the optical conductivity with decreasing temperature below the charge

ordering transition, T_{co} = 235 K, reflecting the development of a charge gap in the CO state. Notably, the optical conductivity spectra of the CO systems $La_{1.67}Sr_{0.33}NiO_4$ [229] (see Sect. 3.4.3), $La_{1/3}Sr_{2/3}FeO_3$ [230] (see Sect. 3.4.2), and Fe_3O_4 [231] exhibit similar changes due to charge-ordering. Second, in the CO state, Okimoto et al. observed an asymmetry between the charge gap measured with the electric field oriented in the plane of the e_g orbitals (**E**∥**b**), Δ_b = 0.34 eV (at H = 0), and that measured with the electric field perpendicular to the *ab*-plane (**E**∥**c**), Δ_c = 0.18 eV (H = 0), consistent with the *CE*-type charge and orbital ordering expected for this material (Fig. 12c, d). Finally, the charge-ordered structure gradually "melts," and the charge gaps Δ_b and Δ_c collapse, upon application of a magnetic field, leading to an eventual "magnetic-field-induced" insulator-metal transition into a ferromagnetic metallic phase at $H_c \sim$ 6.5 T. This magnetic-field induced transition involves a redistribution of spectral weight up to energies as high as ~3 eV, suggesting that the melting of the charge ordered state involves a modification of electronic states over a very wide energy range. This transition also reflects the strong connection between charge and Neel ordering. An interesting question not addressed in these studies is whether there is evidence for electronic phase separation behavior [9] at any stage of the magnetic-field-induced "melting process", which might for example provide information about the process by which charges order (or disorder), and about the relationship between inhomogeneous phases in different phase regimes.

Temperature-induced "melting" or "disordering" of the charge-ordered state, and evidence for electronic phase separation behavior, has been explored in optical studies of the $(La,Bi)_{1-x}Ca_xMnO_3$ (x > 0.5) system [159, 232]. Neutron scattering studies show that the $(La,Bi)_{1-x}Ca_xMnO_3$ (x > 0.5) system exhibits three distinct temperature regimes [22, 233] (Fig. 13a): a high-temperature paramagnetic metal regime (T > T_O), characterized by ferromagnetic correlations arising from thermally-activated hopping of e_g electrons between Mn^{3+} and Mn^{4+} sites; a "charge-structural" temperature regime ($T_O > T > T_N$), in which charge superlattice intensity evolves due to incipient charge ordering; and an antiferromagnetic insulator regime (T < T_N), which is associated with long range charge/orbital ordering. The low frequency (<1 eV) optical conductivity in the high temperature phase (T > T_O) is characterized by a small polaron response similar to that observed in the paramagnetic phase of the manganese perovskites at low doping (0.3 < x < 0.5); this includes a Drude-like response due to activated hopping of the small polarons between Mn^{3+} and Mn^{4+} sites, and a broad mid-infrared (MIR) absorption band near 0.25 eV, attributable to photoionization of the small polarons (Fig. 13b) [159]. However, in the "charge-structural" temperature regime, $T_O > T > T_N$, the MIR band splits into two components [159]: (A) a remnant of the small polaron contribution, which decreases in intensity with decreasing temperature due to the gradual freezing out of the mobile small polarons, and (B) a higher energy peak near 0.6 eV that gradually evolves with a BCS-type temperature dependence into a complete charge gap at T_N. Below the Neel temperature (T < T_N), the optical response exhibits only a distinct charge gap, the development of which coincides with a resolvable splitting of the 555 cm^{-1}
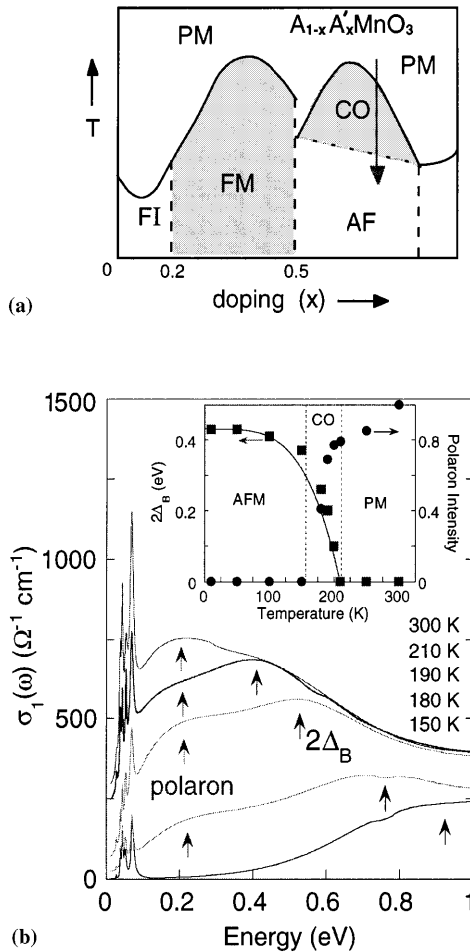
Fig. 13. (*top*) Phase diagram for $(La,Bi)_{1-x}Ca_xMnO_3$. (*bottom*) Optical conductivity of $Bi_{1-x}Ca_xMnO_3$ ($x \sim 0.87$) as a function of temperature, and (*inset*) gap energy 2Δ and polaron absorption intensity as a function of temperature [159]

Mn—O stretch mode; this confirms that charge gap formation below T_N is associated with long-range charge ordering. The most interesting feature of these optical results is that the "melting" transition between T_O and T_N is typified by "phase separation" behavior, i.e., a coexistence of both charge-ordered "domain" regions having predominantly AFM correlations, and "ferromagnetic" domain regions in which $Mn^{3+} \rightarrow O \rightarrow Mn^{4+}$ polaronic hopping persists. This phase-separation behavior is reminiscent of the domain formation and percolation behavior observed near the MI transitions of other systems, most notably through the doping-induced "melting" transition in $La_{1-x}Sr_xMnO_3$ ($x \sim 0.5$) [234], and through the Mott–Hubbard transition of VO_2 films [94]. Indeed, the ubiquity of this behavior suggests that phase

separation and domain formation is the natural means by which strongly charge-spin-lattice-coupled systems transit between disparate phase regimes. However, more detailed experimental study is warranted, particularly involving Raman scattering studies, which can best elucidate the impact of electronic phase separation on the lattice and spin degrees of freedom.

3.4.2
$La_{1−x}Sr_xFeO_3$

$La_{1/3}Sr_{2/3}FeO_3$ exhibits an interesting transition below T_{CO} = 198 K to a "valence-skipping" CO state that is characterized by sequential 2:1 ordering of Fe^{3+} and Fe^{5+} (1, 1, 1) sheets, as shown in the inset of Fig. 14a. The valence-skipping CO state of $La_{1/3}Sr_{2/3}FeO_3$ is reminiscent of the "site-diagonal" description of CDW formation in the bismuthates, wherein inequivalent Bi^{3+} and Bi^{5+} sites develop. However, it should be reiterated that magnetic interactions are likely to be important in the formation of the CO state in
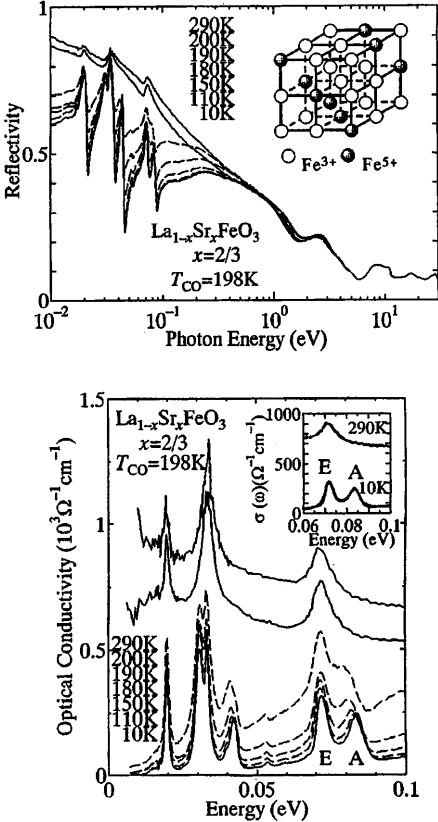
Fig. 14. (*top*) Optical reflectivity spectra. (*bottom*) Optical conductivity spectra of $La_{1.33}Sr_{0.67}FeO_3$ as a function of temperature. (*Top inset* – charge-ordering structure of $La_{1.33}Sr_{0.67}FeO_3$) [232]

$La_{1/3}Sr_{2/3}FeO_3$, in contrast with CDW or bipolaron development in the bismuthates.

Recent optical studies revealed two interesting consequences of the charge-ordering transition in $La_{1/3}Sr_{2/3}FeO_3$ [230] (Fig. 14). First, the CO transition activates several new optical phonon modes due to the additional periodic charge modulation. Interestingly, the spectral intensity of the activated phonon modes increases discontinuously at T_{CO}, consistent with the first-order nature of the CO transition. Second, the CO transition results in a continuous opening of an optical gap ($2\Delta_{max} \sim 0.13$ eV) with decreasing temperature below T_{CO}, presumably reflecting the effects of antiferromagnetic spin-ordering on the charge gap. Similar changes in optical or Raman spectra have also been observed through the CO transitions of $Pr_{0.6}Ca_{0.4}MnO_3$ [226, 227], $Bi_{1-x}Ca_xMnO_3$ (x = 0.74, 0.82) [159], $A_{0.5}Ba_{0.5}CoO_3$ (A = Gd, Eu, Sm) [235], and $La_{1.67}Sr_{0.33}NiO_4$ [229].

3.4.3
$A_{2-x}Sr_xNiO_4$

The two-dimensional nickelate systems $La_2NiO_{4.125}$ and $La_{1.67}Sr_{0.33}NiO_4$ are particularly noteworthy because they exhibit "charge-ordering" ($T_{CO} \sim 110$ K in $La_2NiO_{4.125}$, and $T_{CO} \sim 240$ K in $La_{1.67}Sr_{0.33}NiO_4$) transitions to an insulating phase in which the charge carriers order in striped domain regions along the [1, 1, 0] direction of the square Ni lattice. This charge ordering phenomena has been observed directly in neutron scattering [27, 28] and electron diffraction [23] measurements, and inferred from resistivity, magnetic susceptibility, and specific heat measurements [236, 237].

The high temperature phase of $La_{1.67}Sr_{0.33}NiO_4$ is characterized in the optical response by a peak near 0.5 eV, and by the absence of a Drude-like response, which is in contrast with the large Drude response observed in the three-dimensional $RNiO_3$ system [157]. Early interpretations of this high temperature optical response in $La_{1.67}Sr_{0.33}NiO_4$ invoked a small-polaron picture [106, 238]. However, more recently it was suggested [229] that the high temperature optical response of $La_{1.67}Sr_{0.33}NiO_4$ is dominated by fluctuations of the low temperature charge-ordered state above the ordering temperature T_{co}, which create a pseudogap and suppress the low frequency conductivity relative to that of the three-dimensional $RNiO_3$ system. Similar evidence for fluctuations of the ground state well above the transition temperature was also predicted for quasi-1D charge-density-wave (CDW) systems [239], and observed in quasi-two-dimensional charge-density-wave (CDW) systems such as *2H*-$TaSe_2$ [240]. McMillan [241] argued that the non-BCS-type behavior in two-dimensional CDW systems arises from the small coherence lengths in these systems, which cause T_c to be governed by lattice entropy rather than the entropy associated with particle-hole excitations across a gap. However, a similar formalism has not yet been extended to the effects of dimensionality on charge-ordering behavior in the layered transition metal perovskites.

Optical spectroscopic studies of CO behavior below T_{co} in $La_{1.67}Sr_{0.33}NiO_4$ reveal several interesting features, as shown in Fig. 15. First, as a function
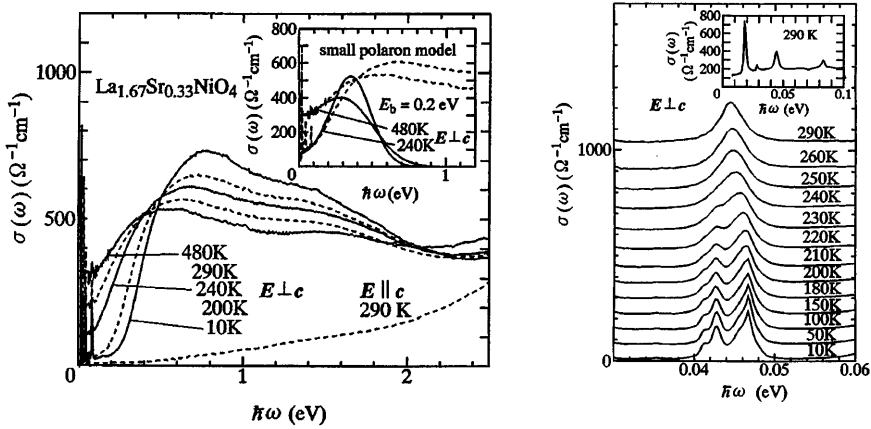
Fig. 15. (*left*) Optical conductivity spectra of $La_{1.67}Sr_{0.33}NiO_4$ as a function of temperature. (*right*) Splitting of ~ 0.044 eV Eu mode in $La_{1.67}Sr_{0.33}NiO_4$ below the charge-ordering transition [228]

of decreasing temperature below the charge-ordering transition T_{co}, optical spectral weight below 0.4 eV is suppressed and transferred to energies as high as 2 eV, reflecting the freezing out of itinerant charge. As in the case of the three-dimensional nickelates, the resulting gap in the optical conductivity has an onset that exhibits a BCS-like temperature dependence, typical of a CDW or SDW gap, but is associated with a gap parameter $2\Delta/k_B T_{co} \sim 13$ that is much larger than the conventional mean-field value of 3.5. While this enhanced gap parameter may reflect the effects of electronic correlations in this system, one also expects a non-BCS-type gap parameter due to a suppression of the ordering temperature in low dimensional systems [239, 241]. However, it is worth pointing out that a dramatic redistribution of spectral weight, as well as the development of an optical gap with a large gap parameter, is also observed below the charge-ordering transition of the three-dimensional manganites, $Pr_{0.6}Ca_{0.4}MnO_3$ [226, 227] and $Bi_{1-x}Ca_xMnO_3$ (x = 0.74, 0.82) [159], and thus there is as yet no compelling evidence for dimensionality effects in the optical response of $La_{1.67}Sr_{0.33}NiO_4$ below T_{co}.

Optical studies of $La_{1.67}Sr_{0.33}NiO_4$ below T_{co} also reveal two important lattice effects in the charge-ordered state (right, Fig. 15): a splitting of the doubly-degenerate (E_u) Ni—O bending mode near 0.044 eV, which is likely due to the lowering of crystal symmetry by the developing charge stripes, and the appearance of additional phonon peaks, which may arise from the "folding" of zone-boundary phonon modes onto the Γ point due to the additional superlattice periodicity of the charge-ordered state.

Finally, Raman measurements of $La_{1.67}Sr_{0.33}NiO_4$ [53, 242] show that the high temperature phase (T > T_{co}) is characterized by broad intraband electronic scattering that is reasonably well described by a collision-limited response (Eq. 11) [53]. However, several significant changes in the Raman scattering response occur in concert with the developing optical gap below the charge-
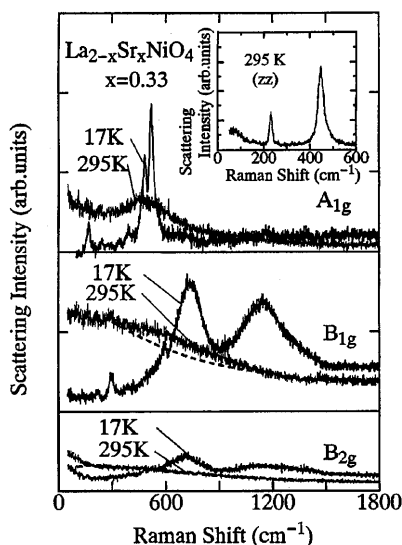
Fig. 16. Raman scattering spectra of $La_{1.67}Sr_{0.33}NiO_4$ as a function of temperature for various scattering geometries [53]

ordering transition, T_{co} [53, 242] (Fig. 16): a rapid disappearance of the intraband electronic scattering response; an abrupt development of Raman-inactive phonon peaks near 169 cm^{-1}, 483 cm^{-1}, and 519 cm^{-1} in the A_{1g} spectrum, presumably due to activation by lattice distortions accompanying the charge ordering transition; and the appearance of two-magnon excitations near both 735 cm^{-1} and 1150 cm^{-1} in the B_{1g} spectrum, which have been associated with double spin-flips within and across the domain walls, respectively.

3.5
Paramagnetic Metal to Non-Magnetic Insulator Transitions

3.5.1
$La_{1-x}Sr_xCoO_3$

The Co perovskite system $La_{1-x}(Sr,Ba)_xCoO_3$ exhibits rich behavior as a function of doping x. The undoped $LaCoO_3$ system exhibits successive magnetic ($T_m = 100$ K) and non-magnetic insulator $\rightarrow$ paramagnetic metal ($T_c = 500$ K) transitions that are associated with thermally induced excitations above a spin- and charge-gap, respectively. The latter transition is evidenced in the optical conductivity by a dramatic redistribution of spectral weight from above 1.3 eV to low energies with increasing temperature (Fig. 17) [89]. Interestingly, charge gap development through the paramagnetic metal $\rightarrow$ non-magnetic insulator transition in $LaCoO_3$ is remarkably similar in several respects to those observed by optical reflectivity [243, 244] and Raman scattering [50–52] in the so-called Kondo insulators, which include FeSi, SmB$_6$,
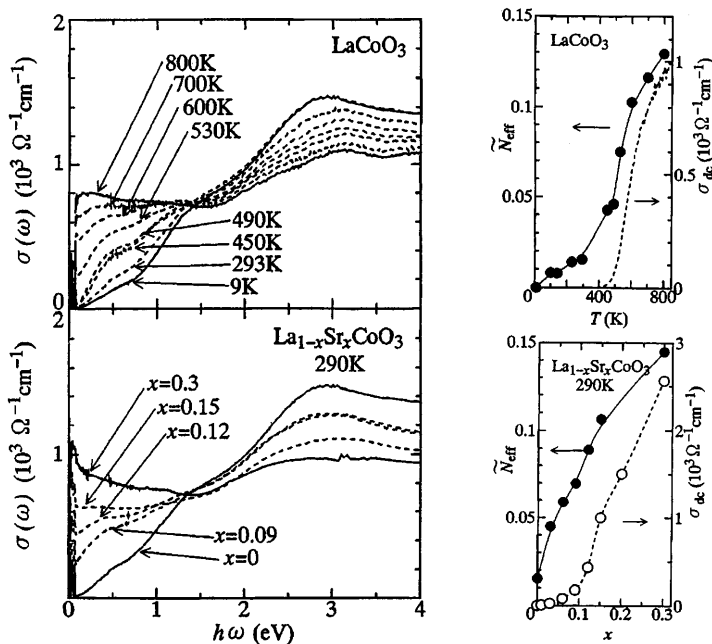
Fig. 17. (*top*) Optical conductivity and N_{eff} of $LaCoO_3$ as a function of temperature. (*bottom*) Optical conductivity and N_{eff} of $La_{1-x}Sr_xCoO_3$ as a function of x [89]

$Ce_3Bi_4Pt_3$ [245]): charge gap development in the Kondo insulators involves a redistribution of spectral weight from low to high frequencies, and influences electronic states over an energy scale that is much higher than the characteristic temperature at which gap development occurs. In the case of the Kondo insulators, the dramatic spectral weight redistribution is nicely accounted for in calculations of the periodic Anderson model [72].

In $LaCoO_3$, the successive charge and spin transitions derive primarily from two key features of the electronic structure (Table 6): (i) a small charge-transfer-type gap in the high-spin state, $\Delta_{CT} \sim 0.1$–0.2 eV [4, 40, 89], which is conducive to a thermally-induced Mott–Hubbard transition; and (ii) comparable values for the crystal field splitting (10Dq) between the t_{2g} and e_g levels and the Hund's rule coupling energy [246], which appears to be primarily responsible for the small spin gap ($\Delta_s \sim 0.02$–0.03 eV) between the low-spin ground state configuration, $(t_{2g})^6$ (S = 0), and the high-temperature excited spin state. There is some debate as to whether the high temperature spin state

Table 6. Electronic parameters for various cobalt perovskite systems

Material	Δ_{CT}	Δ_S	References
$LaCoO_3$	$\sim$0.1–0.2 eV	$\sim$0.02–0.03 eV	40, 89
$La_{0.4}Sr_{0.6}CoO_3$	$\sim$1 eV	$\sim$4.3 eV	89

of LaCoO$_3$ has a high-spin $(t_{2g})^4(e_g)^2$ (S = 2) or an intermediate-spin $(t_{2g})^5(e_g)^1$ (S = 1) configuration, but substantial recent evidence appears to support the latter. For example, photoemission measurements on LaCoO$_3$ [247] have been interpreted as favoring a $(t_{2g})^5(e_g)^1$ (S = 1) high-temperature configuration [248], while LDA + U calculations suggest that the S = 1 state is more stable than the S = 2 state in the high temperature regime due to strong p-d hybridization and orbital ordering [249]. Significantly, a key signature of the $(t_{2g})^5(e_g)^1$ (S = 1) state at high temperatures should be the presence of Jahn–Teller lattice distortions arising from the orbital degeneracy of the e_g electron in this configuration. Indeed, Yamaguchi et al. [250] observed an anomalous splitting of several Co—O infrared optical modes at high temperatures, which they associate with local Jahn-Teller lattice distortions that accompany the transition to the thermally excited intermediate $(t_{2g})^5(e_g)^1$ (S = 1) spin state of the Co^{3+} ions.

The doped La$_{1-x}$(Sr,Ba)$_x$CoO$_3$ system exhibits giant magnetotransport, double-exchange ferromagnetism [251], and possibly charge-ordering behavior for the commensurate doping level x = 0.5 [235], similar to the properties observed in the manganese perovskite system A$_{1-x}$A$'_x$MnO$_3$. Apart from Raman scattering evidence for interesting phonon intensity enhancements below the MI transition in the charge-ordered phase [235], there has as yet been little optical study of the La$_{1-x}$(Sr,Ba)$_x$CoO$_3$ system in the CO regime. However, several features of the optical response measured through the MI and spin transitions of LaCoO$_3$ and in the lightly-doped phase of La$_{1-x}$Sr$_x$CoO$_3$ are worth noting. First, La$_{1-x}$Sr$_x$CoO$_3$ exhibits a doping-induced MI transition with increasing x that has a nearly identical signature in the optical conductivity to the thermally-induced MI transition in LaCoO$_3$, namely a dramatic redistribution in spectral weight from above 1.3 eV to low energies with increasing x (La$_{1-x}$Sr$_x$CoO$_3$) or temperature (LaCoO$_3$) (Fig. 17). As stated previously, not only does this behavior reveal a symmetry between thermally- and doping-induced effects, but it typifies the bandfilling-controlled Mott–Hubbard transitions in other 3d transition metal oxides La$_{2-x}$Sr$_x$CuO$_4$ [84], Nd$_{2-x}$Ce$_x$CuO$_4$ [84], Pr$_{2-x}$Ce$_x$CuO$_4$ [83], and Y$_{1-x}$Ca$_x$VO$_3$ [68], and Y$_{1-x}$Ca$_x$TiO$_3$ [65]. Interestingly, the optical spectral weight changes observed both as a function of increased doping in La$_{1-x}$Sr$_x$CoO$_3$, and increased temperature in LaCoO$_3$, presage the respective MI transitions measured via the d.c. conductivity (right, Fig. 17), as they do in other doped Mott–Hubbard systems [64]. This precursor behavior in the optical response may be indicative of multiphase behavior at low doping or temperature in these systems, wherein small metallic domains nucleate at low doping or temperature, eventually evolving in size with doping until the bulk MI transition is achieved.

As in the case of other "colossal magnetoresistance" systems such as EuB$_6$ [41], EuO [183], and the perovskite manganites A$_{1-x}$A$'_x$MnO$_3$ (x < 0.5) [37, 38], hole-doping in LaCoO$_3$ also appears to lead to the formation of magnetic polarons with a large effective spin number (S = 10–16) [40], induced in part by the strong exchange interaction between the 2p hole and the Co 3d spins. An interesting open question regarding the La$_{1-x}$Sr$_x$CoO$_3$ system concerns the

possibility of an electronically inhomogeneous ferromagnetic phase comprised of coexisting hole-rich and hole-poor regions, similar to that observed in $A_{1-x}A'_xMnO_3$ (see Sect. 3.3.1). Recent measurements of the critical exponents of the paramagnetic-ferromagnetic phase transition in $La_{1-x}Sr_xCoO_3$ indeed suggest such behavior [252]; this is significant, as the $La_{1-x}Sr_xCoO_3$ system lacks the large Jahn-Teller distortions of the $A_{1-x}A'_xMnO_3$ system, and hence a careful comparison of electronic inhomogeneity in these two systems may afford some insight into how electron-lattice coupling influences electronic inhomogeneity in the ferromagnetic phases of these systems. Optical studies comparing the metal-insulator transitions and ferromagnetic phases of these two systems would consequently be highly informative.

4
Summary

This article has attempted to convey, from the unique perspective of optical measurements, the intricate and complex phase behavior created in the ternary transition metal oxides by the strong coupling of spin-, charge-, and lattice-degrees of freedom. In spite of the numerous experimental studies of metal-insulator transitions in perovskite-related oxides described in this article, it is clear that many important avenues remain to be explored. For example, the ground state of lightly doped antiferromagnetic insulators can be variously charge-ordered, superconducting, or non-Fermi liquid metallic [224], but it is not yet known how the complex interplay among the spin-, charge-, lattice-, and orbital-degrees-of-freedom favors one ground state over another in the ternary transition metal oxides. Furthermore, neither the process by which the charge-ordered states of transition metal perovskites "melt", either as a function of temperature, magnetic field, or doping away from commensurate values of the bandfilling, into complex metallic phases, nor the nature of these complex phases, is well understood. Finally, perhaps the most intriguing unresolved questions concern the nature of electronic inhomogeneity in the transition metal perovskites; in particular, how ubiquitous is such behavior across the transition metal series (i.e., is it specific to charge-transfer type systems such as the manganites, cobaltites, nickelates, etc., and if so, why?), what is the relationship between various forms of electronic inhomogeneity observed in different phase regimes of the transition metal perovskites, and what is the role of dimensionality, the exchange interaction, electron-phonon coupling, etc., on the nature and stability of electronic inhomogeneity.

To address these and many other questions in the complex oxides adequately, we must increasingly rely upon sophisticated experimental methods that are capable of conveying detailed information about the intricate relationship among the lattice-, spin-, charge-, and orbital degrees of freedom on widely varying spatial and temporal scales. Fortunately, numerous optical techniques are beginning to show promise in unveiling new aspects of the rich physics associated with metal-insulator transitions in complex oxides.

For example, near-field and time-resolved optical techniques provide an opportunity for exploring the charge dynamics of TM oxide systems on atomic spatial scales (of particular importance in inhomogeneous and charge-ordered phases), and on short time scales (e.g., polaron hopping times). Resonant Raman scattering, having clearly demonstrated its efficacy in the high T_c cuprates, needs to be more generally applied in the complex oxides to elucidate specific details regarding the importance and nature of electron-lattice and electron-spin interaction effects. Electronic Raman scattering has been shown to be quite effective at probing changes in the charge-, spin-, and lattice-dynamics through various metal-insulator transitions. Future extensions of these investigations should further exploit the relative ease with which pressure, magnetic field, and time-resolved studies can be performed using this technique, to enable more detailed investigations of the low frequency excitation spectra of TM oxides, and of the evolution of these spectra across various phase boundaries. Finally, new techniques such as resonant X-ray Raman spectroscopy [253] are evolving as a means by which important **q**-dependent information about inelastic excitations can be explored, possibly providing new insights into charge-stripe formation and orbital fluctuations. The marriage of these promising optical techniques with the rich physical phenomena exhibited by the complex oxides appears certain to provide many years of fruitful exploration and discovery.

5
References

1. Zaanen J, Sawatzky GA, Allen JW (1985) Phys Rev Lett 55: 418
2. Torrance JB, Lacorre P, Asavaroengchai C, Metzger RM (1991) J Sol State Chemistry 90: 168
3. Sawatzky GA (1990) Earlier and recent aspects of superconductivity. In: Bednorz JG, Müller KA (eds) Springer Series in Solid State Physics, Springer, Berlin Heidelberg New York, vol 90, p 345
4. Arima T, Tokura Y, Torrance JB (1993) Phys Rev B 48: 17,006
5. Brinkman WF, Rice TM (1970) Phys Rev B 2: 4302
6. Goodenough JB (1955) Phys Rev 100: 564
7. Goodenough JB (1958) J Phys Chem Solids 6: 287
8. Kanemori J (1959) J Phys Chem Solids 10: 87
9. Moreo A, Yunoki S, Dagotto E (1999) Science 283: 2034
10. Emery VJ, Kivelson SA, Zachar O (1997) Phys Rev B 56: 6120
11. Millis AJ, Shraiman BI, Mueller R (1996) Phys Rev Lett 77: 175
12. Roder H, Zhang J, Bishop AR (1996) Phys Rev Lett 76: 1356
13. Varma CM (1996) Phys Rev B 54: 7328
14. Yu ZG, Zang J, Gammel JT, Bishop AR (1998) Phys Rev B 57: R3241

15. Moskvin AS (1998) Physica B 252: 186
16. Takano M, Kawachi J, Nakanishi N, Takeda Y (1981) J Solid State Chem 39: 75
17. Battle PD, Gibb TC, Lightfoot P (1990) J Solid State Chem 84: 271
18. Li JQ, Matsui Y, Park SK, Tokura Y (1997) Phys Rev Lett 79: 297
19. Jirak Z, Krupicka S, Simsa Z, Dlouha M, Vratislav S (1985) J Magn Magn Mater 53: 153
20. Tomioka Y, Asamitsu A, Moritomo Y, Kuwahara H, Tokura Y (1995) Phys Rev Lett 74: 5108
21. Chen CH, Cheong SW (1996) Phys Rev Lett 76: 4042
22. Cheong SW, Hwang HY (1999) In: Tokura Y (ed) Colossal magnetoresistance oxides. Gordon and Breach
23. Chen CH, Cheong SW, Cooper AS (1993) Phys Rev Lett 71: 2461
24. Hayden SM, Lander GH, Zarestky J, Brown PJ, Stassis C, Metcalf P, Honig JM (1992) Phys Rev Lett 68: 1061
25. Sachan V, Buttrey DJ, Tranquada JM, Lorenzo JE, Shirane G (1995) Phys Rev B 51: 12,742
26. Sternlieb BJ, Hill JP, Wildgruber UC, Luke GM, Nachumi B, Moritomo Y, Tokura Y (1996) Phys Rev Lett 76: 2169
27. Tranquada JM, Buttery DJ, Rice DE (1993) Phys Rev Lett 70: 445
28. Tranquada JM, Lorenzo JE, Buttrey DJ, Sachan V (1995) Phys Rev B 52: 3581
29. Zaanen J, Gunnarsson O (1989) Phys Rev B 40: 7391
30. Zaanen J, Littlewood PB (1994) Phys Rev B 50: 7222
31. Inui M, Littlewood PB (1991) Phys Rev B 44: 4415
32. Poilblanc D, Rice TM (1989) Phys Rev B 39: 9749
33. Kato M, Machida K, Nakanishi H, Fujita M (1990) J Phys Soc Jpn 59: 1047
34. Mizokawa T, Fujimori A (1998) Phys Rev Lett 80: 1320
35. Anshukova NV, Golovashkin AI, Ivanova LI, Rusakov AP (1992) Superconductivity 5: 644
36. Mott NF (1990) Metal insulator transitions. Taylor and Francis, London
37. Jaime M, Salamon MB, Rubinstein M, Treece RE, Horwitz JS, Chrisey DB (1996) Phys Rev B 54: 11,914
38. Jaime M, Hardner HT, Salamon MB, Rubinstein M, Dorsey P, Emin D (1997) Phys Rev Lett 78: 951
39. Yoon S, Liu HL, Schollerer G, Cooper SL, Han PD, Payne DA, Cheong SW, Fisk Z (1998) Phys Rev B 58: 2795
40. Yamaguchi S, Okimoto Y, Taniguchi H, Tokura Y (1996) Phys Rev B 53: R2926
41. Nyhus P, Yoon S, Kauffman M, Cooper SL, Fisk Z, Sarrao J (1997) Phys Rev B 56: 2717
42. Stern F (1963) Solid state physics, Academic Press, New York, vol 15
43. Kohn W (1964) Phys Rev 133: A171
44. Millis AJ, Coppersmith SN (1990) Phys Rev B 42: 10,807
45. Webb BC, Sievers AJ, Mihalisin T (1986) Phys Rev Lett 57: 1951
46. Hayes W, Loudon R (1978) Scattering of light by crystals. Wiley, New York
47. Heyen ET, Rashkeev SN, Mazin II, Andersen OK, Liu R, Cardona M, Jepsen O (1990) Phys Rev Lett 65: 3048
48. Heyen ET, Kircher J, Cardona M (1992) Phys Rev B 45: 3037
49. Tajima S, Yoshida M, Koshizuka N, Sato H, Uchida S (1992) Phys Rev B 46: 1232
50. Nyhus P, Cooper SL, Fisk Z (1995) Phys Rev B 51: 15,626
51. Nyhus P, Cooper SL, Fisk Z, Sarrao J (1995) Phys Rev B 52: 14,308
52. Nyhus P, Cooper SL, Fisk Z, Sarrao J (1997) Phys Rev B 55: 12,488
53. Yamamoto K, Katsufuji T, Tanabe T, Tokura Y (1998) Phys Rev Lett 80: 1493
54. Katsufuji T, Tokura Y (1994) Phys Rev B 49: 4372
55. Liu HL, Yoon S, Cooper SL, Cheong SW, Han PD, Payne DA (1998) Phys Rev B 58: R10,115
56. Klein MV (1975) Light scattering in solids I. In: Cardona M (ed) Topics in applied physics. Springer, Berlin Heidelberg New York, vol 8, p 169
57. Kosztin J, Zawadowski A (1991) Sol St Commun 78: 1029

58. Ipatova I, Subashiev AV, Voitenko VA (1981) Sol St Commun 37: 893
59. Zawadowski A, Cardona M (1990) Phys Rev B 42: 10,732
60. Chandrasekhar M, Cardona M, Kane EO (1977) Phys Rev B 16: 3579
61. Klein MV, Cooper SL, Slakey F, Rice JP, Bukowski ED, Ginsberg DM (1989) In: Fukuyama H, Maekawa S, Malozemoff AP (eds) Strong correlations and superconductivity. Springer, Berlin Heidelberg New York
62. Cooper SL, Klein MV (1990) Comments Condens Matter Phys 15: 19
63. Fujishima Y, Tokura Y, Arima T, Uchida S (1992) Phys Rev B 46: 11,167
64. Katsufuji T, Okimoto Y, Tokura Y (1995) Phys Rev Lett 75: 3497
65. Taguchi Y, Tokura Y, Arima T, Inaba F (1993) Phys Rev B 48: 511
66. Inaba F, Arima T, Ishikawa T, Katsufuji T, Tokura Y (1995) Phys Rev B 52: R2221
67. Crandles DA, Timusk T, Garrett JD, Greedan JE (1994) Phys Rev B 49: 16,207
68. Kasuya M, Tokura Y, Arima T, Eisaki H, Uchida S (1993) Phys Rev B 47: 6197
69. Crandles DA, Timusk T, Garrett JD, Greedan JE (1992) Physica C 201: 407
70. Imada M, Fujimori A, Tokura Y (1998) Rev Mod Phys 70: 1039
71. Makino H, Inoue IH, Rozenberg MJ, Hase I, Aiura Y, Onari S (1998) Phys Rev B 58: 4384
72. Georges A, Kotliar G, Krauth W, Rozenberg MJ (1996) Rev Mod Phys 68: 13
73. Ahn JS, Bak J, Choi HS, Noh TW, Han JE, Bang Y, Cho JH, Xia QX (1999) Phys Rev Lett 82: 5321
74. Okimoto Y, Katsufuji T, Okada Y, Arima T, Tokura Y (1995) Phys Rev B 51: 9581
75. Dagotto E, Moreo A, Joynt R, Bacci S, Gagliano E (1990) Phys Rev B 41: 2585
76. Hybertsen MS, Stechel EB, Foulkes WMC, Schlüter M (1992) Phys Rev B 45: 10,032
77. Eskes H, Meinders MBJ, Sawatzky GA (1991) Phys Rev Lett 67: 1035
78. (a) Eskes H, Oles AM (1994) Phys Rev Lett 73: 1279; (b) Eskes H, Oles AM (1997) Physica B 230/232: 828
79. Stephan W, Horsch P (1990) Phys Rev B 42: 8736
80. Ohta Y, Tsutsui K, Koshibae W, Shmozato T, Maekawa S (1992) Phys Rev B 46: 14,022
81. Sega I, Prelovsek P (1990) Phys Rev B 42: 892
82. Jaklic J, Prelovsek P (1995) Phys Rev B 52: 6903
83. Cooper SL, Thomas GA, Orenstein J, Rapkine DH, Millis AJ, Cheong SW, Cooper AS (1990) Phys Rev B 41: 11,605
84. Uchida S, Ido T, Takage H, Arima T, Tokura Y, Tajima S (1991) Phys Rev B 43: 7942
85. Romberg H, Alexander M, Nücker N, Adelmann R, Fink J (1990) Phys Rev B 42: 8768
86. Chen CT, Sette F, Ma Y, Hybertsen MS, Stechel EB, Foulkes WM, Schlüter M, Cheong SW, Cooper AS, Rupp LW, Batlogg B, Soo YL, Ming ZH, Krol A, Kao YH (1991) Phys Rev Lett 66: 104
87. Pellegrin E, Nücker N, Fink J, Molodtsov SL, Gutierrez A, Navas E, Strebel O, Hu Z, Domke M, Kaindl G, Uchida S, Nakamura Y, Markl J, Klauda M, Saemann-Ischenko G, Krol A, Peng JL, Li ZY, Greene RL (1993) Phys Rev B 47: 3354
88. Allen JW, Olson CG, Maple MB, Kang JS, Liu LZ, Park JH, Anderson RO, Ellis WP, Markert JT, Kalichaouch Y, Liu R (1990) Phys Rev Lett 64: 595
89. Tokura Y, Okimoto Y, Yamaguchi S, Taniguchi H, Kimura T, Takagi H (1998) Phys Rev B 58: R1699
90. Jarrell M, Freericks JK, Pruschke T (1995) Phys Rev B 51: 11,704
91. Tokura Y, Taguchi Y, Okada Y, Fujishima Y, Arima T, Kumagai K, Iye Y (1993) Phys Rev Lett 70: 2126
92. Katsufuji T, Tokura Y (1994) Phys Rev B 50: 2704
93. Reedyk M, Crandles DA, Cardona M, Garrett JD, Greedan JE (1997) Phys Rev B 55: 1442
94. Choi HS, Ahn JS, Jung JH, Noh TW, Kim DH (1996) Phys Rev B 54: 4621
95. Batlogg B, Emery VJ (1996) Nature 382: 20

96. Cooper SL, Reznik D, Kotz AL, Karlow MA, Liu R, Klein MV, Lee WC, Giapintzakis J, Ginsberg DM, Veal BW, Paulikas AP (1993) Phys Rev B 47: 8233
97. (a) Lyons KB, Fleury PA, Remeika JP, Cooper AS, Negran TJ (1988) Phys Rev B 37: 2353; (b) Lyons KB, Fleury PA, Schneemeyer LF, Waszczak JV (1988) Phys Rev Lett 60: 732
98. Sulewski PE, Fleury PA, Lyons KB, Cheong SW, Fisk Z (1990) Phys Rev B 41: 225
99. Tokura Y, Koshihara S, Arima T, Takagi H, Ishibashi S, Ido T, Uchida S (1990) Phys Rev B 41: 11,657
100. Cooper SL, Thomas GA, Millis AJ, Sulewski PE, Orenstein J, Rapkine DH, Cheong SW, Trevor PL (1990) Phys Rev B 42: 10,785
101. Blumberg G, Abbomonte P, Klein MV, Lee WC, Ginsberg DM, Miller LL, Zibold A (1996) Phys Rev B 53: R11,930
102. Timusk T, Tanner DB (1989) In: Ginsberg DM (ed) Physical properties of high temperature superconductors I. World Scientific, Singapore, p 339
103. Tanner DB, Timusk T (1992) In: Ginsberg DM (ed) Physical properties of high temperature superconductors III. World Scientific, Singapore, p 363
104. Thomas GA, Rapkine DH, Cooper SL, Cheong SW, Cooper AS, Schneemeyer LF, Waszczak JV (1992) Phys Rev B 45: 2474
105. Dagotto E, Moreo A, Ortolani F, Poilblanc D, Riera J, Scalapino DJ (1992) Phys Rev B 45: 10,107
106. Bi XX, Eklund PC (1993) Phys Rev Lett 70: 2625
107. Tranquada JM, Axe JD, Ichikawa N, Moodenbaugh AR, Nakamura Y, Uchida S (1997) Phys Rev Lett 78: 338
108. Hayden SM, Aeppli G, Mook HA, Perring TG, Mason TE, Cheong SW, Fisk Z (1996) Phys Rev Lett 76: 1344
109. Pennington CH, Durand DJ, Slichter CP, Rice JP, Bukowski ED, Ginsberg DM (1989) Phys Rev B 39: 274
110. Lyons KB, Fleury PA, Singh RRP, Sulewski P (1991) In: Reiter G, Horsch P, Psaltakis GC (eds) Dynamics of magnetic fluctuations in high temperature superconductors. Plenum, New York, p 159
111. Blumberg G, Liu R, Klein MV, Lee WC, Ginsberg DM, Gu C, Veal BW, Dabrowski B (1994) Phys Rev B 49: 13,295
112. Rübhausen M, Rieck CT, Dieckmann N, Subke KO, Bock A, Merkt U (1997) Phys Rev B 56: 14,797
113. Varma CM, Littlewood PB, Schmitt-Rink S, Abrahams E, Ruckenstein AE (1989) Phys Rev Lett 63: 1996
114. Ruvalds J, Virostzek A (1991) Phys Rev B 43: 5498
115. Collins RT, Schlesinger Z, Holtzberg F, Chaudhari P, Feild P (1989) Phys Rev B 39: 6571
116. Cooper SL, Gray KE (1994) In: Ginsberg DM (ed) Physical properties of high temperature superconductors IV. World Scientific, Singapore p 61, and references therein
117. Takenaka K, Mizuhashi K, Takagi H, Uchida S (1994) Phys Rev B 50: 6534
118. Batlogg B, Hwang HY, Takagi H, Cava RJ, Kao HL, Kwo J (1994) Physica C 235/240: 130
119. Lichtenberg F, Catana A, Mannhart J, Schlom DG (1992) Appl Phys Lett 60: 1138
120. Homes CC, Timusk T, Liang R, Bonn DA, Hardy WN (1993) Phys Rev Lett 71: 1645
121. Karlow MA, Cooper SL, Kotz AL, Klein MV, Han PD, Payne DA (1993) Phys Rev B 48: 6499
122. Eskes H, Oles AM (1997) Phys Rev B 55: 2032
123. Pei S, Jorgensen JD, Dabrowski B, Hinks DG, Richards DR, Mitchell AW, Newsam JM, Sinha SK, Vaknin D, Jacobson AJ (1990) Phys Rev B 41: 4126
124. Tanh TD, Koma A, Tanaka S (1980) Appl Phys 22: 205
125. Tajima S, Uchida S, Masaki A, Takagi H, Kitazawa K, Tanaka S, Sugai S (1987) Phys Rev B 35: 696

126. Tajima S, Uchida S, Masaki A, Takagi H, Kitazawa K, Tanaka S, Katsui A (1985) Phys Rev B 32: 6302
127. Mattheiss LF, Hamann DR (1983) Phys Rev B 28: 4227
128. Bansil A, Kaprzyk S (1991) Phys Rev B 43: 10,335
129. Mattheiss LF, Hamann DR (1988) Phys Rev Lett 60: 2681
130. Cox DE, Sleight AW (1979) Acta Crystallogr B 35: 1
131. Weber W (1987) Jpn J Appl Phys 26: 981
132. Yoshioka D, Fukuyama H (1985) J Phys Soc Jpn 54: 2996
133. Rice TM, Sneddon L (1981) Phys Rev Lett 47: 689
134. Juarczek E, Rice TM (1986) Europhys Lett 1: 225
135. Kostur VN, Allen PB (1997) Phys Rev B 56: 3105
136. Puchkov AV, Timusk T, Karlow MA, Cooper SL, Han PD, Payne DA (1996) Phys Rev B 54: 6686
137. Puchkov AV, Timusk T, Karlow MA, Cooper SL, Han PD, Payne DA (1995) Phys Rev B 52: R9855
138. Sugai S (1989) Sol St Commun 72: 1187
139. Sato H, Tajima S, Takagi H, Uchida S (1989) Nature 338: 241
140. Uchida S, Tajima S, Masaki A, Sugai S, Kitazawa K, Tanaka S (1985) J Phys Soc Japan 54: 4395
141. Blanton SN, Collins RT, Kelleher KH, Rotter LD, Schlesinger Z, Hinks DG, Zheng Z (1993) Phys Rev B 47: 996
142. Fujimori A, Hase I, Namatame H, Fujishima Y, Tokura Y, Eisaki H, Uchida S, Takegahara K, de Groot FMF (1992) Phys Rev Lett 69: 1796
143. Inoue IH, Hase I, Aiura Y, Fujimori A, Haruyama Y, Maruyama T, Nishihara Y (1995) Phys Rev Lett 74: 2539
144. Morikawa K, Mizokawa T, Kobayashi K, Fujimori A, Eisaki H, Uchida S, Iga F, Nishihara Y (1995) Phys Rev B 52: 13,711
145. Dougier P, Fan JC, Goodenough JB (1975) J Solid State Chem 14: 247
146. Zhang XY, Rozenberg MJ, Kotliar G (1995) Phys Rev Lett 74: 1500
147. Thomas GA, Rapkine DH, Carter SA, Millis AJ, Rosenbaum TF, Metcalf P, Honig JM (1994) Phys Rev Lett 73: 1529
148. Thomas GA, Rapkine DH, Carter SA, Rosenbaum TF, Metcalf P, Honig DF (1994) J Low Temp Phys 95: 33
149. Gunnarsson O, Koch E, Martin RM (1996) Phys Rev B 54: R11,026
150. Lu JP (1994) Phys Rev B 49: 5687
151. Torrance JB, Lacorre P, Nazzal AI, Ansaldo EJ, Niedermayer Ch (1992) Phys Rev B 45: 8209
152. Canfield PC, Thompson JD, Cheong SW, Rupp LW (1993) Phys Rev B 47: 12,357
153. Obradors X, Paulius LM, Maple MB, Torrance JB, Nazzal AI, Fontcuberta J, Granados X (1993) Phys Rev B 47: 12,353
154. Garcia-Munoz JL, Rodriguez-Carvajal J, Lacorre P (1994) Phys Rev B 50: 978
155. Arima T, Tokura Y (1995) J Phys Soc Jpn 64: 2488
156. Garcia-Munoz JL, Rodriguez-Carvajal J, Lacorre P (1992) Europhys Lett 20: 241
157. Katsufuji T, Okimoto Y, Arima T, Tokura Y, Torrance JB (1995) Phys Rev B 51: 4830
158. Sreedhar K, Honig JM, Darwin M, McElfresh M, Shand PM, Xu J, Crooker BC, Spalek J (1992) Phys Rev B 46: 6832
159. Liu HL, Cooper SL, Cheong SW (1998) Phys Rev Lett 81: 4684
160. Barker AS, Halperin BI, Rice TM (1968) Phys Rev Lett 20: 384
161. Barker AS, Remeika JP (1974) Phys Rev B 10: 987
162. Callagan A, Moeller CW, Ward R (1966) Inorg Chem 5: 1573
163. Maeno Y, Hashimoto H, Yoshida K, Nishizaki S, Fujita T, Bednorz JG, Lichtenberg F (1994) Nature (London) 372: 532
164. Puchkov AV, Schabel MC, Basov DN, Startseva T, Cao G, Timusk T, Shen ZX (1998) Phys Rev Lett 81: 2747

165. Bozovic I, Kim JH, Harris JS, Eom CB, Phillips JM, Cheung JT (1994) Phys Rev Lett 73: 1436
166. Yamanaka A, Asayama N, Sasada M, Inoue K, Udagawa M, Nishizaki S, Maeno Y, Fujita T (1996) Physica C 263: 516
167. Kirillov D, Suzuki Y, Antognazza L, Char K, Bozovic I, Geballe TH (1995) Phys Rev B 51: 12,825
168. Fujioka K, Okamoto J, Mizokawa T, Fujimori A, Hase I, Abbate M, Lin HJ, Chen CT, Takeda Y, Takano M (1997) Phys Rev B 56: 6380
169. Cox PA, Edgell RG, Goodenough JB, Kamnett A, Naishi CC (1983) J Phys C 16: 6221
170. Singh DJ (1996) J Appl Phys 79: 4818
171. Cao G, McCall S, Shepard M, Crow JE, Guertin RP (1997) Phys Rev B 56: 321
172. Iliev MN, Litvinchuk AP, Lee HG, Chen CL, Dezaneti LM, Chu CW, Ivanov VG, Abrashev MV, Popov VN (1999) Phys Rev B 59: 364
173. Kostic P, Okada Y, Collins NC, Schlesinger Z, Reiner JW, Klein L, Kapitulnik A, Geballe TH, Beasley MR (1998) Phys Rev Lett 81: 2498
174. Katsufuji T, Kasai M, Tokura Y (1995) Phys Rev Lett 76: 126
175. Schiffer P, Ramirez AP, Bao W, Cheong SW (1995) Phys Rev Lett 75: 3336
176. Hwang HY, Cheong SW, Radaelli PG, Marezio M, Batlogg B (1995) Phys Rev Lett 75: 914
177. Zener C (1951) Phys Rev 82: 403
178. Anderson PW, Hasegawa H (1955) Phys Rev 100: 675
179. de Gennes PG (1960) Phys Rev 118: 141
180. Millis AJ, Littlewood PB, Shraiman BI (1995) Phys Rev Lett 74: 5144
181. Millis AJ, Mueller R, Shraiman BI (1996) Phys Rev Lett 77: 175
182. Millis AJ (1998) Nature 392: 147
183. Torrance JB, Shafer MW, McGuire TR (1972) Phys Rev Lett 29: 1168
184. Cheong SW, Hwang HW, Batlogg B, Rupp LW (1996) Sol St Commun 98: 163
185. Majumdar P, Littlewood P (1998) Phys Rev Lett 81: 1314
186. Ramirez AP, Subramanian MA (1997) Science 277: 546
187. Majumdar P, Littlewood P (1998) Nature (London) 395: 479
188. Jung JH, Kim KH, Noh TW, Choi EJ, Yu J (1998) Phys Rev B 57: 11,043
189. Jung JH, Kim KH, Eom DJ, Noh TW, Choi EJ, Yu J, Kwon YS, Chung Y (1997) Phys Rev B 55: 15,489
190. Kaplan SG, Quijada M, Drew HD, Tanner DB, Xiong GC, Ramesh R, Kwon C, Venkatesan T (1996) Phys Rev Lett 77: 2081
191. Quijada M, Cerne J, Simpson JR, Drew HD, Ahn KH, Millis AJ, Shreekala R, Ramesh R, Rajeswari M, Venkatesan T (1998) Phys Rev B 58: 16,093
192. Okimoto Y, Katsufuji T, Ishikawa T, Urushibara A, Arima T, Tokura Y (1995) Phys Rev Lett 75: 109
193. Sarma DD, Shanthi N, Krishnakumar SR, Saitoh T, Mizokawa T, Sekiyama A, Kobayashi K, Fujimori A, Weschke E, Meier R, Kaindl G, Takeda Y, Takano M (1996) Phys Rev B 53: 6873
194. Barker AS, Remeika JP (1970) Sol St Commun 8: 1521
195. Feinleib J, Paul W (1967) Phys Rev 155: 841
196. Barker AS, Verleur HW, Guggenheim HJ (1966) Phys Rev Lett 17: 1286
197. Verleur HW, Barker AS, Berglund CN (1968) Phys Rev 172: 788
198. Ishihara S, Yamanaka M, Nagaosa N (1997) Phys Rev B 56: 686
199. Shiba H, Shiina R, Takahashi A (1997) J Phys Soc Japan 66: 941
200. Kilian R, Khaliullin G (1998) Phys Rev B 58: R11,841
201. Saitoh E, Okimoto Y, Tomioka Y, Katsufuji T, Tokura Y (1999) Phys Rev B 60: 10,362
202. Kim KH, Gu JY, Choi HS, Park GW, Noh TW (1996) Phys Rev Lett 77: 1877
203. Kim KH, Jung JH, Noh TW (1998) Phys Rev Lett 81: 1517
204. Billinge SJL, DiFrancesco RG, Kwei GH, Neumeier JJ, Thompson JD (1996) Phys Rev Lett 77: 715
205. Louca D, Egami T (1997) J Appl Phys 81: 5484

206. Podobedov VB, Weber A, Romero DB, Rice JP, Drew HD (1998) Phys Rev B 43: 43
207. Louca D, Egami T, Brosha EL, Röder H, Bishop AR (1997) Phys Rev B 56: R8475
208. Booth CH, Bridges F, Kwei GH, Lawrence JM, Cornelius AL, Neumeier JJ (1998) Phys Rev Lett 80: 853
209. Arovas DP, Guinea F (1998) Phys Rev B 58: 9150
210. Riera J, Hallberg K, Dagotto E (1997) Phys Rev Lett 79: 713
211. Dagotto E, Yunoki S, Malvezzi AL, Moreo A, Hu J, Capponi S, Poilblanc D, Furukawa N (1998) Phys Rev B 58: 6414
212. Jung JH, Kim KH, Lee HJ, Ahn JS, Hur NJ, Noh TW, Kim MS, Park JG (1999) Phys Rev B 59: 3793
213. Salamon MB (unpublished results)
214. Perring TG, Aeppli G, Moritomo Y, Tokura Y (1997) Phys Rev Lett 78: 3197
215. Moritomo Y, Asamitsu A, Kuwahara H, Tokura Y (1996) Nature (London) 380: 141
216. Chauvet O, Goglio G, Molinie P, Corraze B, Brohan L (1998) Phys Rev Lett 81: 1102
217. Dessau DS, Saitoh T, Park CH, Shen ZX, Villella P, Hamada N, Moritomo Y, Tokura Y (1998) Phys Rev Lett 81: 192
218. Park JH, Kimura T, Tokura Y (1998) Phys Rev B 58: R13,330
219. Romero DB, Podobedov VB, Weber A, Rice JP, Mitchell LF, Sharma RP, Drew HD (1998) Phys Rev B 58: R14,737
220. Mitchell JF, Argyriou DN, Jorgensen JD, Hinks DG, Potter CD, Bader SD (1997) Phys Rev B 55: 63
221. Kimura T, Tomioka Y, Asamitsu A, Tokura Y (1998) Phys Rev Lett 81: 5920
222. Verwey EJW, Haaymann PW, Romeijn FC (1941) J Chem Phys 15: 181
223. Tomioka Y, Asamitsu A, Kuwahara H, Moritomo Y, Tokura Y (1996) Phys Rev B 53: R1689
224. Kivelson SA, Fradkin E, Emery VJ (1998) Nature 393: 550
225. Cheong SW, Hwang HY (1999) In: Tokura Y (ed) Colossal magnetoresistance oxides. Gordon and Breach
226. Okimoto Y, Tomioka Y, Onose Y, Otsuka Y, Tokura Y (1998) Phys Rev B 57: R9377
227. Okimoto Y, Tomioka Y, Onose Y, Otsuka Y, Tokura Y (1999) Phys Rev B 59: 7401
228. Wollan EO, Koehler WC (1955) Phys Rev 100: 5455
229. Katsufuji T, Tanabe T, Ishikawa T, Fukuda Y, Arima T, Tokura Y (1996) Phys Rev B 54: R14,230
230. Ishikawa T, Park SK, Katsufuji T, Arima T, Tokura Y (1998) Phys Rev B 58: R13,326
231. Park SK, Ishikawa T, Tokura Y (1998) Phys Rev B 58: 3717
232. Calvani P, DeMarzi G, Dore P, Lupi S, Maselli P, D'Amore F, Gagliardi S, Cheong SW (1998) Phys Rev Lett 81: 4504
233. Bao W, Axe JD, Chen CH, Cheong SW (1997) Phys Rev Lett 78: 543
234. Roy M, Mitchell JF, Ramirez AP, Schiffer P (1998) Phys Rev B 58: 5185
235. Moritomo Y, Takeo M, Liu XJ, Akimoto T, Nakamura A (1998) Phys Rev B 58: R13,334
236. Ramirez AP, Gammel PL, Cheong SW, Bishop DJ, Chandra P (1996) Phys Rev Lett 76: 447
237. Cheong SW, Hwang HY, Chen CH, Batlogg B, Rupp LW, Carter SA (1994) Phys Rev B 49: 7088
238. Crandles DA, Timusk T, Garrett JD, Greedan JE (1993) Physica C 216: 94
239. Lee PA, Rice TM, Anderson PW (1973) Phys Rev Lett 31: 462
240. Wilson JA, DiSalvo FJ, Mahajan F (1975) Adv Phys 24: 117
241. McMillan WL (1977) Phys Rev B 16: 643
242. Blumberg G, Klein MV, Cheong SW (1998) Phys Rev Lett 80: 564
243. Schlesinger Z, Fisk Z, Zhang HT, Maple MB, DiTusa JF, Aeppli G (1993) Phys Rev Lett 71: 1748
244. Bucher B, Schlesinger Z, Canfield PC, Fisk Z (1994) Phys Rev Lett 72: 522
245. Aeppli G, Fisk Z (1992) Comments Condens Matter Phys 16: 155
246. Raccah PM, Goodenough JB (1967) Phys Rev 155: 932

247. Abbate M, Fuggle JC, Fujimori A, Tjeng LH, Chen CT, Potze R, Sawatzky GA, Eisaki H, Uchida S (1993) Phys Rev B 47: 16,124
248. Potze RH, Sawatzky GA, Abbate M (1995) Phys Rev B 51: 11,501
249. Korotin MA, Ezhov SY, Solovyev IV, Anisimov VI, Khomskii DI, Sawatzky GA (1996) Phys Rev B 54: 5309
250. Yamaguchi S, Okimoto Y, Tokura Y (1997) Phys Rev B 55: R8666
251. Yamaguchi S, Taniguchi H, Takagi H, Arima T, Tokura Y (1995) J Phys Soc Japan 64: 1885
252. Mira J, Rivas J, Vázquez M, García-Beneytez JM, Arcas J, Sánchez RD, Señarís-Rodríguez MA (1999) Phys Rev B 59: 123
253. Kuiper P, Guo JH, Sathe C, Duda LC, Nordgren J, Pothuizen JJM, de Groot FMF, Sawatzky GA (1998) Phys Rev Lett 80: 5204
254. Liu HL, Yoon S, Cooper SL, Cao G, Crow JE (1999) Phys Rev B 60: R6980

Author Index Volumes 1–98

Diemann E, see Müller A (1973) *14*: 23–47

Dirken MW, see Thiel RC (1993) *81*: 1–40

Dobiás B (1984) Surfactant Adsorption on Minerals Related to Flotation. *56*: 91–147

Doi K, Antanaitis BC, Aisen P (1998) The Binuclear Iron Centers of Uteroferrin and the Purple Acid Phosphatases. *70*: 1–26

Domcke W, see Bradshaw AM (1975) *24*: 133–170

Donnio B, Bruce DW (1999) Metallomesogens 95: 193–247

Dophin D, see Morgan B (1987) *64*: 115–204

Doughty MJ, Diehn B (1980) Flavins as Photoreceptor Pigments for Behavioral Responses. *41*: 45–70

Drago RS (1973) Quantitative Evaluation and Prediction of Donor-Acceptor Interactions. *15*: 73–139

Dreher C, see Buchler JW (1995) *84*: 1–70

Drillon M, Darriet J (1992) Progress in Polymetallic Exchange-Coupled Systems, some Examples in Inorganic Chemistry. *79*: 55–100

Duffy JA (1977) Optical Electronegativity and Nephelauxetic Effect in Oxide Systems. *32*: 147–166

Dunham WR, see Bearden AJ (1970) *8*: 1–52

Dunn MF (1975) Mechanisms of Zinc Ion Catalysis in Small Molecules and Enzymes. *23*: 61–122

Ealtough DJ, see Izatt RM (1973) *16*: 161–189

Egami T (2001) Local Atomic Structure of CMR Manganites and Related Oxides. *98*: 115–160

Eller PG, see Ryan RR (1981) *46*: 47–100

Emmerling A, see Fricke J (1991) *77*: 37–88

Emsley E (1984) The Composition, Structure and Hydrogen Bonding of the β-Diketones. 57: 147–191

Englman R (1981) Vibrations in Interaction with Impurities. *43*: 113–158

Epstein IR, Kustin K (1984) Design of Inorganic Chemical Oscillators. *56*: 1–33

Ermer O (1976) Calculations of Molecular Properties Using Force Fields. Applications in Organic Chemistry. *27*: 161–211

Ernst RD (1984) Structure and Bonding in Metal-Pentadienyl and Related Compounds. *57*: 1–53

Erskine RW, Field BO (1976) Reversible Oxygenation. *28*: 1–50

Evain M, Brec R (1992) A new Approach to Structural Description of Complex Polyhedra Containing Polychalcogenide Anions. *79*: 277–306

Fackler PH, see Clarke MJ (1982) *50*: 57–58

Fajans K (1967) Degrees of Polarity and Mutual Polarization of Ions in the Molecules of Alkali Fluorides, SrO and BaO. *3*: 88–105

Fan M-F, see Lin Z (1997) *87*: 35–80

Fee JA (1975) Copper Proteins – Systems Containing the "Blue" Copper Center. *23*: 1–60

Feeney RE, Komatsu SK (1966) The Transferrins. *1*: 149–206

Fehlner TP (1997) Metalloboranes. *87*: 111–136

Felsche J (1973) The Crystal Chemistry of the Rare-Earth Silicates. *13*: 99–197

Ferreira R (1976) Paradoxical Violations of Koopmans' Theorem, with Special Reference to the 3d Transition Elements and the Lanthanides. *31*: 1–21

Fichtinger-Schepman AMJ, see Reedijk J (1987) *67*: 53–89

Fidelis IK, Mioduski T (1981) Double-Double Effect in the Inner Transition Elements. *47*: 27–51

Field BO, see Erskine RW (1976) *28*: 1–50

Figlar J, see Maroney MJ (1988) *92*: 1–66

Fischer J, see Mathey F (1984) *55*: 153–201

Fischer S, see Tytho KH (1999) *93*: 125–317

Follmann H, see Lammers M (1983) *54*: 27–91

Naegele JR, Ghijsen J (1985) Localization and Hybridization of 5f States in the Metallic and Ionic Bond as Investigated by Photoelectron Spectroscopy. *59/60*: 197–262

Nag K, Bose SN (1985) Chemistry of Tetra- and Pentavalent Chromium. *63*: 153–197

Nalewajski RF (1993) The Hardness Based Molecular Charge Sensitivities and Their Use in the Theory of Chemical Reactivity. *80*: 115–186

Natan MJ, see Hoffman BM (1991) *75*: 85–108

Neilands JB, see Liu A (1984) *58*: 97–106

Neilands JB, see Chimiak A (1984) *58*: 89–96

Neilands JB (1972) Evolution of Biological Iron Binding Centres. *11*: 145–170

Neilands JB (1984) Methodology of Siderophores. *58*: 1–24

Neilands JB (1966) Naturally Occurring Non-Porphyrin Iron Compounds. *1*: 59–108

Neilands JP, see Cheh AM (1976) *29*: 123–169

Nelson JH, see Mathey F (1984) *55*: 153–201

Nickerson DP, see Wong L-L (1997) *88*: 175–208

Nieboer E (1975) The Lanthanide Ions as Structural Probes in Biological and Model Systems. *22*: 1–47

Nieter Burgmeier SJ (1998) Electron Transfer in Transition Metal-Pteridine Systems. *92*: 67–120

Nocek JM, see Hoffman BM (1991) *75*: 85–108

Nomoto K, see Sugiura Y (1984) *58*: 107–135

Novack A (1974) Hydrogen Bonding in Solids. Correlation of Spectroscopic and Crystallographic Data. *18*: 177–216

Nultsch W, Häder D-P (1980) Light Perception and Sensory Transduction in Photosynthetic Prokaryotes. *41*: 111–139

Nyholm RS, see Hall DI (1973) *15*: 3–51

O'Keeffe M, see Brese NE (1992) *79*: 307–378

O'Keeffe M, Hyde BG (1985) An Alternative Approach to Non-Molecular Crystal Structures with Emphasis on the Arrangements of Cations. *61*: 77–144

O'Keeffe M (1989) The Prediction and Interpretation of Bond Lengths in Crystals. *71*: 161–190

Odom JD (1983) Selenium Biochemistry. Chemical and Physical Studies. *54*: 1–26

Oehme I, see Wolfbeis OS (1996) *85*: 51–98

Oelkrug D (1971) Absorption Spectra and Ligand Field Parameters of Tetragonal 3d-Transition Metal Fluorides. *9*: 1–26

Oosterhuis WT (1974) The Electronic State of Iron in Some Natural Iron Compounds: Determination by Mössbauer and ESR Spectroscopy. *20*: 59–99

Orchin M, Bollinger DM (1975) Hydrogen-Deuterium Exchange in Aromatic Compounds. *23*: 167–193

Ostrovskii PI (1999) Packing and Molecular Conformation, and Their Relationship with LC Phase Behaviour. *94*: 199–240

Ozaki Y, see Kitaagawa T (1987) *64*: 71–114

Pace LJ, see Ibers JA (1982) *50*: 1–55

Padhye SB, see West DC (1991) *76*: 1–50

Paolesse R, see Licoccia S (1995) *84*: 71–134

Parr RG, see Chattaraj PK (1993) *80*: 11–26

Patil SK, see Ramakrishna VV (1984) *56*: 35–90

Peacock RD (1975) The Intensities of Lanthanide $f \leftrightarrow f$ Transitions. *22*: 83–122

Pearson RG (1993) Chemical Hardness – An Historial Introduction. *80*: 1–10

Pecoraro VL, see Slebodnick C (1997) *89*: 51–108

Pelikán P, see Boca R (1989) *71*: 57–97

Penfield KW, see Solomon EI (1983) *53*: 1–56

Penneman RA, Ryan RR, Rosenzweigh A (1973) Structural Systematics in Actinide Fluoride Complexes. *13*: 1–52